Unifying information on reactivity of NiFe hydrogenases from different sample handling and spectroelectrochemical techniques

Wangzhe Li

Linacre College

Hilary Term 2026

A thesis submitted to the Board of the Faculty of Physical Sciences, for the degree of

Doctor of Philosophy, University of Oxford

Unifying information on [NiFe]-hydrogenases from different sample handling and spectroelectrochemical techniques

Wangzhe Li, Linacre College, University of Oxford

A thesis submitted for the degree of Doctor of Philosophy, Hilary Term 2026

This thesis investigates the catalytic mechanism and reactivity of [NiFe]-hydrogenases from *E. coli* by developing and implementing integrated spectroscopic, structural, and electrochemical approaches.

By employing an *in-situ* infrared microspectroelectrochemical method to determine the redox dependence of catalytic intermediates, an *ex-situ* electrochemical system was designed for precise redox poising of single crystals while maintaining their accessibility for further measurements. This approach yielded high-resolution crystal structures of key catalytic intermediates, including the Ni_a-SI, Ni_a-R, Ni_a-C, and Ni_a-L states. Furthermore, the proximal cluster in *E. coli* Hyd-1 exhibits a distinctive conformational change associated with its redox activity. A collection of inhibitor-bound crystal structures is also reported, providing insights into the effects of inhibitors.

A novel spectroelectrochemical methodology enables *in-situ* X-ray absorption spectroscopy measurements of biological samples at ambient temperature. This technique was validated through XANES potential titration and EXAFS analysis on the model metalloprotein Cu-azurin.

Overall, this work highlights the value of integrated methodologies and constitutes a significant contribution to bioinorganic chemistry, offering a versatile paradigm for investigating mechanisms in a broad range of metalloenzymes under diverse conditions.

Acknowledgements

I would first like to express my deepest gratitude to my supervisor, Prof. Kylie Vincent. Her unwavering support and invaluable guidance have been instrumental throughout my DPhil studies. I am grateful for the opportunity she provided me to join the KAV research group, and for her constant encouragement and mentorship over the years.

I extend my sincere thanks to Dr. Stephen Carr for providing the essential protein crystals during the initial phase of my project and for instructing me in protein crystallisation techniques. I also acknowledge his significant collaboration on the X-ray crystallography component of this thesis, which included data collection, analysis, and the creation of exemplary figures. Special thanks are due to Phil and Non for their expert guidance throughout my DPhil. Their countless helpful and inspirational discussions were pivotal to my work. I am grateful to Dr. Stephen Best for his insightful input into the design of the XAS-SEC cell, and to Prof. Sofia Diaz-Moreno for her guidance on XAS theory and analysis.

A big thank you to Sam, who has been a fantastic colleague, flatmate, and teammate, and with whom I shared the experience of gaining 10 kg in Oxford. My thanks also extend to the rest of the KAV group members, Ting, Shinny, Jiawen, and also including the 'whisky society' members Xu, Yu, Jiaao, Barney, and Jack. Each of you made my time in the lab both meaningful and enjoyable.

Most importantly, I thank my parents for their immense support and motivation, both financial and emotional. Finally, I wish to thank my partner, Jinyang, for her companionship, unconditional support, patience, and love.

Abbreviations

CE	counter electrode
CV	cyclic voltammetry
Cys	cysteine
cyt*b*	cytochrome *b*
***D. vulgaris* MF/ *Dv*MF**	*Desulfovibrio vulgaris* Miyazaki F
delta TM	delta transmembrane
***E. coli*.**	*Escherichia coli*
EPR	electron paramagnetic resonance
EXAFS	extended X-ray absorption fine structure
IR	infrared
MBH	membrane bound hydrogenase
OCP	open circuit potential
PCET	proton coupled electron transfer
PFE	protein film electrochemistry
SHE	standard hydrogen electrode
SEC	spectroelectrochemistry / spectroelectrochemical
ν_{CO}	carbon monoxide vibrational stretch
ν_{CN}	cyanide vibrational stretch
WE	working electrode
XAS	X-ray absorption spectroscopy

Table of Contents

Chapter 1: Introduction

Overview

Hydrogen is attractive as a clean transportable fuel for the post-fossil fuel era.[1–3] The best industrial catalysts presently available for fuel cells or electrolytic H_2 production are expensive metals like platinum (Pt) or palladium (Pd).[4,5] However, hydrogen has been utilised as an energy source in nature for billions of years through a class of metalloproteins called hydrogenases.[1,6,7] These enzymes can catalyse the interconversion between molecular hydrogen (H_2) and protons (H^+) ($H_2 \rightleftharpoons 2H^+ + 2e^-$) at comparable turnover frequencies (> 1000 s^{-1}) to precious metal catalysts by adopting earth-abundant metals in their active site.[8] Hydrogenases can catalyse either the oxidation of H_2 or the reduction of H^+ *in vivo*, depending on their types and physiological functions.[7] This has drawn significant research interest in understanding the chemistry of hydrogenases and their applications in biocatalysis, fuel cells, and as inspiration for biomimetic catalysis.[9–12]

1.1 Types of Hydrogenases

Three phylogenetically distinct types of hydrogenases are classified based on their gene sequences and active site composition: [FeFe]-, [Fe]-, and [NiFe]-hydrogenases. In this section, [FeFe]- and [Fe]- hydrogenases will be briefly introduced, while [NiFe]-hydrogenases will be discussed in greater detail in the next section.

1.1.1 [FeFe]-hydrogenases

[FeFe]-hydrogenases are found in anaerobic prokaryotes and some unicellular eukaryotes.[7,13] Their catalytic active site, known as the H-cluster, is a cubic [4Fe4S] cluster coordinated by a binuclear FeFe centre. The two iron atoms in the bimetallic centre are named "Fe_p" (Fe proximal) and "Fe_d" (Fe distal) with respect to their distance to the [4Fe4S] cluster. Each Fe is coordinated by one terminal CO and CN^- ligand, with an additional bridging CO ligand between them. A five-atom ligand, aza-dithiolate, is also coordinated at the bridging position, linking the two-iron centre.[14,15] The molecular structure of the active site "H-cluster" is shown in Figure 1.1.

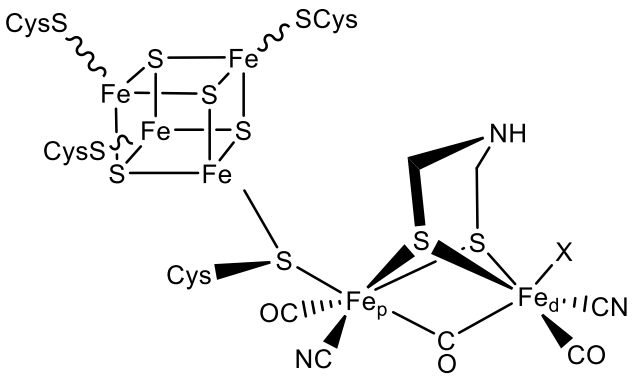

Figure 1.1: The "H-cluster" active site structure. The two-iron site anchors to a cubic [4Fe4S] cluster by a sulfide from cysteine. X represents distinct ligands, such as H^- and CO.

The distal Fe_d has an open coordination site and is believed to bind the substrate (H_2). The aza-dithiolate ligand plays a critical role in the catalytic mechanism by serving as a proton acceptor, facilitating the heterolytic cleavage of H_2 via a frustrated Lewis pair (FLP) mechanism.[13,16]

Recent advances in understanding [FeFe]-hydrogenases have been achieved through the use of synthetic active sites introduced into the apoenzyme.[17] Artificial active sites incorporated

into native enzymes have been utilised to investigate catalytic mechanisms and explore biocatalytic applications.

1.1.2 [Fe]-hydrogenases

[Fe]-hydrogenases, also known as H_2-forming methylene-tetrahydromethanopterin (methylene-H_4MPT) dehydrogenases, are found in methanogens. These enzymes lack FeS clusters and exhibit distinct catalytic properties. Their enzymatic function is to catalyse the reversible reduction of methylene-H_4MPT to methenly-H_4MPT^+ coupled with H^+/H_2.[18]

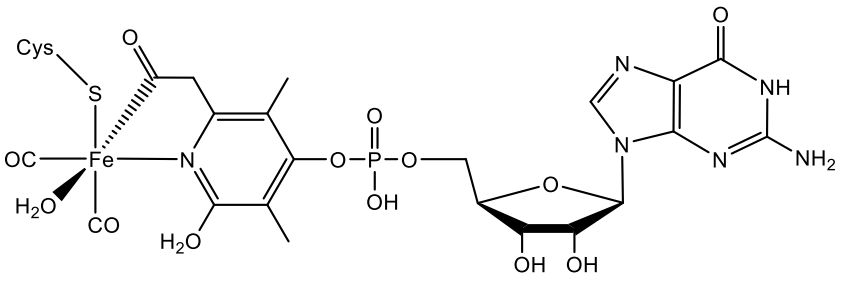

Figure 1.2: The chemical structure of the FeGP cofactor of [Fe]-hydrogenase in the open form.

The active site of [Fe]-hydrogenases contains a mononuclear Fe metal ion in an octahedral coordination environment, with two CO ligands, a thiolate residue from a cysteine, and a bidentate guanilypyridinol cofactor via a sp^2-hybridized nitrogen and an acyl group carbon. The sixth coordination site at the catalytic centre, trans to the acyl ligand, is occupied by a solvent molecule and is proposed to be the H_2-binding site.[18,19]

1.1.3 [NiFe]-hydrogenases

[NiFe]-hydrogenases are widespread in bacteria and archaea. They contain a binuclear metal active site with one Ni and one Fe. Unlike [FeFe]-hydrogenases, [NiFe]-hydrogenases are primarily involved in hydrogen oxidation but exhibit some catalytic activity toward H_2 production. The classification, architecture, and catalytic mechanism of [NiFe]-hydrogenases will be discussed in detail in this section.

Classification of [NiFe]-hydrogenases

[NiFe]-hydrogenases have been classified into four main groups by Vignais and Billoud based on sequence analyses of protein subunits. The following section summarises the categorised groups and their functions.[6]

Group 1: Membrane-bound H_2 uptake hydrogenases. These hydrogenases facilitate respiratory H_2 oxidation linked to quinone reduction. The electrons are transferred to anaerobic acceptors for reduction, such as NO_3^-, CO_2, and SO_4^{2-}. In the case of aerobic respiration, H_2 oxidation is coupled to O_2 reduction. [20] The [NiFe]-hydrogenase-1 (Hyd-1) and [NiFe]-hydrogenase-2 (Hyd-2) from *Escherichia coli* (*E. coli*), studied in this thesis, both belong to Group 1 and will be discussed separately later.

Group 2: This group comprises two types of NiFe-hydrogenases: H_2 uptake hydrogenases (2a) and H_2 sensing, or regulatory hydrogenases (2b). Group 2b hydrogenases exhibit low H_2 oxidation activity and function as H_2 sensors in a signal transduction cascade, regulating

hydrogenase gene transcription in response to H_2.

Group 3: Cytoplasmic cofactor-coupled bidirectional hydrogenases, which are further divided into four subgroups. These enzymes reversibly couple H_2 oxidation to the reduction of soluble cofactors at other subunits. Examples include F_{420} (3a), $NADP^+$ (3b), coenzyme M-disulfide bond-coenzyme B (CoM-S-S-CoB) (3c), and NAD^+ (3d).

Group 4: Membrane-bound H_2-evolving hydrogenases. These multimeric enzymes remove excess electrons generated from the anaerobic oxidation of small organic compounds, such as CO or formate, via the reduction of protons in water.

Additionally, there is a group 5 Actinobacterial H_2 uptake [NiFe]-hydrogenase. This unique hydrogenase was identified approximately a decade ago, distinguished by its distinctive sequence compared to other 4 groups and exceptional low K_m for H_2. It plays a critical role in the atmospheric H_2 cycle, consuming up to 80% of atmospheric H_2 annually.[21]

In addition to classification based on biological functions, [NiFe]-hydrogenases are commonly categorised into two types based on their resistance to O_2.[22–24] The "standard" hydrogenases, which catalyse H^+/H_2 under anaerobic conditions *in vivo*, lose their activity in the presence of exogenous O_2. These enzymes, which cannot function in the presence of O_2, are also referred to as "O_2-sensitive" hydrogenases. After inactivation by O_2, these enzymes are not permanently damaged and can undergo reactivation under anaerobic conditions through reduction. In contrast, a few [NiFe]-hydrogenases possess unique defence mechanisms against O_2, enabling them to maintain catalytic activity in the presence of O_2.[25] These enzymes are termed O_2-tolerant [NiFe]-hydrogenases. The details of O_2 tolerance will be discussed further

in Section 1.3.4. Hyd-1 and Hyd-2 from *E. coli* studied in this thesis are O_2-tolerant and O_2-sensitive, respectively.

Escherichia coli [NiFe]-hydrogenases

E. coli, an enteric facultative anaerobe, natively produces four membrane-bound [NiFe]-hydrogenases, named Hyd-1 to Hydrogenase-4 (Hyd-4). Hyd-1 and Hyd-2 are Group 1 respiratory H_2-uptake hydrogenases, while Hyd-3 and Hyd-4 are Group 4 H_2-evolving hydrogenases.[26,27] The focus of this thesis is on the former two periplasmic membrane-bound enzymes, Hyd-1 and Hyd-2.

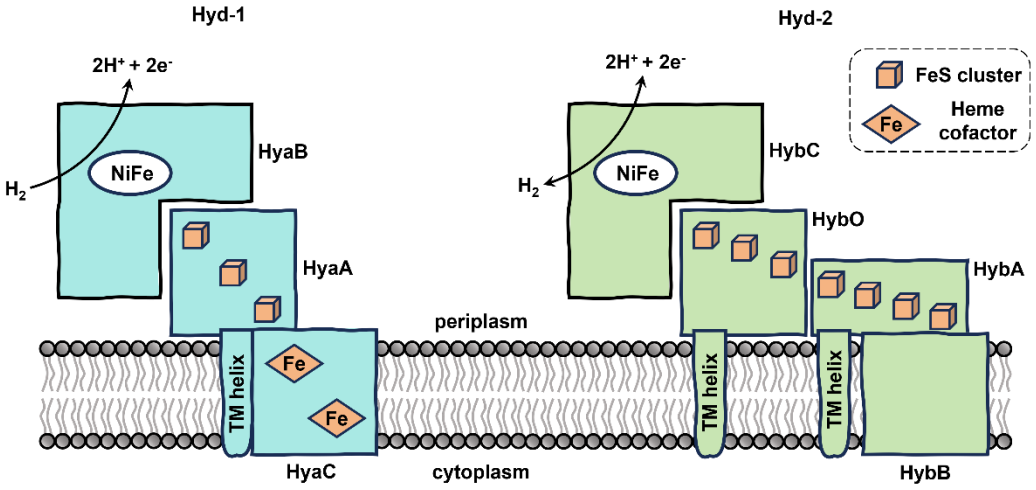

Figure 1.3: Representation of two native periplasmic membrane-bound *E. coli* hydrogenases, Hyd-1 on the left and Hyd-2 on the right. Figure prepared with Microsoft PowerPoint.

Hyd-1 and Hyd-2 are both Group 1 hydrogenases, sharing aligned gene sequences for their basic unit, an αβ heterodimer: HyaB and HyaA in Hyd-1, and HybC and HybO in Hyd-2 (Figure 1.3). Both Hyd-1 and Hyd-2 anchor their heterodimers to the membrane at the periplasmic

side via a single C-terminal transmembrane (TM) alpha-helix connected to the β subunit. However, the compositions of Hyd-1 and Hyd-2 differ primarily in their electron transfer subunits (Figure 1.3).

- **Hyd-1** interfaces with a transmembrane (TM) *b*-type cytochrome (cyt *b*) protein (HyaC) attached to the β subunit, anchoring it to the membrane. This cytochrome acts as a redox couple, facilitating electron exchange between the hydrogenase's catalytic centre and the menaquinone pool (MK/MKH_2) via two heme groups. The bimetallic active site is accommodated at the surface of HyaB, which is very close to the electron transfer relay (FeS clusters) in HyaA. The three FeS clusters of Hyd-1 have distinct compositions. There is a [4Fe3S], a [3Fe4S] and a [4Fe4S] cluster in order of distance from the active site from nearest to furthest.[28]

- **Hyd-2**, in contrast, contains a ferredoxin (HybA) containing four [4Fe4S] clusters, which is attached to the β subunit (HybO) to enable electron transfer with the membrane-coupled MK/MKH_2 pool. HybA is anchored at the periplasmic side of the membrane by a C-terminal TM helix and another integral membrane protein, HybB, which consists of 10 TM helices. More importantly, in the β subunit, HybO, Hyd-2 adopts three FeS clusters as electron-transfer units just like HyaC in Hyd-1, but it has [4Fe4S], [3Fe4S] and [4Fe4S] instead, with respect to the distance to active site. The difference in the proximal FeS cluster is the primary factor for their oxygen-tolerance.[29–34]

Both Hyd-1 and Hyd-2 are H_2-uptake [NiFe]-hydrogenases, exhibiting activity in H_2 oxidation. Physiologically, Hyd-2 does not couple to a TM HyaC-type quinone reductase like Hyd-1 to

generate a proton gradient. Instead, it can accept electrons from the quinone/quinol pool to produce H_2, making it a bidirectional hydrogenase *in vitro*. Extensive electrochemical assays have confirmed that Hyd-2 is a reversible catalyst for H^+/H_2, whereas Hyd-1 functions almost exclusively as an H_2 oxidiser at neutral pH.[24]

[NiFeSe]-hydrogenases

[NiFeSe]-hydrogenases share a very similar structural folding pattern to [NiFe]-hydrogenases. The major difference lies in one of the terminal cysteine residues that coordinate to the Ni at the active site. In [NiFeSe]-hydrogenases, this cysteine is replaced by a selenocysteine, while the rest of the active site features remain comparable to those of [NiFe]-hydrogenases.[35]

[NiFeSe]-hydrogenases exhibit an opposite catalytic bias in H_2/H^+ interconversion: unlike [NiFe]-hydrogenases, which favour H_2 oxidation, [NiFeSe]-hydrogenases have been shown to possess greater activity towards H_2 production. Additionally, they demonstrate significant O_2 tolerance.[36]

1.2 The Architecture of [NiFe]-hydrogenases

The catalytic unit of both *E. coli* Hyd-1 and Hyd-2 are very similar, and it is a heterodimer consisting of two subunits. The crystal structure of *E. coli* Hyd-1 is shown in Figure 1.4. The unit cell in the protein crystal contains a dimer of heterodimers. The large α-subunit contains the bimetallic active site, located close to the hydrophobic side of the subunit. The smaller β-

subunit contains three FeS clusters, which enable highly efficient electron transfer from the surface of the protein to the active site. The combination of the α and β subunits results in the active site being deeply buried within the protein in a hydrophobic pocket. The enzyme's fast catalysis is facilitated by selective gas channels throughout the protein and efficient proton transfer routes from the active site to the surface.

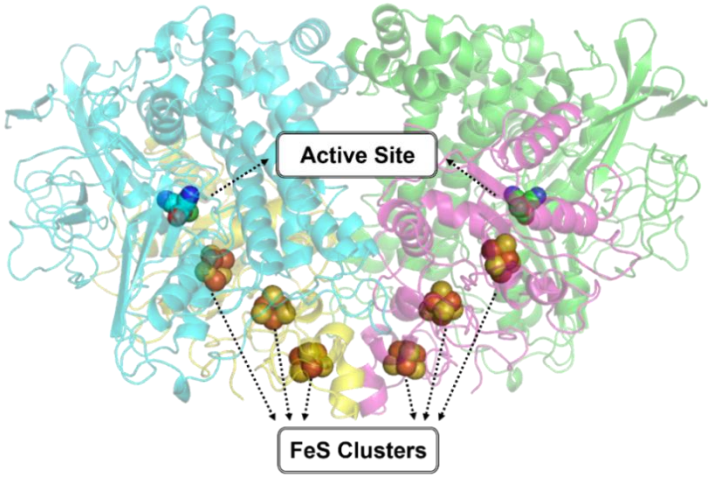

Figure 1.4: X-ray crystal structure of *E. coli* Hyd-1 (PDB code 9EQI, this work) solved with reference to structures from Fontecilla-Camps.[37] It adopts a unit cell containing a dimer of heterodimers. The small subunit is coloured yellow and magenta, and the large subunit cyan and green. The active site and FeS clusters are also noted. Image was generated in PyMOL.

1.2.1 Active Site

The active site of Hyd-1 is located in the large α-subunit. It is a bimetallic cluster comprising one Ni and one Fe ion, as shown in the Figure 1.5. The Ni ion is coordinated by four cysteine residues: two in terminal positions that anchor the active site to the protein backbone, and

two that bridge to the Fe ion. The Fe ion is further coordinated by three biologically unusual ligands: one carbonyl (CO) and two cyanide (CN^-) ligands.[20,29] These ligands help stabilise the active site via hydrogen bonding to serine (Ser) and arginine (Arg) residues.[38–40] An open coordination site, denoted as X in Figure 1.5, exists at the bridging position between the Ni and Fe ions. It can be either H^-, OH^- or H_2O depending on redox levels. The redox-active Ni ion varies between +1, +2, and +3 oxidation states during catalysis, while the Fe ion remains redox-silent, maintaining a +2 oxidation state. The CO and CN^- ligands bonded to the Fe ion are thought to buffer electronic variations in the active site, favouring fast catalysis.[29]

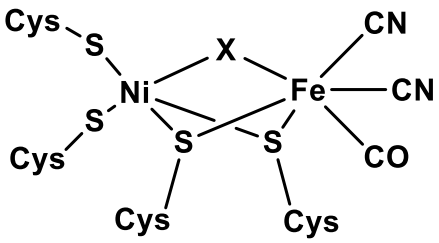

Figure 1.5: The active site structure of the [NiFe]-hydrogenase. The bridging ligand X can be either H^-, OH^- or H_2O depending on redox levels.

1.2.2 Iron-sulfur Clusters

Efficient electron transfer within [NiFe]-hydrogenases is crucial for their catalytic activity. As the active site is buried within the protein, the enzyme utilises three FeS clusters in the smaller β-subunit as electron relays to exchange electrons between the active site and other redox partners. These clusters are named the proximal, medial, and distal FeS clusters, based on their distance from the active site.[7] The medial and distal FeS clusters are consistent in composition and conformation across Hyd-1 and Hyd-2, adopting [3Fe4S] and [4Fe4S] structures,

respectively.[20] The proximal FeS cluster differs between O_2-sensitive and O_2-tolerant Group 1 [NiFe]-hydrogenases and plays a critical role in O_2 tolerance.

- **O_2-tolerant hydrogenases** (e.g., *E. coli* Hyd-1) accommodate a unique [4Fe3S] proximal cluster.[29,41]
- **Standard hydrogenases** (e.g., *E. coli* Hyd-2) contain a standard cubane [4Fe4S] proximal cluster.[20]

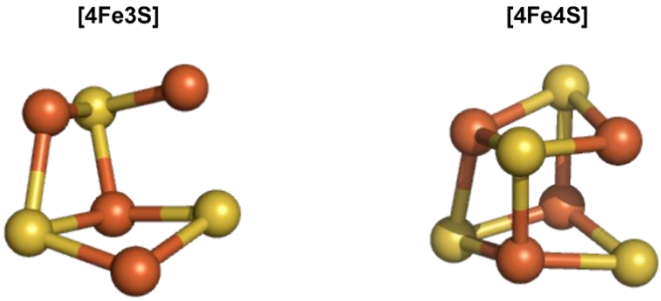

Figure 1.6: The structure of oxidised forms of proximal clusters in O_2-tolerant and O_2-sensitive [NiFe]-hydrogenases. Left: oxidised conformation of [4Fe3S] proximal cluster of Hyd-1, and Right: oxidised distorted cubane conformation of [4Fe4S] proximal cluster of Hyd-2. Image was generated in PyMOL.

The [4Fe4S] cluster in standard hydrogenases is coordinated by four cysteine residues and undergoes one redox transition, sustaining just two redox forms. In contrast, the special proximal [4Fe3S] cluster in O_2-tolerant hydrogenases is coordinated by six cysteine residues and can undergo two redox transitions at physiologically attainable potentials. This allows the proximal cluster to provide an additional electron compared to standard hydrogenases, enabling the full reduction of O_2 attacking at the active site to water.[30,31] The structural differences between the proximal clusters are shown in Figure 1.6.

Table 1.1: Reduction potentials of the FeS clusters in O_2-tolerant and O_2-sensitive hydrogenases.

	FeS cluster reduction potentials vs SHE / mV			
	Proximal		**Medial**	**Distal**
O_2-tolerant	**$[4Fe3S]^{5+/4+}$**	**$[4Fe3S]^{4+/3+}$**	**$[3Fe4S]^{1+/0}$**	**$[4Fe4S]^{2+/+}$**
Ec Hyd-1[42]	+ 211 ± 15	+ 4 ± 30	+ 212 ± 30	-
Aa Hase I[43]	+ 98 ± 20	+ 4 ± 15	+78 ± 20	-65 ± 20
O_2-sensitive	**$[4Fe4S]^{2+/+}$**		**$[3Fe4S]^{1+/0}$**	**$[4Fe4S]^{2+/+}$**
Dv MF[44]	< -300		- 70	< -300
D. gigas[45]	- 290		- 70	- 340

The redox properties of [Fe-S] cluster in [NiFe]-hydrogenases have been studied using EPR and Mössbauer spectroscopies coupled with electrochemical methods.[43,46–48] Table 1.1 compares the reduction potentials of two O_2-tolerant hydrogenases (*E. coli* Hyd-1 and *Aquifex aeolicus* membrane-bound hydrogenase (MBH)) and two O_2-sensitive hydrogenases (from *Desulfovibrio vulgaris strain* Miyazaki F (*Dv*MF*)* and *Desulfovibrio gigas* (*D. gigas*)). Although the proximal [Fe-S] cluster of O_2-tolerant hydrogenases exhibits two redox transitions, both of its reduction potentials are significantly higher than those of standard hydrogenases. The higher reduction potentials of [Fe-S] clusters in O_2-tolerant hydrogenases have been proposed to be critical for their O_2 tolerance and contribute to different redox properties of active site states between O_2-tolerant and O_2-sensitive hydrogenases, such as equilibrium potentials between two redox states.[49]

1.2.3 Gas Channels

The fast catalysis of [NiFe]-hydrogenases also relies on efficient substrate mass transport within the protein. The protein matrix adopts specific hydrophobic tunnels to facilitate the exchange of gaseous substrates between the active site and the protein surface. However, these gas channels are not exclusive to H_2, the natural substrate; non-polar inhibitors, such as O_2 and CO, can also be transported through these routes.[50]

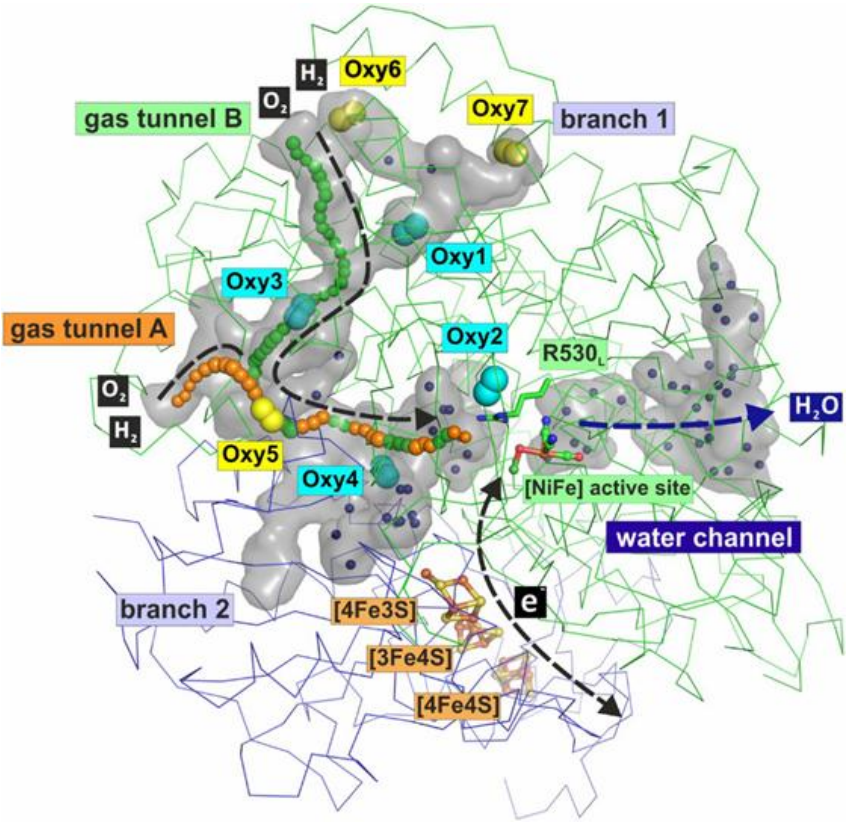

Figure 1.7: The hydrophobic gas tunnel and the hydrophilic water channel of [NiFe]-hydrogenase. The channels are shown as grey surfaces and the directions of the flow of H_2 /O_2 molecules, electrons, and water molecules are illustrated as black and blue dashed arrows. Two gas tunnels noted A and B locate on the large subunit of the enzyme. Adapted with permission from J. Kalms *et al, Proc. Natl. Acad. Sci.* U.S.A., 2018, 115 (10) E2229-E2237. Copyright (2018) National Academy of Sciences.

The gas channels of [NiFe]-hydrogenases have been determined through a combination of experimental evidence and computational methods.[50–53] A recent krypton-infused crystallographic study and a molecular dynamics study of an O_2-tolerant hydrogenase from *Ralstonia eutropha* MBH revealed several sites of krypton atoms within a hydrophobic tunnel network leading to the active site via two tunnel entrances (Figure 1.7).[50] Molecular dynamics revealed that O_2 molecules remain for longer periods of time at the same sites where krypton atoms were found suggesting that the gas channel revealed by noble gas atoms is likely also shared by smaller hydrophobic gases such as O_2 and H_2.

Both entrances are located in the large subunit. Tunnel A, with a minimal diameter of ~1.4 Å and a length of ~33 Å, is categorised as the primary gas tunnel and is located at the interface between the large and small subunit, whereas tunnel B has a minimal diameter of ~1.3 Å and length of ~52 Å, and is in the opposite direction relative to the small subunit. This Y-shaped gas channel in the O_2-tolerant hydrogenase closely resembles that of the O_2-sensitive hydrogenase from *D. fructosovorans* which was mapped using the xenon-soaking method.[52] This similarity is unsurprising, given the high conservation of protein sequences across group 1 and 2 [NiFe]-hydrogenases.

However, the molecular dynamics simulation of MBH is based on the crystal structure of a heterodimer *in vitro*, whereas Hyd-1 and Hyd-2 from *E. coli* adopt a dimer of heterodimers structure. As a result, the primary gas tunnel proposed in *R*. *eutropha* MBH is obscured in the dimer of heterodimers configuration, and the exact gas exchange route in *E. coli* hydrogenases requires further investigation.

1.3 The Catalytic Mechanism of [NiFe]-hydrogenases

[NiFe]-hydrogenases catalyse both H^+ reduction and H_2 oxidation. During the activation and catalysis process, the nickel-iron bimetallic active site undergoes a series of structural and electronic changes, accompanied by conformational changes in amino acid residues in the secondary coordination sphere. These active site states accumulate at different redox levels and often interconvert via proton-coupled electron transfer (PCET) steps.[54] Consequently, they are referred to as active site redox species and have been extensively characterised using biophysical techniques.[54–59] In general, the active site states are classified into two types: those involved in the catalytic turnover cycle, denoted as catalytically active states (often with the subscript “a”), and those not involved, referred to as inactive states. The outline mechanism of [NiFe]-hydrogenases for H_2 oxidation is shown in Figure 1.8.

Inactive States: Ni-A and Ni-B

The inactive states, Ni-A and Ni-B, are typically found in as-isolated and air-oxidised or anaerobically oxidised hydrogenases. Both states feature a Ni (III) Fe (II) bimetallic active site.

- **Ni-A** is known as the "unready" state because it requires a significant amount of time to reductively activate the enzyme from this state. The structural details of the Ni-A state are still under debate. Volbeda and co-workers proposed that Ni-A contains an oxidised bridging cysteine ligand, specifically a sulfonated cysteine between the Ni and Fe ions.[60] Earlier studies, however, suggested the presence of a peroxide ligand

(OOH^-).[61] Despite these uncertainties, Ni-A is recognised as the most oxidised form of the active site in [NiFe]-hydrogenases and may actually be a collection of related oxidised states, for example, with different oxidised cysteines (some of them assigned as Ni-SU). Notably, Ni-A and Ni-B are not electrochemically interconvertible.

- **Ni-B** contains a hydroxy ligand (OH^-) at the bridging position between the Ni and Fe ions.[62,63] Reductive activation of Ni-B occurs on a timescale of seconds. One-electron reduction of the inactive states Ni-A and Ni-B yields the Ni-SU and Ni-SI_r states, respectively. These states are also catalytically inactive, with the Ni ion in the +2 oxidation state.[60] The subscript "r" in Ni-Si_r stands for the "ready" state, indicating its readiness to convert to active states.

Active States: Ni_a-SI, Ni_a-R, Ni_a-C, and Ni_a-L

Subsequent protonation and removal of the bridging hydroxy ligand as water from Ni-SI_r produces the most oxidised active state, Ni_a-SI.[39] During catalysis, redox chemistry occurs exclusively at the Ni ion, while the Fe ion remains formally in a low-spin +2 oxidation state.[64] The Ni_a-SI state is proposed to be the starting point for catalysis, where H_2 binds to the active site, due to its proposed vacant coordination site at the bridging position. [40] The name of the state, Ni_a-SI was given as it shows no EPR signal because it possesses diamagnetic EPR silent Ni(II)Fe(II) active site. Moreover, this state is hard to trap under oxidised, as-isolated or reduced conditions while it is generally found under mildly reducing conditions.[64,65] Consequently, there are only very limited amounts of crystallographic data available, but they

all show a vacant bridging coordination site in the active site, consistent with other spectroscopic and computational results.[66]

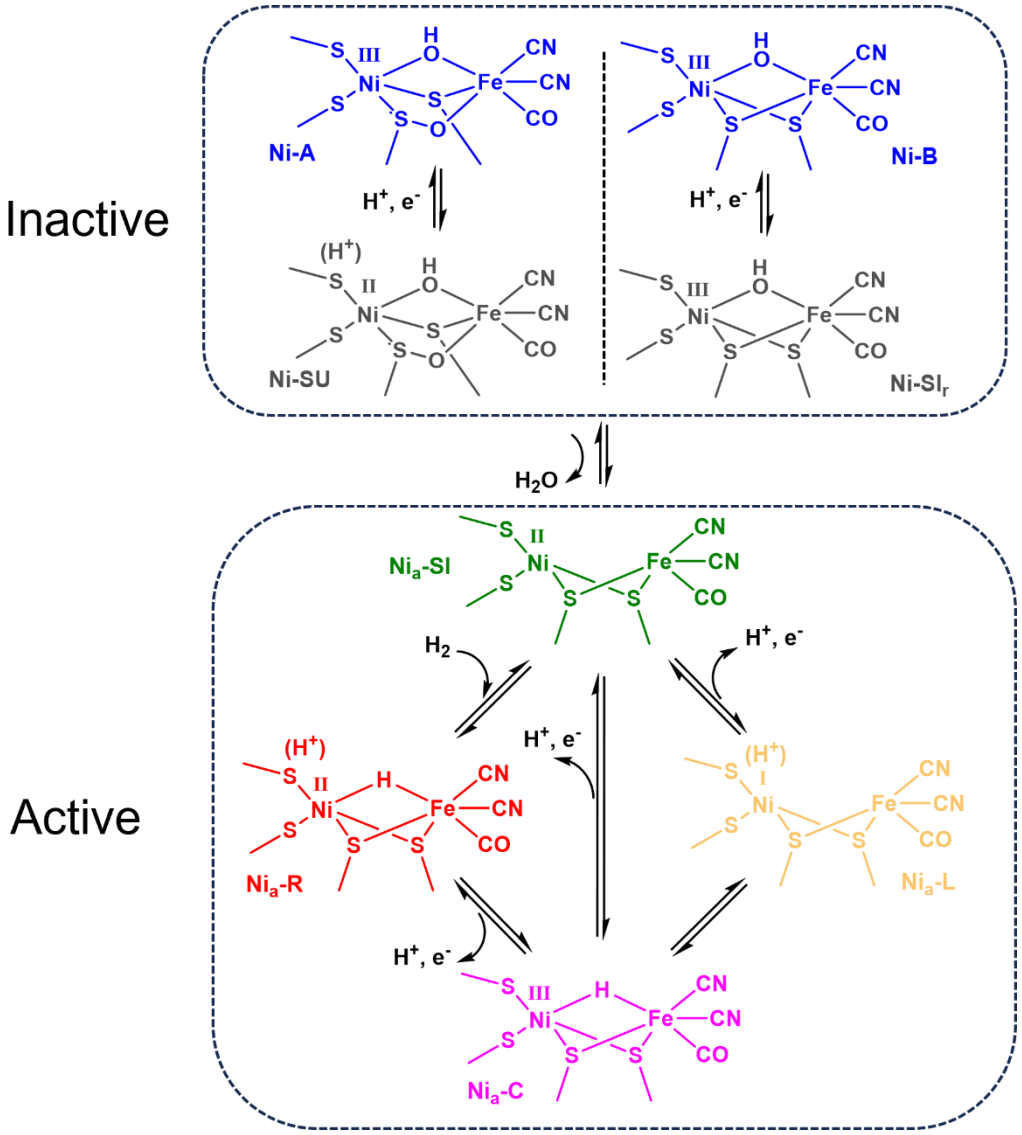

Figure 1.8: Overview of the active site states present in [NiFe]-hydrogenases (the colour coding is consistent throughout this thesis). Inactive and active states are separated into different boxes and the catalytic cycle of H^+/H_2 is shown in the bottom box. The subscript "a" indicates the state is catalytically active, while the subscript "r" represents a "ready" state.

The Ni_a-SI state is considered as the initial state that reacts with the incoming H_2 from the gas

channel. The substrate is likely to bind side-on to nickel (proximal to the end of gas channel) in an η^2, Kubas-type fashion although there is no direct evidence for the complex between H_2 and the enzyme. H_2 activation is proposed to occur through a frustrated Lewis pair mechanism on the basis of what is known for [FeFe]-hydrogenases based on a well-studied immediate proton acceptor (the pendant base), but for [NiFe]-hydrogenases the exact immediate base is still under debate.[7] The frustrated Lewis pair architecture of Ni_a-SI active site state is thought to facilitate fast heterolytic fission of H–H bond. The relatively electron-deficient bimetallic centre (Ni_a-SI is the most oxidised active state) with a vacant coordination site which acts as a Lewis acid while an adjacent amino acid residue likely acts as a Lewis base. When H_2 binds as a η^2 ligand to metal (the Michaelis complex), the frustrated Lewis pair helps to polarize the dihydrogen bond, lowering the activation energy for heterolytic fission although again there is no direct evidence.[67] This step produces a new active site state, Ni_a-R, which features an additional proton and a hydride at the active site. The hydride, from the heterolytic fission of dihydrogen, occupies the bridging position, similar to the hydroxy ligand in the Ni-B state. Multiple Ni_a-R species have been identified spectroscopically, thought to representing different proton-binding sites during proton transfer away from the active site.[54] Identifying the exact amino acid residues involved in the proton transfer pathway remains a key research focus. Ultra-high-resolution X-ray crystallography and computational studies suggest that the initial proton acceptor is one of the terminal cysteine thiolates coordinated to the Ni ion, though the subsequent acceptor sites are still debated.[67]Additionally, a pendant arginine group close to the active site has been proposed as a crucial proton acceptor[41], but this mechanism is disputed due to the high pKa of free arginine, making it unlikely to be

deprotonated at physiological pH. Spectroelectrochemical studies have further shown that the arginine group is not critical for the Ni_a-SI to Ni_a-R conversion, suggesting it may instead play a role in transient hydrogen-bonding networks.[68]

Complete removal of the proton from the active site, coupled with one-electron oxidation by the proximal FeS cluster, converts the Ni_a-R state to the Ni_a-C state. This state features a Ni (III) ion and a bridging hydride and has been well characterised by EPR and nuclear resonance vibrational spectroscopy, though structural evidence remains limited.[69,70] To complete the catalytic cycle, Ni_a-C is believed to convert back to Ni_a-SI via two pathways: either through one-electron oxidation and proton removal or through tautomerisation. The tautomer of Ni_a-C, Ni_a-L, is formed by transferring two electrons from the bridging hydride to the Ni (III) ion, resulting in a Ni(I) ion and a proton at the active site. Subsequent proton removal is associated with a terminal cysteine thiolate and a glutamate residue. The loss of the proton, combined with one-electron oxidation, re-forms the Ni_a-SI state.[68,71] The Ni_a-L state was initially identified as an artificial state under cryogenic illumination of Ni_a-C but has since been shown to participate in the catalytic cycle under turnover conditions.[71]

1.4 Inhibition of [NiFe]-hydrogenases

Apart from H_2 molecules, which react at the active site of [NiFe]-hydrogenases, the protein active site can interact with several other inhibitors, which presumably access the active site via hydrophobic gas channels in the protein.

1.4.1 Oxygen

Dioxygen (O_2) is a well-known inactivation source of hydrogenases. It inhibits [Fe] and [FeFe] hydrogenases irreversibly, while [NiFe]-hydrogenases are generally inhibited reversibly. Based on their behaviour toward O_2, [NiFe]-hydrogenases can be further categorised into two groups: oxygen-sensitive, in which O_2 is reversibly bound to the active site and inactivates the enzyme; and O_2-tolerant, which are still able to catalyse H_2 oxidation when O_2 is present. For example, Hyd-1 as an O_2-tolerant hydrogenase, not only can maintain more than 50% of its activity under 1% O_2 in solution, but also the activity is fully recoverable after exposure to O_2.[72,73]

The mechanisms by which O_2 inhibits and reacts with the active site differ between oxygen-sensitive and oxygen-tolerant [NiFe]-hydrogenases. Upon oxygen attacking, the exogenous O_2 is proposed to form a Ni-O_2 adduct at the active site, and the enzyme then initiates its reduction. O_2 reduction requires 4 electrons in total from the enzyme. In the Ni_a-SI state, in which the active site is vacant, the Ni (II) can provide one electron for O_2 reduction. This means only three additional electrons are required from the [FeS] clusters to reduce each oxygen atom in O_2 from the 0-oxidation state to -2, producing water and a hydroxide ligand that remains as a bridging ligand at the active site (two electrons from the proximal cluster and one from the medial or the distal cluster). This process converts the active site to the inactive Ni-B state, which acts as an "active-site-protected" state. The bridging hydroxide ligand functions like a "cap," preventing further O_2 damage.[49]

The proximal FeS cluster

Oxygen-tolerant [NiFe]-hydrogenases, such as Hyd-1, have evolved a unique proximal [4Fe3S] cluster that can provide two electrons. Combined with one electron from the medial [3Fe4S] cluster, these enzymes can fully reduce incoming O_2 at the Ni_a-SI level and quickly convert to the protected Ni-B state, which can be easily reactivated by external electrons or substrate. This capability is key to their O_2 tolerance. In contrast, oxygen-sensitive [NiFe]-hydrogenases, which accommodate a [4Fe4S] proximal cluster capable of providing only one electron, are at a much higher risk to convert to the unready Ni-A state.[20,30]

Crystallographic data and molecular dynamics studies suggest that O_2 and H_2 share the same gas channel in [NiFe]-hydrogenases.[50] The Ni-B state, resulting from O_2 inhibition, has been studied in detail through available crystal structures, confirming the geometry of the active site and other parts of the protein. However, the exact redox conformation of the proximal [4Fe3S] cluster in oxygen-tolerant [NiFe]-hydrogenases remains unclear. While the [4Fe3S] cluster adopts three redox states, only the reduced conformation has been clearly identified. In air-oxidised protein crystals, a mixture of two oxidised conformations of this cluster results in merged crystallographic data.[33,67]

1.4.2 Carbon Monoxide

Carbon monoxide (CO) is a common inhibitor of hydrogen-cycling catalysts, particularly for precious metal-based catalysts like platinum (Pt). CO strongly inhibits Pt, a process often referred to as CO poisoning, as it severely hinders catalytic activity.[74] Reactivating platinum

catalysts typically requires harsh oxidative treatments to remove CO. In contrast, [NiFe]-hydrogenases are more resistant to CO poisoning, allowing their catalytic activity to recover quickly once CO is removed.[75]

The inhibitory effect of CO on [NiFe]-hydrogenases has been extensively investigated using various characterisation methods. The inhibited active site state is termed Ni-SCO. Protein film electrochemistry (PFE) experiments have revealed that CO acts as a competitive inhibitor across the entire potential window for both hydrogen oxidation and proton reduction in many [NiFe]-hydrogenases, including Hyd-1 and Hyd-2. Additionally, PFE studies suggest that the CO molecule interacts with the Ni_a-SI state (which has a vacant bridging position). CO inhibits Hyd-2 more strongly than Hyd-1 under turnover conditions due to the larger population of Ni_a-SI states during catalysis in Hyd-2.[75,76]

The crystal structure of the Ni-SCO state has been reported exclusively for O_2-sensitive [NiFe]-hydrogenases. In this state, the exogenous CO ligand binds to the Ni ion via the carbon atom in a bent conformation (Ni–C≡O). The CO molecule is oriented towards the gas channel, suggesting that CO migrates into the enzyme through this pathway.[77,78]

1.4.3 Cyanide

Even though cyanide (CN^-) and CO are isoelectronic they have distinct coordination properties. While CO is a weak sigma donor and strong pi acceptor, CN^- is a strong σ-donor ligand that coordinates with many transition metals and inhibits several metalloproteins. Studies on the [NiFe]-hydrogenase from *Azotobacter vinelandii* revealed that cyanide acts as a strong

inhibitor of H_2 oxidation activity when O_2 is present, but has less inhibitory effect on the reduced activated enzyme in H_2 atmosphere.[79] Furthermore, spectrophotometric assays on the hydrogenase from *A. vinelandii* demonstrated that cyanide causes irreversible inhibition when the enzyme is in its oxidised state.[80]

Protein film electrochemistry (PFE) assays show that the addition of cyanide accelerates the formation of the Ni-B state on Hyd-1 and Hyd-2.[81] In the presence of cyanide, there is no effect on enzyme catalysis at low potentials. However, cyanide suppresses H_2 oxidation activity above -100 mV for Hyd-1, and above -200 mV for Hyd-2. Infrared (IR) spectroscopy evidence suggests that at low concentrations, CN^- quickly coordinates with the Ni ion at a terminal position, favouring the oxidation of Ni (II) to Ni (III) and facilitating the formation of the inactive Ni-B state, thereby diminishing enzyme activity. In contrast to the weak interaction between Hyd-2 and CN^- (with a dissociation constant, K_d = 0.84 mM), Hyd-1 forms an irreversible species at high cyanide concentrations, though only limited spectroscopic evidence is available for this interaction. Chapter 6 of this thesis reports the crystal structure of cyanide-bound Hyd-1, providing further insights into this inhibition mechanism.

1.4.4 Isocyanide

Isocyanide (RNC) (Figure 1.9) has a functional group that is isoelectronic to both CO and CN^-. Due to the negative charge on carbon and the positive charge on nitrogen, RNCs are better σ-donors but weaker π-acceptors than CO. The σ-donating effect increases with the inductive effect of the alkyl group (R) attached to the nitrogen. Owing to their electronic structure and

the ability to vary the alkyl groups, RNCs have been widely studied as gas substrate analogues for many gas-processing metalloproteins, such as heme proteins (CO analogues),[82] nitrogenase (N_2 analogues),[83,84] and carbon monoxide dehydrogenase (CO analogues).[85]

RNCs have been studied in *E. coli* hydrogenases as reversible inhibitors using PFE and IR spectroelectrochemistry.[75] The varying sizes of RNCs are particularly interesting, as their bulkiness can demonstrate the flexibility of the active site. A range of isocyanides with different alkyl groups, up to *tert*-butyl isocyanide (^{t}Bu RNC), were tested with Hyd-1 and Hyd-2 in solution. Most tested RNCs were able to access the active site and bind to it, indicating considerable flexibility in the gas channels. The inhibition constant (K_i) of methyl isocyanide for Hyd-2 is in the range of 5–20 μM, approximately two orders of magnitude smaller than that for Hyd-1, revealing that Hyd-2 is more sensitive to methyl isocyanide.

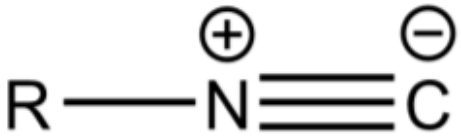

Figure 1.9: The general molecular structure of isocyanide (RNC). The carbon site is able to coordinate with transition metals, serving as a σ-donor ligand. R represents the different alkyl groups.

However, no crystal structure of RNC-bound [NiFe]-hydrogenases has been reported to date, as RNCs bind the active site only under specific redox conditions. Therefore, trapping RNC-bound crystals is valuable for investigating the flexibility of [NiFe]-hydrogenases at the active site and determining the exact coordination geometry of these ligands. In this thesis, crystals of both Hyd-1 and Hyd-2 in the Ni_a-SI state were generated, and the first RNC-inhibited [NiFe]-

hydrogenase crystal structures are reported.

1.5 Techniques and Challenges for Studying Hydrogenase Chemistry

As [NiFe] hydrogenases are metalloproteins, a number of different biophysical techniques are able to provide detailed information on the geometric and electronic structure of their active site. A comprehensive understanding of their catalytic properties is achieved by unifying information from each method. The common techniques employed in the field are discussed in the following sections.

1.5.1 Solution Assays and Gas Chromatography

Solution assays are a conventional method for quantitatively measuring enzyme activity, usually using spectrophotometry with a product dye. The H_2 oxidation activity of hydrogenases is indirectly measured by the intense colour change of an artificial electron acceptor. For example, the oxidised form of viologen derivatives can quickly accept electrons from the enzyme after H_2 splitting, turning an intense blue colour upon reduction. The rate of colour change of the electron acceptor is monitored and used to determine the catalytic activity of the enzyme.[86]

The catalytic activity of hydrogenases in H_2 production is directly monitored using gas chromatography. An artificial electron donor, typically sodium dithionite, and an electron

mediator, such as viologen derivatives, are mixed with hydrogenases anaerobically in a sealed vial. The H_2 content produced over time is quantitatively analysed using gas chromatography.[87]

1.5.2 Protein Film Electrochemistry

Protein film electrochemistry (PFE) is a powerful technique for quantitatively studying the catalytic activity of hydrogenases in both directions (H_2 oxidation and H_2 production) and providing mechanistic insights into the enzyme.[88] By immobilising hydrogenase enzymes directly onto an electrode surface, direct electron transfer between the electrode and the protein is achieved. The sensitive electrochemical response in PFE allows for the monitoring of current changes in response to redox levels (applied electrochemical potential), working conditions (e.g. pH or substrate concentration), and the presence of exogenous inhibitors. In addition to catalytic activity, PFE studies can extract important information such as oxidative inactivation/reductive reactivation, catalytic bias, and overpotential of hydrogenases. PFE is not a quantitative measurement of enzyme activity, as it is difficult to quantify the exact amount of enzyme adsorbed on the electrode surface, but can measure changes in activity, e.g. following introduction of an inhibitor.

1.5.3 Infrared Spectroscopy

Owing to the unique coordination structure at the active site of [NiFe]-hydrogenases, infrared (IR) spectroscopy is arguably the most common and versatile spectroscopic method for studying their chemistry. The intrinsic CO and CN^- ligand at the Fe ion serve as intense IR probes,

providing insights into the electronic and geometric structures of the active site. The ν_{CO} and ν_{CN} stretching bands appear in the 2200-1800 cm^{-1} region, avoiding overlap with other absorption features, such as those from solvents or peptide bonds. These absorption bands are highly sensitive to changes at the active site, with their positions shifting in response to: 1) formal oxidation state change of Ni, 2) ligand association/dissociation, 3) proton hopping from/to active site and 4) inhibitor binding. As a result, each active site state has a distinct ν_{CO} and ν_{CN} band position, enabling IR spectroscopy to study the speciation and composition of active site states.[56]

IR spectroscopy is not limited by the physical state of the sample, allowing hydrogenase samples to be measured at cryogenic temperatures in a frozen state or at ambient temperatures in solution. Additionally, time-resolved IR methods can investigate specific state-to-state conversions within the catalytic cycle, capturing short-lived transient intermediate states that conventional IR methods cannot detect.[89] The chemistry of catalysis is often studied *in-situ* or *operando*. IR spectroscopy is frequently coupled with other techniques, particularly electrochemistry, to study enzyme dynamics under electrochemical control. In this thesis, an *in-situ* IR spectroelectrochemical method is employed to study *E. coli* Hyd-1 and Hyd-2. The detailed theory of IR spectroscopy will be discussed in Chapter 2.

1.5.4 X-ray Absorption Spectroscopy

X-ray absorption spectroscopy (XAS) has been one of the primary biophysical techniques for studying the active site structure and composition of [NiFe]-hydrogenases.[90,91] However, the

structural information provided by XAS is limited to a short range around the detecting element, as it targets a specific element at a specific absorption energy range.

Early XAS studies confirmed the connectivity of the [NiFe]-hydrogenase active site and resolved uncertainties of ligand atom identifications.[90] On the other hand, XAS provides valuable information about the electronic and geometric properties of the Ni centre. The edge position and pre-edge features are closely related to the oxidation state and crystal field splitting profile of the Ni ion. XAS is capable of reporting on all active site states of [NiFe]-hydrogenases, from Ni(III) to Ni(I), complementing the limitations of IR and electron paramagnetic resonance (EPR) spectroscopy. IR spectroscopy indirectly monitors the Ni centre at the active site through IR-active ligands on the adjacent Fe ion, while EPR spectroscopy cannot measure states with Ni(II), a d8 transition metal centre with no unpaired electrons.

A major challenge in XAS measurements of biological samples is radiation-induced damage, also known as photodamage, caused by intense and energetic X-ray irradiation on dilute protein samples, such as [NiFe]-hydrogenases. Enzymes can be damaged by photoelectrons or reactive oxygen species generated during photochemical reactions. This damage can alter the electronic and geometric structure of the metal active site, compromising the integrity of the data. In general, the damage process occurs through two pathways. The primary pathway involves direct interaction with X-ray, which causes ionisation, ejecting photoelectrons or Auger-Meitner electrons from the metal centre and its surrounding atoms. This creates a core hole on the ionised atoms and can directly break chemical bonds, leading to immediate changes in the oxidation state of the metal and changes to its local structure. The secondary

pathway is indirect, radical-mediated and often more significant in hydrated biological samples. The primary electron cascade leads to the radiolysis of water molecules in the solvent and the protein matrix, generating highly reactive species like hydrated electrons (e^- (aq)) and hydroxyl radicals (·OH). These radicals, particularly the hydrated electrons, are potent reducing agents that can diffuse to the metal active site and cause reduction.

The photodamage is governed by several factors, and the strategies for damage mitigation should be carefully considered to obtain high quality data. The total absorbed dose on the sample is the major factor: higher total energy deposited per unit mass leads to greater damage. The intensity of the incident X-ray beam can be altered by external filters (plates such as aluminium, copper, lead or amorphous carbon). Apart from selecting a suitable X-ray dose, continuously translating or oscillating the sample through the X-ray beam ensures that a fresh, unexposed volume is constantly being probed, preventing localised damage accumulation. On the other hand, cryo-cooling is the most widely used and practical method for photodamage mitigation. It can disperse the heat generated from the X-ray exposure, preventing it from causing irreversible damage to biological samples. By cooling samples to liquid nitrogen or helium temperatures, the diffusion of radicals and the rate of secondary chemical reaction are severely hindered, dramatically increasing the dose tolerance of the sample and allowing for longer data collection times.

Overall, preventing photodamage is crucial for obtaining accurate XAS spectra. Later, in Chapter 7, a novel XAS spectroelectrochemical method is described, enabling XAS measurements of biological samples at ambient temperature. The detailed theory of XAS is

discussed in Chapter 2.

1.5.5 X-ray Crystallography

The catalytic properties of [NiFe]-hydrogenases are intrinsically linked to their structure. If protein crystals are available, X-ray crystallography can provide a detailed three-dimensional atomic arrangement of the entire protein, including the active site, secondary coordination sphere, and [Fe-S] clusters. When X-rays interact with a crystal, they are diffracted by the electron clouds of the regularly arranged atoms in the crystal lattice, producing a characteristic diffraction pattern. This pattern, typically represented as a plot of intensity versus angle, contains information about the spacing and arrangement of atoms within the crystal. The diffraction data are related to the reciprocal lattice, a concept in reciprocal space, where reciprocal lattice vectors describe the periodicity of the crystal structure. To interpret the diffraction data, a Fourier transform is applied, converting it from reciprocal space to real space. The Fourier transform acts as a bridge between these two spaces, enabling the reconstruction of the electron density distribution within the crystal. The result is an electron density map, which provides a visual representation of the probability of finding electrons in different regions of the crystal. By analysing this map, the positions of atoms within the crystal can be determined, allowing the complete atomic structure of the molecule to be reconstructed. This method, known as X-ray crystallography, is a cornerstone technique in structural biology and chemistry, enabling researchers to study the three-dimensional folding and function of molecules at an atomic level.

However, X-ray crystallography presents several challenges. The primary challenge is obtaining high-quality, well-ordered protein crystals, as this is essential for acquiring a high-resolution electron density map. Locating hydrogen atoms in the electron density map is particularly difficult, as hydrogen has minimal electron density around its nucleus (slightly higher for hydrides than for protons), requiring ultra-high-quality diffraction data.[67] Additionally, protein crystals are often not in definable or homogeneous oxidation states during preparation, leading to low occupancy of certain atoms in the electron density map due to the limited speciation of the corresponding state across all repeating units. In Chapter 4, a controllable redox method for *E. coli* Hyd-1 and Hyd-2 single crystals is demonstrated, and active-site-state-enriched crystal structures are reported.

1.5.6 Electron Paramagnetic Resonance

Electron paramagnetic resonance (EPR) spectroscopy is a powerful technique used to study metalloprotein systems containing one or more unpaired electrons. EPR studies provide valuable insights into the metal oxidation state, metal centre symmetry, spin state and distribution, d-orbital electronic configuration, and exchange coupling between metal ions. In the case of [NiFe]-hydrogenases, EPR reveals critical information about catalytic and electron transfer mechanisms, such as the redox states and redox potentials of FeS clusters, the formal oxidation states of Ni during the catalytic cycle, and the enzyme inactivation and reactivation processes.[46]

The origin of the EPR signal lies in the energy splitting of electron spin states under an external

magnetic field, a phenomenon known as the Zeeman effect. An unpaired electron has spin moments, m_s = ±½. Under an external magnetic field, the energy of these two spin states splits, and transitions between them are allowed according to the selection rule $\Delta m_s = \pm 1$. The EPR spectrum is the first derivative of the absorption spectrum, and three interactions within the molecule give rise to the EPR signal:

1. **Spin-Orbital Coupling**: The interaction between the orbital and spin angular momentum, described by the quantum number *J*, directly affects the *g*-value and, consequently, the splitting energy.

2. **Hyperfine Interactions**: In molecules such as [NiFe]-hydrogenases, which contain multiple metal cofactors, there is a possibility of multiple unpaired electrons. These electrons can couple with each other, similar to *J*-coupling in nuclear magnetic resonance (NMR).

3. **Nuclear Hyperfine Interactions**: In addition to the applied magnetic field, unpaired electrons can interact with the local magnetic field produced by nearby nuclei. This interaction leads to further splitting of the energy levels, appearing as multiple lines in the EPR spectrum. For example, the nuclear hyperfine coupling provides evidence of the presence of a hydride ligand at the active site of [NiFe]-hydrogenases.[93,94]

1.6 Challenges in Unifying Information from Biophysical Characterisation

Biological samples are typically measured in three states: solution, frozen, and crystalline. While the characterisation methods mentioned above provide detailed information about samples, they are not usually performed under the same conditions.

Temperature and experimental conditions

Temperature is a key difference between characterisation methods. Versatile spectroscopic techniques, such as IR spectroscopy, allow samples to be measured in any phase (solution, frozen, or crystalline) without temperature constraints. In contrast, crystal structures of metalloproteins are typically collected from protein crystals at cryogenic temperatures, which are drastically different from physiological working conditions. Similarly, conventional XAS and EPR measurements also require samples to be in frozen states. On the other hand, biological activity assays employ enzymes in solution, mimicking *in vitro* conditions with artificial redox partners that align with the enzymatic state *in vivo*. As a result, the "snapshot" of atomic positions obtained from X-ray crystallography and the active site features interpreted from XAS and EPR may not reflect the enzyme's behaviour under working conditions, especially when the crystalline sample is in an undefined redox state. Therefore, each individual technique is limited in its ability to provide comprehensive insights into enzyme catalysis, necessitating new methodologies to bridge the knowledge gaps between them. The main goal of this thesis is to unify information from different methodologies to have a deeper understanding of [NiFe]-

hydrogenase chemistry (Figure 1.10).

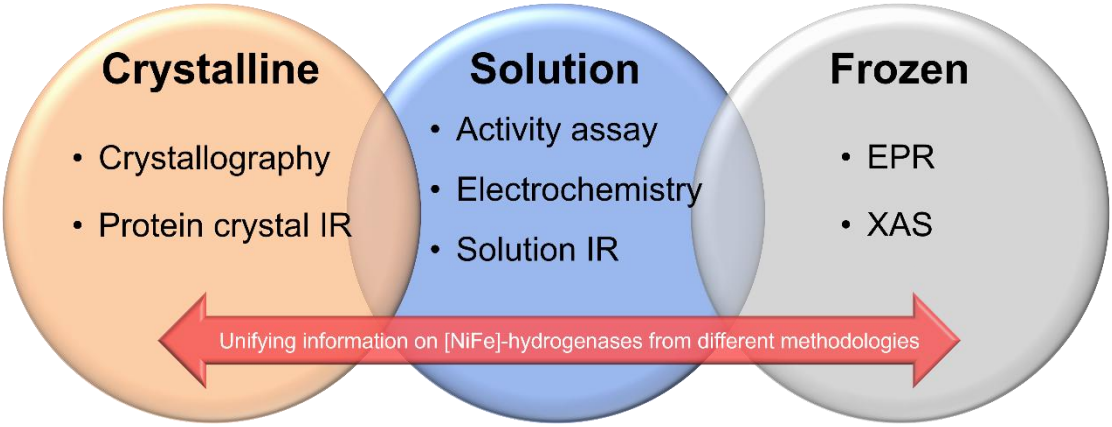

Figure 1.10: Schematic representation of how these biophysical methods can be combined to study [NiFe]-hydrogenases.

Electrochemistry and redox proteins

Electrochemistry is a crucial technique for studying redox proteins such as [NiFe]-hydrogenases, though it is typically restricted to aqueous systems. This is because the free movement of electrolytes in an electrochemical cell is essential for accurate electrochemical measurements. Solid electrochemistry, a frontier research topic in energy storage, sensing, and advanced materials, utilises nanomaterials and non-lattice oxides or organic electrolytes.[95] Protein film electrochemistry (PFE), an electrochemical assay for enzymes in an electrode-immobilised state, provides valuable information about catalytic properties. This is because electrochemical control over redox proteins can mimic their working conditions where they are in contact with redox partner proteins.[88]

In the field of catalysis, which includes enzymes, real-time characterisation is critical.[64] Simple

measurements on pre-prepared catalyst samples (*ex-situ* measurements) often fail to reflect catalytic properties under working conditions. Therefore, catalytic studies increasingly rely on *in-situ* and *operando* characterisation methods. *In-situ* refers to obtaining information about the catalyst under conditions similar to its working environment, while *operando* involves studying the catalyst while it is actively functioning. Therefore, combining electrochemistry and other characterisation methods is promising to study redox proteins *in-situ*.

Challenges and innovations in metalloprotein studies

Metalloproteins, such as [NiFe]-hydrogenases, present unique challenges due to their low yield and fragility, making them incompatible with common *in-situ* setups used for heterogeneous catalysis studies. Currently, only a few methods utilise customised experimental setups to study metalloproteins *in-situ* or *operando*. For example: coupling of IR spectroscopy and electrochemistry into a thin layer cell allows the two techniques to work simultaneously on a small amount of enzyme.[56,96] Moreover, protein film IR electrochemistry, inspired by PFE, bridges spectroscopy and enzyme activity, enabling *operando* characterisation.[54,55] In this thesis, novel methodologies are employed and developed to bridge the gaps between spectroscopy- and structural-based approaches: an IR microspectroelectrochemical method combines IR microspectroscopy and electrochemistry to study protein crystals *in-situ*, providing active site state speciation information.[96] A customised flowing electrochemical cell allows rational manipulation of protein crystals into defined redox levels, making it possible to unify the information from spectroscopy and structural

determination. Furthermore, a spectroelectrochemical method enables photodamage-free XAS characterisation simultaneous with electrochemical control.[97] These methods systematically demonstrate new strategies for studying metalloproteins more comprehensively, integrating structural, spectroscopic, and functional insights.

1.7 Aim and Scope of the Thesis

The mechanism of hydrogenases has been investigated using a wide range of biophysical techniques. However, most of these techniques focus on a single property. To achieve a comprehensive understanding of hydrogenase mechanisms, it is essential to unify activity, structural, and spectroscopic information. This thesis aims to demonstrate the advantages of combining multiple biophysical and sample-handling techniques to study not only [NiFe]-hydrogenases but also other metalloproteins. Several novel methodologies are employed and developed in this thesis, including:

- *In-situ* IR microspectroelectrochemical assays on protein crystals,
- Electrochemical manipulation of protein single crystals for precise redox control, and
- *In-situ* XAS spectroelectrochemical setups for ambient-temperature measurements on biological samples.

Chapter 2 describes the theory and experimental methods used in this research.

Chapter 3 is the first experimental results chapter and describes experiments in which a single crystal of Hyd-1 and Hyd-2 are determined. Combining IR microspectroscopy and

electrochemistry, *in-situ* characterisation can be achieved, thus the redox behaviour of Hyd-1 and Hyd-2 in crystallo form can be investigated. Detailed electrochemical titration on Hyd-1 and Hyd-2 single crystals allow extraction of detailed population distribution of active site states at different redox levels under different conditions. Hyd-2, in contrast to Hyd-1, shows proton reduction activity at low potential, and hence has a different speciation of active site states than Hyd-1. The results in Chapter 3 established a reference databank of the redox-dependence of both Hyd-1 and Hyd-2 states. The conditions to generate, in a crystal, a majority population of each of the long-lived active site states (Ni-B, Ni_a-SI, Ni_a-R, and Ni_a-C) have been studied.

While the method in Chapters 3 allows electrochemical control over Hyd-1 and Hyd-2 crystals, it lacks sample accessibility for further experiments, such as structural determination. Chapter 4 describes the development of an *ex-situ* electrochemical setup for precise redox control of protein crystals. This setup uses a cycling electrolyte and redox mediator between an electrochemical cell and an external crystal-poising container, driven by a peristaltic pump. It enables the generation and collection of Hyd-1 and Hyd-2 single crystals at specific redox levels, enriching specific active site states.

Chapter 5 presents high-resolution crystal structures of active-site-state-enriched hydrogenase crystals. The electrochemical poising process preserves crystal integrity, and the atomic composition and locations around the active site are highly consistent with IR spectra. The first rationally generated Ni_a-SI (with additional proof from the Ni-SCO crystal structure), Ni_a-C, and Ni_a-L (pH 8) crystal structures are reported, providing new mechanistic insights into

proton transfer pathways. Additionally, the super-oxidised state of the proximal FeS cluster in Hyd-1 is structurally determined for the first time, revealing a distinctive oxidised conformation.

Chapter 6 extends the methods described in previous sections to investigate the effects of inhibitors on electrochemically generated single crystals in the Ni_a-SI state. Inhibitors studied include cyanide and a range of isocyanides (methyl, ethyl, isopropyl, *n*-butyl, and *t*-butyl). A collection of inhibitor-bound crystal structures is reported, supported by IR evidence, and the flexibility of the protein gas channel and active site is explored.

Chapter 7 describes a novel spectroelectrochemical set-up utilising a synchrotron X-ray source and customised flow-cell system to achieve *in-situ* XAS measurements on biological samples at ambient temperature. Successful XANES potential titration and EXAFS studies on the model metalloprotein Cu-azurin demonstrate that this setup minimises the risk of photodamage induced by intense X-rays, opening possibilities for studying other metalloproteins.

Overall, this thesis makes a significant contribution to the field of bio-inorganic chemistry by developing methods for combining X-ray diffraction and XAS with electrochemistry and provides new structural insight into specific states of [NiFe]-hydrogenases.

1.8 References

1 W. Lubitz and W. Tumas, *Chem. Rev.*, 2007, **107**, 3900–3903.

2 I. Dincer and H. Ishaq, *Renewable Hydrogen Production*, Elsevier, 2022, pp. 35–90.

3 I. Staffell, D. Scamman, A. Velazquez Abad, P. Balcombe, P. E. Dodds, P. Ekins, N. Shah and K. R. Ward, *Energy Environ. Sci.*, 2019, **12**, 463–491.

4 H. Ishaq, I. Dincer and C. Crawford, *Int. J. Hydrogen Energy*, 2022, **47**, 26238–26264.

5 A. I. Osman, N. Mehta, A. M. Elgarahy, M. Hefny, A. Al-Hinai, A. H. Al-Muhtaseb and D. W. Rooney, *Environ. Chem. Lett.*, 2022, **20**, 153–188.

6 P. M. Vignais and B. Billoud, *Chem. Rev.*, 2007, **107**, 4206–4272.

7 W. Lubitz, H. Ogata, O. Rüdiger and E. Reijerse, *Chem. Rev.*, 2014, **114**, 4081–4148.

8 C. Madden, M. D. Vaughn, I. Díez-Pérez, K. A. Brown, P. W. King, D. Gust, A. L. Moore and T. A. Moore, *J. Am. Chem. Soc.*, 2012, **134**, 3, 1577–1582.

9 S. Hardt, S. Stapf, D. T. Filmon, J. A. Birrell, O. Rüdiger, V. Fourmond, C. Léger and N. Plumeré, *Nat. Catal.*, 2021, **4**, 251–258.

10 T. B. Rauchfuss, *Science*, 2007, **316**, 553–554.

11 H. A. Reeve, L. Lauterbach, P. A. Ash, O. Lenz and K. A. Vincent, *Chem. Commun.*, 2012, **48**, 1589–1591.

12 J. S. Rowbotham, H. A. Reeve and K. A. Vincent, *ACS Catal.*, 2021, **11**, 2596–2604.

13 D. W. Mulder, E. M. Shepard, J. E. Meuser, N. Joshi, P. W. King, M. C. Posewitz, J. B. Broderick and J. W. Peters, *Structure*, 2011, **19**, 1038–1052.

14 J. Esselborn, N. Muraki, K. Klein, V. Engelbrecht, N. Metzler-Nolte, U.-P. Apfel, E. Hofmann, G. Kurisu and T. Happe, *Chem. Sci.*, 2016, **7**, 959–968.

15 J. Duan, M. Senger, J. Esselborn, V. Engelbrecht, F. Wittkamp, U.-P. Apfel, E. Hofmann, S. T. Stripp, T. Happe and M. Winkler, *Nat. Commun.*, 2018, **9**, 4726.

16 J. A. Birrell, P. Rodríguez-Maciá, E. J. Reijerse, M. A. Martini and W. Lubitz, *Coord. Chem. Rev.*, 2021, **449**, 214191.

17 D. W. Mulder, E. S. Boyd, R. Sarma, R. K. Lange, J. A. Endrizzi, J. B. Broderick and J. W. Peters, *Nature*, 2010, **465**, 248–251.

18 S. Shima, O. Pilak, S. Vogt, M. Schick, M. S. Stagni, W. Meyer-Klaucke, E. Warkentin, R. K. Thauer and U. Ermler, *Science*, 2008, **321**, 572–575.

19 G. Huang, T. Wagner, M. D. Wodrich, K. Ataka, E. Bill, U. Ermler, X. Hu and S. Shima, *Nat. Cata.l*, 2019, **2**, 537–543.

20 S. E. Beaton, R. M. Evans, A. J. Finney, C. M. Lamont, F. A. Armstrong, F. Sargent and S. B. Carr,

Biochem. J., 2018, **475**, 1353–1370.

21 S. Caspar, F. Bärbel and L. Oliver, *Appl. Environ. Microbiol.*, 2013, **79**, 5137–5145.

22 G. Goldet, A. F. Wait, J. A. Cracknell, K. A. Vincent, M. Ludwig, O. Lenz, B. Friedrich and F. A. Armstrong, *J. Am. Chem. Soc.*, 2008, **130**, 11106–11113.

23 H. S. Shafaat, O. Rüdiger, H. Ogata and W. Lubitz, *Biochim. Biophy. Acta*, 2013, **1827**, 986–1002.

24 M. J. Lukey, A. Parkin, M. M. Roessler, B. J. Murphy, J. Harmer, T. Palmer, F. Sargent and F. A. Armstrong, *J. Biol. Chem.*, 2010, **285**, 3928–3938.

25 M. Saggu, I. Zebger, M. Ludwig, O. Lenz, B. Friedrich, P. Hildebrandt and F. Lendzian, *J. Biol. Chem.*, 2009, **284**, 16264–16276.

26 G. Sawers, *Anton. Leeuw. Int. J. G.*, 1994, **66**, 57–88.

27 K. Trchounian, S. Blbulyan and A. Trchounian, *J. Bioenerg. Biomembr.*, 2013, **45**, 253–260.

28 A. Volbeda, P. Amara, C. Darnault, J.-M. Mouesca, A. Parkin, M. M. Roessler, F. A. Armstrong and J. C. Fontecilla-Camps, *Proc. Natl. Acad. Sci.*, 2012, **109**, 5305–5310.

29 R. M. Evans, P. A. Ash, S. E. Beaton, E. J. Brooke, K. A. Vincent, S. B. Carr and F. A. Armstrong, *J. Am. Chem. Soc.*, 2018, **140**, 10208–10220.

30 J. Fritsch, P. Scheerer, S. Frielingsdorf, S. Kroschinsky, B. Friedrich, O. Lenz and C. M. T. Spahn, *Nature*, 2011, **479**, 249–252.

31 Y. Shomura, K.-S. Yoon, H. Nishihara and Y. Higuchi, *Nature*, 2011, **479**, 253–256.

32 S. Frielingsdorf, J. Fritsch, A. Schmidt, M. Hammer, J. Löwenstein, E. Siebert, V. Pelmenschikov, T. Jaenicke, J. Kalms, Y. Rippers, F. Lendzian, I. Zebger, C. Teutloff, M. Kaupp, R. Bittl, P. Hildebrandt, B. Friedrich, O. Lenz and P. Scheerer, *Nat. Chem. Biol.*, 2014, **10**, 378–385.

33 T. Goris, A. F. Wait, M. Saggu, J. Fritsch, N. Heidary, M. Stein, I. Zebger, F. Lendzian, F. A. Armstrong, B. Friedrich and O. Lenz, *Nat. Chem. Biol.*, 2011, **7**, 310–318.

34 M.-E. Pandelia, W. Nitschke, P. Infossi, M.-T. Giudici-Orticoni, E. Bill and W. Lubitz, *Proc. Natl. Acad. Sci.*, 2011, **108**, 6097–6102.

35 M. C. Marques, R. Coelho, A. L. De Lacey, I. A. C. Pereira and P. M. Matias, *J. Mol. Biol.*, 2010, **396**, 893–907.

36 M. C. Marques, C. Tapia, O. Gutiérrez-Sanz, A. R. Ramos, K. L. Keller, J. D. Wall, A. L. De Lacey, P. M. Matias and I. A. C. Pereira, *Nat. Chem. Biol.*, 2017, **13**, 544–550.

37 A. Volbeda, P. Amara, C. Darnault, J.-M. Mouesca, A. Parkin, M. M. Roessler, F. A. Armstrong and J. C. Fontecilla-Camps, *Proc. Natl. Acad. Sci.*, 2012, **109**, 5305–5310.

38 A. Volbeda, M.-H. Charon, C. Piras, E. C. Hatchikian, M. Frey and J. C. Fontecilla-Camps,

Nature, 1995, **373**, 580–587.

39 Y. Higuchi, H. Ogata, K. Miki, N. Yasuoka and T. Yagi, *Structure*, 1999, **7**, 549–556.

40 H. Ogata, W. Lubitz and Y. Higuchi, *J. Biochem.*, 2016, **160**, 251–258.

41 R. M. Evans, E. J. Brooke, S. A. M. Wehlin, E. Nomerotskaia, F. Sargent, S. B. Carr, S. E. V Phillips and F. A. Armstrong, *Nat. Chem. Biol.*, 2016, **12**, 46–50.

42 M. M. Roessler, R. M. Evans, R. A. Davies, J. Harmer and F. A. Armstrong, *J. Am. Chem. Soc.*, 2012, **134**, 15581–15594.

43 M.-E. Pandelia, W. Nitschke, P. Infossi, M.-T. Giudici-Orticoni, E. Bill and W. Lubitz, *Proc. Natl. Acad. Sci.*, 2011, **108**, 6097–6102.

44 A. S. Pereira, P. Tavares, I. Moura, J. J. G. Moura and B. H. Huynh, *J. Am. Chem. Soc.*, 2001, **123**, 2771–2782.

45 M.-E. Pandelia, W. Nitschke, P. Infossi, M.-T. Giudici-Orticoni, E. Bill and W. Lubitz, *Proc. Natl. Acad. Sci.*, 2011, **108**, 6097–6102.

46 P. Wulff, C. C. Day, F. Sargent and F. A. Armstrong, *Proc. Natl. Acad. Sci.*, 2014, **111**, 6606–6611.

47 H. Adamson, M. Robinson, J. J. Wright, L. A. Flanagan, J. Walton, D. Elton, D. J. Gavaghan, A. M. Bond, M. M. Roessler and A. Parkin, *J. Am. Chem. Soc.*, 2017, **139**, 10677–10686.

48 M. Asso, B. Guigliarelli, T. Yagi and P. Bertrand, *Biochim. Biophy. Acta*, 1992, **1122**, 50–56.

49 M. Teixeira, I. Moura, A. V Xavier, J. J. Moura, J. LeGall, D. V DerVartanian, H. D. Peck and B. H. Huynh, *J. Biol. Chem.*, 1989, **264**, 16435–16450.

50 J. Kalms, A. Schmidt, S. Frielingsdorf, T. Utesch, G. Gotthard, D. von Stetten, P. van der Linden, A. Royant, M. A. Mroginski, P. Carpentier, O. Lenz and P. Scheerer, *Proc. Natl. Acad. Sci.*, 2018, **115**, E2229–E2237.

51 P. Wang, R. B. Best and J. Blumberger, *J. Am. Chem. Soc.*, 2011, **133**, 3548–3556.

52 Y. Montet, P. Amara, A. Volbeda, X. Vernede, E. C. Hatchikian, M. J. Field, M. Frey and J. C. Fontecilla-Camps, *Nat. Struct. Biol.*, 1997, **4**, 523–526.

53 P.-P. Liebgott, F. Leroux, B. Burlat, S. Dementin, C. Baffert, T. Lautier, V. Fourmond, P. Ceccaldi, C. Cavazza, I. Meynial-Salles, P. Soucaille, J. C. Fontecilla-Camps, B. Guigliarelli, P. Bertrand, M. Rousset and C. Léger, *Nat. Chem. Biol.*, 2010, **6**, 63–70.

54 P. A. Ash, R. Hidalgo and K. A. Vincent, *ACS Catal.*, 2017, **7**, 2471–2485.

55 R. Hidalgo, P. A. Ash, A. J. Healy and K. A. Vincent, *Angew. Chem. Int. Ed.*, 2015, **54**, 7110–7113.

56 P. A. Ash, S. E. T. Kendall-Price and K. A. Vincent, *Acc. Chem. Res.*, 2019, **52**, 3120–3131.

57 M. Kampa, M.-E. Pandelia, W. Lubitz, M. van Gastel and F. Neese, *J. Am. Chem. Soc.*, 2013,

135, 3915–3925.

58 M. Stein and W. Lubitz, *Curr. Opin. Chem. Biol.*, 2002, **6**, 243–249.

59 C. Fichtner, C. Laurich, E. Bothe and W. Lubitz, *Biochemistry*, 2006, **45**, 9706–9716.

60 A. Volbeda, L. Martin, E. Barbier, O. Gutiérrez-Sanz, A. L. De Lacey, P.-P. Liebgott, S. Dementin, M. Rousset and J. C. Fontecilla-Camps, *J. Biol. Inorg. Chem.*, 2015, **20**, 11–22.

61 H. Ogata, S. Hirota, A. Nakahara, H. Komori, N. Shibata, T. Kato, K. Kano and Y. Higuchi, *Structure*, 2005, **13**, 1635–1642.

62 S. E. Beaton, R. M. Evans, A. J. Finney, C. M. Lamont, F. A. Armstrong, F. Sargent and S. B. Carr, *Biochem. J.* 2018, **475**, 1353–1370.

63 R. M. Evans, P. A. Ash, S. E. Beaton, E. J. Brooke, K. A. Vincent, S. B. Carr and F. A. Armstrong, *J. Am. Chem. Soc.*, 2018, **140**, 10208–10220.

64 W. Lubitz, H. Ogata, O. Rüdiger and E. Reijerse, *Chem. Rev.*, 2014, **114**, 4081–4148.

65 M. Senger, K. Laun, B. Soboh and S. T. Stripp, *Catalysts*, 2018, **8**, 530.

66 Y. Ilina, C. Lorent, S. Katz, J.-H. Jeoung, S. Shima, M. Horch, I. Zebger and H. Dobbek, *Angew. Chem. Int. Ed.*, 2019, **58**, 18710–18714.

67 H. Ogata, K. Nishikawa and W. Lubitz, *Nature*, 2015, **520**, 571–574.

68 S. Kendall-Price, DPhil thesis, University of Oxford, 2022.

69 S. Foerster, M. Stein, M. Brecht, H. Ogata, Y. Higuchi and W. Lubitz, *J. Am. Chem. Soc.*, 2003, **125**, 83–93.

70 H. Ogata, T. Krämer, H. Wang, D. Schilter, V. Pelmenschikov, M. van Gastel, F. Neese, T. B. Rauchfuss, L. B. Gee, A. D. Scott, Y. Yoda, Y. Tanaka, W. Lubitz and S. P. Cramer, *Nat. Commun.*, 2015, **6**, 7890.

71 R. Hidalgo, P. A. Ash, A. J. Healy and K. A. Vincent, *Angew. Chem. Int. Ed.*, 2015, **54**, 7110–7113.

72 K. A. Vincent, A. Parkin, O. Lenz, S. P. J. Albracht, J. C. Fontecilla-Camps, R. Cammack, B. Friedrich and F. A. Armstrong, *J. Am. Chem. Soc.*, 2005, **127**, 18179–18189.

73 R. Gonzalez, DPhil thesis, University of Oxford, 2016.

74 P. Trens, R. Durand, B. Coq, C. Coutanceau, S. Rousseau and C. Lamy, *Appl. Catal. B.*, 2009, **92**, 280–284.

75 M. Chung, DPhil thesis, University of Oxford, 2016.

76 M. J. Lukey, A. Parkin, M. M. Roessler, B. J. Murphy, J. Harmer, T. Palmer, F. Sargent and F. A. Armstrong, *J. Biol. Chem.*, 2010, **285**, 3928–3938.

77 T. Imanishi, K. Nishikawa, M. Taketa, K. Higuchi, H. Tai, S. Hirota, H. Hojo, T. Kawakami, K.

Hataguchi, K. Matsumoto, H. Ogata and Y. Higuchi, *Acta Crystallogr. F*, 2022, **78**, 66–74.

78 H. Ogata, Y. Mizoguchi, N. Mizuno, K. Miki, S. Adachi, N. Yasuoka, T. Yagi, O. Yamauchi, S. Hirota and Y. Higuchi, *J. Am. Chem. Soc.*, 2002, **124**, 11628–11635.

79 L. A. Hyndman, R. H. Burris and P. W. Wilson, *J. Bacteriol.*, 1953, **65**, 522–531.

80 L. C. Seefeldt and D. J. Arp, *J. Bacteriol.*, 1989, **171**, 3298–3303.

81 S. V Hexter, M.-W. Chung, K. A. Vincent and F. A. Armstrong, *J. Am. Chem. Soc.*, 2014, **136**, 10470–10477.

82 T. Tomita, S. Ogo, T. Egawa, H. Shimada, N. Okamoto, Y. Imai, Y. Watanabe, Y. Ishimura and T. Kitagawa, *J. Biol. Chem.*, 2001, **276**, 36261–36267.

83 B. K. Burgess, J. F. Rubinson and J. L. Corbin, *Inorganica Chim. Acta*, 1983, **79**, 54–55.

84 J. F. Rubinson, J. L. Corbin and B. K. Burgess, *Biochemistry*, 1983, **22**, 6260–6268.

85 M. Kumar and S. W. Ragsdale, *J. Am. Chem. Soc.*, 1995, **117**, 11604–11605.

86 Y. Ren, X. H. Xing, C. Zhang and Z. Gou, *Biotechnol. Lett.*, 2005, **27**, 1029–1033.

87 F. Lu, P. R. Smith, K. Mehta and J. R. Swartz, *Int. J. Hydrogen Energy*, 2015, **40**, 9113–9124.

88 F. A. Armstrong, R. M. Evans, S. V Hexter, B. J. Murphy, M. M. Roessler and P. Wulff, *Acc. Chem. Res.*, 2016, **49**, 884–892.

89 B. L. Greene, C.-H. Wu, P. M. McTernan, M. W. W. Adams and R. B. Dyer, *J. Am. Chem. Soc.*, 2015, **137**, 4558–4566.

90 Z. Gu, J. Dong, C. B. Allan, S. B. Choudhury, R. Franco, J. J. G. Moura, I. Moura, J. LeGall, A. E. Przybyla, W. Roseboom, S. P. J. Albracht, M. J. Axley, R. A. Scott and M. J. Maroney, *J. Am. Chem. Soc.*, 1996, **118**, 11155–11165.

91 H. Wang, C. Y. Ralston, D. S. Patil, R. M. Jones, W. Gu, M. Verhagen, M. Adams, P. Ge, C. Riordan, C. A. Marganian, P. Mascharak, J. Kovacs, C. G. Miller, T. J. Collins, S. Brooker, P. D. Croucher, K. Wang, E. I. Stiefel and S. P. Cramer, *J. Am. Chem. Soc.*, 2000, **122**, 10544–10552.

92 R. S. K. Ekanayake, V. A. Streltsov, S. P. Best and C. T. Chantler, *J. Appl. Crystallogr.*, 2024, **57**, 125–139.

93 S. Foerster, M. Stein, M. Brecht, H. Ogata, Y. Higuchi and W. Lubitz, *J. Am. Chem. Soc.*, 2003, **125**, 83–93.

94 M. M. Roessler, R. M. Evans, R. A. Davies, J. Harmer and F. A. Armstrong, *J. Am. Chem. Soc.*, 2012, **134**, 15581–15594.

95 K.-M. Weitzel, *Curr. Opin. Electrochem.*, 2021, **26**, 100672.

96 P. A. Ash, S. B. Carr, H. A. Reeve, A. Skorupskaitė, J. S. Rowbotham, R. Shutt, M. D. Frogley, R. M. Evans, G. Cinque, F. A. Armstrong and K. A. Vincent, *Chem. Commun.*, 2017, **53**, 5858–5861.

97 S. P. Best, V. A. Streltsov, C. T. Chantler, W. Li, P. A. Ash, S. Hayama and S. Diaz-Moreno, *J. Synchrotron Radiat.*, 2021, **28**, 472–479.

Chapter 2: Theory and Experiment

The metalloprotein hydrogenase is the primary focus of this thesis. It exhibits a series of catalytic intermediates under different redox conditions and during catalysis through efficient electron transfer via a chain of iron-sulfur clusters between the bimetallic active site and a redox partner which interacts on the protein surface. The latter can be native redox subunits, redox mediators, or electrodes. [1–4] Electrochemical methods, therefore, are very powerful for investigating hydrogenase chemistry and will be used as the primary biophysical technique in this work. This chapter will describe the theory of electrochemistry, the fundamentals of electrochemical/spectroelectrochemical cell designs, and the experimental procedures.

Two spectroscopy techniques are predominantly utilized in this work: infrared (IR) and X-ray absorption spectroscopy (XAS). IR spectroscopy is the main characterisation method to study [NiFe]-hydrogenase, due to the presence of intrinsic CO and CN^- ligands at the active site. XAS is useful for targeting the redox-active Ni center.[4–8] The fundamental theory of both spectroscopies will be presented in this chapter, alongside the experimental procedures for specific cell setups. Sample preparation procedures, including protein preparation and crystallisation, are also described in this chapter.

2.1 Electrochemistry

2.1.1 Electrochemical Reaction at Equilibrium

Nernst Equation

The redox reactions in electrochemical cells consist of transferring electrons from a reducing agent to an oxidising agent, which can be divided into two half-reactions occurring at the anode and cathode. A presentation of the half-cell reduction (Equation 2.1) demonstrates the reaction at cathode, where α and β are the stoichiometric coefficients, n is the number of electrons involved in this redox reaction, Ox and Red stand for oxidised and reduced forms, respectively. Similarly, at the anode, half-cell oxidation has the opposite flow of electrons, where a reduced species loses electrons to generate its oxidised form.

$$\alpha Ox + ne^- \rightleftharpoons \beta Red \tag{2.1}$$

The redox couple will reach equilibrium with the applied potential from the electrode, and the concentrations of the individual species at the electrode-solution interface can be calculated from the Nernst equation (Equation 2.2), which relates the ratio of the Ox and Red species to their standard reduction potential (E°_{red}) and the applied potential (E)

$$E = E^{\circ}_{red} - \frac{RT}{nF}\, ln\left(\frac{[Red]^{\beta}}{[Ox]^{\alpha}}\right) = E^{\circ}_{red} - \frac{RT}{nF}\, ln\,(Q) \tag{2.2}$$

E°_{red} is the standard reduction potential measured under standard conditions (all activities are 1 mol L^{-1} or 1 atm at 25 °C), where R is the gas constant (8.314 J mol^{-1} K^{-1}), T is the temperature in Kelvin, n is the number of electrons involved in the redox reaction, F is the Faraday constant (96485 C mol^{-1}), α and β are the stoichiometric coefficients of the

oxidised and reduced species in the cell half-reaction. The argument of the logarithm can also be expressed as the reaction quotient, Q. Activity which measures the "effective concentration" is commonly applied in the Nernst equation. However, since the redox-active species involved in electrochemical reactions in this thesis are dilute (approximately 1 mM), it is acceptable to use concentration instead.[9]

The interconversion between Ox and Red at a specific applied potential E establishes a dynamic equilibrium, where the concentration ratio $\frac{[Red]^{\beta}}{[Ox]^{\alpha}}$ remains constant, as defined by Equation 2.2. This relationship is illustrated in Figure 2.1, which shows how the concentrations of Ox and Red vary with the potential applied to the electrode. The standard reduction potential E°_{red} is the potential where the concentrations (more precisely, activities) of Ox and Red are equal (at the intersection of two concentration curves).

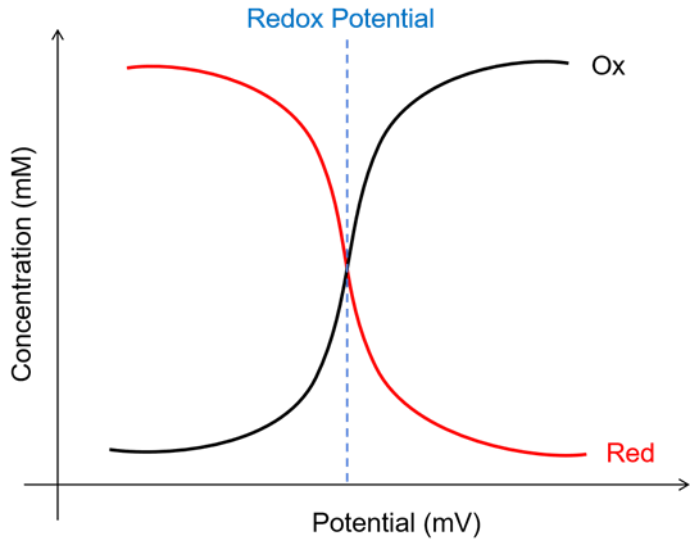

Figure 2.1: The concentration of the redox active species in its oxidised (Ox) and reduced (Red) forms as a function of the potential.

The Gibbs free energy change (ΔG) for a complete electrochemical cell reaction is directly

related to the electrical work the system can perform. The maximum electrical work is given by $-nFE$, where E is the electromotive force (EMF) of the cell. For a cell reaction, the relationship is：

$$\Delta G = -nF\Delta E \tag{2.3}$$

where ΔE is the difference in potential between the cathode and anode half-cells.

In comparison to the Nernst equation (Equation 2.2), the relationship between Gibbs free energy and the reaction quotient Q (for the full cell reaction) can be written as:

$$\Delta G = \Delta G^{\circ} + RT\ ln\ (Q) \tag{2.4}$$

For a reversible reaction at equilibrium, $Q = K$ (equilibrium constant), ΔG is equal to 0, therefore, the relationship between ΔG° and K is:

$$\Delta G^{\circ} = -RTln(K) \tag{2.5}$$

If $\Delta G^{\circ} < 0$, then $K > 1$, indicating that the equilibrium favours the product side.

Proton-Coupled Electron Transfer

Electron transfer processes often occur alongside proton transfer to balance the charge. This is defined as proton-coupled electron transfer (PCET). The general half-cell reaction equation with one proton involved is shown in Equation 2.6.

$$Ox + ne^{-} + H^{+} \rightleftharpoons RedH \tag{2.6}$$

The equilibrium potential of this redox couple can be studied using the Nernst equation to

obtain Equation 2.7:

$$E = E^{\circ}_{red} - \frac{RT}{nF}\, ln\left(\frac{[RedH]}{[Ox][H^+]}\right) \tag{2.7}$$

The term $pH = -\log[H^+]$, can be extracted from the argument, and at room temperature (25 °C), the equation can be rewritten to show that the redox potential is pH-dependent:

$$E = E^{\circ}_{red} - \frac{0.059}{n}\, log\left(\frac{[RedH]}{[Ox]}\right) - \frac{0.059}{n} pH \tag{2.8}$$

[NiFe]-hydrogenases undergo multiple PCET processes during fast catalysis. These PCET processes can occur via two mechanisms: concerted PCET, where electron and proton transfer happen simultaneously, or stepwise PCET, where one occurs directly after the other.[5,10] The remaining mechanistic challenges in the PCET of [NiFe]-hydrogenases such as whether they are concerted or stepwise, and which amino acid is involved in proton transfer will be addressed later in this thesis.

Non-Equilibrium Electrochemistry

When an external power supply creates a potential difference where the electrode potential differs from the Nernstian potential of the redox couple, a redox reaction occurs, inducing current flow. The current allows the exchange of electrons between redox-active species in solution and the polarized electrode, altering the reduced and oxidised forms of the species until the Nernstian potential of the redox couple reaches that of the working electrode. The relationship between current, applied potential, and the kinetics of electrolysis will be discussed in Section 2.1.3.

Electroanalytical chemistry uses non-equilibrium electrochemical reactions, which are heavily applied in this thesis to study [NiFe]-hydrogenases. Among electroanalytical methods, the three-electrode system is commonly used to set up an electrochemical cell, and all electrochemical measurements in this thesis were performed using various three-electrode cells.

2.1.2 Three-Electrode System

The three-electrode system comprises a working electrode (WE), reference electrode (RE), and counter electrode (CE), which are controlled by an external power supply, the potentiostat. The WE is often referred to as the indicator electrode, which is made of an electrochemically inert material, and its electrode-solution interface is where the electrochemical reactions of interest take place. The RE behaves as an ideally non-polarisable electrode, and its interfacial potential difference remains fixed due to the constant species composition at the electrode-solution interface. Hence, the WE potential is indirectly measured by the potential difference between WE and RE via a voltmeter, according to Equation 2.9:

$$E = \Delta\varphi_{WE} - \Delta\varphi_{RE} = (\varphi_{elec} - \varphi_{sol})_{WE} - (\varphi_{elec} - \varphi_{sol})_{RE} \quad (2.9)$$

As the difference between the RE and electrolyte solution is constant, any changes in applied potential directly impact the WE. The three-electrode system takes advantage of implementing a counter electrode to complete the circuit and achieve the electron-neutrality of the solution. The current therefore flows between WE and CE, which is measured by an ammeter. The closed loop between WE and CE allows minimising the current between WE and

RE, which prevents RE potential drift caused by undesired electrochemical reactions at its interface. Ideally, the CE should have a much larger surface area than the WE to avoid current-induced rate-limiting processes at the WE. However, low concentrations of redox mediators and biological samples (mM) studied in this thesis produce relatively low current (mA) at high-surface-area WE, hence the size of CE is not critical.

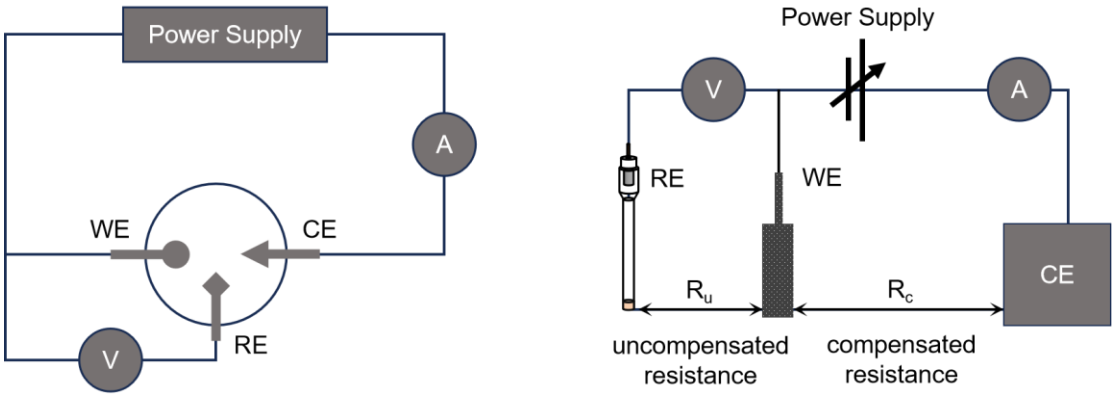

Figure 2.2: (Left) The simplified representation of a three-electrode cell system. (Right) Diagram of electrodes and circuit showing the uncompensated and compensated resistance.

In this thesis, all potentials are reported against the standard hydrogen electrode (SHE). The SHE comprises a Pt wire immersed in a 1 M H^+ (aq) solution under 1 bar H_2 at 298K. Converting measured potentials to SHE depends on whether a saturated calomel electrode (SCE) or silver/silver chloride reference electrode is used. The SCE is a half-cell composed of mercurous chloride (Hg_2Cl_2, calomel) in contact with a metallic mercury pool, with saturated KCl as the filling solution. The E° value is +0.244 V versus SHE at standard conditions, and its half-cell reaction is as follows:[11]

$$Hg_2Cl_2\ (s) + 2e^- \rightleftharpoons 2Hg\ (l) + 2Cl^-\ (aq) \qquad (2.10)$$

The silver/silver chloride reference electrode is made up of a silver wire coated with silver chloride, immersed in 3 M KCl solution. The E° value is +0.201 V versus SHE at standard conditions, and its half-cell reaction is as follows:[12]

$$AgCl\ (s) + e^{-} \rightleftharpoons Ag\ (s) + Cl^{-}\ (aq) \tag{2.11}$$

The conductivity of a circuit depends on the conduction of electrons and ions. A poorly conducting solvent system will result in large impedance and hence create a large iR drop. An addition of supporting electrolyte can increase the ionic strength of the solution, overcoming the energy lost due to resistance. In Figure 2.2, the resistance between WE and CE is called compensated resistance. Despite the resistance being directly related to the ionic strength of the solution and their separation, the iR drop can be compensated for by adjusting the power supply from the potentiostat. However, the resistance between the WE and RE is uncompensated; hence, the real potential at WE is $E_{real} = E_{applied} - iR_u$. The iR drop effect in electrochemical measurements in this work is assumed negligible due to the close distance between WE and RE, high ionic strength of the solution, and low currents.

The three-electrode cell system is used to perform two types of electroanalytical experiments in this work: cyclic voltammetry and chronoamperometry.

Cyclic Voltammetry

In cyclic voltammetry (CV), the WE potential is swept back and forth at a given rate in a chosen potential window. Changing the potential at the WE induces current flow through the WE in

response. In the case of redox-active species at the WE electrode-solution interface, as the potential is stepped to a lower limit, the oxidised form will get reduced to produce a reductive current, and the process is reversed when the potential is stepped back to the higher limit. The current is then plotted as a function of potential to give a voltammogram. In this thesis, CV is employed to study the redox mediator properties of the electrolyte buffer solution and the redox potential of biological samples. The reductive or oxidative current of a redox couple gives rise to reduction and oxidation peaks on a voltammogram, and the redox potential of the redox couple is the mean of the two peak positions for a reversible redox process.

Cyclic voltammetry is also widely applied to investigate the catalytic properties of [NiFe]-hydrogenases, including activity profiling and inactivation mechanisms.[13–15] The magnitude of the catalytic current generated by the enzyme during potential sweep experiments directly correlates with its intrinsic activity. Analysis of the complete CV profile enables extrapolation of optimal operating potentials and identification of electrochemical conditions that promote inactive states.

Chronoamperometry

The second electroanalytical method is chronoamperometry (CA). The current of WE is measured as a function of time at a given potential. In addition, the applied potential is adjustable to different values, and the current in response will be subsequently monitored. CA is commonly applied to study the catalytic current of [NiFe]-hydrogenases in the presence of substrates in protein film electrochemistry assays.[4] Furthermore, CA is also capable of studying

the effects of inhibitors, as the catalytic current reflects the impacts of the addition of inhibitors.[16] In this thesis, CA is primarily employed for two purposes. Firstly, spectroelectrochemical methods couple CA to IR and XAS spectroscopy: controllable stepped potential allows these spectroscopic techniques to monitor enzymes at different redox levels, either in steady state or in equilibrium, including any changes in features with respect to potential jumps. Secondly, CA allows a chosen potential to be constantly applied on WE to perform electrolysis in the cell, and the current reading indicates when equilibrium has been achieved. This method is applied for electrochemical poising of a biological sample at a chosen potential with selected mediators, with details discussed in Chapters 4 and 5.

2.1.3 The Electrode-Solution Interface

The electron transfer process at electrodes is key for an electrochemical reaction. The electrons can be passed from an electrode to redox-active species in solution, or vice versa. The energy, or the Gibbs energy of the electrons in an electrode, solely depends on the electrode potential. According to band theory, the orbitals of metals interact with each other to emerge as a set of molecular orbitals that extend throughout the solid, and the electrons in the electrode populate the unfilled orbitals up to the Fermi level, which indicates the average energy of electrons at the potential. Polarising an electrode negatively or positively can change the Fermi level to a higher or lower position, respectively, and hence induce the redox reaction at the electrode.[9]

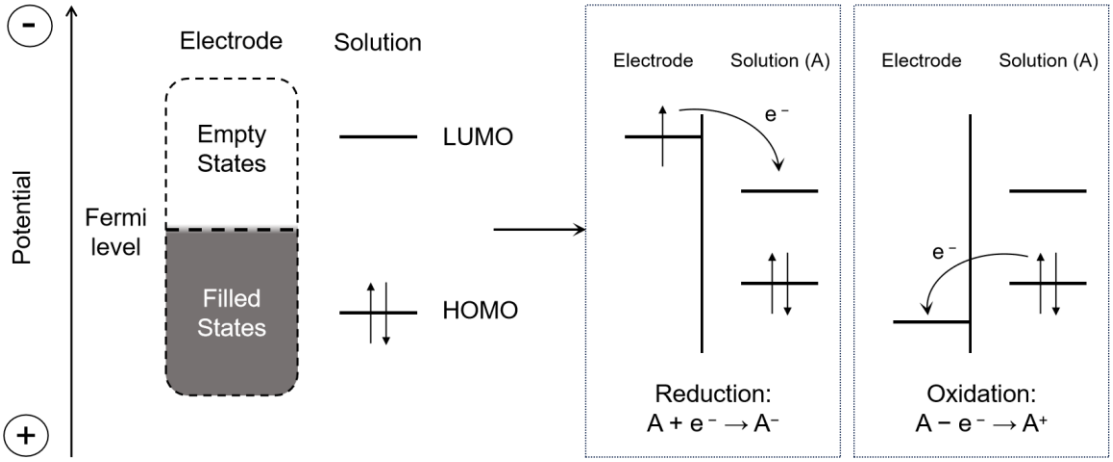

Figure 2.3: The effect of changes in the Fermi level of an electrode by changing the electrode's polarisation. Depending on the relative energy of the Fermi level, the electron can leave the electrode to the LUMO of a redox-active species in solution to achieve reduction, or the direction of electron flow is reversed to complete the oxidation reaction.

A molecular orbital has fixed energy, and the direction of electron flow between an electrode and redox-active species depends on the energy of the Fermi level. In Figure 2.3, the energy of the Fermi level is higher than the HOMO but lower than the LUMO of the redox-active species, so the electron transfer process is not thermodynamically favourable. When a more negative potential is applied to the electrode, the Fermi level is brought higher, higher than the LUMO of the redox species, and the electrons will spontaneously leave the electrode to the LUMO of the redox species, so the reduction occurs. Conversely, a more positive potential can be applied to the electrode, and the positively polarised electrode will lead the Fermi level to decrease. Once the energy of the Fermi level is lower than the HOMO of the redox-active species, the electrons can flow from the HOMO of the molecule to the electrode to proceed with oxidation. The applied potential at which no net flow of electrons occurs between the

electrode and the redox-active species is the equilibrium potential for that specific solution composition. This equilibrium potential depends on the ratio of oxidised to reduced species, as described by the Nernst equation.

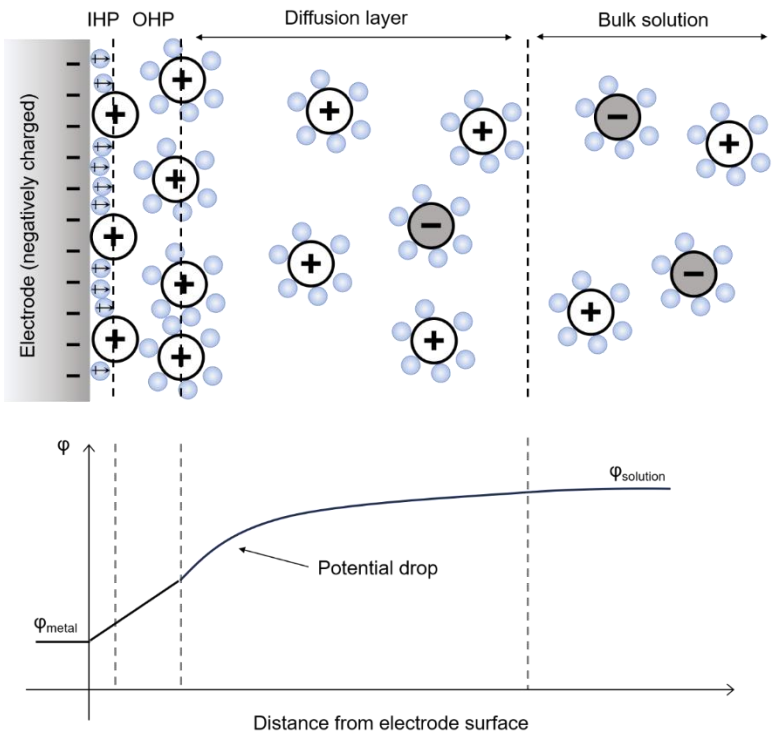

Figure 2.4: The schematic representation of the Grahame model of the electrode-solution interface (top) and the change in potential with distance from the electrode (bottom). (Top) The interface structure consists of the electrode, inner Helmholtz plane (IHP), outer Helmholtz plane (OHP), the diffusion layer, and the bulk solution. The blue spheres represent solvent molecules. (Bottom) The solution potential changes drastically at the double layer while gradually increasing in the diffusion layer.

The molecular arrangements near electrodes consist of the electrode polarisation and the composition of the solution. At a polarised electrode, the massive electric field will influence the polar or charged molecules in the solution to adopt certain orientations, which in general

comprises the electrical double layer, diffusion layer, and bulk solution with respect to the distance from the electrode, as shown in Figure 2.4.

The molecules or ions near the electrode react to a polarised electrode differently compared to those in bulk solution. In Figure 2.4, the electrode is negatively charged; the generated electric field drives the molecules (water) close to the electrode to arrange themselves so that their permanent dipole moment is directed away from the electrode. The positively charged ions will be attracted towards the electrode, with some of them being specifically adsorbed. Therefore, the potential of the solution is minimised by those ordered species near it. As a result, the solvent molecules and charged species at the electrode surface are better-ordered than in any other part of the solution, and the layer of ordered solvent at the electrode is defined as the inner Helmholtz plane (IHP). The ions or molecules in the IHP are not sufficient to compensate for the potential at the electrode. Hence, excess negative charge at the electrode will induce a net movement of solvated cations in the solution to migrate near the electrode. These solvated cations do not touch the electrode, and the region they are allocated in, right beside the IHP, is called the outer Helmholtz plane (OHP). These two highly ordered layers coat the electrode, and the electrode-solution interface can be considered as a capacitor.[17]

However, the electrical double layer cannot completely screen the charges on a polarised electrode (in Figure 2.4, the excess negative charges can still be felt by charged species in the solution). As a result, a region with an even distribution of charges (more cations than anions in the case shown in Figure 2.4) is accumulated to form the diffusion layer. In contrast, the

molecules in bulk solution have a higher degree of freedom. They are oriented randomly, and their movements are due to Brownian motion or forced convection.

2.1.4 Kinetics of Electrochemical Reactions

The equilibrium of a dynamic electron transfer process can be predicted by thermodynamics as described in the last section. However, the rates at which the equilibrium is perturbed (developing a new equilibrium after a potential switch or the addition of new redox species) can be directly manifested as measurable current, owing to the electron exchange process at the electrode-solution interface. The current or the kinetics of electron transfer are affected by the following factors:[18]

- Heterogeneous electron transfer rate between electrode and redox active species in solution at interface.
- Adsorption/desorption of redox active species at the electrode.
- Reorganization of ions and solvent molecules.
- Mass transport, including diffusion, migration, and convection.

Heterogeneous Electron Transfer Kinetics

The rate of continuous exchange of electrons at metal-solution interfaces between the electrode and redox-active species can be quantitatively measured as current (I in A) or as

current density (j in A cm^{-2}), which takes account of its proportionality to the unit of electrode area. Therefore, the amount of redox-active species in solution that gets reduced or oxidised per unit of time is proportional to the rate of electron transfer. The rate of reduction and oxidation reactions at each side of the electrode can be expressed as:

$$Rate\ of\ reduction = \frac{d[Ox]}{dt} = k_{red}[Ox]_0 \tag{2.12}$$

$$Rate\ of\ oxidation = \frac{d[Red]}{dt} = k_{ox}[Red]_0 \tag{2.13}$$

where k_{red} and k_{ox} stand for the rate constant of electron transfer for the reduction and oxidation reaction at the cathode and anode, respectively, with units of s^{-1} (first order). $[Ox]_0$ and $[Red]_0$ are the concentrations of the oxidised and reduced species at the electrode surface, respectively. The current densities j_c and j_a obey Faraday's law, where the number of moles of electrons transferred is proportional to the rate of change in the concentration of redox-active species. Hence, according to Equation 2.14, j_c and j_a can be expressed as:

$$j_c = \nu F \frac{d[Ox]}{dt} = \nu F k_{red}[Ox]_0 \tag{2.14}$$

$$j_a = \nu F \frac{d[Red]}{dt} = \nu F k_{ox}[Red]_0 \tag{2.15}$$

in which ν is the valency of the redox-active species and F is the Faraday constant. The net current density considers both redox reactions, so it is given by:

$$j = j_a - j_c = \nu F k_{ox}[Red]_0 - \nu F k_{red}[Ox]_0 \tag{2.16}$$

The electron transfer behaves in an analogous manner to chemical processes, and the energy profile diagram describes the change in Gibbs free energy along with the reaction coordinate as shown in Figure 2.5. The diagram describes a redox reaction going through a path with an

energy barrier, from the oxidised species and an electron to a transition state followed by the reduced product.

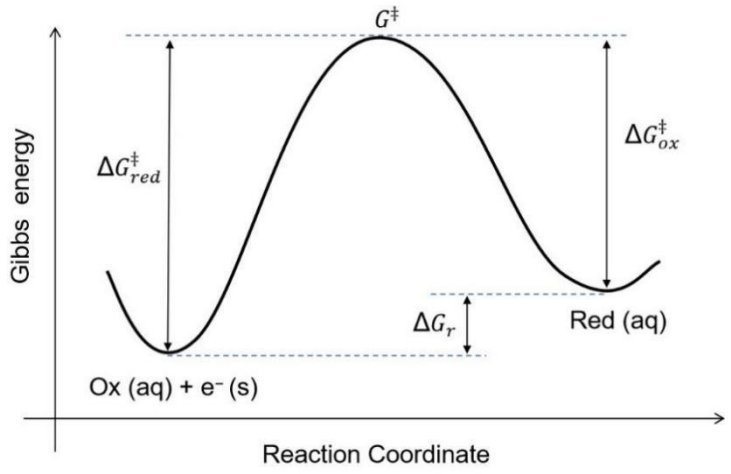

Figure 2.5: The reaction coordinate diagram of a redox couple. The energy barriers of both the forward and backward reactions are noted as $\Delta \boldsymbol{G^{\ddagger}_{red}}$, $\Delta \boldsymbol{G^{\ddagger}_{ox}}$, and the change in free energy of the reaction is noted as $\Delta \boldsymbol{G_r}$.

Transition state theory predicts the rate of the reduction reaction k_{red} to be:

$$k_{red} = A_c e^{\frac{-\Delta G^{\ddagger}_{red}}{RT}} \tag{2.17}$$

where A_c is a measurement of the rate of collision between redox active species and cathode surface, and it is proportional to temperature; and $\Delta G^{\ddagger}_{red}$ is the free energy of activation. As the reaction at an electrode is reversible, similarly k_{ox} can be expressed as:

$$k_{ox} = A_a e^{\frac{-\Delta G^{\ddagger}_{ox}}{RT}} \tag{2.18}$$

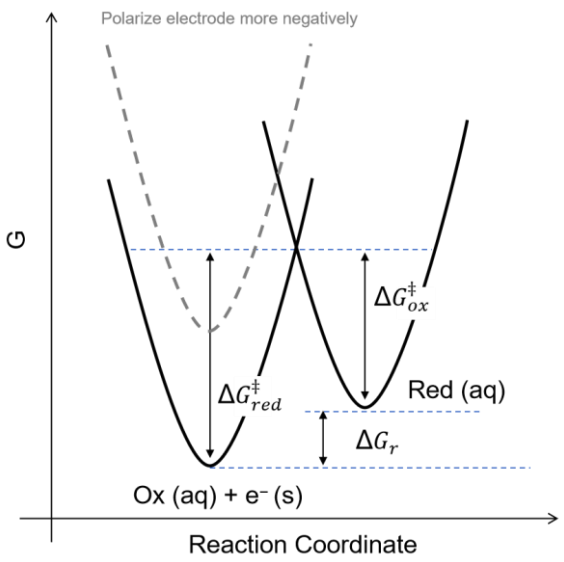

Figure 2.6: The reaction coordinate diagram shows the potential wells of both reactants and products of a redox reaction with vertically adjustable potential wells due to changes in electrode polarisation.

The electrochemical potential of redox-active species in both oxidised and reduced forms remain constant throughout the electrochemical reactions, while the electron's electrochemical potential can be altered by the external power supply via different polarisation of the electrode (different applied potential). Figure 2.6 demonstrates the potential wells of oxidised and reduced species of a reversible electrochemical reaction with a change in electrode polarisation. In the reaction coordinate diagram, the oxidation reaction is spontaneous due to lower activation energy. However, changes in the energy of the electron on the electrode will affect the total Gibbs energy of the "Ox + e⁻" potential well. Hence, if the electrode is switched to a more negative potential, the electrons on the electrode will have higher Gibbs energy (to do work), and the left-hand potential well is moved vertically upwards. This will lead to changes of activation energy $\Delta G^{\ddagger}_{red}$, $\Delta G^{\ddagger}_{ox}$, and change of Gibbs energy of the reaction ΔG_r allowing us to predict the shift in the equilibrium position and the change in the

rate constants for the forward and backward reactions.

For a reversible redox couple, a state of dynamic equilibrium is achieved when the applied potential (E) equals the equilibrium potential ($E_{1/2}$) for that system. If a potential different from the current $E_{1/2}$ is applied, it disrupts this dynamic balance. The difference between the applied potential and the equilibrium potential is termed the overpotential (η), where

$$\eta = E - E_{1/2} \tag{2.19}$$

The application of an overpotential ($\eta \neq 0$) drives the net reaction in the direction that consumes the excess energy, leading to a change in the concentrations of the redox species. This change in concentrations shifts the equilibrium potential $E_{1/2}$ itself, as described by the Nernst equation. The system thus evolves dynamically, establishing a new equilibrium condition where the concentrations have adjusted such that the new $E_{1/2_}$new matches the applied potential E. Therefore, applying any potential other than the initial equilibrium potential initiates a net reaction that continues until a new composition of oxidised and reduced species is established, corresponding to a new equilibrium state.

The driving force of the equilibrium perturbation is essentially the $\Delta\Delta G_r = \nu F\eta$, as Figure 2.6 shows the changing applied potential, hence changing overpotential, will change the ΔG_r. Similarly, a change in overpotential will also change the activation energy of the reversible reaction ($\Delta G_{red}^{\ddagger}$ and $\Delta G_{ox}^{\ddagger}$) by a fraction α, called symmetry factor, which can be expressed as:

$$\Delta G_{red}^{\ddagger} = \Delta G_{red}^{\ddagger}{}^{\circ} + \alpha\nu F\eta \tag{2.20}$$

$$\Delta G_{ox}^{\ddagger} = \Delta G_{ox}^{\ddagger\circ} - (1-\alpha)\nu F\eta \tag{2.21}$$

The symmetry factor (α) describes the shapes of potential wells of the reduced and oxidised forms of the redox reaction, hence the relative position of the transition state to reactants and products (the Hammond postulate).

Substituting Equation 2.20 and 2.21 into 2.17 and 2.18 gives the Eyring equation:

$$k_{red} = A_c \exp\left(\frac{\Delta G_{red}^{\ddagger\circ}}{RT}\right) + \exp(\frac{-\alpha\nu F\eta}{RT}) = k_{red}^{\circ} \exp(\frac{-\alpha\nu F\eta}{RT}) \tag{2.22}$$

$$k_{ox} = A_a \exp\left(\frac{\Delta G_{ox}^{\ddagger\circ}}{RT}\right) + \exp\left(\frac{(1-\alpha)\nu F\eta}{RT}\right) = k_{ox}^{\circ} \exp(\frac{(1-\alpha)\nu F\eta}{RT}) \tag{2.23}$$

The Eyring equation can be substituted into Equation 2.16. When the applied potential is equal to the equilibrium potential (η=0), the magnitude of j_c and j_a is the same so that the net current density is zero. This specific current density is denoted as j_0:

$$j_0 = j_c = j_a = \nu F k_{red}^{\circ}[Ox] = \nu F k_{ox}^{\circ}[Red] \tag{2.24}$$

Therefore, the Bulter-Volmer equation can be obtained to express the net current density:

$$j = j_0 \exp\left[\frac{(1-\alpha)\nu F\eta}{RT}\right] - j_0 \exp\left[\frac{\alpha\nu F\eta}{RT}\right] \tag{2.25}$$

Overall, the Eyring equation and Butler-Volmer equation predict the rate constant and the current density as a function of overpotential. Experimentally, if the current is not diffusion-limited (mass transport is not sufficient), faster electrolysis could be achieved via higher overpotential, which is crucial for electrochemical poising experiments demonstrated in Chapters 4 and 5.

2.1.5 Mass Transport at Electrodes

Apart from the electron transfer at the electrode-solution interface, physical processes play important roles in the kinetics of dynamic electrochemical reactions. For example, bulk electrolysis proceeds with the reactants moving towards the electrode interface and being subsequently transported back to the bulk solution after the redox reaction. The transportation of mass (ions or redox mediators and redox proteins in the case of hydrogenase studies) undergoes three mechanisms in general: diffusion, migration, and convection.

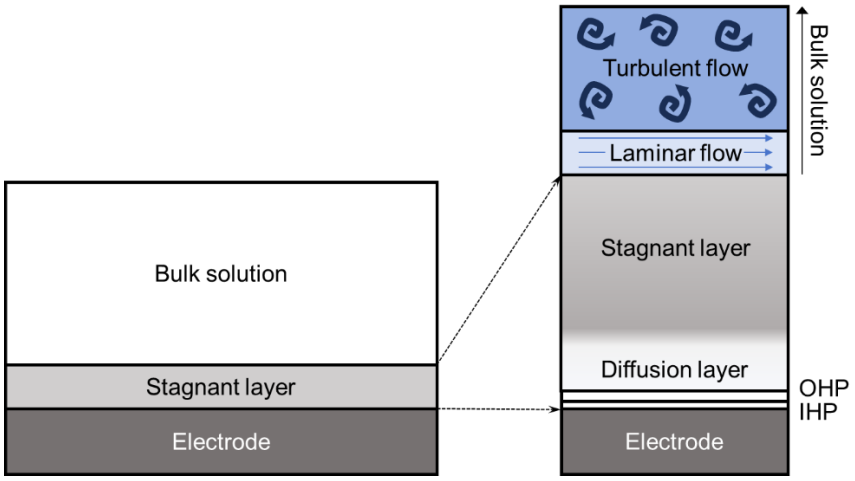

Figure 2.7: The electrode-solution interface consists of multiple layers. The Helmholtz plane and diffusion layer are only up to a few nanometres thick, whereas the stagnant layer is much thicker, and it depends on solvent viscosity and convection. Beyond it, convection dominates the mass transport, which has two types of flow.

Figure 2.7 schematically demonstrates the electrode-solution interface in a convection system, which is composed of multiple layers with distinct solution structures. The Helmholtz planes and the diffusion layer are only up to a few nanometres thick, whereas a thin layer of solution called the stagnant layer, further away from the electrode, remains almost immobile due to

electrokinetic phenomena. The stagnant layer can be up to a few micrometres thick depending on solvent viscosity and convection, and its mass transport solely depends on diffusion. Beyond this layer, convection is the main mass transport mechanism, which exhibits laminar flow (movement of solution sheets) and turbulent flow (irregular manner movements).[17]

Diffusion

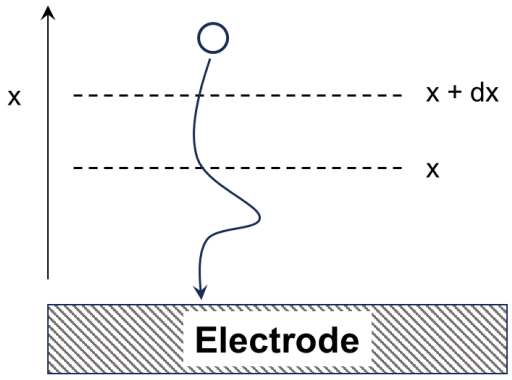

Figure 2.8: Diffusion of molecules has one net direction of movement, which is perpendicular to the electrode plane. The random movements in other directions are cancelled out.

Diffusion arises from the increase of entropy in the system through reorganising uneven solution concentration gradients to maximise homogeneity. For example, if a solute has different concentrations at two regions in a solution system, entropy acts as the driving force to cause the solute to move from high concentration to lower regions until the differences are evened out. This phenomenon is the predominant mass transport mechanism within the diffusion layer proximal to the electrode, where the solution is relatively stationary. In the electrochemical process, a redox reaction (i.e., reduction) takes place at the electrode-solution

interface. This will cause the concentration of reduced species to build up near the electrode and hence establish a concentration gradient. Diffusion will lead the oxidised species to have a net movement (flux) towards the electrode, and similarly, the reduced species will move in the opposite direction.

The rate of linear diffusion to a planar surface, as shown in Figure 2.8, can be mathematically expressed as Fick's 1st law, which follows Equation 2.26 for species A:

$$J = -D_A \frac{\partial [A]}{\partial x} \tag{2.26}$$

J is the diffusional flux, which measures the number of moles of material diffusing through a unit area per second; D_A is the diffusion coefficient of species A, which relates to its characteristic, e.g., hydrodynamic radius. $\frac{\partial [A]}{\partial x}$ is the concentration gradient.

In practice, the more relevant information is generally the change in concentration as a function of time, which is described in Fick's 2nd law, shown in Equation 2.27 for species A:

$$\frac{\partial [A]}{\partial t} = D_A \left(\frac{\partial^2 [A]}{\partial x^2} \right) \tag{2.27}$$

Only the concentration gradient orthogonal to the electrode surface will be considered, as movements parallel to the electrode statistically cancel out between a large number of solute species.

Migration

Migration is a type of mass transport caused by electrostatic interactions between the charged

electrode and oppositely charged ions in electrochemical processes. The external electric field is created by the electrical potential drop at the electrode-solution interface. Hence, the Coulombic forces induce the movement of ions to migrate or retreat from the electrode. The migration flux, J_m, is complicated to calculate when other types of mass transport mechanisms occur simultaneously (e.g., diffusion), but its proportionality can be expressed as in Equation 2.28:

$$J_m \propto -u[A]\frac{\partial \varphi}{\partial x} \tag{2.28}$$

where u is the ionic mobility, which depends on the ionic charge density and solution viscosity; $[A]$ is the concentration of the mobile ion; and $\frac{\partial \varphi}{\partial x}$ is the strength of the electric field.

Generally, in electrochemical studies, especially in voltammetric studies, high concentrations of redox-inert electrolyte are adopted. This ensures the electrolyte ions screen out the electric field generated at the electrode when a potential difference is applied. Therefore, the electrode-solution interface region can be treated as "neutral," so migration is no longer significant. The majority of electrochemical buffers used in this work are made for protein crystals, which contain high levels of salt (e.g., 150 mM NaCl), thus eliminating migration contributions. However, electrophoresis techniques depend on mass transport by migration. Gel electrophoresis utilises the electrostatic interaction between the external electric field and charged DNA and protein fragments to separate them by molecular weight.

Convection

Convection is the key mass transport mechanism for moving species over large distances (e.g., < 0.5 mm). The movement of convection is introduced by mechanical forces occurring in the solution system, and it can be categorised into natural convection and forced convection.[17,18]

Natural convection arises from a static solution system with a thermal gradient or solution density difference. In the former case, the convective flux is created by the movement of solution molecules from higher thermal energy to lower energy if the reaction at the electrode has a change in enthalpy, whereas the latter could be induced by a cooler solution surface caused by evaporation, leading the deficient surface region to exchange mass with the bulk.

Forced convection is introduced by external forces such as stirring, pumping the solution with mass flows, or bubbling gases. Two types of flow are generally considered, depending on the Reynolds number, which measures the ratio of inertial force to viscous force in a flow:

- Laminar flow: At low Reynolds number, solvent moves in a highly ordered sheet-like format.
- Turbulent flow: At high Reynolds number, solvent moves in different manners or directions, resulting in more sufficient mixing.

It is rational that the stronger the bulk solution convection, the narrower the stagnant layer, which directly relates to the diffusion-limited current in many electrochemistry studies, i.e., rotating disc voltammetry. The net rate of the redox reaction (manifested as current) at the electrode is not only related to the overpotential but also mass transport, mainly diffusion. In

the case of an oxidation-only scenario at an electrode, the diffusion-limited current is given by Equation 2.29:

$$I_{lim} = nFA[Red]_0 \frac{D_{Red}}{\delta_{max}} \tag{2.29}$$

Where I_{lim} is the diffusion limited current; n is the number of electrons involved in the redox reaction; F is the Faraday constant; A is the area of the electrode (assumed to be a plane); $[Red]_0$ is the bulk concentration of the reduced species; D_{Red} is the diffusion constant of reducible species; and δ_{max} is the stagnant layer thickness.

Multiple mass transport mechanisms can be complicated in a single electrochemical setup. Therefore, static solutions with high concentrations of redox-inert electrolyte can rule out the contribution of convection and migration, or, on the other hand, introduce forced convection to reduce the stagnant layer thickness, allowing for fast equilibration of the bulk solution and electrode interface. In this thesis, the former setup is adopted for the microspectroelectrochemical cell for single protein crystal potential titration in Chapters 3, whereas the latter setup precisely describes the *ex-situ* protein crystal posing electrochemical cell in Chapters 4 and 5. The design of these setups will be described later in this thesis.

2.2 Infrared Spectroscopy

Infrared (IR) spectroscopy is a powerful analytical method to study the interactions between a sample and IR light. Photons with a certain energy (wavenumber) will be absorbed by a molecule with quantized vibrational energy levels under selection rules. The specific energy

absorbed is related to the structure and chemical environment of the molecule. Therefore, IR spectroscopy is primarily employed to identify functional groups within a sample.

IR spectroscopy is a versatile technique that is able to measure all states of the sample (solid, liquid, gas, crystal, etc). In this work, it is employed to study the CO and CN^- ligands in [NiFe]-hydrogenases, primarily in the crystalline state via both transmission and reflection detection modes.

2.2.1 Harmonic Oscillator Hamiltonian and Selection Rules

The Hamiltonian operator and Schrödinger equation

The signal in IR spectroscopy arises from the excitation of a vibrational state from a lower energy level to a higher one. Figure 2.9 shows the basic physical relationships between the excitation and the corresponding spectrum, where ψ_i and ψ_f are the wavefunctions of the initial and final states, and ΔE represents the difference in energy between these states. The absorption peak position is the energy of the photon that a molecule absorbs, which directly reflects the magnitude of ΔE, but is generally given in units of wavenumbers. The intensity of the peak in the spectrum is related to the feasibility of the transition (depending on ψ_i and ψ_f, as discussed in the selection rules later in this chapter), the concentration of the sample, and the population of ψ_i. Therefore, a quantum model for vibrations in molecules needs to be set up to find the energy and wavefunctions that represent the vibrational energy levels. The simplest vibrational model is the stretching between a diatomic molecule, which can be approximated to simple harmonic motion (derivation in the next section). The harmonic

oscillator Hamiltonian can be set up for solving the Schrödinger equation $\hat{H}\psi = E\psi$.

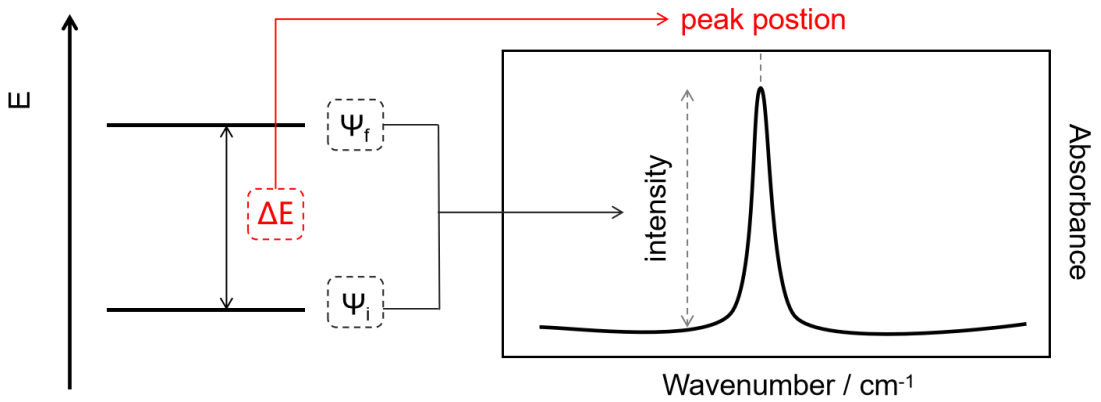

Figure 2.9 Interpreting and explaining an IR spectrum. The vibrational states before and after the transition and the energy of the transition are translated into the IR spectrum.

For a diatomic molecule with the bond length $\vec{r}$, the Hamiltonian operator consists of the kinetic and potential energy terms, which can be expressed as:

$$\hat{H}_{diatomic} = -\frac{\hbar^2}{2M}\nabla_{CM}^2 - \frac{\hbar^2}{2\mu}\nabla_{int}^2 + V(r) \tag{2.30}$$

where $\hbar$ is the reduced Planck constant, M is the total mass of the diatomic molecule, ∇_{CM}^2 is the Laplacian operator of the whole molecule in Cartesian coordinates, μ is the reduced mass of the molecule, ∇_{int}^2 is the Laplacian operator of the internal bond length variation in cartesian coordinates, and V is potential energy as a function of bond length.

Consider the diatomic molecule: the vibrational energy does not depend on where in space the centre of mass is, hence the first term with ∇_{CM}^2 corresponds to translation kinetic energy of the whole molecule which changes the total energy by a fixed amount and does not affect the spectrum. The second term with ∇_{int}^2 represents the vibrational kinetic energy of interest due to a change in bond length $\vec{r}$. The potential energy of the diatomic molecule is not

dependent on the spatial position but only related to the distance between atoms, the length of bond, r (not $\vec{r}$ since orientation does not matter).

Using the approximation of the potential energy of the harmonic oscillator, the potential energy can be rewritten as $V(x) = \frac{1}{2}kx^2$, where k is force constant and $x = r - r_e$ is the displacement from equilibrium internuclear distance. Substituting $V(x)$ and converting the Laplacian operator from Cartesian coordinates to spherical coordinates, the Hamiltonian operator for the harmonic oscillator can be written as:

$$\widehat{H}_{diatomic} = -\frac{\hbar^2}{2\mu}\frac{d^2}{dx^2} + \frac{1}{2}kx^2 \tag{2.31}$$

and hence the Schrödinger equation:

$$\left(-\frac{\hbar^2}{2\mu}\frac{d^2}{dx^2} + \frac{1}{2}kx^2\right)\Psi(x) = E\Psi(x) \tag{2.32}$$

Solving the Schrödinger equation can obtain the solution for both $\Psi(x)$ and E (discussed in the next section). The wavefunctions $\Psi(x)$ have only one integer quantum number n with values 0, 1, 2, 3 and so on and they are the product of a Gaussian and a polynomial part. The Gaussian part constrains the shape of the wavefunctions, and the polynomial part determines the nodal structure.

Selection Rules

Different quantum numbers n yield sequential vibrational states with different energies. However, the transitions between vibrational states within a molecule follow selection rules that determine whether the transition between two states is allowed, and hence result in the

intensity of the absorption band on the spectrum. A molecule with an electric dipole will experience a torque under an external electric field of an electromagnetic wave. A transition caused by a dipole interaction with the light's electric field (IR irradiation) only occurs if the magnitude of the transition dipole moment integral, μ_{fi}, is not zero, which can be written as:

$$\mu_{fi} = \left| \int \Psi_f^* \, \hat{\mu} \, \Psi_i \, d\tau \right| \tag{2.33}$$

where Ψ_f and Ψ_i are the final and initial wavefunction, $\hat{\mu}$ is the dipole moment operator and τ indicates the integral is over all the variables Ψ depends on. Rewriting the transition dipole moment integral in all the variables as a function of bond length displacement x, using a Taylor series expansion approximation, the integral is given as:

$$\mu_{fi} \approx \left. \frac{d\mu(x)}{dx} \right|_{x=0} \cdot \int_{-\infty}^{\infty} \Psi_f(x) \, x \, \Psi_i(x) \, dx \tag{2.34}$$

The first term from the Taylor series expansion indicates it is non-zero only if a bond displacement causes a change in dipole moment. The second integral term is non-zero when the product of the three functions has even parity. Since x is an odd function, the integral is non-zero when Ψ_f is odd and Ψ_i is even, or vice versa. Therefore, the vibrational transition is allowed when two conditions are satisfied:

1. Vibration must induce a change in dipole moment:

$$\Delta\mu > 0$$

2. The vibrational energy can only change by the quantum number difference in 1

$$\Delta n = \pm 1$$

These two conditions are known as the selection rules for vibrational spectroscopy. In practice, the second selection rule does not always hold true, as real molecular vibrations are more complicated than a simple harmonic oscillator. For example, overtone bands correspond to transitions that have $\Delta n = \pm 2$.

In practice, the totally symmetric representation of the molecular point group is considered instead of calculating the transition dipole moment integral. If the transition dipole moment function $\Psi_f^* \hat{\mu} \Psi_i$ is totally symmetric, then the integral is non-zero and the transition is allowed. If the function is anti-symmetric, the transition is not allowed. In the case of the fundamental vibrational transition n=0 to n=1, the symmetry of the ground state wavefunction is the same as the totally symmetric representation in the point group of the molecule. Therefore, the symmetry of the excited state wavefunction must match the symmetry of the transition moment operator $\hat{\mu}$. The symmetry characteristics of $\hat{\mu}$ can be transformed as x, y, and z, so that the excited state wavefunction must have one of these factors. Similarly, the transition will only be allowed if the molecular vibration has the same symmetry as $\hat{\mu}$, by verifying the irreducible representations transformed by vibrational modes to the character table. In summary, the transition will be allowed if the vibration has the symmetry of x, y, or z, which also translates to the condition for an IR-active molecule.

The intensity of the absorption peak is also related to the population of each state. If the transition is allowed, then the populations of the initial and final states satisfy the Boltzmann distribution (Equation 2.35):

$$\frac{N_f}{N_i} = exp\left(-\frac{\Delta E}{kT}\right) \tag{2.35}$$

where N_f and N_i are the populations of the final and initial energy levels, respectively, ΔE is the energy gap between these two states, k is the Boltzmann constant, and T is the temperature in Kelvin. The smaller the energy gap or the higher the temperature, the more molecules are populated in the higher energy state. Heating the sample promotes molecules to an excited vibrational state, and therefore hot bands are more pronounced at higher temperatures.

2.2.2 Harmonic and Anharmonic Oscillator

Harmonic Oscillator

Vibrations in a molecule change atomic distances and angles through stretching and bending, which induce changes in the dipole moment leading to IR absorption. The simplest molecular vibration is the symmetric stretching in a diatomic molecule.

The bond length between a diatomic molecule is not fixed; it changes while the bond is stretching. This scenario is comparable to two masses connected by a spring, where the length of the spring at rest corresponds to the equilibrium bond length r_e. When the bond length is equal to r_e, the force on the atoms is zero, making the system a good approximation to the harmonic oscillator. In the harmonic oscillator model, the atoms undergo simple harmonic motion. When the bond stretches, the atoms separate, or when the bond contracts, they move towards each other. Both directions of movement are accounted for as one vibrational mode, or one degree of freedom of molecular vibration. Linear molecules adopt $3N-5$ vibrational modes, while non-linear molecules have $3N-6$ (where N is the number of atoms in the

molecule). Of the total 3N degrees of freedom, those in which atoms do not move in the same direction result in vibrations.[9]

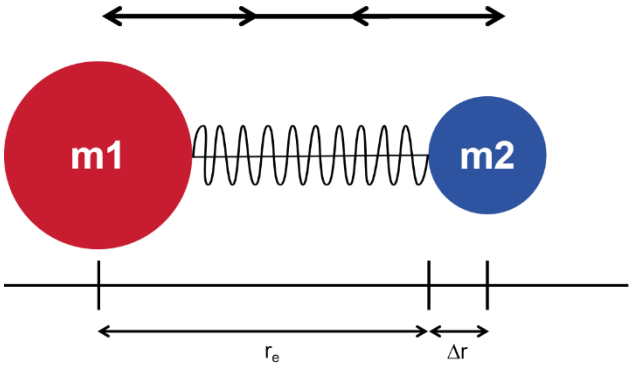

Figure 2.10: Representation of the harmonic oscillator of a diatomic molecule with atomic masses m1 and m2. Both directions of movement are one stretching vibrational mode.

Figure 2.10 shows the schematic representation of a diatomic bond vibration. Considering the bond is elastic, the vibration obeys Hooke's law, where the force between atoms is proportional to the bond displacement from the equilibrium position:

$$F = -k(r - r_e) = -kx \tag{2.36}$$

where k is the force constant, and x is the displacement of bond, equal to $r - r_e$. The potential energy is the negative integral of F over the displacement, $E = -\int F\,dx$. Solving the integration with the condition that $F = 0$ at $x = 0$, the potential energy of this harmonic oscillator is:

$$E = \frac{1}{2}kx^2 \tag{2.37}$$

which is shown in Figure 2.11 as a grey parabola. Each quantised energy level is a solution of the Schrödinger equation, $\Psi(x)$, in which the vibrational quantum number n (sometimes

specifically denoted as v) takes values of 0, 1, 2, 3, and so on. The energy level expression is shown in Equation 2.38, where h is the Planck constant, and v is the vibrational frequency of the bond. The harmonic oscillator model predicts that the vibrational levels are equally spaced with a difference of hv, starting with the ground state when $n = 0$. According to Equation 2.38, the energy is not zero when $n = 0$, and this is called zero-point energy.

$$E(n) = \left(n + \frac{1}{2}\right) hv \tag{2.38}$$

Anharmonic Oscillator

The harmonic oscillator is a satisfactory model when the displacement of the bond from the equilibrium position is small, but it does not accurately describe the vibration at high energy levels. In reality, at high compression, nuclear repulsion becomes the major factor, while at high extension, the diatomic bond will break. Therefore, the real behaviour of a molecular vibration is actually an anharmonic oscillator, where the energy of the vibration is more precisely expressed in the Morse potential (Equation 2.39), and its plot is shown in Figure 2.11, directly compared with the harmonic oscillator energy well.

$$E = D_e \left[1 - e^{(-ax)}\right]^2 \tag{2.39}$$

In Equation 2.39, D_e is the dissociation energy of the bond, or the depth of potential energy well as shown in Figure 2.11; x is the displacement of bond from the equilibrium position; equal to $r - r_e$, a is the width of well, equal to $\sqrt{k_e/2D_e}$, which k_e is the force constant at the bottom of the well.

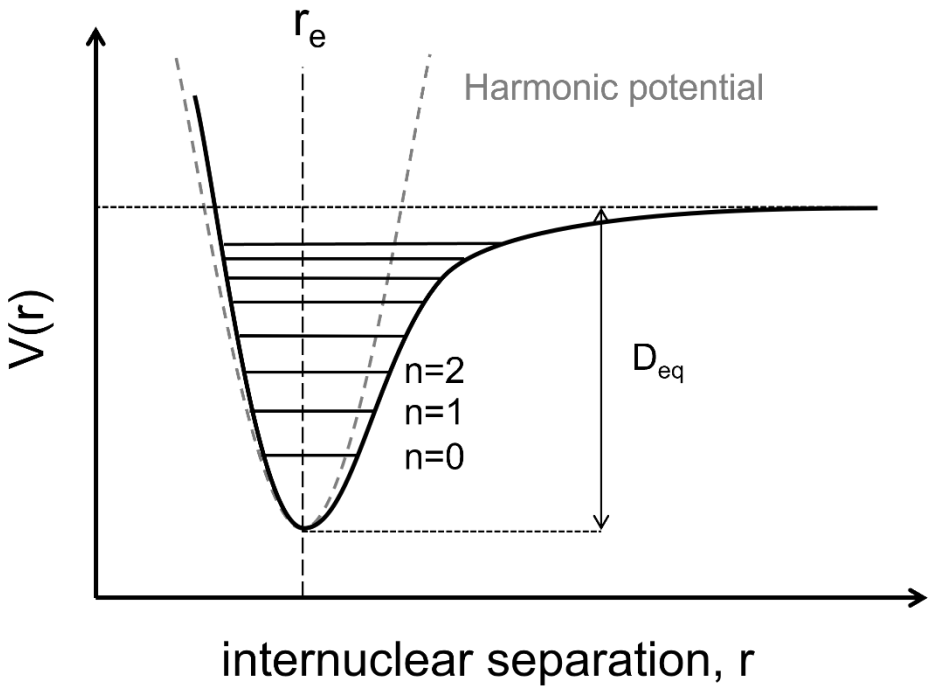

Figure 2.11 Potential energy of a diatomic molecule as a function of internuclear separation. The harmonic potential describes the energy of the harmonic oscillator in grey dashed plot. The Morse potential reflects the behaviours of the potential energy in the anharmonic oscillator. When r is large, the bond eventually breaks, and the dissociation energy D_e is the depth of the potential well. The equilibrium bond length corresponds to the bottom of the well, denoted as r_e.

In reality, the vibrational energy levels are not equally spaced. As shown in Figure 2.11, in the anharmonic oscillator potential energy well, as the quantum number increases, the energy between states decreases until reaching bond dissociation. Therefore, based on Equation 2.37, the energy of vibrational states now needs to account for anharmonicity, x_a, and the new expression is:

$$E(n) = \left(n + \frac{1}{2}\right) hv - \left(n + \frac{1}{2}\right)^2 hv \cdot x_a \tag{2.40}$$

The second term in the equation represents the effect of anharmonicity, which increases at

higher vibrational levels. Furthermore, anharmonicity causes the selection rules of the harmonic oscillator ($\Delta n = \pm 1$) to fail, allowing overtone transitions with $\Delta n > \pm 1$.

The frequency in Equations 2.38 and 2.40 corresponds to the specific energy absorbed during a transition between vibrational energy levels. The vibrational frequencies (often converted to units of wavenumbers) of chemical bonds depend on their nature, bond stiffness, and atomic mass. The relationship is given by Equation 2.40, where c is the speed of light, k is the force constant of the vibrating bond, and μ is the reduced mass. In practice, when vibrations of polyatomic modes are considered, the effective mass is used in this equation instead of the reduced mass for diatomic vibrations.

$$v\ (cm^{-1}) = \frac{1}{2\pi c}\sqrt{\frac{k}{\mu}} \tag{2.41}$$

The vibrational frequency is proportional to the force constant of the bond, as shown in Equation 2.41. The force constant is a quantitative measure of the strength of the bond. The stronger the bond, the larger the force constant and the higher the vibrational frequency (wavenumber). Therefore, the force constant is also proportional to the bond order of a bond. For example, the force constants of C−O (alcohol), C=O (carbonyl), and C≡O (carbon monoxide) are roughly in linear increasing order.

The reduced mass of atoms is calculated by the product of atomic masses on either side of bond over the sum of them as shown in Equation 2.42:

$$\mu = \frac{m_1\, m_2}{m_1 + m_2} \tag{2.42}$$

Changing the mass on either side of a bond will change the reduced mass of the bond, hence

altering the vibrational frequency. Rational isotopic substitution is commonly employed to identify a vibrational band associated with a particular functional group, as the shift of the absorption band can be precisely calculated when k is known.

The two physical properties, force constant and reduced mass, of common chemical bonds result in their characteristic vibrational frequency within the mid-infrared range between 400 to 4000 cm^{-1}. This makes IR spectroscopy a powerful tool for assigning functional groups to molecules.

2.2.3 Beer-Lambert Law

In Figure 2.9, the intensity of an absorption band in the IR spectrum was discussed as depending on several factors. The selection rules, which depend on wavefunctions and the relative populations between vibrational states, have been covered. However, the concentration of the sample is practically the most relevant factor influencing the intensity of the absorption peak in the spectrum.

Absorption of IR light at specific energies by an IR-active molecule is key to constructing the IR spectrum. Therefore, absorbance (A) is used to describe the amount of light that a sample can absorb at a given energy. In practice, absorbance is measured by comparing the intensity of incident and transmitted light, and its relationship is given as:

$$A = -\log\left(\frac{I_t}{I_0}\right) \tag{2.43}$$

where I_0 is the intensity of the light entering the sample, and I_t is the intensity of the light

detected after passing through the sample. $\frac{I_t}{I_0}$ is referred to as transmittance, describing the ratio of light intensities in spectroscopic measurements.

The amount of light absorbed by an IR-active sample depends on the absolute number of molecules the IR beam passes through. Thus, absorbance can be expressed in terms of the number of molecules absorbing at a specific energy, as given by the Beer-Lambert law:

$$A = \varepsilon c l \tag{2.44}$$

The term ε is the molar extinction coefficient, also known as molar absorptivity, c stands for the concentration of the sample, and l is the path length, usually in cm. The Beer-Lambert law makes IR spectroscopy a powerful quantitative tool.

The molar extinction coefficient is an intrinsic property of a molecule that describes how strongly the molecule can absorb light at a given energy. It also qualitatively reflects the selection rules of a vibrational transition. In a simple vibrational model, ε is equal to the square of the change in dipole moment during bond length displacement, $\frac{d\mu}{dx}$:

$$\varepsilon = \left(\frac{d\mu}{dx}\right)^2 \tag{2.45}$$

This means the greater the change in dipole moment by bond vibration, the greater the ε, and hence the greater the absorbance A. Therefore, functional groups containing polar bonds with large dipole moments, such as CN and CO in [NiFe]-Hydrogenases, have very intensive absorption bands, making IR spectroscopy important and useful for studying them.

2.2.4 IR Absorption of Carbonyl and Cyanide Ligands

Molecular carbon monoxide (CO) and cyanide (the simple ion with a nitrile functional group) have exceptionally intense IR absorption bands due to their asymmetrical stretches of CO and CN bonds, which appear at 2143 and 2158 cm^{-1}, in aqueous solution respectively. [19,20]

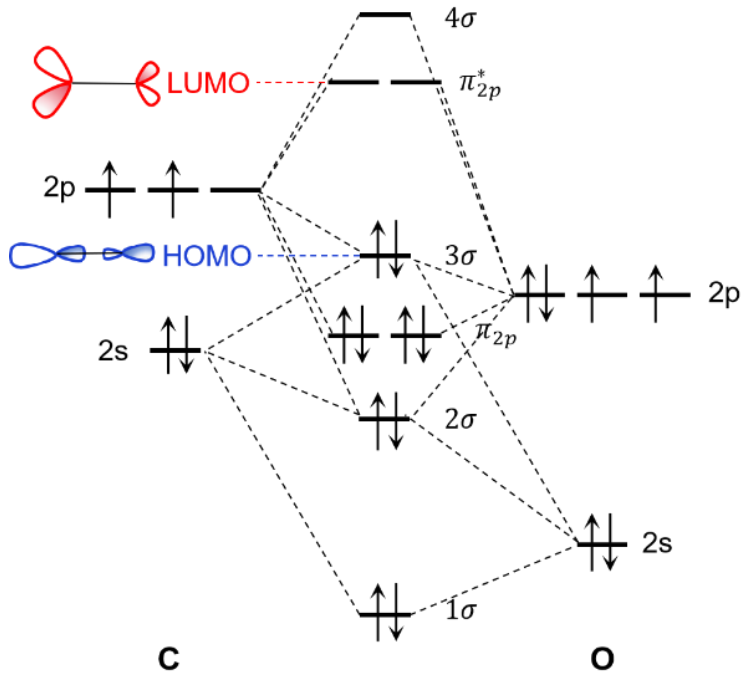

Figure 2.12: The molecular orbital diagram of CO, highlighting the symmetry of HOMO (blue) and LUMO (red). The diagram demonstrates sp mixing between carbon and oxygen, so the sigma orbitals interfere with each other due to the close energy levels.

CO and CN^- are isoelectronic species, and the molecular orbital diagram of CO is shown in Figure 2.12, which also qualitatively describes that of CN^-. The bond order of CO is 3, suggesting a triple bond between carbon and oxygen, consisting of 1 σ and two π bonds. In Figure 2.12, the most energetic filled molecular orbital (HOMO), denoted as 3σ, has σ-symmetry character and its shape is shown in blue. This molecular orbital has both s and p

orbital characters due to "sp mixing" from the small energy gap between those σ molecular orbitals (1σ to 4σ), which are constructed by interference between both 2s and 2p orbitals from carbon and oxygen. The LUMO is the π anti-bonding orbital with degeneracy of 2, and its shape is described in red in Figure 2.12.

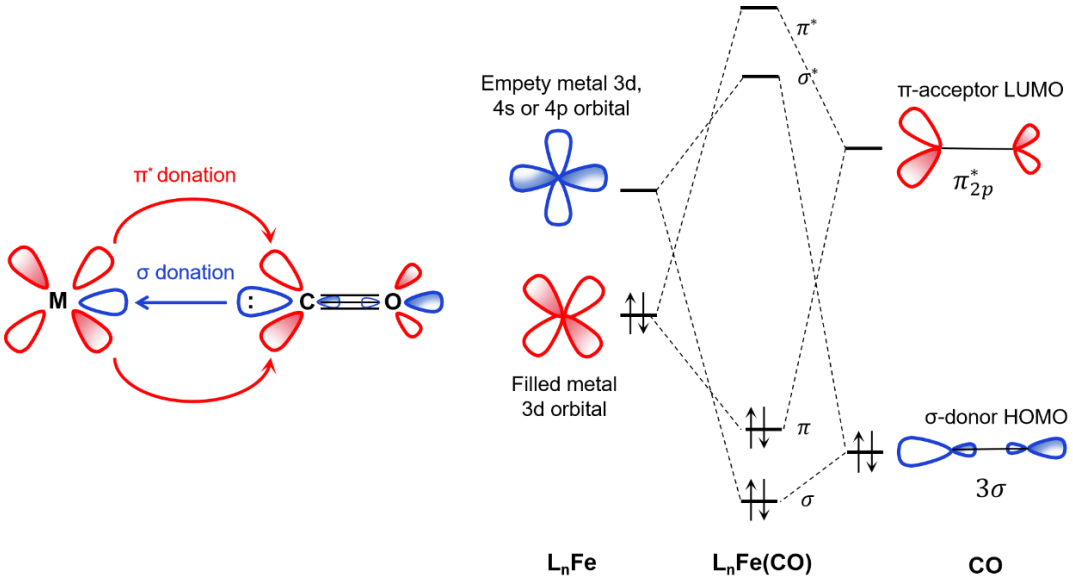

Figure 2.13: Left) Representation of pπ-dπ synergic bonding between a transition metal and π-acidic CO ligand. The in-phase σ-symmetry (blue) orbitals construct the coordination bond, and the in-phase π-symmetry (red) orbitals allow backbonding donation. Right) The segment molecular orbital diagram of synergic bonding of a transition metal complex (FeL$_n$ as an example) and CO.

The σ-character HOMO and π-character LUMO of CO (also in the case of CN^-) make it an excellent ligand to transition metals, and the interaction between the ligand and metal is shown in Figure 2.13, left panel. The overall interaction between CO and CN^- is referred to as a synergic effect. The HOMO on CO, as discussed before, has σ-symmetry character, which can form a coordination bond to transition metals by donating electron density towards empty orbitals of the metal centre. On the other hand, CO and CN^- are often referred to as π-acceptor

ligands due to their capacity to accept electrons from filled metal orbitals with π-symmetry into their empty π-anti-bonding orbital. In Figure 2.13, the dπ-pπ backbond donation is shown in red on the left.

The right panel of Figure 2.13 shows the molecular orbital diagram of CO and a coordinating iron centre. The strength of the coordination bond (σ-symmetry) depends on the energy levels of the HOMO on CO (constant) and the empty orbital on the metal (variable). The more electron-deficient the metal is, the easier it is for the metal to accept electrons from the HOMO of CO to form the coordination bond. The degree of dπ-pπ backbonding interaction, on the other hand, can affect the vibrational frequency of the ligated CO bond more significantly. As electrons are donated from the metal into the π-anti-bonding orbital of CO, the bond order of CO decreases and the bond weakens, increasing its double-bond character. Therefore, the force constant k will decrease as the CO bond weakens due to backbonding donation, which also reduces the vibrational frequency (Equation 2.40).

Several factors related to the electronic structures of metals can affect the synergic bonding between the transition metal and CO/CN^- ligands, which leads to altered absorption band positions in the IR spectrum. The oxidation state of the transition metal centre can vary via redox reactions. When the oxidation state of the metal increases, the valence d-orbitals feel a stronger effective nuclear charge, hence becoming more stabilized, which brings them closer in energy to the donor orbitals on the ligands (CO or CN^-), resulting in a stronger coordination bond (σ-symmetry). The increasing oxidation state also indicates the rise of electron deficiency at the metal, improving the σ-donation from the ligand to the metal. On the other hand, losing

electrons from the valence shell of the metal decreases the π-backbonding donation since the energy of the filled d-orbitals is further away from the π* anti-bonding orbital at the ligand, weakening the Lewis basicity of the metal. Therefore, the vibrational frequency of a π-acidic ligand increases with the metal oxidation state. Table 2.1 shows how the ν_{CO} absorption band position changes with the oxidation state of iron with only CO as a ligand.[21]

Table 2.1: ν_{CO} of iron carbonyl complexes with different formal iron oxidation states observed in infrared spectroscopy.

	$[Fe(CO)_6]^{2+}$	$Fe(CO)_5$	$[Fe(CO)_4]^{2-}$
Formal oxidation state	+2	0	-2
ν(CO) / cm^{-1}	2215	2030	1815

Transition metals generally comprise multiple coordination sites. The vibrational frequencies of carbonyl or cyano ligands depend on the co-ligands in the metal complex. When strong σ-donating ligands are bonded to a carbonyl metal complex, the electron density of the metal increases, leading to a higher energy HOMO on the metal, hence a greater π-backbonding effect. Therefore, the addition, dissociation, or substitution of ligands on the metal complex will change the electron density at the metal, hence altering the vibrational frequencies of carbonyl or cyano ligands.

The IR-active ligands (one CO and two CN^-) are anchored at the terminal position on iron, pointing in the opposite direction to nickel at the active site of NiFe-hydrogenases. The formal

oxidation state of iron with three π-acidic ligands attached remains constant at +2 throughout the catalytic cycle, while the other metal ion, nickel, changes its oxidation state between +1, +2, and +3. The change in the oxidation state of nickel affects the overall electronic structure of the active site, thus altering the vibrational frequency of the π-acidic ligands during catalysis. Although the active site of NiFe-hydrogenases remains highly conserved in catalysis, the ligand at the bridging position varies between hydroxide, water, remaining vacant, and hydride at different redox levels. The alternating ligand at the bridging position affects the electron density of iron, hence the vibrational frequency of CO and CN^-. Therefore, the absorption bands of CO and CN^- vibrations are very sensitive to the coordination and electronic structure of the active site. Each redox state, with a specific arrangement of coordination and metal oxidation state, reflects three distinct bands in the IR spectrum (one CO and two CN^-), making IR spectroscopy a useful tool for studying the active site redox chemistry of [NiFe]-hydrogenases. This will be discussed in more detail in Chapter 3.

2.2.5 Detection Modes

Modern IR spectrometers have abandoned monochromators and adopted interferometers, which allow the entire spectral range of interest to be collected simultaneously by Fourier-transforming the time-domain data to the frequency-domain. This efficient data acquisition method is called Fourier-transform infrared (FTIR) spectroscopy and is employed in all IR spectra collected in this work.

IR spectroscopy is compatible with a wide range of sample geometries, allowing the sample to

be measured under different conditions and methods. Three detection modes, transmission, reflection, and attenuated total reflectance (ATR), are commonly applied in studying biological samples. In this thesis, the transmission and reflection modes are used to acquire IR spectra.

Transmission

Transmission is the most traditional detection mode of IR measurement, and the schematic representation of sample arrangement in transmission mode is shown in Figure 2.14. The sample (in any state: gas, solution, liquid, or solid) is sandwiched between two optical windows (CaF_2) and placed in a holder. The incident IR beam passes through the sample, where specific wavelengths are absorbed, and the transmitted light is received at a detector. The amount of light at the corresponding wavelength (absorbance) is proportional to the path length and the sample's concentration (Equation 2.43). The path length in the "sandwich" transmission setup can be adjusted by a plastic spacer, typically between 25 to 100 µm. Biological samples, which often have relatively low concentrations, could benefit from a thicker path length to produce a more pronounced signal, but this often accompanies saturation of the signal from the solvent (e.g., water, O-H stretching at 3000 to 3700 cm^{-1} and bending around 1600 cm^{-1}).[22]

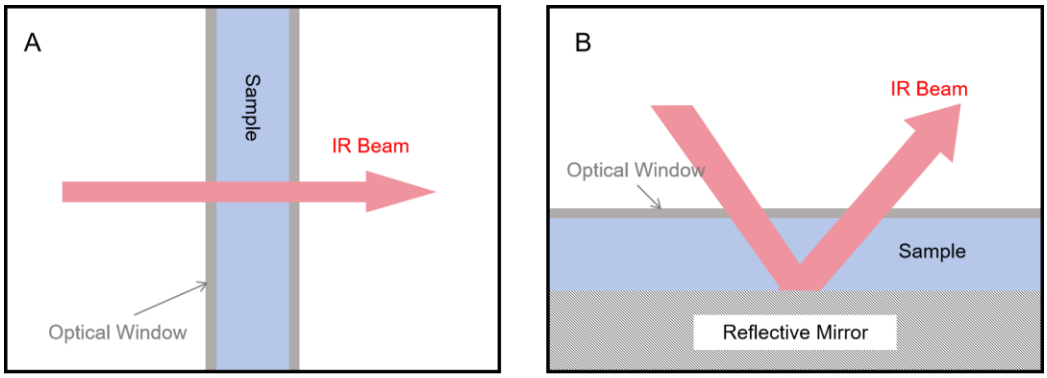

Figure 2.14 A) The configuration of the transmission IR spectroscopy detection mode, the sample thickness is controlled by a gasket. B) Representation of the reflection IR spectroscopy detection mode.

Reflection

The reflection detection mode in IR spectroscopy is known as reflectance-absorption IR spectroscopy. The absorbance here also follows the Beer-Lambert law, like in the transmission mode, but the sample geometry is different, as shown in Figure 2.14B. The incident IR beam passes through a thin layer of the sample before being reflected by a reflective plane opposite the incident angle. The reflected light passes through the sample again and is then collected by a detector. The reflection mode setup allows the IR light to pass through the sample twice, effectively doubling the path length. This means the reflection mode is superior in measuring dilute samples compared to transmission, but it is often limited by non-perfect reflective surfaces and stronger interference fringes.

A multiple layer setup (window, buffer, and crystal sample) with different refractive indices in the reflectance IR cell often results in multiple internal reflections, causing the reflected IR

beams to superimpose on one another. In this thesis, the IR spectra of the protein crystal sample, which is measured via reflection mode, has a background spectrum recorded next to the sample. This means the IR beam passes through different mediums in the background and sample channels, leading to the appearance of sinusoidal interference fringes. However, due to the high effective concentration of protein in the protein crystal, the interference is generally not disruptive in data analysis. The setup of the reflective IR spectroelectrochemical cell will be described later in this chapter.

2.3 X-ray Absorption Spectroscopy

X-ray absorption spectroscopy (XAS) is a core quantum-level technique that studies the absorption coefficient of incident X-rays as a function of their energy, without discriminating the nature of the sample. Core electrons of the atom of interest can absorb the powerful and intense X-rays from synchrotron radiation. Hence, XAS measurement focuses on transitions from core electronic states of the atom to the excited electronic states (LUMO) or the continuum (where the metal is ionized). The former is known as X-ray absorption near-edge structure (XANES), and the latter as extended X-ray absorption fine structure (EXAFS). These two methods provide complementary structural and electronic information for samples. XANES reports on electronic features and symmetry of the metal coordination centre, and analysing EXAFS data can explore numbers, nature, and distances of neighbouring atoms (ligands) around the metal of interest.

2.3.1 Principle of X-ray Absorption Spectroscopy

X-rays are light with energies ranging from approximately 500 eV to 500 keV, or wavelengths from approximately 2.5 to 0.025 nm.[9] In this energy regime, light is absorbed by all matter through the photoelectric effect. In an XAS experiment, the sample of interest is irradiated with a chosen range of specific energies. A fraction of the incident X-rays is absorbed by a specific atom, leading to excitation of its core electrons and potentially ionization of the atom. This amount of absorption or the probability of absorption is expressed as the absorption coefficient μE, which is a function of the energy of the incident light. Hence, a typical XAS spectrum is a plot of μ against irradiation energy, and in general, the XAS spectrum consists of several common features:

1) A sharp rise in absorption at a specific incident energy.

2) Several small peaks and shoulders on or prior to the sharp rise.

3) Oscillation occurs after the sharp rise, with the amplitude and frequency gradually decreasing.

Every atom has core-level electrons with well-defined binding energies. The probing element is selected in advance by tuning the X-ray energy to an appropriate absorption edge, and therefore XAFS is element-specific. Figure 2.15B shows the XAS spectrum of air-oxidised Ni-substituted rubredoxin measured at the Ni K-edge, at 4K, with all features mentioned above found in the spectrum. The sharp rise of μ is called the absorption edge and corresponds to the specific energy required to excite a 1s electron of Ni(III) into the LUMO or higher energy orbitals. In contrast, the lower μ before the edge indicates that the photon energies are not

sufficient to excite electrons from the core. It takes approximately 8345 eV to excite an electron from the 1s orbital of Ni (III) to 4p, leading to a sharp increase in the XAS spectrum, called the Ni K-edge, which refers to the excited electron coming from the principal quantum number n=1, where L-edges and M-edges refer to n=2 and n=3, respectively. Figure 2.15A shows the energy level diagram for Ni (III) K-edge transitions, and each transition has its XAS features in the X-ray absorption near-edge structure (XANES) and extended X-ray absorption fine structure (EXAFS) spectra.

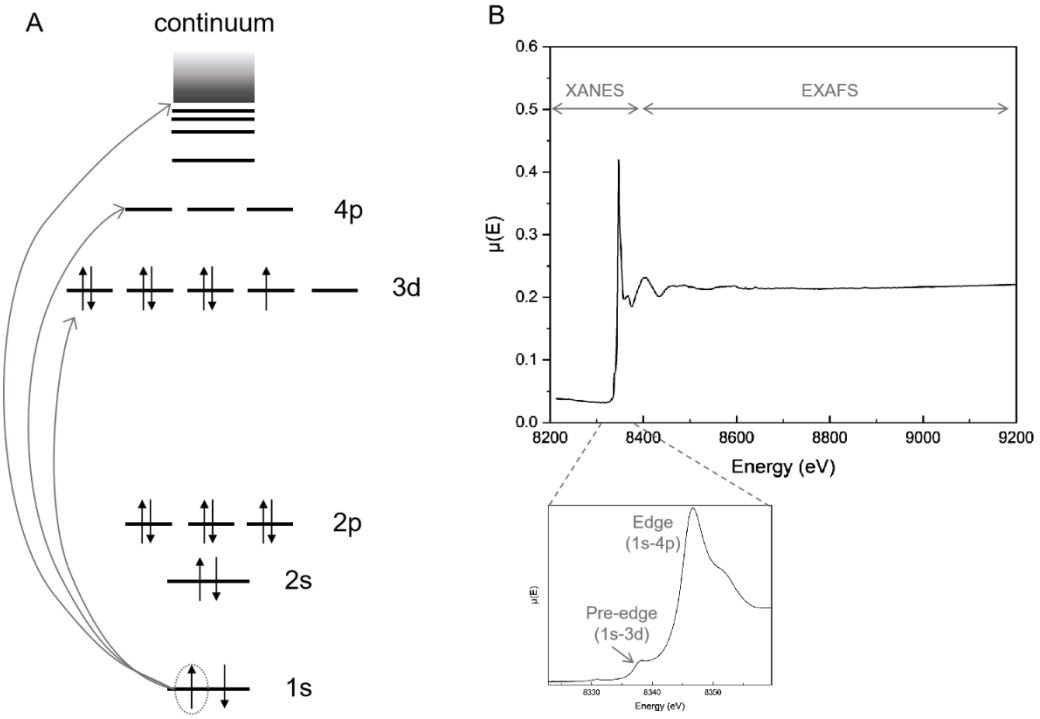

Figure 2.15: A) The energy level diagram for K-edge transitions (1s to 3d, 4p and continuum) for Ni (III). B) The XAS spectrum of air-oxidised Ni-substituted rubredoxin at the K-edge at 4K. Ni is in the +3 oxidation state and the spectrum is measured by fluorescence mode. The enlarged diagram shows the pre-edge and edge features.

X-ray absorption near-edge structure

X-ray absorption near-edge structure (XANES) contains all features near or on the edge, which provides detailed information about the electronic and coordination environment of the absorbing atom, especially metals. The dominant XANES edge feature, the sharp rise known as the "white line," comes from the 1s to np dipole transition at the K-edge, where np represents the lowest unoccupied p orbital of the absorbing atom (Figure 2.15A). This electronic transition has $\Delta l = 1$, and it is quantum mechanically allowed, hence it has very intense absorption. The edge position reflects the energy between the 1s and np orbitals and is therefore very sensitive to electron density, or the oxidation state of the absorbing metal. A higher oxidation state of a metal ion means an increasing attraction from the nucleus to outer electrons. Electrons in the 1s orbital have the least shielding effect and will experience the highest effective nuclear charge compared to outer shell electrons. Therefore, more energy is required to knock out the 1s electron of a higher oxidation state metal, and the edge position will shift to higher energy. Conversely, the white line shifts to lower energy when the metal is reduced or the electron density on it decreases, e.g. due to ligand exchange or dissociation. In Figure 2.15B, the Ni (III) K-edge position (8345 eV) is significantly higher than that of metallic Ni (8332.8 eV).[23]

Transition metals are defined as elements whose atoms have an incomplete d subshell or whose cations have an incomplete d subshell. The quadrupole electronic transition between 1s and nd orbitals has $\Delta l = 2$, and it is Laporte-forbidden, hence it is relatively much weaker in intensity. This weak absorption occurs prior to the edge but reveals valuable information

about the coordination geometry of the absorbing atom (Figure 2.15B enlarged diagram). The Ni ion, in the case of rubredoxin as shown in Figure 2.15B, adopts a distorted tetrahedral structure, where the mixing of metal 4p and 3d orbitals is allowed. Despite the 1s to 3d transition being quadrupolar, the intensity is enhanced due to dipole-allowed p-characteristics in this non-centrosymmetric conformation.

Extended X-ray absorption fine structure

At energies greater than the LUMO of the absorbing metal, the irradiated X-ray can eject the core hole electron (1s electron at the K-edge) to the continuum (Figure 2.15A), interfering with neighbouring atoms and then getting scattered back to the absorbing metal. The excess energy absorbed by the excited electron (photoelectron) is carried off as translational kinetic energy, which is also expressed as its wavelength due to wave-particle duality. Figure 2.16 demonstrates how the EXAFS signal is generated. When the incident X-ray energy is higher than the ionization energy threshold, the photoelectron leaves the absorbing metal (grey) with a certain wavelength (solid circular wave) and is backscattered (dashed circular wave) by surrounding atoms (red). At energy E_1, the backscattered wave constructively interferes with the outgoing wave, leading to an increase in the absorption coefficient. Conversely, at E_2, where E_2 is greater than E_1, the wavelength of the outgoing photoelectron is shorter, so it destructively interferes with the backscattered wave (Figure 2.16 right), hence a lower absorption coefficient at E_2. As the XAS spectrum scans through photon energies in the EXAFS region, the outgoing and backscattered photoelectrons alternately superimpose,

which reflects as an oscillating spectroscopic phenomenon in the EXAFS region.

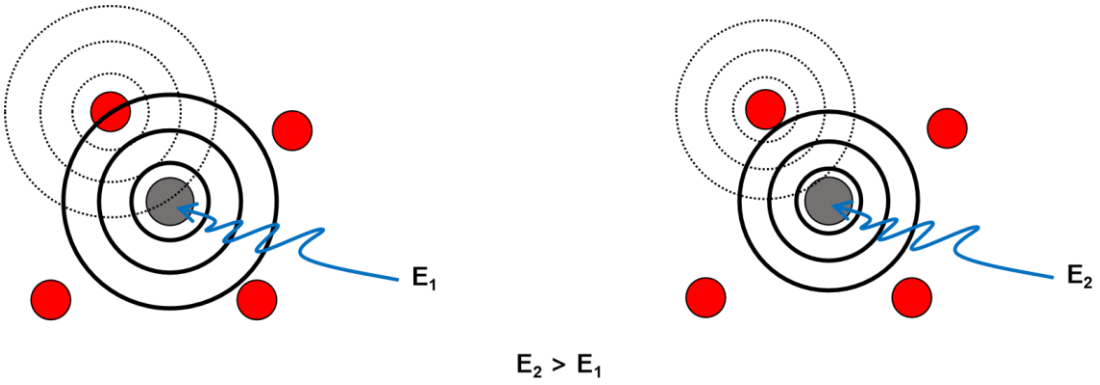

Figure 2.16: A schematic representation of the outgoing and backscattered photoelectron wave, which illustrates the concept of interference in EXAFS. Left: constructive interference. Right: destructive interference.

The EXAFS phenomenon factor χ, also known as the oscillatory portion of the absorption coefficient, is given by the equation when the photoelectron is modelled as a plane sinusoidal wave:

$$\chi \propto cos\left(2\pi\frac{2D}{\lambda}\right) \tag{2.47}$$

λ is the wavelength of the photoelectron, given by the de Broglie relation, λ = h/p, h is Planck's constant and p is momentum. D is the distance between the absorbing atom and the scattering atom, where constructive interference is achieved when the round-trip distance is multiples of the wavelength, 2D = nλ. The scattering from neighbouring atoms may not be perfectly ideal; such probabilities as inelastic backscattering and failure in scattering must be considered. The equation can therefore be expressed as follows: provided the wavenumber k is introduced as $k = \frac{2\pi}{\lambda} = \frac{2\pi}{h}\sqrt{2m_e(E-E_0)}$ and $f(k)$ is a

proportionality constant related to the possible elastic scattering.

$$\chi(k) = f(k)\cos(2kD) \tag{2.48}$$

Although the equation can describe the simplified EXAFS phenomenon, many factors need to be considered to construct a refined mathematical equation that can reflect reality. The well-approximated EXAFS equation is shown below:[24]

$$\chi(k) = S_0^2 \sum_i N_i \frac{f_i(k)}{kD_i^2} e^{-\frac{2D_i}{\lambda(k)}} e^{-2k^2\sigma_i^2} \ sin(2kD_i + \delta_i(k)) \tag{2.49}$$

The summation, $\sum$, considers each individual neighbouring atom that the photoelectron can scatter off, and the subscript i denotes the specific scattering atom. N_i is the degeneracy, revealing the number of equivalent backscattering atoms at a distance D_i. The additional $\delta_i(k)$ term in the trigonometric calculation is the phase shift correction due to different atomic potentials between the absorber and backscatter atom. The kD_i^2 term in the denominator introduces a reduction in scattering possibility due to the spherical property of the photoelectron wave instead of a planar one. The term S_0^2 is introduced as the amplitude reduction factor to correct the incomplete overlap phenomenon between the final state of the absorbing atom and its initial state (typically between 0.7 and 1.05). This is an atomic intrinsic process and is independent of k or D, hence it is the multiplier for all scattering. Some photoelectric phenomena which suppress EXAFS are strongly distance-dependent, such as inelastic scattering. The longer the process takes, the higher the probability of changing the final state of the absorbing atom. Therefore, a term $e^{-\frac{2D_i}{\lambda(k)}}$ is introduced in EXAFS by assigning a mean free path for the photoelectron $\lambda(k)$ which also constrains and reflects that EXAFS is a local phenomenon (typically within 10 Å). Variations in absorber and scatter distances can

be introduced by thermal and static disorder. A new term $e^{-2k^2\sigma_i^2}$ is used to modify the EXAFS equation with a new factor, σ_i^2, the mean square radial displacement of a specific scattering, also known as the Debye-Waller factor, physically defined as the variance in the half path length.

2.3.2 Detection Mode: Transmission and Fluorescence

XAFS measurements are often conducted using two detection modes with different sampling geometries and data collection methods: transmission and fluorescence. Schematic representations of each mode are shown in Figure 2.17.

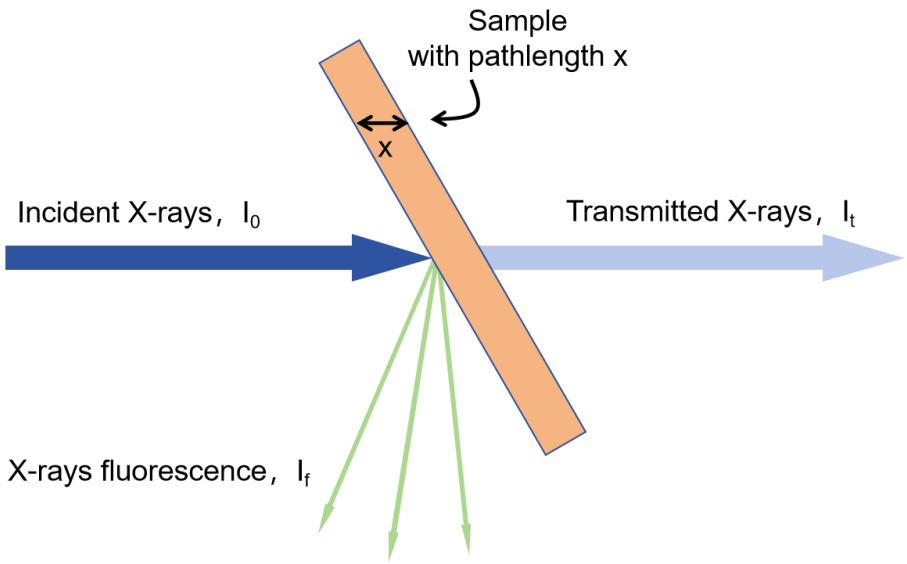

Figure 2.17: The configuration of transmission and fluorescence XAS detection modes.

Just like other spectroscopic measurements, the transmission mode in XAFS follows the classic Beer-Lambert law as described earlier in Equation 2.42. The light passes across the sample; XAFS signals will be recorded if any light is absorbed by an element in the sample

(Figure 2.17). The intensities of the incident X-ray (I_0) and the transmitted X-ray (I_t) are measured using ion chambers with a high voltage across them. The absorption coefficient $\mu(E)$ in transmission mode is expressed by the equation, where x is the path length:

$$\mu(E) = \frac{1}{x} ln\left(\frac{I_0(E)}{I_t(E)}\right) \quad (2.50)$$

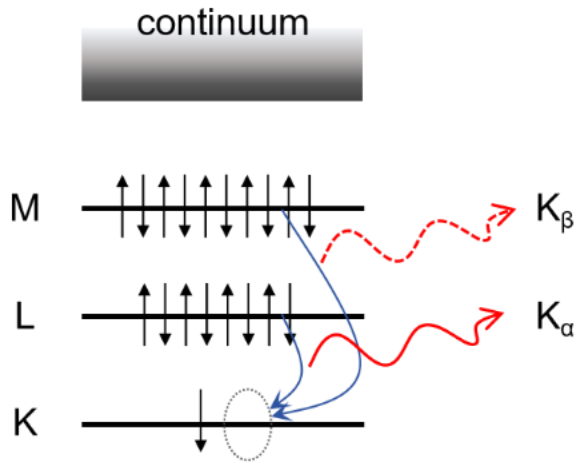

Figure 2.18: The fluorescence phenomenon describes the decay of the excited state after a photoelectron is produced following X-ray irradiation. Depending on the principal quantum number of the relaxing electron, the photo-emitted X-rays are called K_α (from the L shell) and K_β (from the M shell).

A transmission XAFS measurement is ideal for concentrated and homogeneous samples. However, fluorescence measurement is much preferred for low-concentration and thin samples. Following core electron X-ray absorption, the atom becomes excited. The leftover core hole will decay within a few femtoseconds (e.g. the core-hole lifetime for the Cu K-edge is approximately 0.5 fs) as a higher-energy core-level electron fills the deeper core hole, ejecting an X-ray of well-defined energy as fluorescence (Figure 2.18). The probability of emission is directly proportional to the absorption probability. For example, an L-shell

electron dropping into the K level gives the K_α fluorescence line, which has much higher intensity than K_β, which comes from the M shell, due to selection rules. The energy dependence of the absorption coefficient $\mu(E)$ in fluorescence mode can be written as:

$$\mu(E) \propto \frac{I_f(E)}{I_0(E)} \tag{2.51}$$

In addition to X-ray fluorescence, the Auger-Meitner effect is the second mechanism of de-excitation of the core hole, in which an electron from a higher energy level drops into the core hole and a second electron is emitted into the continuum. However, the Auge-Meitner effect is much less likely to occur in transition metal (with higher atomic number Z) compared to fluorescence, for example, at Cu K-edge measurements, which are covered in this thesis.

2.3.3 Challenges in X-ray Absorption Spectroscopy

X-rays can penetrate atoms with low or moderate atomic numbers, leading to highly specific results from dilute metalloprotein samples. Metalloproteins comprise functional transition metal sites packed in folded peptide chains. The apo proteins are mainly constituted by low atomic number elements. Therefore, if a single metal site is present, the electronic and geometric information of the metal can be studied using XANES, and the coordination information can be precisely determined using EXAFS.

In general, biological samples are measured in a frozen state in XAS experiments at temperatures well below that of liquid nitrogen. The primary reason for the measurement

condition is to avoid systematic photodamage, also known as photoreduction, from hard X-ray irradiation. Photodamage is a persistent problem that needs to be addressed for XAS focusing on the K-edge of first-row transition metals, such as metalloproteins like [NiFe]-hydrogenases.[7,8,25,26] During the exposure of a metalloprotein sample to an X-ray beam during XAS data collection, photodamage can potentially destroy protein integrity via heating, formation of reactive radicals, and bond breaking.[27] Moreover, the metal centre can be reduced by electron knock-out from nearby atoms. Potential damage to the sample usually occurs on a timescale shorter than an XAS measurement and can be significant and irreversible.[26,28] The impact of undesired photodamage is more significant for solution samples at ambient temperatures than in cryogenic conditions, owing to the free mass transport of the primary and secondary products of water photoionization. However, in XAS studies, the condition of metalloproteins is important to reveal their properties relevant to their functions. Metalloproteins, such as [NiFe]-hydrogenases *in vivo*, work in a solvated state and can have distinct active site structures, protein folding, and side-chain conformations.[29] Many efforts have been made to address this problem, including reporting on softer irradiation L-edge spectra,[7,30] utilising X-ray free-electron lasers, and rapid-freezing methods.[31]

Spectroelectrochemical techniques are powerful for extracting useful in-situ data of redox proteins under electrochemical control. The conventional three-electrode system requires a solution sample for a closed circuit; hence it is challenging to employ XAS-SEC measurements while taking into account photodamage. To address this challenge, Chapter 7 demonstrates a novel flow XAS-SEC cell that is able to record both XANES and EXAFS of blue copper

metalloproteins under electrochemical control with a minimum contribution from photoreduction. The experimental procedure will be discussed later in this chapter.

2.4 Protein Preparation and Crystallisation

2.4.1 Protein Preparation

DeltaTM Hyd-1 and Hyd-2 NOP

Escherichia coli delta transmembrane hydrogenase-1 (deltaTM Hyd-1) and *Escherichia coli* native overproduced hydrogenase-2 (Hyd-2 NOP) were prepared for crystallisation and the protocols used have been published previously.[2,32] The purification methods for both enzymes are similar, consisting of Ni-affinity and size exclusion chromatography. The purified proteins were concentrated to about 5 mg/mL according to Bradford assays. Different from full length Hyd-1 which requires hydroxyapatite chromatography to separate the cytochrome b subunit (cyt b), deltaTM Hyd-1 is isolated without cytochrome-b due to cytoplasmic expression.[14]

Azurin overexpression

The apo azurin overexpression strain (expressed in *E. coli* BL21DE3) was provided and the overexpression assays were supported by Dr. Miguel Ramirez. The azurin prepared was used for testing the XAS-SEC cell described in Chapter 7.

The *E. coli* BL21DE3 cells containing the plasmid for overexpression of apo azurin were used to directly inoculate 10 mL 2xYT (16 g/L bacto-tryptone, 10 g/L yeast extract and 5 g/L NaCl) lysogeny broth (LB) media containing 5 μg/mL kanamycin at 37 °C overnight for preculture. The starter cultures were then transferred into 1 L flasks with pre-heated 2xYT LB media with 50 μg/mL kanamycin. The 1 L cultures were incubated at 180 rpm, 37 °C until reaching an OD_{600} about 1.0-1.5. The expression was then induced by adding 300 mg/L of IPTG (Isopropyl β-D-1-thiogalactopyranoside) followed by 16 hours incubation at 25 °C. The pellets of cells were collected by centrifugation at 8000 *g* for 30 minutes and stored at -80 °C.

The isolated cells were resuspended in phosphate buffer (20 mM, pH 7.2, 1 mM EDTA) in the ice bath for 30 minutes with additional 3 mg lysozyme and 3 μL DNase. The cells were then disrupted by sonication for 10 minutes total (2 seconds on and 6 seconds off) in the ice bath. The lysates were clarified by centrifugation at 18000 g for 30 minutes. Sodium acetate (1M, pH 4.2) was added dropwise to the clear lysate until pH 4.5 or lower, then the turbid lysate was left incubating for 30 minutes in the ice bath. Most of the undesired proteins were precipitated under acidic conditions in the lysate whereas the apo azurin protein contains cations on its surface so that it remains soluble at low pH. Lysate was further clarified by an additional round of centrifugation at 18000 *g* for 30 minutes. The lysate was buffer-exchanged into Tris-HCl (20 mM, pH 8, no salt) and had a resultant volume of ca. 20 mL. Excess $CuSO_4$ (5 mM in Tris buffer (20 mM, pH 8)) was added into the lysate dropwise and the resultant solution was left stirring slowly for 2 hours at 4 °C. The solution turned intense blue after introducing the Cu^{2+} ion to the apoprotein.

The high affinity towards Cu^{2+} allows the apoprotein to undergo a very quick metal constitution process. The precipitation formed was removed by centrifugation at 18000 g for 30 minutes and the purity of the solution was checked before moving to the next step. The supernatant was filtered, buffer-exchanged to phosphate buffer (100 mM, pH 8, EDTA-free), and concentrated down to a small volume (less than 3 mL). The concentrated protein was transferred by lock syringe to the size exclusion column to proceed with size exclusion. The fractions that contained Cu azurin were combined and buffer-exchanged to sodium acetate buffer (1 mM, pH 4.5) to remove unbound metal. The SP Sepharose (cationic exchange) resin was equilibrated with sodium acetate buffer (1 mM, pH 4.5) by flowing through at least 2 column volumes. The equilibrated ion exchange resin was mixed with the protein and incubated with stirring for at least 2 hours.

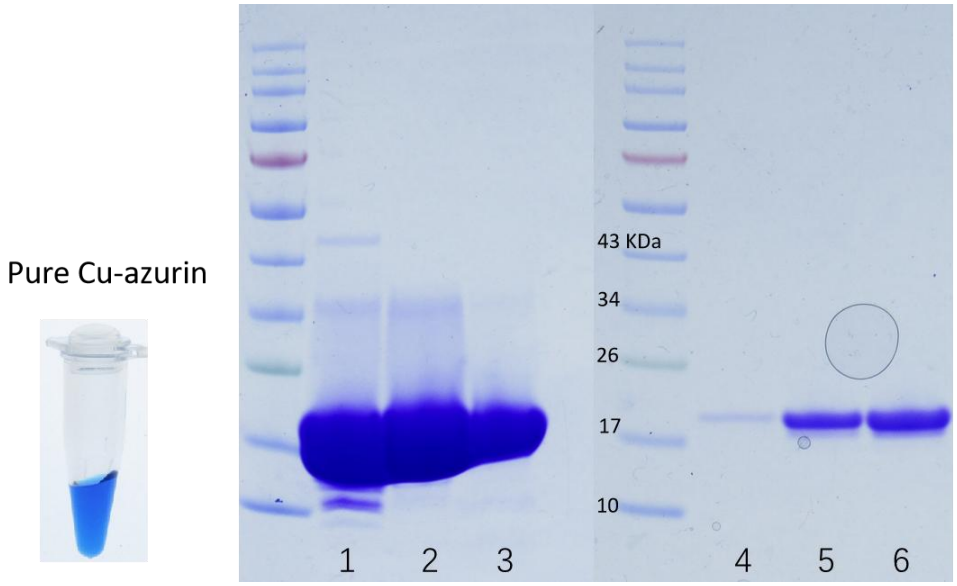

Figure 2.19: SDS-PAGE of azurin during expression and purification. Column 1: lysate after resuspending cells; Column 2: after acidic precipitation; Column 3: after Cu^{2+} reconstitution; Column 4 5 and 6: after ion exchange columns. Expected size of azurin: 14kDa. Note: the protein runs slower

than expected in the SDS-PAGE.

The protein solution was extremely concentrated so that a large quantity of the resin was required (100 cm^3) though many proteins were still not able to bind. The resin was packed and washed by 3 column volumes of sodium acetate (1 mM, pH 4.5). Unbound proteins were collected for the second round. A gradient was run against concentrated sodium acetate solution (300 mM, pH 4.5) in which the high concentration of Na^+ will substitute positively charged Cu Azurin on the resin. The fractions containing the protein were collected and buffer-exchanged to phosphate buffer (100 mM, pH 8, EDTA-free). The yield of 1 litre preparation is ca. 28 mg.

2.4.2 Protein Crystallisation

Crystallisation of Hyd-1 and Hyd-2 was performed by the sitting drop vapour diffusion technique, supervised by Dr Stephen Carr. For both Hyd-1 and Hyd-2 crystallisation, after exchange to size exclusion chromatography buffer, 1.5 µL of 5 mg mL^{-1} protein solution was mixed with an equal amount of chosen crystallisation buffer followed by streak seeding with old smaller crystals. Needle-like or long rod-shape crystals formed in 24 to 48 hours of incubation at 293 K in a strictly anaerobic N_2-purged glovebox. The size, number and form of crystals varied between batches and polyethylene glycol gradient.

All buffers in this work were prepared in ultra-high purity water (MilliQ Millipore, 18 MΩ cm). Buffers were degassed for 20 min/100 mL before bringing into the glovebox, and for large volumes of buffer (1 L), the solutions were stirred overnight in the glovebox to ensure

minimum dissolved O_2. The compositions of buffer solutions used for crystallisation in this work are listed below:

size exclusion chromatography buffer:

20 mM Tris, pH 7.2, 150 mM NaCl, 0.02% (w/v) N-Dodecyl β-D-Maltoside (DDM) detergent, 1 mM Dithiothreitol

Hyd-1 crystallisation buffer:

100 mM Bis-Tris, 200 mM Li_2SO_4, 150 mM NaCl, PEG 3350 (19-21% w/v), pH 4.0.

100 mM Bis-Tris, 200 mM Li_2SO_4, 150 mM NaCl, PEG 3350 (19-21% w/v), pH 6.0.

100 mM Tris HCl, 200 mM Li_2SO_4, 150 mM NaCl, PEG 3350 (19-21% w/v), pH 8.0.

Hydrogenase-2 crystallisation buffer:

100 mM Bis-Tris, 200 mM $MgCl_2$, PEG 3350 (19-22% w/v), pH 6.0.

2.5 Infrared Microspectroelectrochemical Cell Design and Experimental Procedure

In this section, the SEC cell used in Chapter 3 for *in-situ* SEC characterisation of single Hyd-1 and Hyd-2 crystals is explained. The detailed experimental procedure, including information on chemicals and reagents used, is also described. The IR spectra and visible images were acquired using an in-house IR microscope with two main compartments: a Vertex 80 IR spectrometer equipped with a globar silicon carbide IR source (Bruker) and a Hyperion 3000

IR microscope (Bruker).

2.5.1 Cell Design

The detail assembly description of the infrared microspectroelectrochemical cell was published earlier. A few updating modifications on the MSEC cell were adapted for measuring on single protein crystals and the schematic representation of the IR microspectroelectrochemical cell used in this work is shown in Figure 2.20.

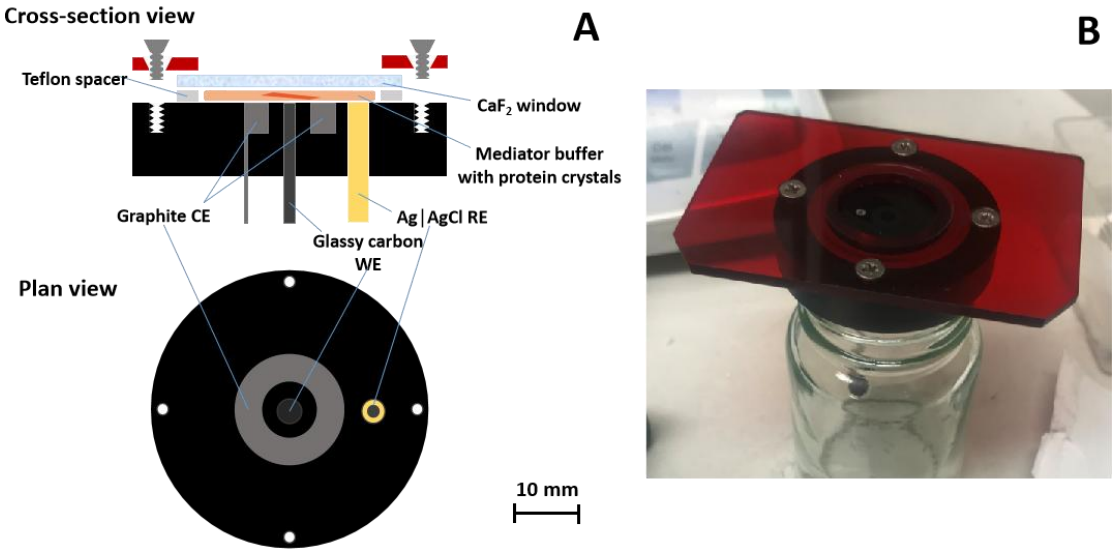

Figure 2.20: A) Schematic representation of the IR microspectroscopic-electrochemical cell used in this work. The arrangement of the WE, RE, CE, respectively are shown. B) Picture of assembled cell.

The main body of the cell consists of a disc-shaped chamber with a 4 mm diameter glassy carbon working electrode (WE, Alfa Aesar) that facilitates locating protein crystals. The WE is surrounded by a graphite ring counter electrode (CE, Goodfellow), and a miniature Ag/AgCl reference electrode (RE, 3 M KCl, 2 mm diameter, eDAQ) is positioned in close proximity to minimise uncompensated resistance. A Teflon spacer (25 to 50 µm) is employed to maintain a uniform solution layer thickness beneath the optical window, which is made of calcium

fluoride (CaF_2, UV grade, 32 mm diameter, 1 mm thickness, Crystran). This design ensures that the solution layer thickness is comparable to the crystal size, reducing water interference in the IR spectra.

The cell is mounted beneath the microscope's IR source. The incident IR beam traverses the optical window, interacts with the crystalline sample, and reflects off the WE, passing through the sample twice. Electron transfer between the WE and the crystalline sample is facilitated by redox mediators in the electrolyte solution. This configuration enables precise and rapid electrochemical control over the single protein crystal during in-situ IR spectroscopic measurements.

2.5.2 Experimental Procedure

Preparation of Redox Mediators

Redox mediator solutions (1 mM each) were prepared inside a nitrogen-filled glovebox using a degassed crystallisation buffer identical to the one used for protein crystallisation. The selection of mediators was guided by the target redox potential range, ensuring the mediators' redox potentials collectively spanned the desired potential window. The complete list of mediators employed in this thesis is provided in Table 2.2.

A 20 µL aliquot of mediator solution was added to a well of the crystallisation plate containing single Hyd-1 or Hyd-2 crystals. The crystals were gently resuspended by pipetting to ensure homogeneous mixing with the mediator-containing buffer. Under the bench-top microscope, a 10 µL aliquot of crystal-containing suspension was pipetted onto the surface of

the glassy carbon working electrode (WE), while an additional 10 µL of mediator solution was applied dropwise to the graphite counter electrode (CE), and a 5 µL aliquot was carefully added to the Ag/AgCl reference electrode (RE). A PTFE spacer was then placed on the cell surface, and approximately 20 µL of mediator solution was pipetted beneath the spacer to act as a gasket, preventing solution spread due to surface tension and ensuring a consistent solution layer thickness. The CaF_2 optical window was carefully screwed onto the cell, ensuring minimal disruption to the crystals. Silicone sealant (Dowsil, SE 9187L Silicone RTV) was applied around the edge of the window to maintain an anaerobic environment within the cell. IR spectra were recorded under *in-situ* electrochemical control, with the WE potential modulated to probe different redox states of the protein crystal. Visible images of the crystal were simultaneously acquired to confirm crystal integrity and orientation.

Table 2.2. Mid-point potentials (E_m) of redox mediators used in this work. The reported values are measured at pH 7 apart from two Eu complexes, which are measured at pH 8.

Redox Mediator	Molecular structure	Literature E_m/ mV
Ferricyanide (FCN)	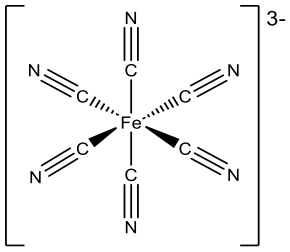	+430[33]

Ferrocenemethanol (FcMeOH)	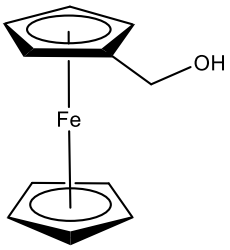	+354[34]
2,6-Dichloroindophenol (DCIP)	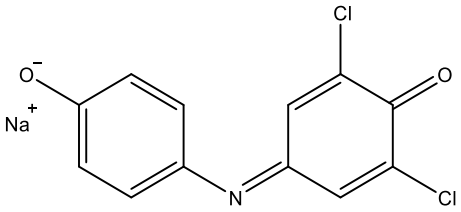	+217[33,35]
Indigo carmine (IC)	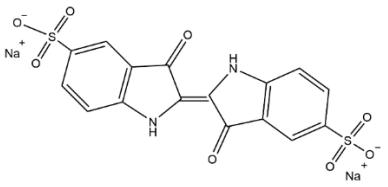	-125[36]
Anthraquinone-2,6-disulfonate (AQDS)	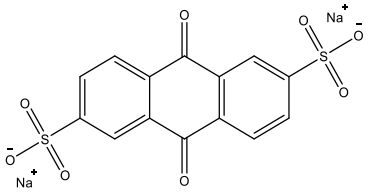	-184[37]
Phenosafranin (PS)	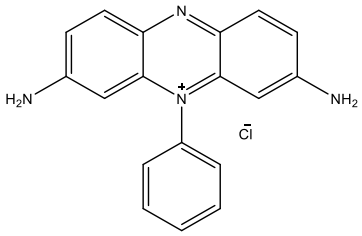	-244[38]
Benzyl viologen (BV)	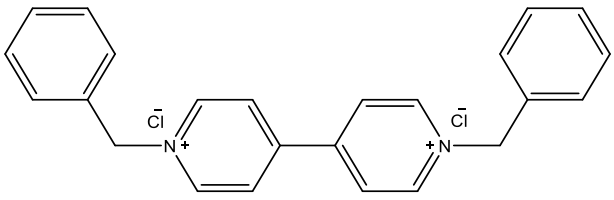	-350[33,39]

Methyl viologen (MV)	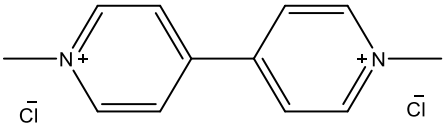	-446[33,39]
EuBAPTA	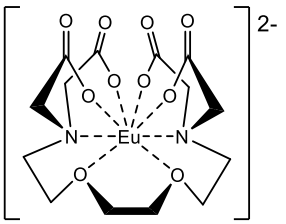	-630[40]
EuEGTA	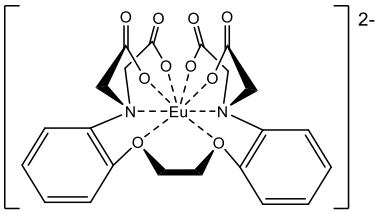	-865[40,41]

2.6 References

1 H. Ogata, K. Nishikawa and W. Lubitz, *Nature*, 2015, **520**, 571–574.

2 S. E. Beaton, R. M. Evans, A. J. Finney, C. M. Lamont, F. A. Armstrong, F. Sargent and S. B. Carr, *Biochem. J.*, 2018, **475**, 1353–1370.

3 K. A. Vincent, A. Parkin and F. A. Armstrong, *Chem. Rev.*, 2007, **107**, 4366–4413.

4 R. M. Evans, P. A. Ash, S. E. Beaton, E. J. Brooke, K. A. Vincent, S. B. Carr and F. A. Armstrong, *J. Am. Chem. Soc.*, 2018, **140**, 10208–10220.

5 P. A. Ash, S. B. Carr, H. A. Reeve, A. Skorupskaitė, J. S. Rowbotham, R. Shutt, M. D. Frogley, R. M. Evans, G. Cinque, F. A. Armstrong and K. A. Vincent, *Chem. Commun.*, 2017, **53**, 5858–5861.

6 P. A. Ash, S. E. T. Kendall-Price, R. M. Evans, S. B. Carr, A. R. Brasnett, S. Morra, J. S. Rowbotham, R. Hidalgo, A. J. Healy, G. Cinque, M. D. Frogley, F. A. Armstrong and K. A. Vincent, *Chem. Sci.*, 2021, **12**, 12959–12970.

7 H. Wang, C. Y. Ralston, D. S. Patil, R. M. Jones, W. Gu, M. Verhagen, M. Adams, P. Ge, C. Riordan, C. A. Marganian, P. Mascharak, J. Kovacs, C. G. Miller, T. J. Collins, S. Brooker, P. D. Croucher, K. Wang, E. I. Stiefel and S. P. Cramer, *J. Am. Chem. Soc.*, 2000, **122**, 10544–10552.

8 Z. Gu, J. Dong, C. B. Allan, S. B. Choudhury, R. Franco, J. J. G. Moura, I. Moura, J. LeGall, A. E. Przybyla, W. Roseboom, S. P. J. Albracht, M. J. Axley, R. A. Scott and M. J. Maroney, *J. Am. Chem. Soc.*, 1996, **118**, 11155–11165.

9 Atkins Peter and Paula de Julio, *Atkins' Physical Chemistry*, Oxford University Press, Oxford, 10 th., 2014.

10 P. A. Ash, R. Hidalgo and K. A. Vincent, *ACS Catal.*, 2017, **7**, 2471–2485.

11 A. K. Grzybowski, *J. Phys. Chem.*, 1958, **62**, 550–555.

12 G. Bates and B. Macaskill, *Pure Appl. Chem.,* 1978, **50**, 1701–1706.

13 F. A. Armstrong, R. M. Evans, S. V Hexter, B. J. Murphy, M. M. Roessler and P. Wulff, *Acc. Chem. Res.*, 2016, **49**, 884–892.

14 M. J. Lukey, A. Parkin, M. M. Roessler, B. J. Murphy, J. Harmer, T. Palmer, F. Sargent and F. A. Armstrong, *J. Biol. Chem.*, 2010, **285**, 3928–3938.

15 V. M. Fernandez, E. C. Hatchikian and R. Cammack, *BBA -Enzymology*, 1985, **832**, 69–79.

16 C. E. Foster, T. Krämer, A. F. Wait, A. Parkin, D. P. Jennings, T. Happe, J. E. McGrady and F. A. Armstrong, *J. Am. Chem. Soc.*, 2012, **134**, 7553–7557.

17 R. W. Browne, *Electrochemistry*, Oxford University Press, 2018, vol. 152.

18 A. C. Fisher, *Electrode Dynamics*, Oxford University Press, 1996, vol. 83.

19 Gerhard Herzberg, *Molecular spectra and molecular structure. II, Infrared and Raman spectra of polyatomic molecules*, D. Van Nostrand Company, Toronto, 1945, vol. 632.

20 G. E. Leroi and W. Klemperer, *J. Chem. Phys.*, 1961, **35**, 774–775.

21 E. Bernhardt, B. Bley, R. Wartchow, H. Willner, E. Bill, P. Kuhn, I. H. T. Sham, M. Bodenbinder, R. Bröchler and F. Aubke, *J. Am. Chem. Soc.*, 1999, **121**, 7188–7200.

22 J.-J. Max and C. Chapados, *J. Chem. Phys.*, 2010, **133**, 164509.

23 J. A. BEARDEN and A. F. BURR, *Rev. Mod. Phys.*, 1967, **39**, 125–142.

24 S. Calvin, *XAFS for Everyone*, CRC Press, Boca Raton, 2nd edn., 2024, vol. 444.

25 R. S. K. Ekanayake, V. A. Streltsov, S. P. Best and C. T. Chantler, *J. Appl. Crystallogr.*, 2024, **57**, 125–139.

26 S. P. Best, V. A. Streltsov, C. T. Chantler, W. Li, P. A. Ash, S. Hayama and S. Diaz-Moreno, *J. Synchrotron Radiat.*, 2021, **28**, 472–479.

27 G. N. George, I. J. Pickering, M. J. Pushie, K. Nienaber, M. J. Hackett, I. Ascone, B. Hedman, K. O. Hodgson, J. B. Aitken, A. Levina, C. Glover and P. A. Lay, *J. Synchrotron Radiat.*, 2012, **19**, 875–886.

28 M. Ferraroni, W. Rypniewski, K. S. Wilson, M. S. Viezzoli, L. Banci, I. Bertini and S. Mangani, *J. Mol. Biol.*, 1999, **288**, 413–426.

29 K. R. Acharya and M. D. Lloyd, *Trends Pharmacol. Sci.*, 2005, **26**, 10–14.

30 M. Kubin, M. Guo, M. Ekimova, M. L. Baker, T. Kroll, E. Källman, J. Kern, V. K. Yachandra, J. Yano, E. T. J. Nibbering, M. Lundberg and P. Wernet, *Inorg. Chem.*, 2018, **57**, 5449–5462.

31 R. Chatterjee, C. Weninger, A. Loukianov, S. Gul, F. D. Fuller, M. H. Cheah, T. Fransson, C. C. Pham, S. Nelson, S. Song, A. Britz, J. Messinger, U. Bergmann, R. Alonso-Mori, V. K. Yachandra, J. Kern and J. Yano, *J. Synchrotron Radiat.*, 2019, **26**, 1716–1724.

32 R. M. Evans, E. J. Brooke, S. A. M. Wehlin, E. Nomerotskaia, F. Sargent, S. B. Carr, S. E. V Phillips and F. A. Armstrong, *Nat. Chem. Biol.*, 2016, **12**, 46–50.

33 R. Cammack, V. M. Fernandez and E. Claude Hatchikian, in *Methods in Enzymology*, Academic Press, 1994, vol. 243, pp. 43–68.

34 C. Cannes, F. Kanoufi and A. J. Bard, *J. Electroanal. Chem.*, 2003, **547**, 83–91.

35 S. Kumar and S. K. Acharya, *Anal. Biochem.*, 1999, **268**, 89–93.

36 P. G. Tratnyek, T. E. Reilkoff, A. W. Lemon, M. M. Scherer, B. A. Balko, L. M. Feik and B. D. Henegar, *The Chemical Educator*, 2001, **6**, 172–179.

37 P. L. Dutton and M. Baltscheffsky, *BBA - Bioenergetics*, 1972, **267**, 172–178.

38 F. P. Guengerich, D. P. Ballou and M. J. Coon, *J. Biol. Chem.*, 1975, **250**, 7405–7414.

39 C. L. Bird and A. T. Kuhn, *Chem. Soc. Rev.*, 1981, **10**, 49–82.

40 T. Chen, P. A. Ash, L. C. Seefeldt and K. A. Vincent, *Faraday Discuss.*, 2023, **243**, 270-286

41 K. A. Vincent, G. J. Tilley, N. C. Quammie, I. Streeter, B. K. Burgess, M. R. Cheesman and F. A. Armstrong, *Chem. Commun.*, 2003, **20**, 2590–2591.

Chapter 3: Characterisation of *E. coli* Hydrogenase Single Crystals Using Microspectroelectrochemistry

In this chapter, microspectroelectrochemistry is applied to single crystals of Hyd-1 and Hyd-2 to generate potential-dependent speciation profiles for these enzymes through oxidative potential titration. The redox transitions between active site states in the crystalline state are studied. More importantly, the experimental conditions for isolating pure Ni_a-SI, Ni_a-C and Ni_a-R are established and employed as a reference to produce hydrogenase single crystals in defined active site states.

3.1 Introduction

Infrared spectroelectrochemistry study on [NiFe]-hydrogenases

Owing to the unique architecture of the [NiFe]-hydrogenase active site which contains two CN^- ligands and a CO ligand, the intense and sensitive vibrational absorption bands of the ligands make IR spectroscopy ideal for studying the redox and coordination states of the active site.[1,2] During the turn-over, the protein active site is proposed to undergo proton coupled electron transfer (PCET) steps converting H_2 and H^+. Thus, combining electrochemistry and IR spectroscopy allows us to study the active site state *in-situ*, and this method is called IR spectroelectrochemistry (SEC).[3–6]

Table 3.1: Infrared peak positions (in cm^{-1}) of the intrinsic active site ν_{CO} band for a range of [NiFe]-hydrogenases in common long-lived redox states. MBH stands for membrane-bound hydrogenase; RH stands for regulatory hydrogenase; SH stands for soluble hydrogenase.

Hydrogenases	*Ni-A*	*Ni-B*	*Ni-SU*	*Ni-SI_r*	*Ni_a-SI*	*Ni_a-C*	*Ni_a-L_I*	*Ni_a-L_{II}*	*Ni_a-L_{III}*	*Ni_a-R_I*	*Ni_a-R_{II}*	*Ni_a-R_{III}*
***D. vulgaris Miyazaki F*[4]**	1956	1955	1946	1922	1943	1961	-	1911	1890	1948	1932	1919
***D. gigas*[7]**	1947	1946	1950	1914	1934	1952	-	-	-	1940	1923	-
***D. fructosovorans*[8]**	1947	1946	1950	1913	1933	1951	-	-	-	1938	1922	-
***A. vinosum MBH*[9]**	1945	1943	1948	1910	1931	1951	1898	-	-	1936	1921	1913
***E. coli Hyd-2*[10]**	-	1957	-	-	1945	1966	1911	-	-	1950	1936	1929
***T.roseopersicina MBH*[11]**	-	1944	-	-	1930	1951	1899	-	-	-	1921	1915
***R. eutropha MBH*[12]**	-	1948	1943	1910	1936	1957	1899	-	-	1948	1926	1919
***E. coli Hyd-1*[13]**	-	1943	-	-	1927	1949	-	1877	1867	-	1922	1914
***A. aeolicus MBH*[14]**	-	1939	-	-	1927	1949	1862	1876	1900	-	1910	-
***R. eutropha RH*[15]**	-	1951	1957	1938	1942	1961	-	-	-	1949	1934	1918
***P. furiosus SH*[16]**	-	1960	-	1934	1950	1967	1917	1922	-	1954	1940	1934
***R. eutropha SH*[17]**	-	1957	-	1946	-	1961	-	-	-	1958	1922	1913
***Synechocystis SH*[18]**	-	1957	-	-	1947	1968	-	-	-	1955	-	-

Furthermore, IR spectroscopy can report on all redox levels of the active site. In contrast, EPR could

only detects paramagnetic states, and hence in case of [NiFe]-hydrogenases, only states having Ni(III) or Ni(I) can be measured. Although only the Ni ion at the bimetallic active changes formal oxidation state during catalysis between Ni(I) and Ni(III), the three IR probe ligands (two CN^- and one CO) coordinated to the adjacent low spin Fe(II) are sensitive to electronic and structural changes at Ni. Therefore, IR spectroelectrochemistry provides comprehensive insight into the chemistry of the [NiFe]-hydrogenases active site at all redox levels. Studies on different NiFe hydrogenases via solution spectroelectrochemistry have provided a general overview of active site IR assignments. This is important to study the enzyme mechanism and the most common redox states of active sites with their redox relationship are shown in Figure 3.1, where the active site states are classified into inactive and active relative to their involvement in catalysis. The active states are denoted with subscript 'a', Ni_a-X, to indicate their involvement in turn-over. Generally in [NiFe]-hydrogenases, the two different types of IR sensitive ligands on Fe, CO and CN^-, have different absorption frequency regions, where CN^- bands (2020 to 2100 cm^{-1}) are measured to have higher wavenumber than the band of CO (1860 to 1970 cm^{-1}).[19] The intrinsic CO bond absorption band ν_{CO} is generally more valuable for interpreting the speciation of the enzyme, since the CO ligand is more sensitive to the electronic change of the active site and the CN^- bands often overlap when multiple active site states are present. Table 3.1 summarises the wavenumber positions of CO bond stretching ν_{CO} at common redox states of different [NiFe] hydrogenases. Among these hydrogenases, group 1 MBH *E. coli* Hyd-1 (O_2-tolerant) and Hyd-2 (O_2-sensitive), are investigated in this chapter.

The active site states

The most oxidised inactive states are Ni-A and Ni-B, which are often found in as-isolated and air-oxidised proteins. They are generally IR-indistinguishable as they have very similar wavenumber positions for the CO ligand on Fe (Table 3.1) and both Ni-A and Ni-B carry a $Ni^{III}Fe^{II}$ bimetallic active site. During catalysis, the redox chemistry takes places formally on the Ni ion, but the Fe ion remains low

spin in +2 oxidation state.[1] One electron reduction of the inactive state Ni-A and Ni-B, yields Ni-SU and Ni-SI_r states respectively which are also catalytically inactive with Ni in the +2 oxidation state.[20]

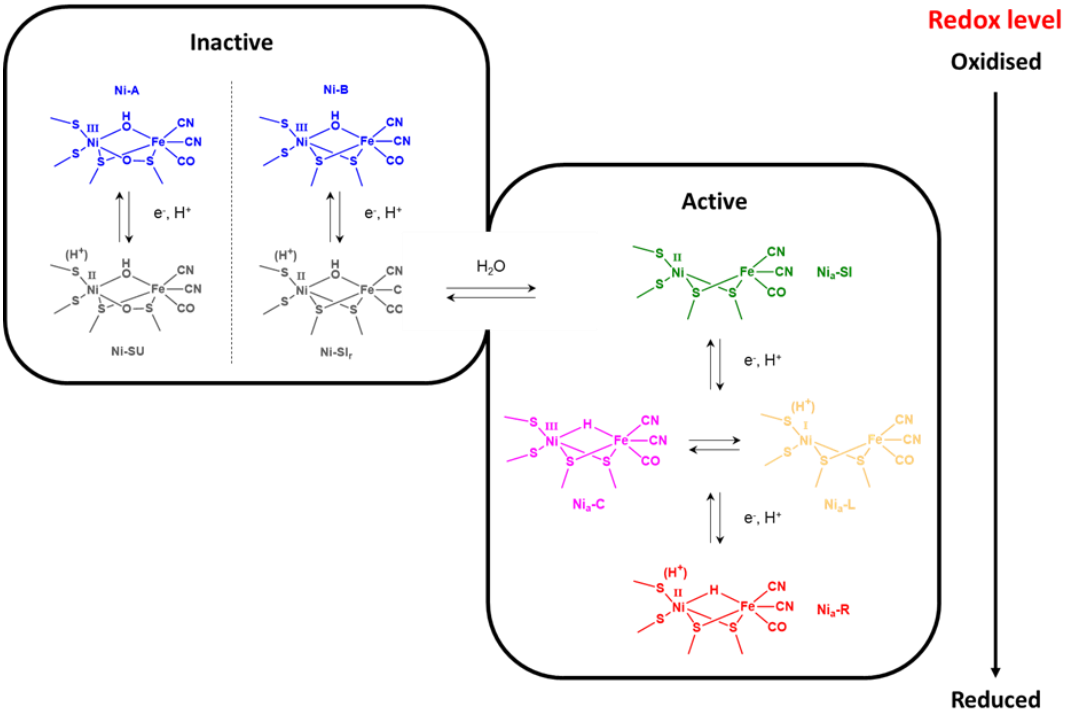

Figure 3.1: The most common redox states of the active site of [NiFe] hydrogenases and their transformation relationships. All states are ordered in redox level from the most oxidised to the most reduced. The colour of each state is consistent through the thesis: blue (Ni-A and Ni-B); grey (Ni-SU and Ni-SI_r); green (Ni_a-SI); magenta (Ni_a-C); pale orange (Ni_a-L); red (Ni_a-R).

Subsequential protonation of the bridging hydroxy ligand in the Ni-SI_r state leads to its release as a water molecule yielding the most oxidised active state, Ni_a-SI.[21] This state is proposed to be where the catalysis starts, and H_2 binds the active site at the vacant bridging coordination site.[22] IR spectroelectrochemical experiments play an important role in assigning the Ni_a-SI state. The name of the state, Ni_a-SI was given as it shows no EPR signal because it possesses a diamagnetic $Ni^{II}Fe^{II}$ active site which is EPR silent. Moreover, it is hard to trap this state either for oxidised, as-isolated or chemically reduced samples, but it is generally found at mildly reducing redox conditions.[1,6,10] The addition of one electron and one proton to the Ni-SI state gives the more reduced Ni_a-C state, where it carries $Ni^{III}Fe^{II}$ but it is ligated with a bridging hydride. At the same redox level, Ni_a-L was observed

after photo-illumination of Ni_a-C at cryogenic temperatures which leads the hydride to leave as a proton to a nearby basic amino acid residue and leave the Ni ion in a +1 oxidation state.[23] This makes the Ni_a-L state easy to distinguish in the IR from Ni_a-C due to a significant electron density difference between the active site in these states. Recent IR spectroelectrochemical experiments showed that Ni_a-L is not only the photoproduct of Ni_a-C but is involved in the catalytic cycle.[24] Furthermore, protonation at different proton acceptor sites near the active site produce long-range effects at the active site which make Ni_a-L show different ν_{CO} bands even though they are in the same redox level.[23,24] The same phenomenon also was observed in the most reduced state of [NiFe]-hydrogenase, the Ni_a-R state.[1,6] An additional proton coupled electron transfer from Ni_a-C generates the Ni_a-R state. Ni_a-R is also proposed to be the product of H_2 coordination to the active site in Ni_a-SI state.[1] After heterolytic cleavage of H_2, the H^- is left as a hydride at the bridging position and a proton is accepted by a nearby base.[25] IR spectroelectrochemical studies have shown multiple Ni_a-R states in different hydrogenases according to the distance of the protonation site with respect to the active site.[26] They are named Ni_a-R_I, Ni_a-R_{II} and Ni_a-R_{III}.

Comprehensive SEC study on [NiFe]-hydrogenases has provided a schematic overview of infrared band position of intrinsic CO vibration for the various active states (Table 3.1). According to the existing data sets, the Ni_a-C state has the highest ν_{CO} band position among the catalytically active states. For any studied [NiFe]-hydrogenase, there is a good agreement between the ν_{CO} band positions of all states relative to the ν_{CO} of the Ni_a-C. Therefore, Ni_a-C is a good candidate for an internal ν_{CO} reference to potentially identify any unknown band. For example, the ν_{CO} of the Ni_a-SI state has on average 19.7 cm^{-1} lower ν_{CO} than that of Ni_a-C, and all the relative positions if Ni_a-SI ν_{CO} from all the studied [NiFe]-hydrogenases lie within 2 standard deviations. This relative relationship is highlighted by Ash *et al.* and shown in Figure 3.2 for the common redox states in [NiFe]-hydrogenases.[19]

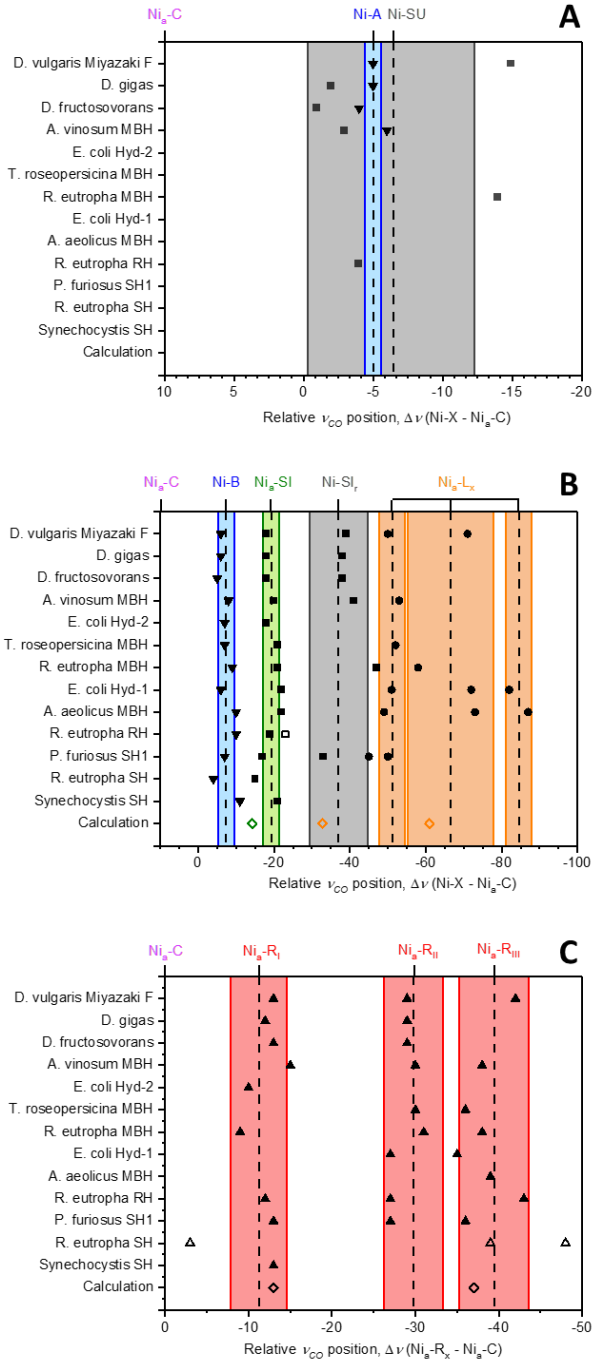

Figure 3.2: Relative ν_{CO} positions of redox states of [NiFe] hydrogenases show similar wavenumber positions with respect to the Ni$_a$-C state. The band width with each ν_{CO} of the state shows the standard deviations of it from all accounted hydrogenases, and the dashed line represents the mean value of the ν_{CO}. (A) Relative positions of the Ni-A and Ni-SU. (B) Relative positions of the Ni-B, Ni$_a$-SI, Ni-SI$_r$ and three Ni$_a$-L states as classified. (C) Relative positions of three Ni$_a$-R states. DFT calculated values for each state are included for comparison.[27–29] Figure reproduced and modified from ref 19, Copyright © 2017 American Chemical Society.

IR microspectroelectrochemical studies on single crystals of [NiFe]-hydrogenases

In contrast to EPR or XAS spectroscopy which generally require frozen samples, IR spectroscopy serves as a versatile technique to study [NiFe]-hydrogenases across a range of sample types. Protein samples can be measured in solution[15], electrode-adsorbed/immobilized,[19] lyophilised[30] and more importantly for this study, in crystalline state via appropriate sampling techniques.[6] The integrity and redox state of a single crystals can be measured via infrared microspectroscopy,[6] and more over can be combined with electrochemical control.[13] An *in-situ* microspectroelectrochemical study on single [NiFe]-hydrogenase crystals has revealed that fine potential control is possible on protein crystals via a custom-designed IR microspectroelectrochemical cell described in Chapter 2, utilising selected redox mediators spanning the potential window relevant to redox states of [NiFe]-hydrogenases.[13,26]

***Escherichia coli* Hyd-1 and Hyd-2**

Hyd-1 and Hyd-2 are both Group 1 hydrogenases constitutively expressed in *Escherichia coli* (*E. coli*). They have homologous gene sequences encoding their core αβ heterodimer and identical active site structures. Hyd-1 is an oxygen-tolerant hydrogenase, benefiting from its unique proximal [4Fe3S] cluster, while Hyd-2 is a standard hydrogenase, sensitive to oxygen. Electrochemical assays have confirmed that Hyd-2 is a reversible catalyst for H^+/H_2 *in vitro*, whereas Hyd-1 functions exclusively as an H_2 oxidiser at neutral pH with a small overpotential (Figure 3.3).

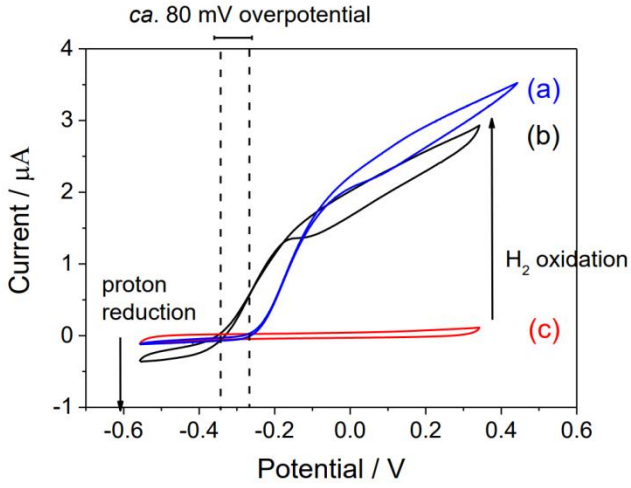

Figure 3.3: Cyclic voltammograms for Hyd-1 (a) and Hyd-2 (b) directly adsorbed on a bare PGE electrode under 1 bar H_2. Trace (c) shows the charging current of the PGE electrode recorded as background. Other conditions: pH 6; 28 ℃; electrode rotation rate, 2000 rpm; scan rate, 10 mV s^{-1}. Data provided by Min-Wen Chung.[31]

Extensive IR spectroelectrochemical characterisation on Hyd-1 and Hyd-2 revealed that both enzymes undergo the same set of active site states during catalysis.[10,19] However, the equilibrium potentials governing these active site states differ significantly. Consequently, under redox control, the speciation of active site states diverges between these enzymes.

The focus of this chapter

IR microspectroscopy demonstrated that electrochemical control over single crystals of *E. coli* Hyd-1 allows navigation through the full range of active site states that are observed in solution or adsorbed on an electrode.[6,13,26] In this chapter, this novel IR microspectroelectrochemical method was employed to study both Hyd-1 and Hyd-2 single crystals at pH 6 via measuring IR spectra *in-situ* on a focused area of a crystal over a series of stepped applied potentials. The spectroelectrochemical study on Hyd-1 and Hyd-2 crystals provide detailed reference information of the catalytic state speciation versus applied potential. This maps out potentials at which pure states are present.

3.2 IR Microspectroelectrochemistry on Hyd-1 Single Crystals

Delta transmembrane (ΔTM) Hyd-1 crystals are used in this section. It has the same αβ heterodimer to Hyd-1 but is expressed without the transmembrane domain and HyaC (Figure 1.3). It shows structural and electrochemical similarity to wild-type Hyd-1.[32] A major advantage of studying crystals grown from ΔTM Hyd-1 is their size, which generally have a width of over 50 µm compare with "needle" shape native Hyd-1 crystals. This enables the use of a wider sampling aperture for IR microspectroscopy and yields spectra with significantly improved signal-to-noise ratios. However, there is no published IR spectroelectrochemical characterisation on ΔTM Hyd-1.

The experimental set-up used in measurements of *E. coli* Hyd-1 crystals is described in Chapter 2.5.2. In this spectroelectrochemical (SEC) study of single crystals, the observed IR bands were interpreted and assigned to specific redox states of the active site according to IR-SEC study on the same and other [NiFe]-hydrogenases (Table 3.1 and Figure 3.2).[1,19] It was also shown that the potential dependence and the absorption band positions of the *E. coli* Hyd-1 has good consistency between solution, electrode-immobilised and crystalline state.[6,26] Each active site state have similar absorption band positions in ν_{CO} which is summarised in Table 3.1 for general Hyd-1 speciation assignment. The comparison of redox speciation curves from oxidative titration of Hyd-1 by three SEC methods with different sample states is shown in Figure 3.4.

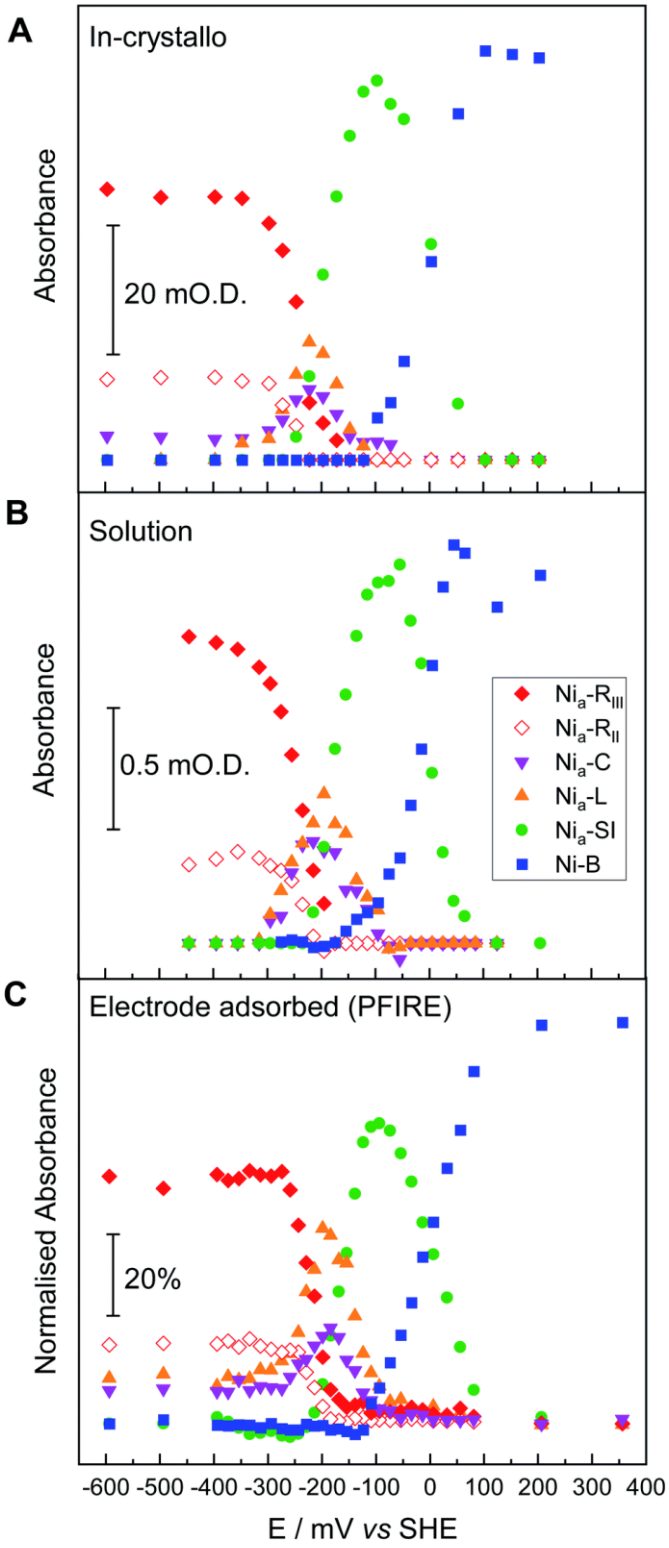

Figure 3.4: Comparison of redox speciation curves (from oxidative titrations) of Hyd1 at pH 5.9 by three IR spectroscopic-electrochemical methods: single crystal IR microspectroelectrochemistry/in crystallo (A); in solution (B); and PFIRE/electrode adsorbed (C). Figure adopted with permission from Ash *et al*, *Chem. Sci.*, 2021,12, 12959-12970, Copyright © the Royal Society of Chemistry.

3.2.1 The As-isolated (asiso) Hyd-1 Crystal

Figure 3.5 shows the visible images of a Hyd-1 single crystal on the glassy carbon working electrode (WE) with 4× and 15× magnification. The protein crystals of ΔTM Hyd-1 were grown up to approximately 100×500×30 micrometres (width, length and thickness) dimension. The effective concentration of protein in the crystal is calculated to be 8 to 10 mM concentration.[26]

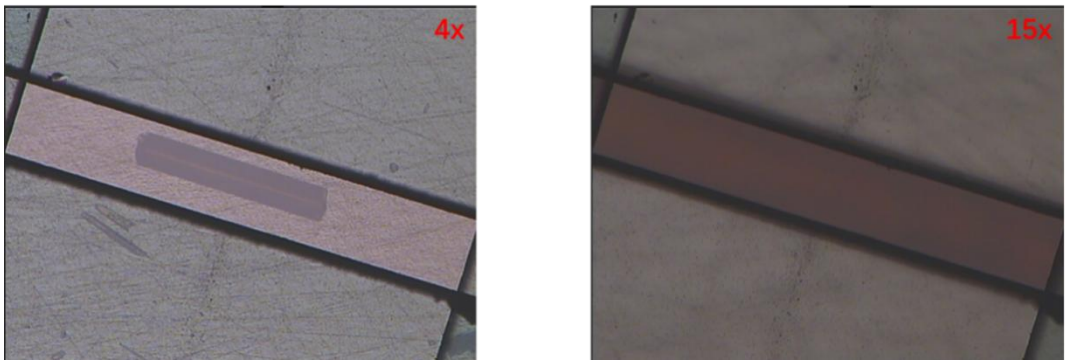

Figure 3.5: Visible image at 4× (Left) and 15× (Right) magnification of a single Hyd-1 crystal on the working electrode of the IR microspectroelectrochemical cell. The 60 × 200 μm^2 sampling area used to collect IR spectra is shown in the 15× image on the right, indicated in the black crosshairs.

The crystals were deposited on the WE, still in crystallisation buffer, but a redox mediator cocktail added. This comprised 1 mM each of [EuBAPTA], methyl viologen (MV), benzyl viologen (BV), anthraquinone-2,6-disulfonate (AQDS), indigo carmine (IC), phenazine methosulfate (PMS), 2,6-dichloroindophenol (DCIP) and ferricyanide (FCN), prepared in the crystallisation mixed buffer (100 mM Bis-Tris, 200 mM $LiSO_4$, 150 mM NaCl and 22% w/v PEG, pH 6). The redox potential of the redox mediators is summarised in Table 2.2. The salts in the crystallisation buffer served as electrolyte in the spectroelectrochemical cell. Connecting three electrodes closed the circuit, and the mediators facilitate fast electron transfer between the WE and protein crystals over the relevant potential range. A cyclic voltammetry measurement of the cell containing the mediator cocktail and protein crystal was performed after an open circuit potential (OCP) IR measurement, prior to reductive activation of the crystals and is shown in Figure 3.6. The cyclic voltammogram demonstrates electrochemical control

within the IR microspectroelectrochemical cell and confirms the redox activity of mediators over the relevant potential range.

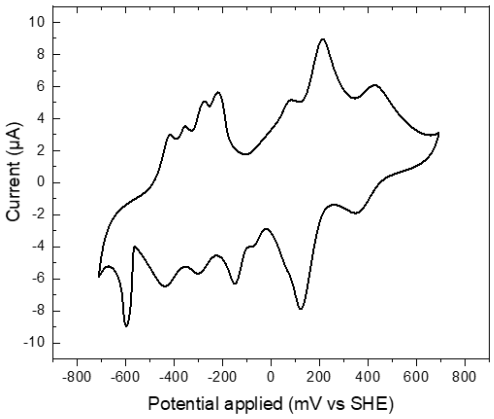

Figure 3.6: Cyclic voltammogram of the microspectroelectrochemical cell, demonstrating the redox couples of the added mediators in the mixed buffer. Recorded at a scan rate: 10 mV / s with hydrogenase crystallisation buffer (100 mM Bis-Tris, 200 mM LiSO4, 150 mM NaCl and 22% w/v PEG, pH 6) with additional 1 mM each of redox mediator EuBAPTA, MV, BV, AQDS, IC, PMS, DCIP and FCN.

Figure 3.7 top panel shows the IR spectrum of the Hyd-1 single crystal displayed in Figure 3.5, measured at OCP (+170 mV vs SHE) covering both ν_{CO} and ν_{CN} regions. The 60 × 200 μm^2 area used to record IR spectra is shown with a black rectangle in Figure 3.5 right panel. The background spectrum was recorded with the same microscope aperture (sampling area, the black cross hair) right next to the crystal with the focus on the WE surface. The spectrum shows that the Hyd-1 crystal at OCP is predominantly in the Ni-B state with a band at 1943 cm^{-1} in the ν_{CO} region. The three bands observed at 2100, 2095, and 2082 cm^{-1} in the ν_{CN} region match the spectroscopic features of the full-length, natively expressed Hyd-1 single crystal.[26] Accordingly, these bands are assigned to the Ni-B state(s). This suggests that multiple (at least two) species are relevant to the 1943 cm^{-1} band. Although the protein crystals were grown in anaerobic conditions, the hydrogenase sample was purified under air and therefore it is expected to have a mixture of oxidised inactive species.[26]

Ni-A and Ni-B are reported for several hydrogenases to have very a similar ν_{CO} bands position (Table

3.1), so the three bands measured at ν_{CN} region may correspond to two overlapping sets of ν_{CN} bands from those two inactive states. The Ni-A state of Hyd-1 have been reported to have an oxidised terminal cysteine ligand on Ni.[32] In addition to Ni-B/Ni-A, the spectrum recorded at OCP shows bands at 1922, 1911 cm^{-1} in the ν_{CO} region and 2072 and 2065 cm^{-1} in ν_{CN} region. The band positions suggest that the crystal contains other oxidised active site states with higher electron density around the active site compared to Ni-B. This will be discussed later in the redox titration of the Hyd-1 crystal, when analysing the redox behaviour of the active species. These bands have not been reported before for full length Hyd-1 at an oxidised redox level, but do observe in the as-isolated Hyd-1-cytb single crystals.[33] DeltaTM Hyd-1 are expressed without cytb so might end up in the same redox speciation compare with native Hyd-1-cytb sample. Since the solution phase spectra of delta TM Hyd-1 have not been measured and so it is unclear whether the novel bands observed under oxidizing conditions are a consequence of truncation or are specific to the crystalline form.

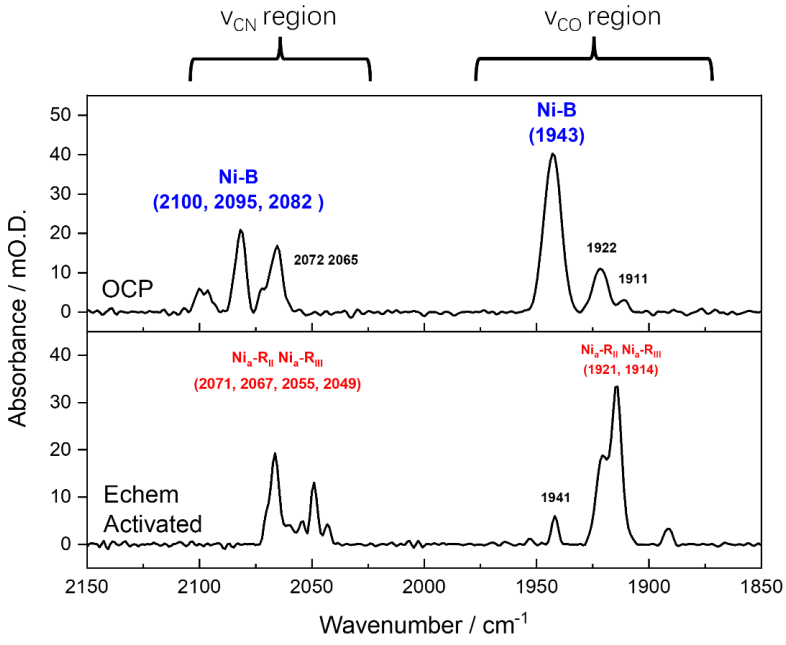

Figure 3.7: IR spectra of the Hyd-1 single crystal on the microspectroelectrochemical cell. (Top) Spectrum recorded at OCP = +170 mV vs SHE. (Bottom) Spectrum recorded after 1 hour reduction at -710 mV vs SHE. Both recorded at 2 cm^{-1} resolution, 512 scans and the background spectrum was recorded at an adjacent site next to the crystal on the WE with the same aperture.

3.2.2 Reductive Activation of the Hyd-1 Single Crystal

The interpretation of IR spectra for Hyd-1 crystals focuses on absorptions in the ν_{CO} region due to the heightened sensitivity of the intrinsic CO ligand vibration to changes in active site electron density. Although IR bands in the ν_{CN} region also shift with redox-level changes and align broadly with assignments from ν_{CO}, their inherent complexity precludes detailed analysis. Consequently, only ν_{CO} vibrations are discussed in this study.

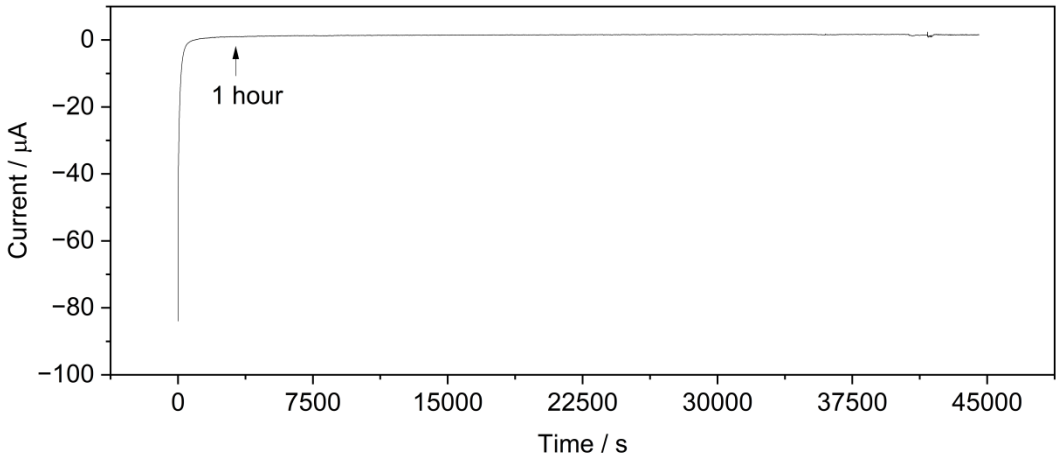

Figure 3.8: Chronoamperometry traces recorded during the full reductive activation of Hyd-1. The marker indicates a quasi-equilibrium has reached after 1 hour.

The chronoamperogram of the full reductive activation is shown in Figure 3.8, showing the cell reached equilibrium before 1 hour. The connective IR spectra of this crystal during this one-hour reductive activation is shown in Figure 3.9a. The majority of the inactive states (Ni-B, 1943 cm^{-1}; unknown band, 1921 cm^{-1}) converts to Ni_a-$R_{II/III}$ states as shown in the first scan in the Figure 3.9a (red spectrum), and the following spectra are highly identical. During the reduction, the predominate peak at 1943 cm^{-1} converts to peak at 1921 and 1914 cm^{-1} as shown in the difference map in Figure 3.9b. The identity of the band at 1921 cm^{-1} at oxidised redox level will be discussed later in this chapter. This indicates the active site states are converted form Ni-B to Ni_a-R(s) in a reasonably fast time scale. However, a residual peak at 1941 cm^{-1} persists in the spectra until scan 12.

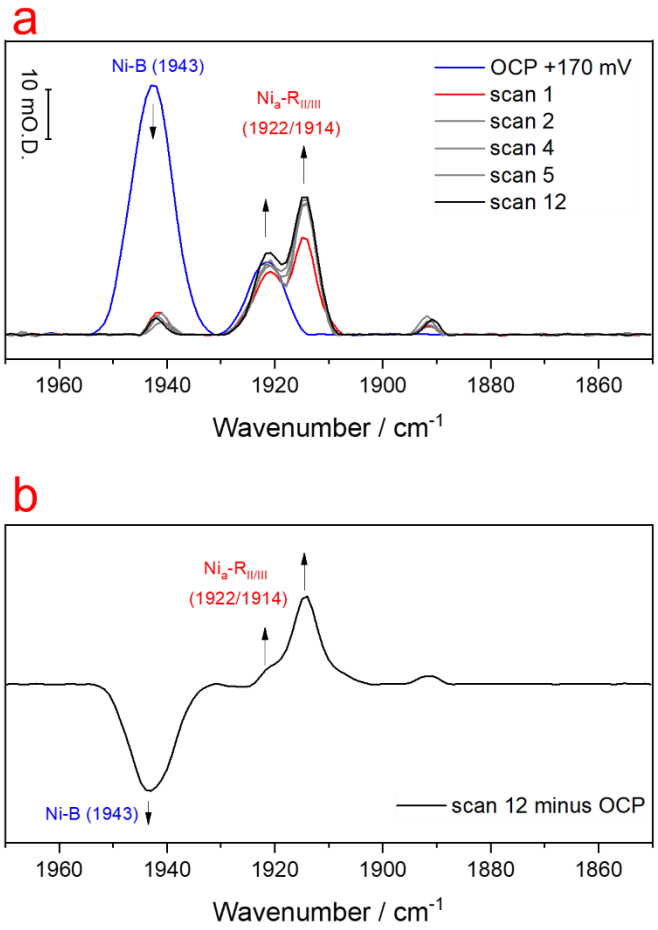

Figure 3.9: (a) The consecutive IR spectra of the Hyd-1 single crystal during the first hour of reductive activation at -710 mV vs SHE. Each spectra takes roughly 5 min to record. (b) The difference spectrum of the Hyd-1 single crystal obtained by spectrum at OCP (+170 mV) minus after one-hour reductive activation at -710 mV.

The spectrum of the reduced crystal (after 1 hour reduction, Figure 3.7 bottom panel) shows two intense bands, 1921 and 1914 cm^{-1} in the ν_{CO} region, along with two weaker bands at 1941 and 1892 cm^{-1}. This suggests that the crystal contains a large portion of active site at the Ni$_a$-R level. The two bands are both assigned to Ni$_a$-R substates as this state is proposed to have multiple protonation sites at different distances to the active site (Ni$_a$-R$_{II}$ and Ni$_a$-R$_{III}$). Detailed assignment of bands to active site states are covered in the next section. Notably, in the spectrum of the reductive activated sample, a band at 1941 cm^{-1} was observed alongside the well-characterised bands associated with Ni$_a$-R (1921 and 1914 cm^{-1}). The position of this band (Figure 3.2) implies this unknown active site state has two

possibilities. In Figure 3.7 top panel, three CN^- bands evident in the spectrum recorded at OCP were discussed, which suggests the existence of two inactive states, possibly Ni-A and Ni-B states. One hour of reduction at -710 mV vs SHE of the Hyd-1 crystal, may be sufficient to reductively activate the ready state, Ni-B, but insufficient to activate Ni-A, consistent with what was observed in other [NiFe]-hydrogenases in solution.[34,35] Alternatively, the band position 1941 cm^{-1} is approximately 10 cm^{-1} lower than that of Ni_a-C, and hence lies in the region of Ni_a-R_I. Although related studies on Hyd-1 have not reported the presence of Ni_a-R_I at any condition,[19,24,26] but this state is common to appear at low redox level in other hydrogenases, such as *DvMF*.[4]

More investigation of the 1941 cm^{-1} band was accomplished via monitoring the single crystal IR spectrum under reductive potential (-710 mV) as a function of time. Figure 3.10A shows the IR spectrum of the Hyd-1 single crystal under a reductive potential (-710 mV) with respect to the time, showing the ν_{CO} region, and its chronoamperometry traces is shown in Figure 3.8.

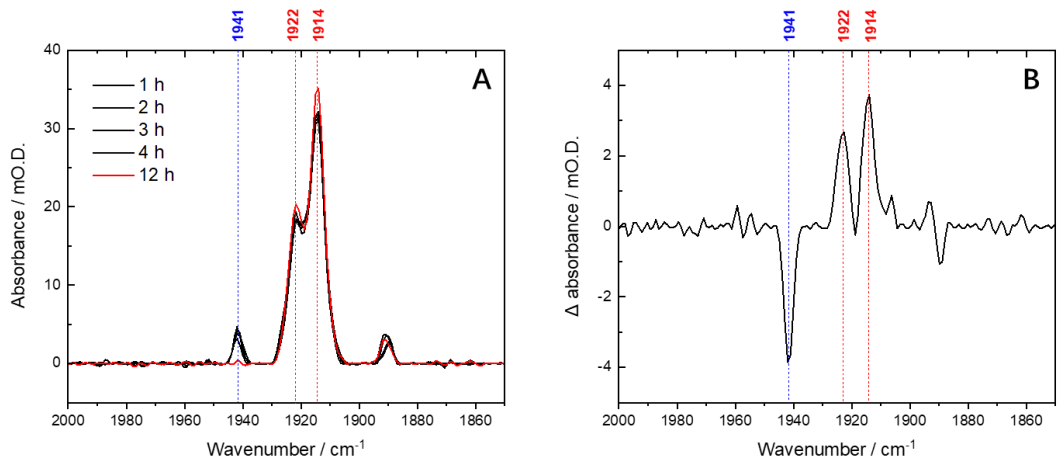

Figure 3.10: A) Spectra of the same Hyd-1 single crystal recorded under reductive potential (-710 mV vs SHE) after different length of poising. B) Difference spectrum calculated from the spectrum after 12-hour reductive activation minus the spectrum after 1-hour.

In the first 4 hours of reduction, each spectrum overlays well, and the 1941 cm^{-1} band persists at the same intensity. Changes were observed after 12 hours of reduction, Figure 3.10A (red spectrum), the spectrum shows no significant absorption around 1941 cm^{-1}, but increased intensity of 1922 and 1914

cm^{-1}. A minor change is also observed at the band at 1892 cm^{-1}, which it shifts to higher wavenumber. The changes are highlighted in the difference spectrum shown in Figure 3.10B, which illustrates the correlation between the loss of the 1941 cm^{-1} band and growth of the 1914/1922 cm^{-1} bands at this long timepoint. The direct conversion from 1941 to 1922 and 1914 cm^{-1} bands reveals two features of the mystery band, 1941 cm^{-1}. First, the band position is in the ν_{CO} region, and it represents an intact active site species involved in the equilibrium between known states, not any residual signal from degraded protein. Second, this state requires long reductive activation to convert to Ni_a-$R_{II/III}$ states (1922 and 1914 cm^{-1} as discussed above). Therefore, it suggests that the 1941 cm^{-1} band is likely to be an unready state like Ni-A or Ni-SU which undergo slow activation, which could be consistent with the 3 CN^- bands observed at OCP in Figure 3.7.

3.2.3 Potential Titration on Hyd-1 Single Crystal, pH 6

The fine potential control provided by the microscopic spectroelectrochemical cell with redox mediator cocktail allows accessing all catalytically relevant intermediate states of Hyd-1 within the crystal. The redox dependence of common states is summarised in scheme 3.1 and more detailed states involved in the catalytic cycle including Ni-SI_r and Ni-A states are shown in Figure 3.1.

After full reductive activation of the Hyd-1 protein crystal by applying constant low potential for 12 h until no Ni-B/Ni-A are present, stepped oxidising potentials were applied to the microsSEC cell to electrochemically manipulate the crystal (oxidative redox potential titration). The size of the oxidative potential jumps (25, 50 and 100 mV) was chosen according to the previous reported Hyd-1 potential-dependence in solution and electrode-immobilised states.[33,36] Fine potential steps (25 mV) were applied at potential windows where equilibrium between states take place. To determine the crystal had fully equilibrated to the applied potential, the potential was held until no further changes to IR spectra were observed (at least three consecutive spectra). For example, the consecutive IR spectra of

the single crystal at +60 mV (stepped from +10 mV) are shown in Figure 3.11, the first spectra after potential jump (light grey) changes dramatically from the last spectrum recorded at +10 mV (red spectrum), and become nearly identical after the fourth spectra. This method is applied in every potential step during the both Hyd-1 and Hyd-2 titration. The final spectrum recorded at each potential step are used in the analysis of the redox titration.

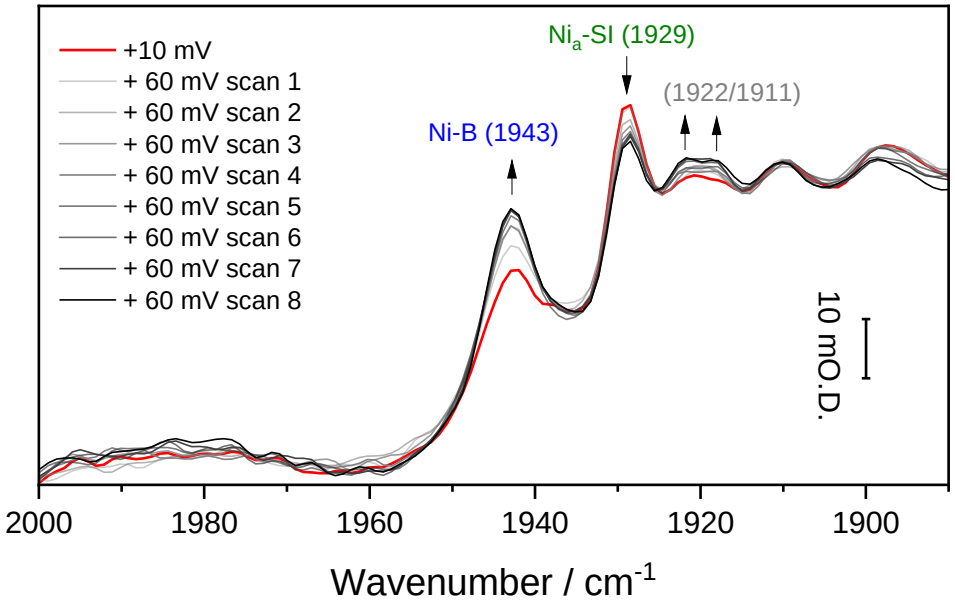

Figure 3.11: The consecutive IR spectra of the Hyd-1 single crystal after the potential shifting from +10 mV to + 60 mV. The red spectrum is the final recorded spectrum at +10 mV.

The chronoamperogram of the oxidative titration is shown in Figure 3.12 that shows the chemical equilibrium was reached at each potential steps. In general 'spectroscopic equilibrium' coincided with net zero current at most applied potentials. However, at potentials more negative than -310 mV, a small residual current (<|20 nA|) was observed. This small residual current is less than 0.5% of the peak current observed during voltammograms of the mediator cocktail in the microSEC cell (Figure 3.6), and small residual currents are expected in thin-layer spectroscopic-electrochemical cells.[26]

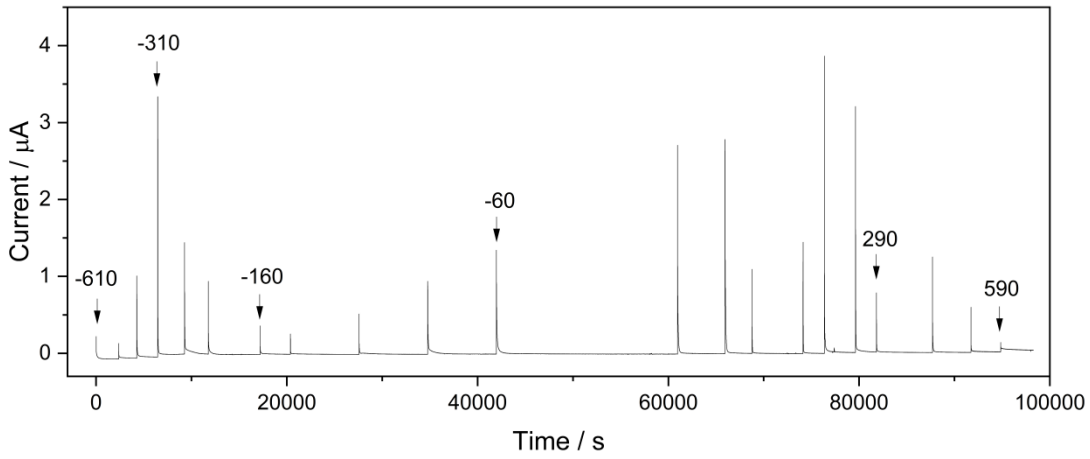

Figure 3.12: Chronoamperometry traces recorded during the oxidative titration of Hyd-1 single crystal, pH 6 in the microSEC cell. The marker indicates the potential was applied. The potential steps between -610 to -310 mV; -310 to -160 mV; -160 to -60 mV; -60 to 290 mV and 290 to 590 mV are 100; 50; 25; 50 and 100 mV.

Figure 3.13 shows a series of spectra for a single Hyd-1 crystal in the micro-SEC cell recorded as a function of applied potential at pH 6, where panel A contains baseline corrected IR spectra at selected potentials with marked spectroscopic changes, in stacked format, and panel B includes spectra in smaller potential steps. The changes in the Hyd-1 active site speciation during the oxidative redox titration can be seen from the potential-dependent shift of IR bands in the ν_{CO} region. Figure 3.13A shows that all the known catalytic states are accessed through the oxidative potential titration. The general potential-dependence of the active site states agreed well with Figure 3.1.

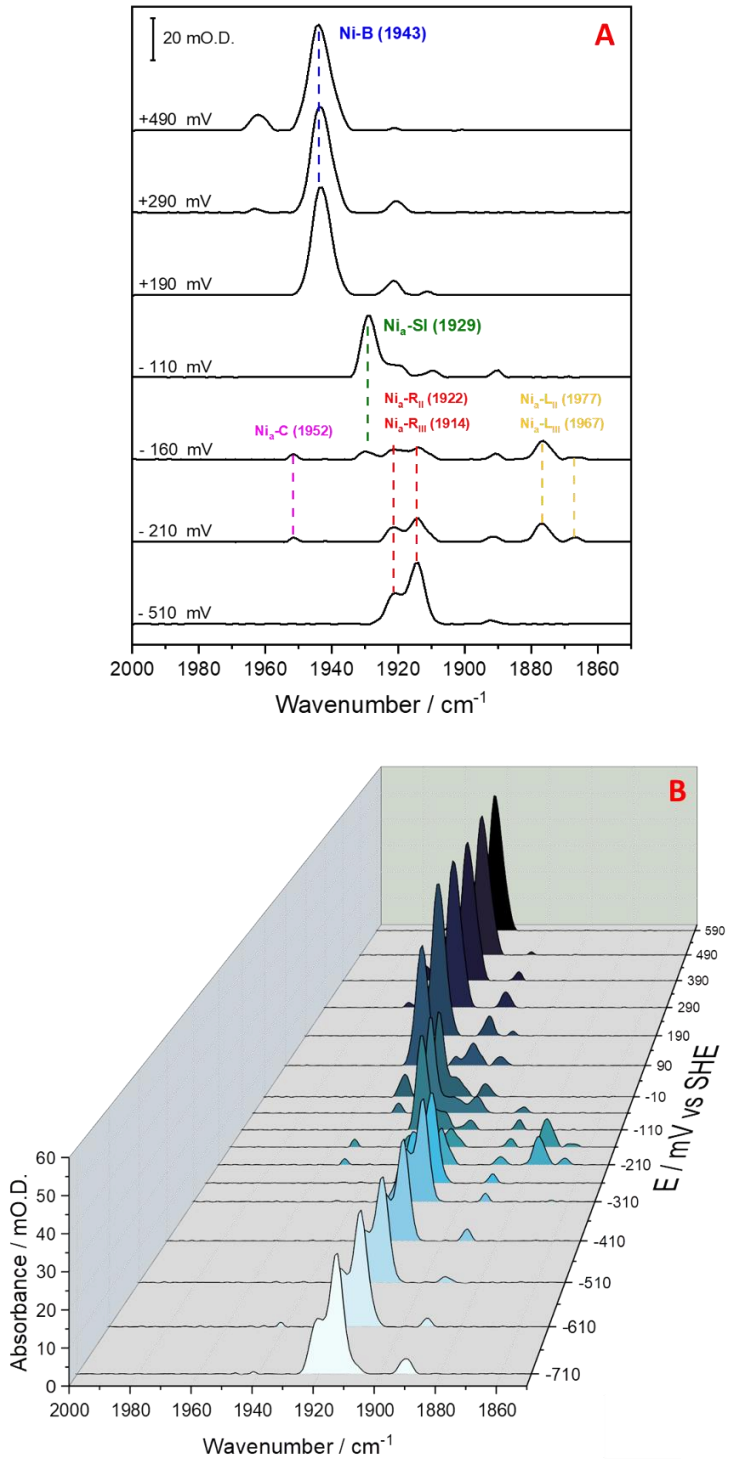

Figure 3.13: The ν_{CO} region of the spectra measured during the oxidative redox titration of a single crystal of Hyd-1 at pH 6. Each spectrum was measured at 2 cm^{-1} resolution, 512 scans and baseline corrected. A) IR spectra in stacking format, showing accumulation of all catalytically relevant states across the measured potential range. B) Waterfall format plot containing IR spectra at smaller potential intervals during the oxidative titration.

The potential dependence of the active site states

In Figure 3.13, at low potential, from -710 mV to -250 mV, the Hyd-1 crystal is mainly dominated by states with ν_{CO} bands at 1922 and 1914 cm^{-1}. The band position of 1922 and 1914 cm^{-1} are assigned to be two Ni_a-R states because they dominate the speciation of the Hyd-1 crystal at the lowest redox potential range and they are consistent with other studies on native *E. coli* Hyd-1 (heterodimer with transmembrane helix and cytochrome b) in different states (Table 3.1).[33] The bands at 1922 and 1914 cm^{-1} are 30 and 38 wavenumbers lower than the reported Ni_a-C respectively and agree well with the general relative band position for Ni_a-R_{II} and Ni_a-R_{III} assigned for other [NiFe]-hydrogenases (Figure 3.2). Both bands are assigned to the Ni_a-R state have been discussed earlier, and are thought to be different protonation of states at the same redox level of the active site. It is worth to note that only Ni_a-R states are present at low potential down to -710 mV. The fact that only the Ni_a-R state(s) is observed at this reducing potential reflects the fact that no appreciable H^+ reduction is catalysed by Hyd-1 at this redox level at pH 6, even under an inert atmosphere. The non-turn-over behaviour of Hyd-1 under these conditions agrees with results from PFE experiments.[37]

When the potential of the WE is stepped up to -210 mV vs SHE, the speciation of the Hyd-1 crystal is dramatically changed, Figure 3.13. The intensity of the Ni_a-R state signal (1922 and 1914 cm^{-1}) decreases while new absorption bands appear at 1952, 1877 and 1867 in the ν_{CO} region. The 1952 cm^{-1}band corresponds to the formation of less reduced Ni_a-C state from Ni_a-R. The band position of Ni_a-C is higher than Ni_a-R, suggesting a more electron-deficient active site which is consistent with Ni^{III} at the active site. At this redox level, the other two low wavenumber species started to appear together with Ni_a-C and they correspond to Ni_a-L states. The position of their ν_{CO} bands is consistent with those for Hyd-1 measured in an electrode-immobilised state and also comparable to those of another O_2-tolerant MBH, from *Aquifex aeolicus*, where the the Ni_a-L states were generated by photolysis Ni_a-C at cryo-temperature.[38] The low wavenumber position of them suggests a very electron-dense active site, which is consistent with the low oxidation state of Ni^{I} ion at the active site. Theoretically, Ni^{I} has much

larger ionic radius compare with Ni^{II} and Ni^{III}. Computational studies on Ni_a-L states suggest that the unusually low ν_{CO} wavenumber positions of them is a result of a metal-metal bond between Ni and Fe, significantly increasing the backbonding donation from Fe to CO.[28] The reason why Ni_a-L has multiple sub-states is proposed to be for a similar reason to that of Ni_a-R, due to different protonation sites with different distance to the active site.[24] Ash and co-workers proposed the absence of the Ni_a-L_I state in Hyd-1 is related to its unique proximal FeS cluster with high redox potential.[26] The hydrogenase active site undergoes several PCET processes to interconvert between different states (Figure 3.1). In studies of the Ni_a-SI to Ni_a-L transition in *P. furiosus* SH, Dyer and co-workers suggested there is a concerted proton and electron transfer to the active site[16], while Ash and co-workers argued for a stepwise, delayed electron transfer process in *E. coli* Hyd-1. The redox potentials of the proximal cluster of Hyd-1 are +3 and +230 mV vs SHE at pH 6 for the 4+/3+ and 5+/4+ couples respectively,[39] which are well-above the redox potential for transition of Ni_a-C to Ni_a-R (-159 mV vs SHE, at pH 6)[24]. This suggests the accumulation of the Ni_a-L_I state in the titration under reducing condition is a thermodynamic preference. When the proximal cluster is reduced, it favors the one base (that protonated amino acid in the Ni_a-L_I state) and perhaps when the cluster is oxidised another base is favored.

Stepping up potential from -210 mV to more oxidised level at -160 mV, the ν_{CO} bands associated to Ni_a-R state (1914 and 1922 cm^{-1}) diminished and a new ν_{CO} band at 1929 cm^{-1} started to form. This peak is attributed to the most oxidised catalytic active state, Ni_a-SI. As shown in Figure 3.13, in the spectrum recorded at -110 mV vs SHE, the distribution of the active site states of the enzyme crystal changed drastically. Accompanied by diminishing Ni_a-R states, the band intensity of Ni_a-L and Ni_a-C states decreased with oxidising potential steps. In contrast, as the redox level increases, the Ni_a-SI state becomes the predominant active site state at -110 mV. This spectral feature corresponds to the more oxidised active site, consistent with a Ni^{II} ion and vacant bridging coordination site.

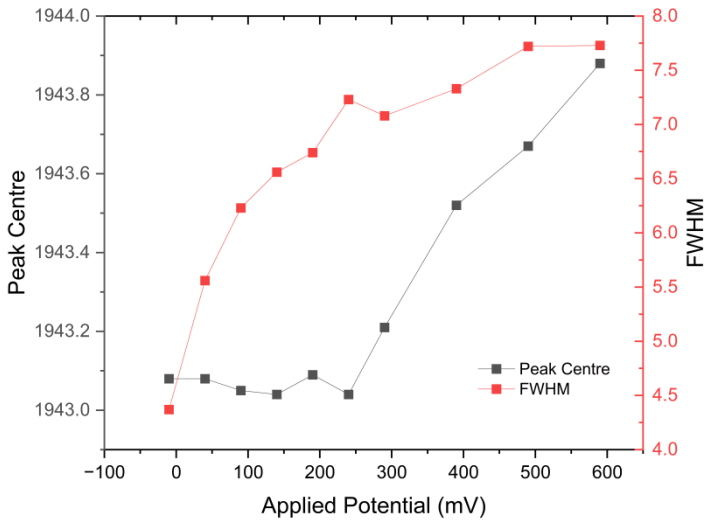

Figure 3.14: The relationship between peak centre, FWHM (full width at half maximum) and the applied potential of the Ni-B peak in the ν_{CO} region.

Subsequent poising of the Hyd-1 crystal at more oxidised potentials reveals how the catalytic active state Ni_a-SI is converted into the inactive, ready state, Ni-B. In Figure 3.13B, spectra recorded at potentials more positive than -10 mV all show a strong absorption band at 1943 cm^{-1} which is assigned to Ni-B, the most oxidised active site state. Oxidising the single crystal beyond physiologically-relevant level (up to +590 mV) shows no significant change in speciation of the sample. The IR spectra show that most of the active site remains at Ni-B (shift from 1943 to 1944 cm^{-1}), but its ν_{CO} absorption band gets broader as the poised potential becomes more positive. Figure 3.14 shows the relationship between peak centre, FWHM (full width at half maximum) and the applied potential of the Ni-B band in the ν_{CO} region. The peak centre started to increase at +240 mV, which just above the $[4Fe3S]^{5+/4+}$ reduction potential of the proximal cluster (ca. 211 mV, Table 1.1). In addition to that, the band is continuously getting broader even at potential far higher than the Ni_a-SI/Ni-B (ca. 0 mV, Figure 3.4). This suggests a sub-species related to Ni-B which is generated at particularly positive potentials, presumably related to different redox conformations of the proximal cluster which induce slight shifts in the Ni-B band through a long-range effect. The different conformations of proximal cluster under

high oxidising potentials are shown in Chapter 5.

There are some unknown bands observed during the oxidative titration at different redox level. They are interpreted in the next section.

3.2.4 Unknown Peak in the Titration

Unknown peak at 1892 cm^{-1} from -710 to -110 mV

During the oxidative titration, the ν_{CO} region of the spectra contains a band at 1892 cm^{-1} from the most negative redox level applied -710 mV, up to -60 mV vs SHE, and it is potential-dependent, disappearing at -10 mV (Figure 3.13 bottom). The spectrum of the Hyd-1 crystal poised at -510 mV during the titration shows the presence of this band (grey shaded) and it is shown in Figure 3.15. It is not clear whether the state associated with the 1892 cm^{-1} band converts to either Ni-B or Ni_a-SI upon oxidation, but the fact that it interconverts with potential into known states of the active site implies that it is not just damaged protein. Time-resolved IR spectroscopy could be employed later to study the interconversion of this state to the others.

The relative band position is 60 cm^{-1} lower than that of Ni_a-C and its occurrence with respect to potential (from the most reduced redox level to approximately the Ni_a-SI redox level suggests that this low wavenumber species might correspond to one of the Ni_a-L states. However, extensive SEC studies on *E. coli* Hyd-1 have reported the wavenumber positions of Ni_a-L_{II} and Ni_a-L_{III} as 1877 and 1867 cm^{-1}, as observed in titrations while the relative wavenumber position of Ni_a-L_I is generally about 50 wavenumbers lower than Ni_a-C with small variance among the [NiFe] hydrogenases family. Further investigations combining comprehensive biophysical techniques are required to interpret this band. A reasonable interpretation of this unknown band could possibly be due to a proton transfer intermediate between Ni_a-L_I and Ni_a-L_{II}. In the equilibrium of Ni_a-C to Ni_a-L, the hydride leaves the bridging position as a proton, consecutively transferred out from the active site by nearby bases. The

accumulation of Ni_a-L_{II} and Ni_a-L_{III} reported in Hyd-1 implies the proton transfer from the first base to the second one is not the rate determining step.

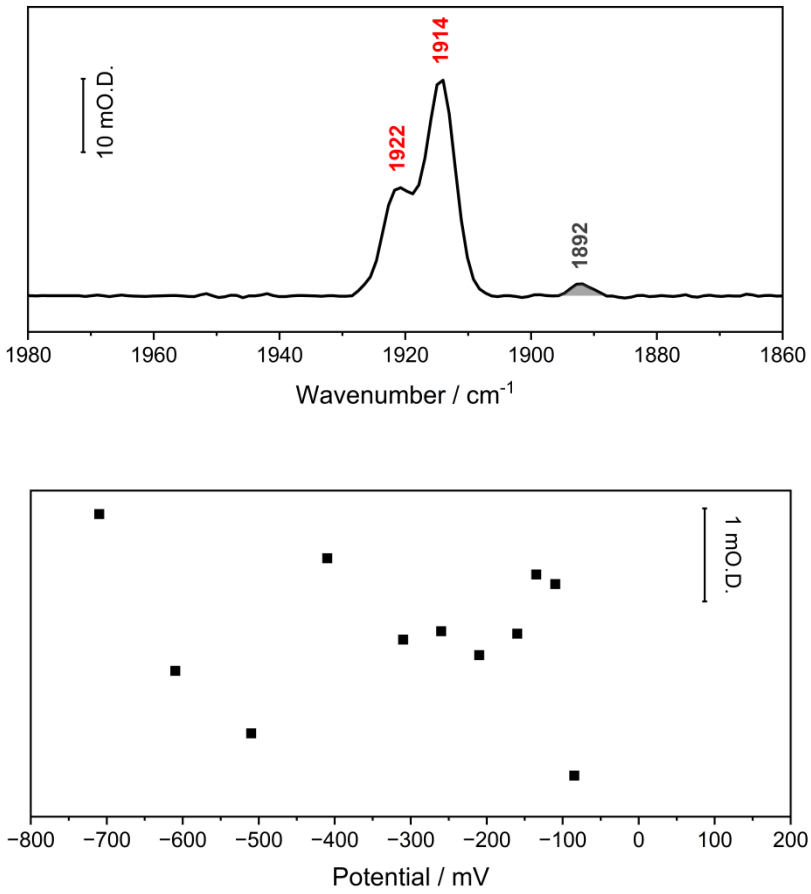

Figure 3.15: Top) IR spectrum of the Hyd-1 crystal at -510 mV during the electrochemically titration, showing in ν_{CO} region. Assigned bands from the Ni_a-R state (1914 and 1922 cm^{-1}) are labelled, with an unidentified band at 1892 cm^{-1} shaded in grey. Data acquired at 2 cm^{-1} resolution with 512 scans, and baseline-corrected. Bottom) The titration curve of the band at 1892 cm^{-1}.

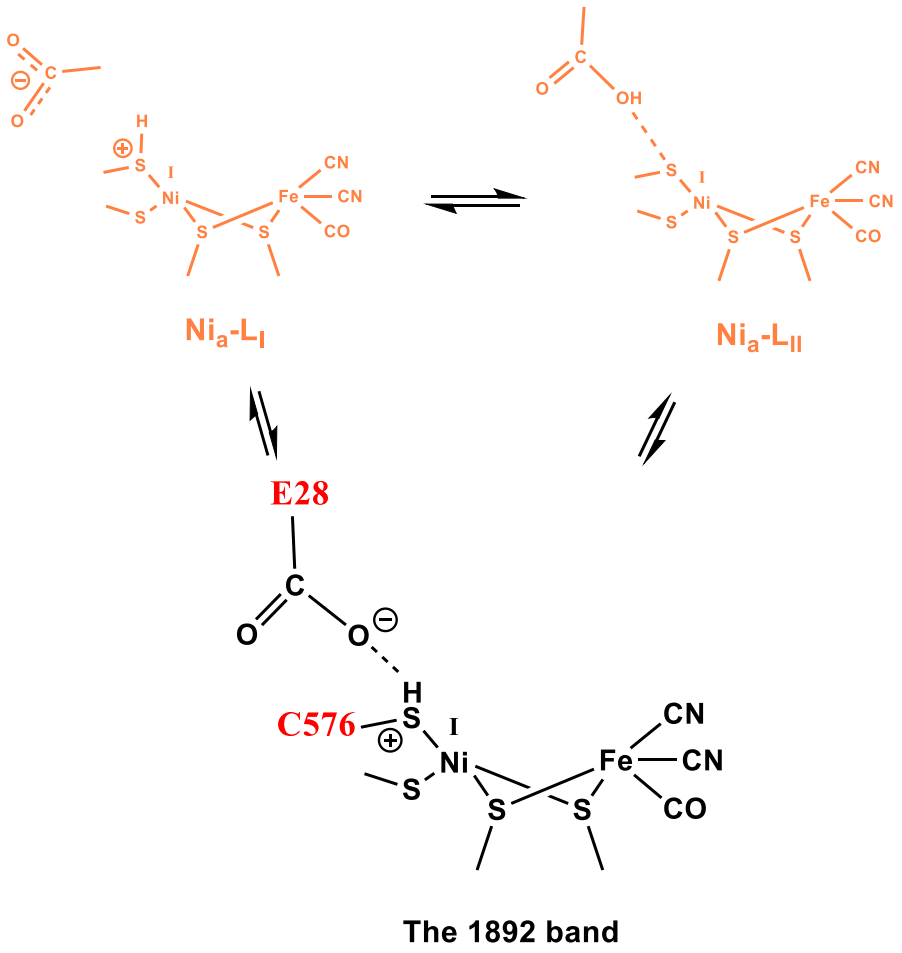

Figure 3.16: The proposed active site structure associated with the unknown band at 1892 cm^{-1}. The carboxylic group of E28 forms a H-bond to the protonated C576. Theoretical Ni$_a$-L$_I$ is assumed to have a protonated C576 residue without forming the H-bond with E28, and Ni$_a$-L$_{II}$ is proposed to have the protonated E28 forming H-bond with C576.

Although one of the biggest puzzles of [NiFe]-hydrogenases is the proton transfer mechanism, it would not be surprising that the first and second proton acceptor could have a H-bond allowing fast transfer. In the crystalline state, the 1892 cm^{-1} band might correspond to a stablised conformation during the proton transfer process which a H-bond forms between the first and second proton acceptor. A glutamate residue next to the bimetallic active, E13 in *A. aeolicus* and E28 in *E. coli* Hyd-1, has been proposed to have two conformations which might be critical to the proton pathway of the enzyme.[40] If the hypothesis is correct, then the 1892 cm^{-1} band could be reasonably associated with one conformation of this glutamate residue which is in phase with the first proton accepter, likely thiolate

ligand to the Ni ion at the active site (Figure 3.16). This could also explain why the band position is between Ni_a-L_{II} and theoretical Ni_a-L_I, with the proposed Ni_a-L_{II} reflecting the same conformation of this glutamate residue, but protonated, as illustrated in Figure 3.16, though the real conformation of either Ni_a-L_I or Ni_a-L_{II} are not resolved. The accumulation of this band, might attributed to the special proximal cluster which stabilises this conformation and differ from other hydrogenases such as Hyd-2. However, this band persists even at low potential (-710 mV), such redox condition that normally Ni_a-L states do not populate.

Nevertheless, this hypothesis needs to be validated via cryogenic IR spectroscopy or time-resolved Ni_a-C to Ni_a-L photolysis, as well as extensive X-ray crystallography and kinetic studies. These methods could provide how this this hypothetical state is inter-converted with other known states and potentially trap and enrich this state to obtain its crystal structure.

Unknown band at 1921 and 1911 cm^{-1} from -110 to +190 mV

Interestingly, there are two additional bands at lower wavenumber position (1921 and 1911 cm^{-1}) which accompany the Ni-B and Ni_a-SI band at different potential (Figure 3.13). Both active site species are potential dependent and start to form together with Ni_a-SI, suggesting those two states are at a similar redox level to Ni_a-SI. However, the 1921 cm^{-1} band here is very hard to monitor by just looking at the low to mild reductive potential range as it is coincident with the band assigned to Ni_a-R_{II} at lower potential (1922 cm^{-1}). As potential is stepped more positive, the Ni_a-R in general diminishes and Ni_a-SI starts forming. Thus the 1921 cm^{-1} can be arguably interpreted as residual Ni_a-R_{II} that persists at -110 mV VS SHE. However, in Figure 3.17 bottom, it is clear that the 1921 cm^{-1} band perseveres in the spectra from the Ni_a-SI redox level until further oxidising potential (+490 mV). Moreover, the spectrum of the aerobic, as-isolated Hyd-1 crystal recorded before the reductive activation shown in Figure 3.7 also shows the absorption band at around 1922 cm^{-1} in the ν_{CO} region. The wavenumber position associated with this band is shifted by about 1 cm^{-1} to higher wavenumber, from 1921 to 1922 cm^{-1},

and this is likely due to a long-range effect from the oxidation of the proximal FeS cluster. Therefore, the occurrence of this band even at oxidising potentials suggests that 1921 cm^{-1} band is likely a distinct active site species from Ni_a-R_{II} state. Figure 3.17 shows the spectrum of the Hyd-1 crystal poised at +190 mV during the titration. At this potential, the unknown bands at 1911 and 1921 cm-1 are presented with the well-known Ni-B peak at 1943 cm^{-1} in the ν_{CO} region.

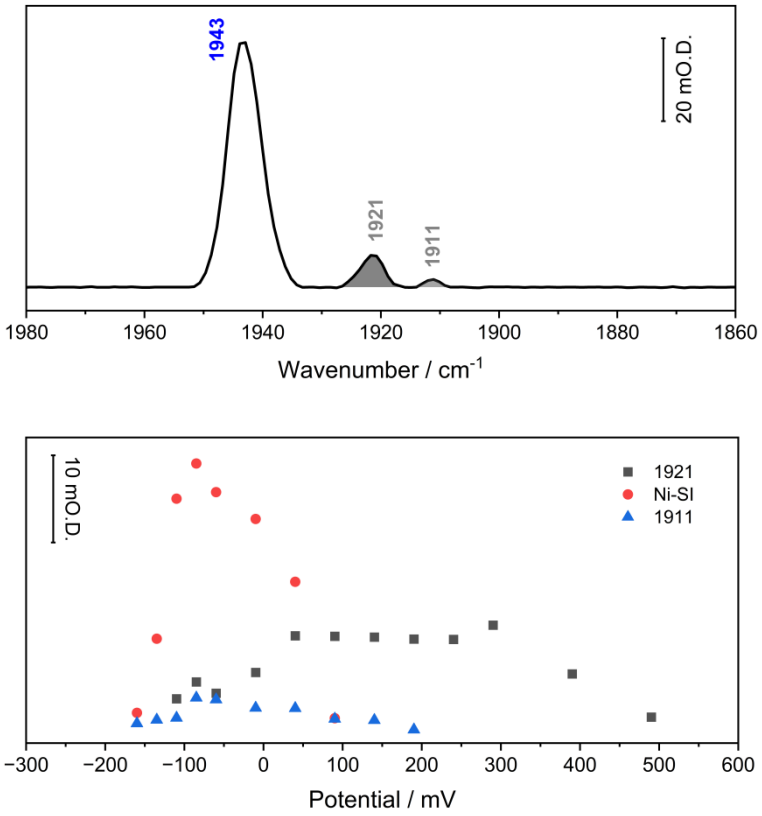

Figure 3.17: Top) IR spectrum of the Hyd-1 crystal at +190 mV during the electrochemically titration, showing in ν_{CO} region. Assigned bands from the Ni-B state (1943 cm^{-1}) are labelled, with an unidentified band at 1911 and 1921 cm^{-1} shaded in grey. Data acquired at 2 cm^{-1} resolution with 512 scans, and baseline-corrected. Bottom) The titration curves of the band at 1921, 1911 cm^{-1} and the band for Ni_a-SI (1929 cm^{-1}).

The other lower wavenumber species, at 1911 cm^{-1}, very likely corresponds to one of the Ni-SI_r states. Many other spectroelectrochemical studies on [NiFe]-hydrogenase reported a band which co-exists with Ni_a-SI with relative wavenumber about -20 cm^{-1} lower than the band of Ni_a-SI (60 cm^{-1} lower than Ni_a-C)[9,12,18] and it was assigned to be an intermediate between Ni-B and Ni_a-SI, the Ni-SI_r state, Figure

3.1. This state has also been studied by EPR spectroscopy, confirming the presence of an EPR-silent Ni^{II} active site. In Figure 3.17 bottom panel, its potential dependence is shown with that of the Ni_a-SI state. This active site species starts to form together with the Ni_a-SI state at -160 mV, but perseveres longer at more oxidising conditions, until +190 mV.

The mechanism of Ni-B and Ni_a-SI interconversion includes a PCET and water association / dissociation. Many studies revealed fast activation from Ni-B to Ni_a-SI, therefore suggesting concerted PCET and fast water transportation in the active site pocket. The increased thermodynamic stability of these states compared with under other conditions could plausibly attributed to the proximal cluster. Based on previous experimental and theoretical studies on the Ni-B to Ni_a-SI transition,[27,41,42] the possible intermediates of the Ni-B to Ni_a-SI via stepwise PCET and H^+ transfer are shown in Scheme 3.2.

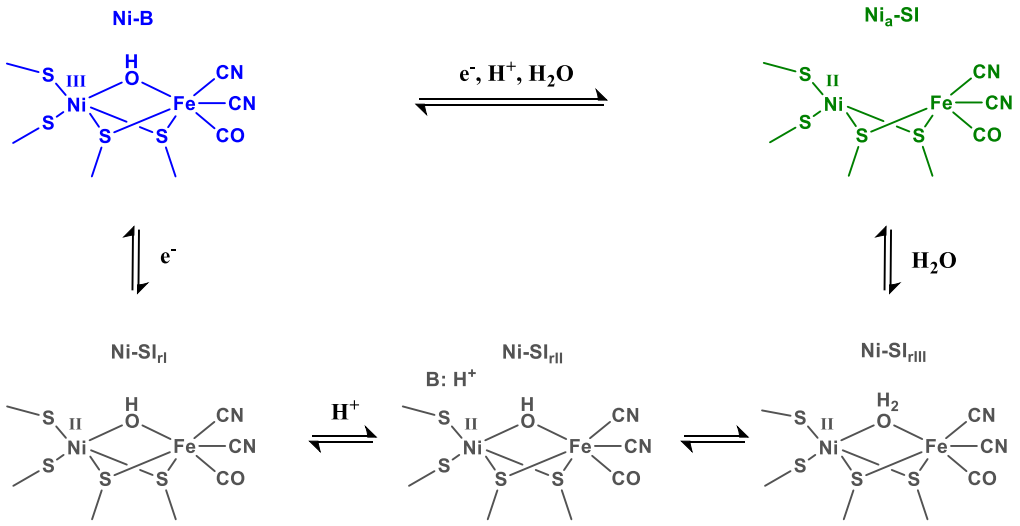

Scheme 3.2: The proposed concerted and stepwise mechanism of Ni-B and Ni_a-SI interconversion. Three possible substates of Ni-$SI_{r(I,II,III)}$ are proposed to have the same redox level to Ni_a-SI.

Three intermediates named Ni-$SI_{r(I,II,III)}$ which have same Ni(II) active site with different protonation positions are proposed between Ni-B and Ni_a-SI, based on previous studies on Ni-SI_r state.[3,43] One electron reduction of the Ni^{III} at the active site in Ni-B produces a more reduced Ni-SI_{rI} state. Then the Ni-SI_{rI} state gets protonated to form Ni-SI_{rII} or Ni-SI_{rIII} depending on the position of the proton as shown in Scheme 3.2. Finally, the protonated hydroxy ligand, water, leaves the active site pocket through the

water tunnel, yielding the Ni_a-SI state with an empty bridging site. All the Ni-SI_r states carry a Ni^{II} ion at the active site and are at the same redox level.

The order of the stepwise PCET is clearly shown in the scheme. When the active site in the Ni-B state is reduced to the Ni_a-SI redox level, the electron transfer process is fast electron transfer from the reduced proximal FeS cluster to the active site Ni ion, yielding one-electron reduction of the active site. The active site in this state should be more electron rich than Ni-B due to Ni^{II}, and also more electron rich than Ni_a-SI due to bridging hydroxy ligand. This agrees with the IR spectroscopy, that bands assigned as Ni-SI_r have lower wavenumber than Ni-B and Ni_a-SI. The stepwise mechanism of Ni-B to Ni_a-SI therefore starts with one electron reduction followed by protonation. In the case of oxidation of Ni_a-SI to Ni-B, the water molecule binds to the active site and is then deprotonated, and this should happen prior to one electron oxidation on Ni at the active site, because the σ-basic hydroxy ligand can stabilize the Ni^{III}.

In the oxidative titration at -110 mV, it is not surprising that the spectrum in the ν_{CO} region contains bands corresponding to Ni_a-SI together with Ni-SI_r related states, because they are at the same redox level. In the ν_{CO} region, apart from the band of Ni_a-SI (1929 cm^{-1}), thus, bands at 1921 and 1911 are assigned to be two of the Ni-SI_r related states. The 1911 cm^{-1} band at Ni_a-SI redox level in the titration possibly corresponds to the Ni-SI_{rI} state as shown in Scheme 3.2. The band position, 1911 cm^{-1} appears to be the lowest among the three distinct active site species, indicating the state associated with it must carry the most electron density at the active site, consistent with the deprotonated Ni-SI_{rI}. Moreover, in other hydrogenases, the population of Ni-SI_{rI} increases, relative to that of Ni_a-SI, with pH, suggesting it is a deprotonated form.[5,9,43,44] On the other hand, the state with a band at 1922 cm^{-1} must consist of a more electron-deficient active site than that at 1911 cm^{-1}, which implies it contains a protonated active site according to Scheme 3.2. However, the position of the proton is hard to identify just from the IR spectra, so the 1922 cm^{-1} band should correspond to either Ni-SI_{rII} or Ni-SI_{rIII}. Those two Ni-SI_r related states have different potential dependence at higher potentials. In the titration,

Figure 3.13 and Figure 3.17 bottom panel, the Ni-SI_{rI} state (1911 cm^{-1}) disappears slightly after the Ni_a-SI state at around +200 mV vs SHE, while the Ni-SI_{rII} or Ni-SI_{rIII} state (1922 cm^{-1}) persists until extremely high potential around +500 mV (shifted to 1921 cm^{-1}). This might indicate the bottleneck of Ni_a-SI to Ni-B conversion is removing the electron out of the active site in the crystalline state. In chapter 5, these bands are interpreted from both IR spectroscopic and crystallographic data.

Unknown band at 1962 cm^{-1} from +290 to 590 mV

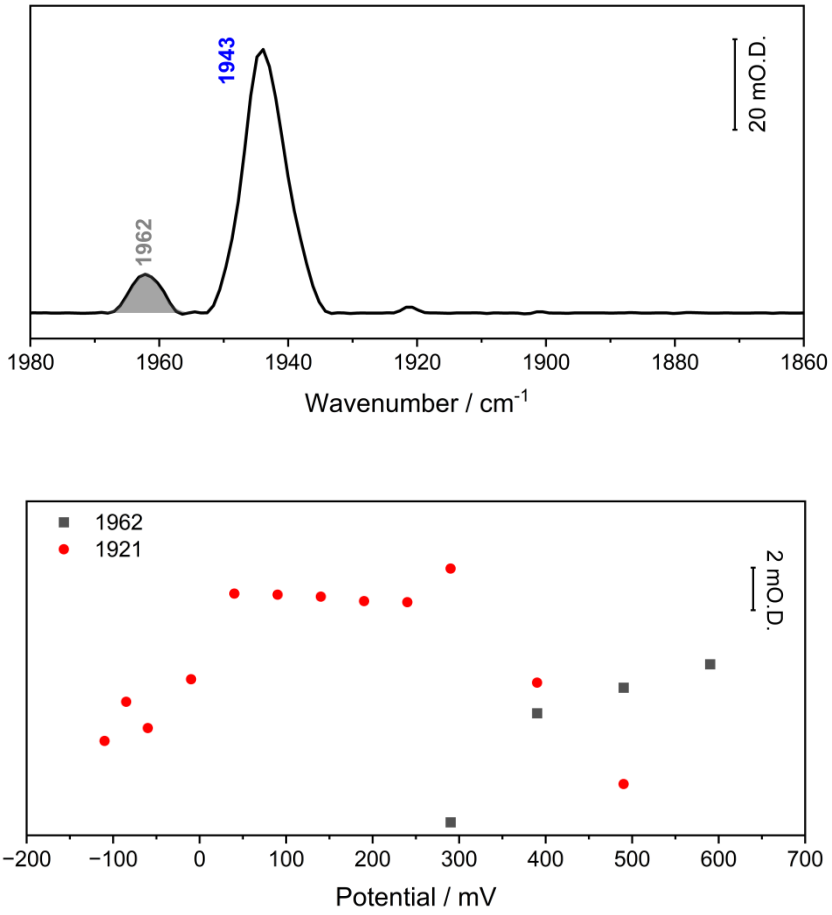

Figure 3.18: Top) IR spectrum of the Hyd-1 crystal at +490 mV during the electrochemically titration, showing in ν_{CO} region. Assigned bands from the Ni-B state (1943 cm^{-1}) are labelled, with an unidentified band at 1962 cm^{-1} shaded in grey. Data acquired at 2 cm^{-1} resolution with 512 scans, and baseline-corrected. Bottom) The titration curves of the band at 1921 and 1962 cm^{-1}.

When the crystal was poised at a more strongly oxidising potential at 290 mV, a high wavenumber band at 1962 cm^{-1} appears (Figure 3.18). As the applied potential increases, the intensity of the band

increases with concomitant decreasing band intensity at 1921 cm^{-1}, while the major band at 1943 cm^{-1} (Ni-B) remains unchanged as shown in Figure 3.18 bottom. We are not aware of any studies that have reported any other ν_{CO} for [NiFe]-hydrogenases with Ni_a-C prepared under high potential. The few high wavenumber species observed in spectra are usually attributed to Ni-A like species with sulfoxygenation at the active site.[17] A similar relative band in [NiFe]-hydrogenase from *DvMF* was found after irradiating a sample in the Ni-A state, so was assigned to the photoproduct of Ni-A and proposed to have dioxygen bound only to Ni^{III}.[45] However, the 1962 cm^{-1} band in the titration was electrochemically generated and it is reversible upon reduction electrochemically on a short time scale (there is a discussion in the next section about the reversibility of spectral changes in a Hyd-1 single crystal). The anaerobic condition in the SEC cell suggests that this high wavenumber species is in equilibrium with either Ni-B (1943 cm^{-1}) or Ni-$SI_{rII/III}$ (1921 cm^{-1}) either electronically or chemically or both. A plausible guess is this band is attributed to the Ni-B state with a long-range effect from proximal cluster which have conformational changes (see crystal structures in Chapter 5), since the signal appears above the $[4Fe3S]^{5+/4+}$ reduction potential of the proximal cluster (211 mV, Table 1.1).

3.2.5 The Reversibility of the Titration on the Hyd-1 Single Crystal

The oxidative titration ends at +590 mV VS SHE, and the IR spectrum for the ν_{CO} and ν_{CN} regions of the Hyd-1 crystal after equilibration are shown in Figure 3.19, top panel. In the ν_{CO} region, there is a strong absorption at 1943 cm^{-1}, assigned as Ni-B and an additional band at 1962 cm^{-1}, which may correlate with a protonated Ni-B as discussed earlier. In the ν_{CN} region, the spectrum shows two Ni-B cyanide bands at 2100 and 2082 cm^{-1}, while the small shoulder band at 2087 cm^{-1} might be associated with the 1962 cm^{-1} species. The electrochemically oxidised spectrum of the Hyd-1 single crystal after being fully activated, is different to the spectrum of the as-isolated state at OCP as shown in Figure 3.7.

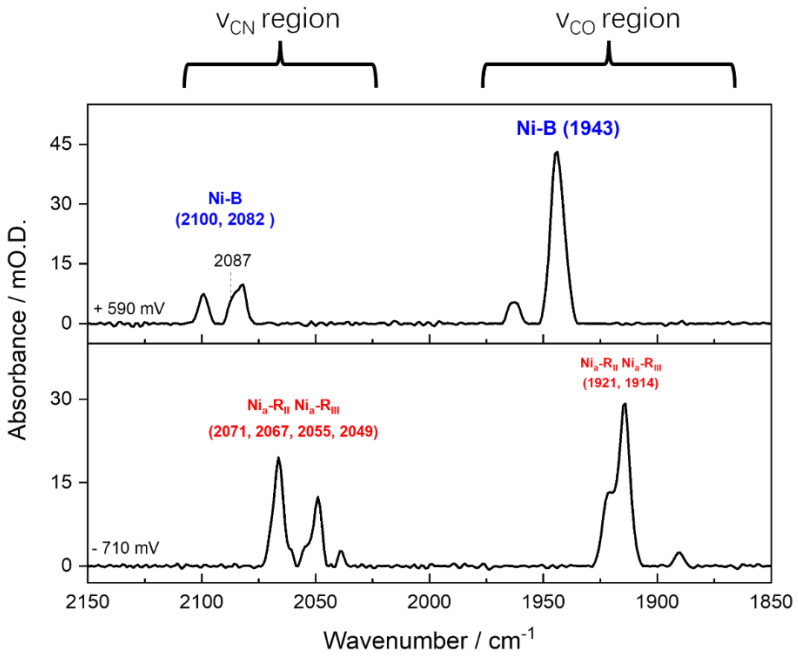

Figure 3.19: The baseline-corrected IR spectra of the Hyd-1 single crystal in the microSEC cell after the oxidative titration showing both ν_{CO} and ν_{CN} regions. Each spectrum was measured at 2 cm^{-1} resolution, 512 scans. (A) The spectrum of the Hyd-1 single crystal at the end of the oxidative titration poised at +590 mV. (B) The spectrum of the same crystal recorded after poising at -710 mV again for 5 min, showing complete reduction of sample.

In Figure 3.7, the spectrum of the as-isolated Hyd-1 crystal includes three unusual bands at ν_{CN} (2082, 2095 and 2100 cm^{-1}) and they are assigned to associate with the 1943 cm^{-1} band in ν_{CO}, suggesting the presence of multiple inactive states, such as the Ni-A and Ni-B states. In Figure 3.19 top panel, after the complete reductive activation and stepping back to a high oxidising potential of +590 mV, the band at 2095 cm^{-1} is no longer present in spectra with the well-characterised Ni-B (1943 cm^{-1}). This demonstrates the active site after electrochemical oxidation is dominated by the catalytically ready state, Ni-B, and the band at 2095 cm^{-1} might plausibly associated to another inactive state that does not reform upon electrochemical oxidation (likely Ni-A). This also address a common issue in [NiFe]-hydrogenase study: wherein the 'as-isolated' sample or 'air-oxidised' samples are often studied to explore the inactive states. However, what has been demonstrated in this thesis is that the anaerobic electrochemical oxidised enzyme has much greater purity in active site states.

Switching the potential from +590 mV to -710 mV produces a fully reduced Hyd-1 single crystal in 10 min. The spectrum in Figure 3.19 bottom panel shows the spectrum measured after 5 minutes after the cell potential was switched to -710 mV and the spectrum takes roughly 5 minutes to measure. The spectrum in Figure 3.19 bottom is essentially identical to the spectrum in Figure 3.7 bottom panel, recorded before the oxidative titration. They share the same speciation of the active site and the absolute intensity. The IR spectra at different time point (each spectra takes roughly 5 min to record) after the potential shifting from +590 mV to -710 mV is shown in Figure 3.20, showing do further change between spectra after the second scan.

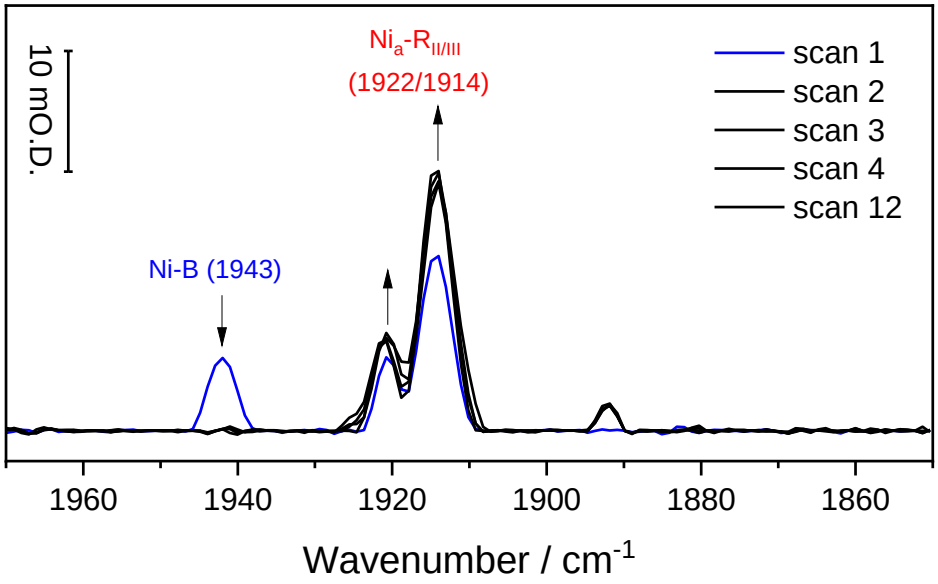

Figure 3.20: The consecutive IR spectra of the Hyd-1 single crystal after the potential shifting from +590 mV to -710 mV, showing do further change on the active site state distribution after the second scan.

The absolute reversibility on a short time scale provides extra evidence to support three conclusions. First, the state associated with the band at 1962 cm^{-1} is not an oxidatively-damaged species. It has fast equilibrium with other known active site states, perhaps Ni-B or Ni-SI$_{rII/III}$ and quickly gets reduced to Ni$_a$-R. This band, however is not observed in the as-isolated spectrum because it starts to form above +290 mV whilst the OCP of the as-isolated spectrum is +170 mV. Second, no unready state is formed

or left after full activation and oxidation to the super oxidised redox level. Third, no degradation or loss of signal is observed though the experiment, showing that the whole enzyme sample under the measurement conditions remains intact after the long experiment in the SEC cell for more than 24 hours.

The potential-dependent speciation plot

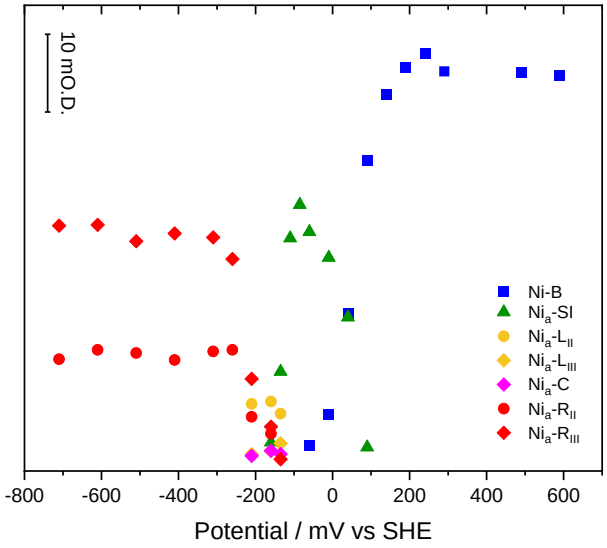

Figure 3.21: The speciation plot of the Hyd-1 single crystal at pH 6 showing how the population of each state varies with potential. Intensities were obtained by fitting each peak with a Gaussian profile.

In order to study the correlation between the hydrogenase active site speciation and applied potential, Figure 3.21 shows the potential-dependent speciation plot of Hyd-1 in the crystalline state. There are four redox levels that can be found in Hyd-1 according to its active site potential-dependent speciation. The Ni_a-R redox level covers the low potential range below -250 mV; the Ni_a-C and Ni_a-L redox level is approximately from -250 to -150 mV; above that is the Ni_a-SI redox level which covers -150 to 0 mV; the highest Ni-B redox level is from 0 mV and above.

From the speciation plot, it is clear to find out the exact potential where the single redox states

enriched crystal can be electrochemically generated. Therefore, the *in-situ* microscopic spectroelectrochemical redox titration could provide referential information of Hyd-1 single crystal speciation which makes it possible to manipulate the single crystal accordingly to generate a defined redox state for downstream structural determination. This is the key focus of this thesis. The conditions for isolating a "single state" Hyd-1 crystal at pH 6 are summarised in Table 3.2.

Table 3.2: The potential windows to target an isolated state of Hyd-1 single crystal at pH6.

Active site state	Redox potential / mV	pH
Ni-B	≥+200	6
Ni_a-SI	-75	6
Ni_a-R	≤-250	6

As described earlier in the chapter, the catalytic intermediates of hydrogenases interconvert though proton-coupled electron transfers. Therefore, apart from the electrode potential which is altered by a potentiostat, the acidity of the buffer solution is the other important condition to adjust the speciation of the active site states. However, many spectroelectrochemical studies on Hyd-1 showed changing pH will mainly change 3 things: 1) The equilibrium between Ni_a-C and Ni_a-L states; 2) IR band position shifting for the states; 3) the redox potentials of the redox transitions of the active site changing.[6,24,26] Changing acidity from pH 4 to pH 8.0 does not affect the overall pattern of the Hyd-1 active site state speciation dramatically, so here in this chapter, only titration data for pH 6 was shown which indicates that Ni-B, Ni_a-SI and Ni_a-R can be electrochemically generated in fairly pure form. In Chapter 5, a Ni_a-L state enriched single Hyd-1 crystal will be discussed via electrochemically poising at pH 8.

The reproducibility of redox titration

Multiple Hyd-1 crystals may be loaded onto the working electrode (WE), usually exhibiting identical

potential-dependent behaviour across different samples.[13] Figure 3.22 shows IR spectra in ν_{CO} region of a deltaTM Hyd-1 single crystal (from an independent batch) at selected applied potentials in a separate oxidative titration. At a reducing potential of -600 mV, the crystal is enriched in the Ni_a-R states (1914 and 1922 cm^{-1}). Stepping the potential to -75 mV accumulates the Ni_a-SI state (1929 cm^{-1}) while further oxidation to +200 mV generates the Ni-B state (1943 cm^{-1}). The identical potential dependence measured from deltaTM Hyd-1 single crystals from different batches aligns fairly consistently with prior results (Figure 3.13), demonstrating a good reproducible electrochemical behaviour in Hyd-1 single crystals. This consistency promotes the development of an *ex-situ* electrochemical cell to poise hydrogenase crystals to a redox level and keep the sample accessible for further characterisation. However, higher potential steps were not performed, so that peak around 1962 cm^{-1} in oxidised potential steps is not observed. The speciation plot and titration curves are not present due to limited potential steps are chosen and measured,

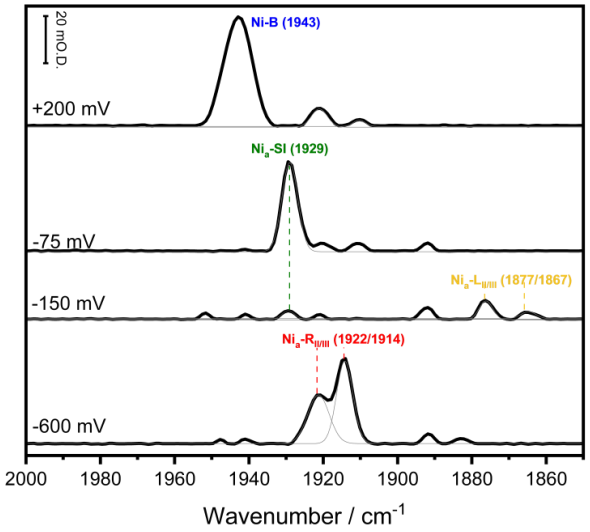

Figure 3.22: The comparison of speciation potential dependence of Hyd-1 single crystal in the same set-up. Baseline-corrected IR spectra showing the ν_{CO} region at selected potential collected from another oxidative potential titration. The gray peaks are the Gaussian fit peaks.

3.3 IR Microspectroelectrochemistry on Hyd-2 Single Crystals

Section 3.2 described the potential dependence of Hyd-1 redox states in a single crystal from the microspectroelectrochemical technique. The speciation plot of Hyd-1 redox states provided an informative map of the conditions to trap a specific redox state at pH 6 as shown in Figure 3.21 and Table 3.2. Similar experiments were then carried out on a Hyd-2 single crystal to map out conditions which stabilise most of the active site states.

Hyd-1 and Hyd-2, two hydrogenases both natively produced by *E. coli*, that are shown to have identical active sites and catalytic intermediates, but they differ in oxygen-tolerance, operating conditions and more importantly, capability to catalyse hydrogen to proton couple.[31,46,47] Hyd-2 is capable of significant H_2 production at pH 6, whereas Hyd-1 shows no measurable proton reduction except in very acidic conditions.[48] The ability of the enzyme to catalyse H^+ reduction affects the ability to perform SEC experiments on Hyd-2 single crystals. Thus, different from experiments on Hyd-1, where the enzyme has negligible catalytic ability in the absence of H_2, Hyd-2 will turn-on to produce H_2 under the same conditions. This suggests the active site states are no longer purely driven by electrochemical equilibria but exhibit a pseudo steady state at reducing potentials since the enzyme is turning over H^+.

3.3.1 The As-isolated Hyd-2 Crystal

Figure 3.23 shows the visible images of a Hyd-2 single crystal on the glassy carbon WE with 15× and 36× magnification. The protein crystals of Hyd-2 were prepared with help from Dr. Steven Carr and have approximately 150×400×50 micrometres (width, length and thickness) dimension depending on the crystallisation methods. The crystal was immersed in mediator cocktail (1 mM each of IC, AQDS, BV, MV and EuBAPTA) prepared in Hyd-2 crystallisation buffer (100 mM Bis-Tris, 200 mM $MgCl_2$, 22%

w/v PEG 3350, 15% v/v glycerol) in pH 6. The experiment was carried out on the MIRIAM beamline B22 at Diamond Light Source with helps from Dr. Stephen Carr and Dr. Rhiannon Evans for protein preparation and data collection. The data analysis in this thesis is processed individually.

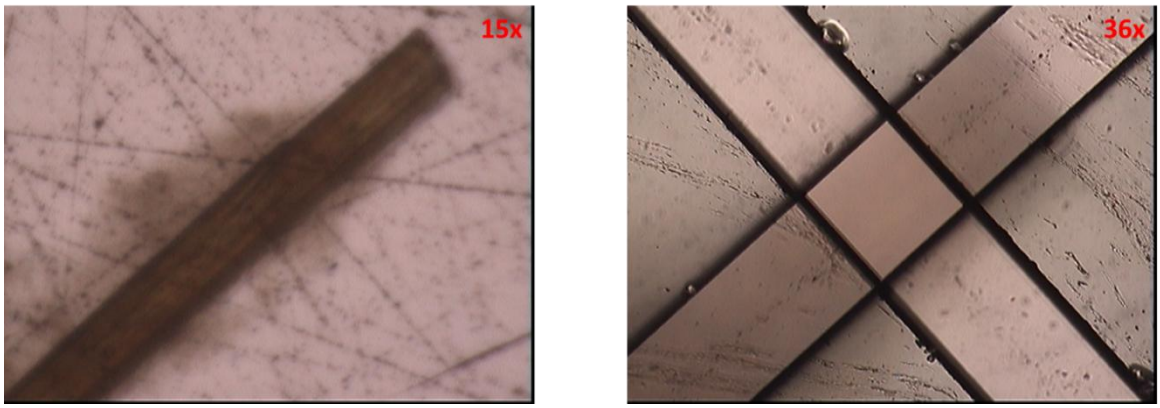

Figure 3.23: Visible image at 15×(Left) and 36×(Right) magnification of a single Hyd-2 crystal on the working electrode of the IR microspectroelectrochemical cell. The 30 × 30 µm^2 sampling area used to collect IR spectra are shown in the 36× image on the right, indicated in the black crosshairs. The smaller sampling compared with that in the Hyd-1 experiment is due to the highly focused and intense synchrotron beam. Redox behavior on distinct positions along the same crystal are assumed to be reproducible based on previous experiments.[13]

Figure 3.24 top panel shows the IR spectrum of the Hyd-2 single crystal measured at OCP (+181 mV vs SHE) containing both the ν_{CO} and ν_{CN} region. The 30 × 30 µm^2 area used to record IR spectra is shown with a black rectangle in Figure 3.23 right panel. The background was recorded with same microscope aperture (sampling area, the black cross hair) right next to the crystal with focus on the WE surface. The much smaller sampling area compared with that used for Hyd-1 single crystal is possible due to the intense and focused synchrotron beam. In the spectrum, at the ν_{CO} region, two bands present at 1958 and 1938 cm^{-1} and the ratio between them is approximately 75%: 25% fitted by Gaussian profile peaks. The band at 1958 cm^{-1} in the ν_{CO} region is the intrinsic CO vibration of the Hyd-2 active site at Ni-B state, whereas the band at 1938 has rarely been reported in Hyd-2 in either solution and electrode-immobilised state. It is rational to classify the band at 1938 cm^{-1} is originated from an

oxidised redox state of Hyd-2 active site as it appears with Ni-B state at OCP at +181 mV vs SHE. In last section, the consistence of relative band positions of hydrogenases active site state compare with Ni_a-C is illustrated by Hyd-1 as an example. Owing to the band position of this oxidised state, -27 cm^{-1} compare with that of Ni_a-C (1964 cm^{-1}) of Hyd-2 which is coincidently very similar to the 1921 cm^{-1} band described in last section in Hyd-1 (-27 cm^{-1} compare with Ni_a-C), the band at 1938 cm^{-1} could be reasonably assigned to one of the sub-species of Ni-SI_r, most likely Ni-SI_{rII} or Ni-SI_{rIII}.

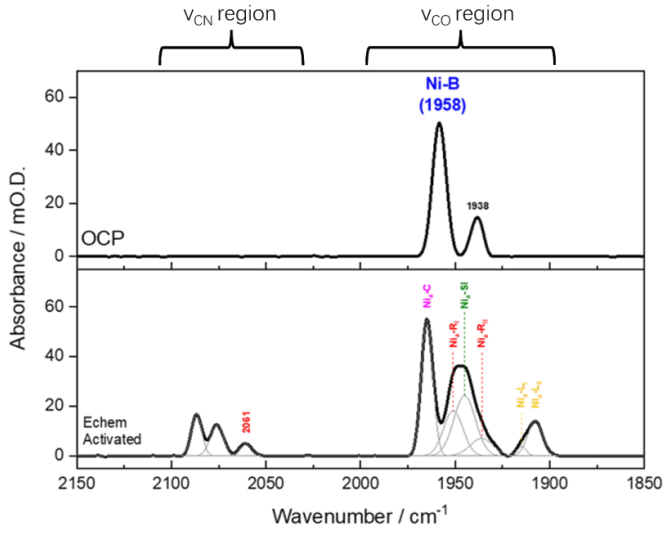

Figure 3.24: The IR spectra of the Hyd-2 single crystal on the microscopic spectroelectrochemical cell. Top) Spectrum recorded at OCP = +181 mV vs SHE, 4 cm^{-1} resolution, 512 scans. Bottom) Spectrum recorded after 1 hour reduction at -600 mV vs SHE, 4 cm^{-1} resolution, 512 scans. Fitted peaks are shown in grey.

In ν_{CN} region of the spectrum at OCP, there are no detectable signal of that crystal. The intensity of IR absorption band for CN ligands in [NiFe]-hydrogenases active site is much smaller than that of CO ligand due to smaller dipole moment along the diatomic ligand and stiffer covalent bonding; and presumably the different relative position harboured at the active site. However, it is hard to rationalize the absence of cyanide ligand signals. It may be due to the intensity of IR absorbance depending on the orientation with respect to the incoming IR light as an electric field oscillating parallel to the bond will give maximal intensity and an electric field oscillating perpendicular to the bond will give zero intensity. Therefore, the cyanide ligands here might happen to have the latter orientation. Figure 3. 25

shows the spectrum of a much bigger and thicker single asiso Hyd-2 crystal measured at OCP (+70 mV) for comparison. Two spectra show very comparable bands in ν_{CO} region, both contains significant amount of Ni-B state (1958 cm^{-1}) and shoulder band at 1938 cm^{-1}. However, the bigger crystal shows two bands at ν_{CN} region at 2092 and 2081 cm^{-1} which is consistent with the two CN^- ligand bands assigned to Ni-B for Hyd-2.[31] The CN bands correspond to 1938 cm^{-1} is probably too small to be detected.

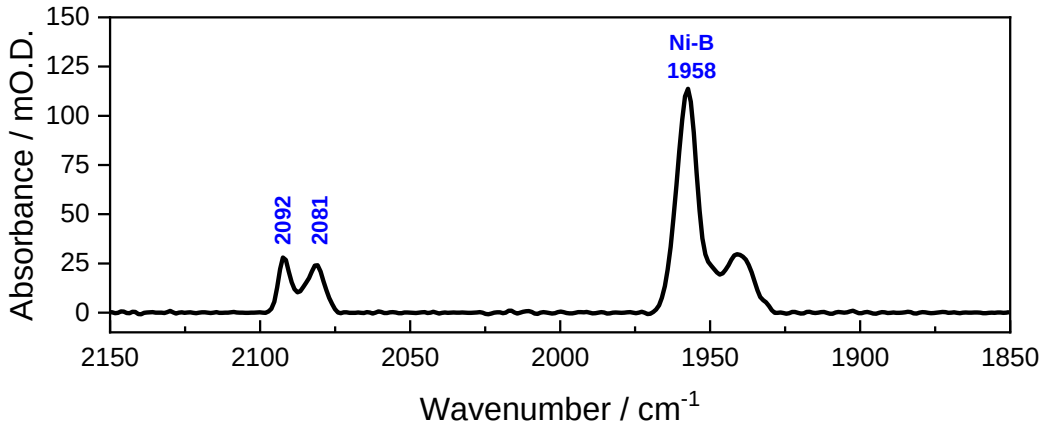

Figure 3.25: The IR spectra of the other Hyd-2 single crystal on the microscopic spectroelectrochemical cell. Spectrum recorded at OCP = +70 mV vs SHE, 4 cm^{-1} resolution, 512 scans.

The cyclic voltammogram of the IR microspectroelectrochemical cell was measured after recording the OCP spectrum, and it is shown in Figure 3.26, which the currents are induced from the mediators in the electrolyte solution (ca. 1 mM of EuBAPTA, MV, AQDS and IC).

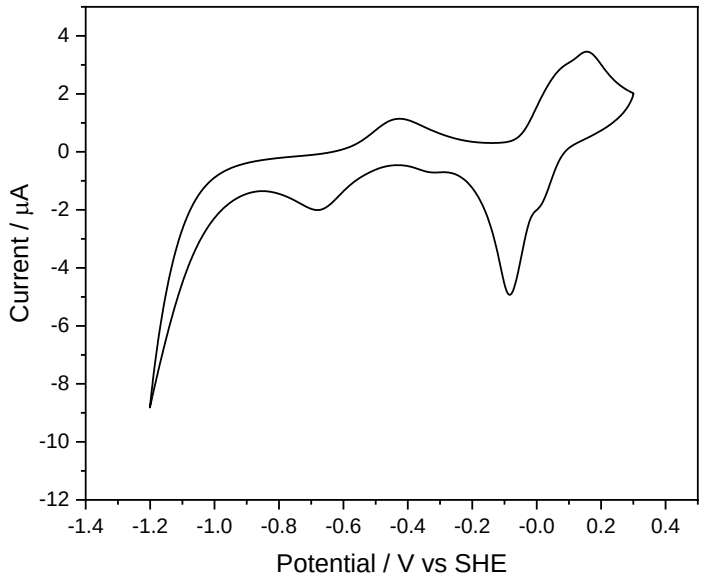

Figure 3.26: Cyclic voltammogram of the microspectroelectrochemical cell, demonstrating the redox couples of the added mediators in the mixed buffer. Recorded at a scan rate: 10 mV / s with hydrogenase crystallisation buffer (100 mM Bis-Tris, 200 mM $MgCl_2$, PEG 3350 22% w/v), pH 6.0.) with additional 1 mM each of redox mediator EuBAPTA, MV, AQDS, IC.

Reductive activation of the Hyd-2 single crystal

In Figure 3.24 bottom panel, the electrochemical activated spectrum of the Hyd-2 single crystal shows drastically different characters in both ν_{CO} and ν_{CN} region. After electrochemically reducing the crystal for 1 hour at -600 mV vs SHE, no detectable signal is shown at 1958 (Ni-B) and 1938 ($Ni\text{-}SI_{rII\ or\ III}$), suggest that the sample has no unready states and is fully activated. The chronoamperogram of the reductive activation is shown in Figure 3.27, showing how current of the cell change over time during the one-hour reductive activation. High negative current was measured at the beginning of reduction when the potential step just shifted from OCP (+181 mV) to -600 mV due to reduction of the oxidised mediators in the cell. However, instead of gradually reaching the equilibrium (like the case in the Hyd-1), the current started to increase at ca. 400 s as shown in Figure 3.27 bottom panel, and did not reach equilibrium till the end of the activation. This is very likely due to the hydrogen production by the Hyd-

2 crystal in the cell at this reducing condition. The current started to decrease at ca. 2000 s, which is probably due to presence of H_2 in the cell.

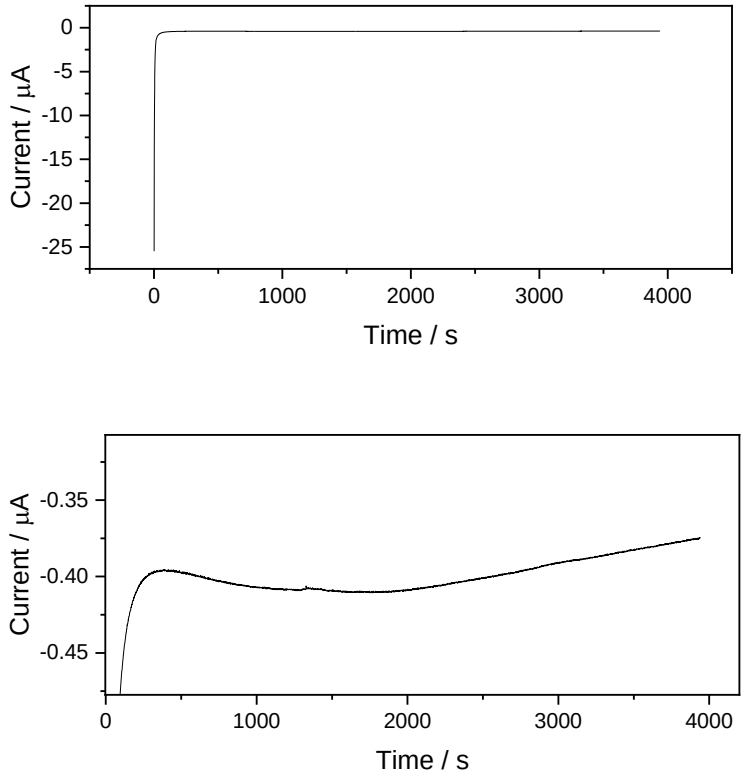

Figure 3.27: Top) Chronoamperometry traces recorded during the reductive activation of Hyd-2 single crystal. Bottom) The enlarged chronoamperometry shows the cell does not reach equilibrium.

The consecutive IR spectra recorded during the reductive activation are shown in Figure 3.28, showing the dynamic changes on active site states during the reduction. The first scan after the potential stepped at -600 mV (light grey spectrum) shows completely lost of band at 1958 cm^{-1}, indicating the activation happened quite fast so that the final merged spectrum shows no contribution from the Ni-B state. The following spectra stabilised at scan 11 with variation in band intensity around 1951, 1945 and 1965 cm^{-1}. This might account for the changing populations of the catalytically active states due to turning-over Hyd-2 sample during the activation.

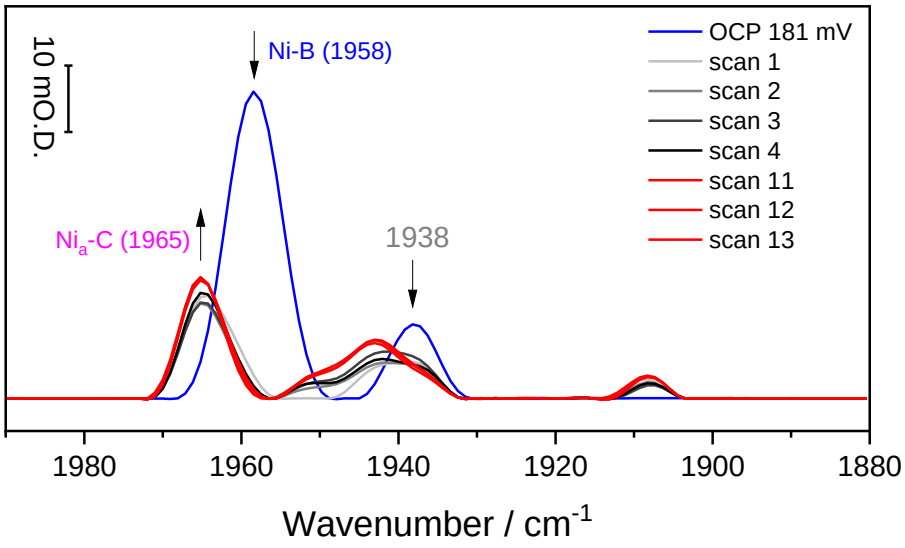

Figure 3.28: The IR spectra of the Hyd-2 single crystal during the reductive activation at different time points, -600mV vs SHE, 4^{-1} resolution, 256 scans, each scans take roughly about 5 min to measure. The first scan after reductive potential steps shows absence of the Ni-B state (1958 cm^{-1} band disappears).

Normally, the as-isolated oxygen sensitive hydrogenases, e.g. *Dv*MF,[45] have a mixture of Ni-A and Ni-B, while in the case of Hyd-2, here the IR spectroscopy suggests such inactive states like Ni-A are absent. The as-isolated Hyd-2 crystal structure shows no oxidation of the terminal cysteine ligand (absence of Ni-A), [49] while the EPR spectrum of as-isolated Hyd-2 suggests the presence of Ni-A.[50] In ν_{CO} region, multiple bands between 1965 to 1907 cm^{-1} indicates the sample contains a mixture of ready states, including reported Ni$_a$-C (1965 cm^{-1}), Ni$_a$-R$_I$ (1951 cm^{-1}) and Ni$_a$-SI (1945 cm^{-1}) states together with 1936 cm^{-1} (Ni$_a$-R$_{II}$), 1915 and 1907 cm^{-1} (Ni$_a$-L$_{I\&II}$).[10,31] The assignment of those unreported states will be discussed in detail in the next section about the redox titration of the same crystal.

The ν_{CN} region of the spectrum on the other hand only shows three bands at 2061, 2076 and 2087 cm^{-1}. The band at 2061 cm^{-1} was previously assigned to one of the Ni$_a$-R$_I$ CN$^-$ vibration.[10] The predominant species at the electrochemically-activated state (-600 mV) are Ni$_a$-C and Ni$_a$-SI as suggested by spectrum in the ν_{CO} region. However, the corresponding CN bands of these two states are often very close in [NiFe]-hydrogenases and have not been reported for Hyd-2 yet. Figure 3.29 shows the full

spectrum (both ν_{CN} and ν_{CO} region) of the same Hyd-2 crystal poised at -125 mV which the enzyme is predominantly in Ni_a-SI state (1945 cm^{-1}). Two CN bands at 2085 and 2074 cm^{-1} are assigned to the Ni_a-SI state which is 2 cm^{-1} different to those in the electrochemically-activated spectrum. Thus, 2076 and 2087 cm^{-1} bands appearing in the activated spectrum could be reasonably assigned to Ni_a-C.

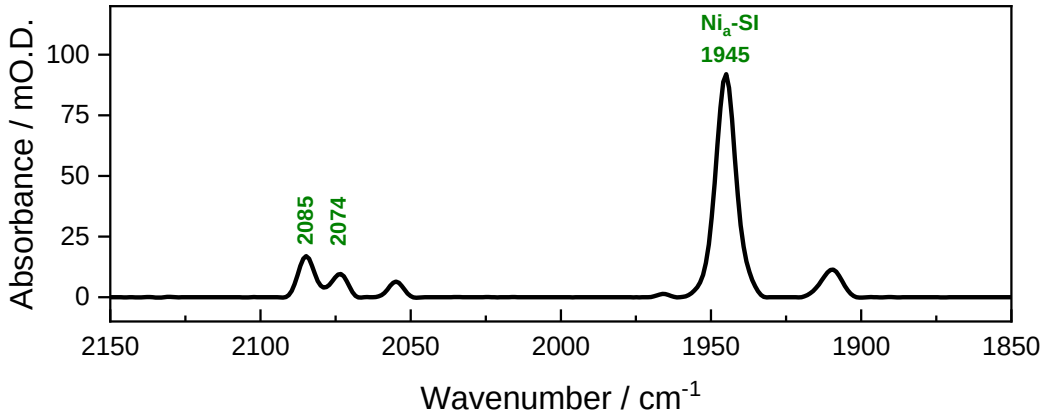

Figure 3.29: The IR spectra of the Hyd-2 single crystal on the microspectroelectrochemical cell shows both ν_{CO} and ν_{CN} region. Spectrum recorded at -125 mV, 4 cm^{-1} resolution, 512 scans.

3.3.2 Potential Titration on Hyd-2 Single Crystal, pH 6

The potential dependence of Hyd-2 bands shared some similarities with Hyd-1 at pH 6. The potential step sequence started with Ni-B predominating at the highest redox level and Ni_a-SI appearing at mild reducing potentials.[33] The potential titration shown in this section focuses on the details of transition from Ni_a-SI to more reducing redox level where the Hyd-2 crystal sample is turning-over. Therefore, after the reductive activation of the Hyd-2 crystal at -600 mV, the potential of the cell was stepped up to the Nia-SI region. After several potential steps were attempted to find the best redox level to start with, the best potential to start the reductive titration was chosen as -50 mV vs SHE with -25 mV reductive potential jumps until 675 mV and then -50 mV jumps to -825 mV.

The reductive titration was performed on Hyd-2 single crystals instead of oxidative titration to minimise the effect of hydrogen gas produced in the sealed-cell at the beginning of the experiment. This was because Hyd-2 has hydrogen production activity at low potential (but at higher potential than the standard potential for the $2H^+/H_2$ couple, since no hydrogen is present in the cell). Additionally, the aim of the experiment was to focus on the equilibrium between the Ni_a-SI and Ni_a-C/Ni_a-L states. Therefore, a reductive titration was performed while minimum hydrogen gas is formed in the cell at potentials around -50 mV to have the highest peak intensity at 1945 cm-1 (Nia-SI). Moreover, the aim of the SEC experiments on Hyd-1 and Hyd-2 single crystals is the identification of conditions for enrichment of active site state. Since in the case of the Hyd-1 experiment, the conditions for isolating Nia-SI, Nia-R and Ni-B were determined, finding the conditions for high population of the Nia-C state is the main focus on small-potential-step titration. Potentials above -50 mV were not attempted due to limited available beamtime.

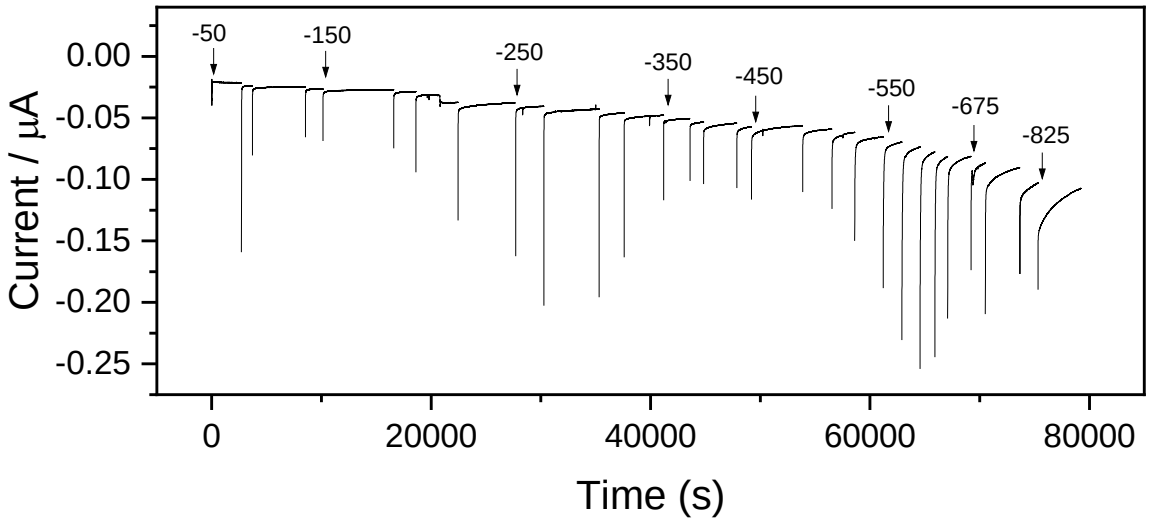

3.30: Chronoamperometry traces recorded during the reductive titration of Hyd-2 single crystal, pH 6 in the microSEC cell. The marker indicates the potential was applied. The potential step is -25 mV between -50 mV and -675 mV, and increases to -50 mV from -675 to -825 mV.

The chronoamperogram of the reductive activation is shown in Figure 3.30. In contrast to the redox titration on Hyd-1, for which nearly all potential steps reached equilibrium, the residual current is increasing along with the reducing potential steps from ca. 25 nA to 100 nA. This indicates that a steady-state was reached during the Hyd-2 titration, rather than equilibrium, especially at lower potentials (e.g. ≤ -450 mV).

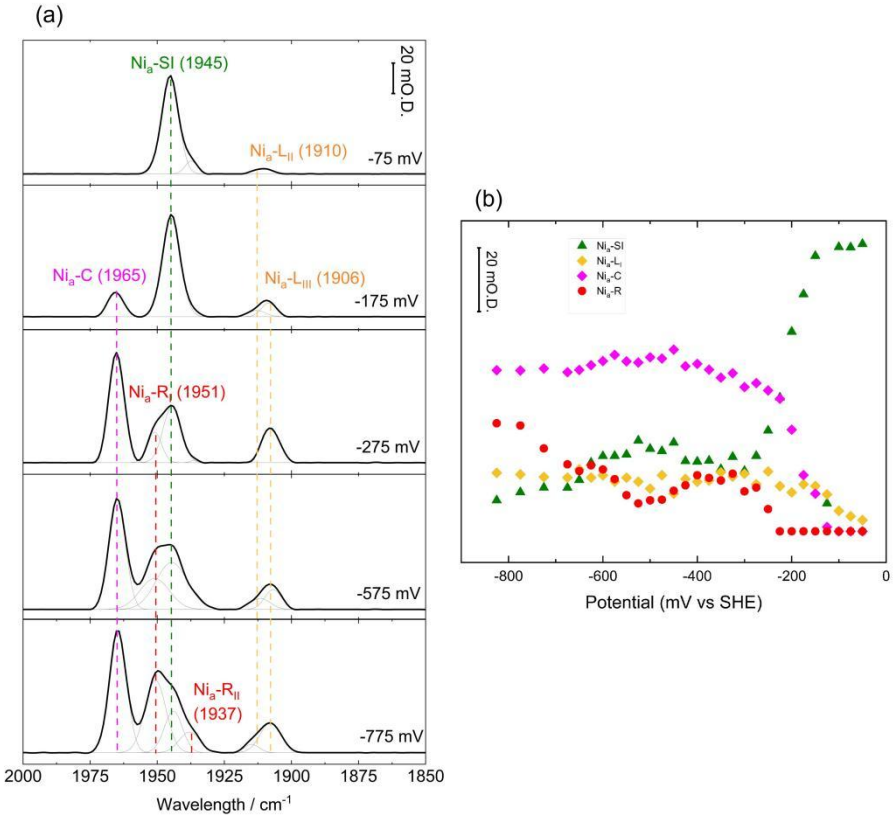

Figure 3.31: (A) The ν_{CO} region of baseline corrected IR spectra of the single Hyd-2 crystal in stacked format, showing accumulation of all catalytically relevant states cross the measured potential range during the reductive redox titration at pH 6. The changing speciation of enzyme active site reflects precise redox control on the crystallo sample in the microSEC cell. Each spectrum was measured in 4 cm^{-1} resolution, 512 scans. The gray lines are Gaussian fit peaks. B) The speciation plot of Hyd-2 single crystal at pH 6 showing how the population of each state varies with potential. The intensity of each peak is fitted with Gaussian peak and population of sub-states are summed.

Figure 3.31 panel A shows the ν_{CO} region of selected IR spectra of the Hyd-2 single crystal during the reductive titration. Compare to the potential titration of Hyd-1 in Figure 3.13, both Hyd-1 and Hyd-2 could accumulate the most oxidised activated redox state, Ni_a-SI, while the drastic difference of speciation appears at lower potential. Instead of having a defined redox region of each activated states, the speciation of Hyd-2 in the crystalline state barely changes at low potential. Figure 3.31 panel B shows the absorbance of each state as a function of potential and reveals the subtle variation in between each state at low potential.

The potential dependence of the active site states

The potential-dependent behaviour of active site states in Hyd-2 single crystals is demonstrated by the reductive titration shown in Figure 3.31. In the panel A, the spectra recorded at -75 mV shows the Ni_a-SI state predominates at this redox level. This assignment is supported by the characteristic band at 1945 cm^{-1} which the position is consistent with prior Hyd-2 studies where Ni_a-SI exhibits a ν_{CO} absorption ~20 cm^{-1} below the Ni_a-C state (1965 cm^{-1}),[10] aligning with the typical 15–25 cm^{-1} downshift observed in most [NiFe]-hydrogenases (Figure 3.2). When Hyd-2 was first studied via IR spectroscopy, it was often compared with the other O_2 sensitive hydrogenase *Dv*MF, which they are proposed to have similar electronic environment within the active site so they have comparable band position of each states.[4] The reported Ni_a-SI band position in ν_{CO} of *Dv*MF is 1943 cm^{-1} and maximize at -150 mV (pH 5.4), supporting the assignment the band at 1945 cm^{-1} to be the Ni_a-SI state.

When the potential is stepped to -175 mV, two new spectral features emerge alongside the dominant band at 1945 cm^{-1} (Ni_a-SI): a lower wavenumber band at 1909 cm^{-1} and a distinct feature at 1965 cm^{-1}. The 1965 cm^{-1} band was reported and assigned to Ni_a-C state of Hyd-2 due to its band position and potential dependence.[31] From the series spectra stacks in Figure 3.31 panel A, it clearly shows band at 1965 cm^{-1} is the highest wavenumber active site states band in ν_{CO} region, consistent with the characteristic signature of Ni(III) in [NiFe]-hydrogenases. A lower wavenumber at 1909 cm^{-1} and a

distinct band at 1965 cm^{-1}. The intensity of 1910 cm^{-1} band increases as the potential is reduced from -75 mV to -175 mV. This band lies 55 wavenumbers below the assigned Ni_a-C ν_{CO} peak and persists in low potentials (blow -75 mV to -775 mV, Figure 3.31 A), suggest this band is associated to the Ni_a-L_{II} state. This assignment is supported by recent cryogenic illumination studies showing similar spectral shifts in *Cupriavidus necator* [NiFe]-hydrogenases.[51]

The active site interconversion reveals a redox equilibrium where the oxidised Ni_a-SI state (1945 cm^{-1}) converts to more reduced forms (Ni_a-C and Ni_a-L states) at -175 mV. Further reduction to -275 mV introduces a new band at 1951 cm^{-1}, assigned to Ni_a-R_I state based on its position (14 cm^{-1} below Ni_a-C) and potential dependence. At this stage, Ni_a-C becomes the dominant species, comprising ~60% of the total active sites. Additional spectral features emerge at extreme reducing potentials (-575 to -775 mV), including a band at 1910 cm^{-1} that we assign to Ni_a-L_I (-55 cm^{-1} relative to Ni_a-C).

The redox speciation of Hyd-2 follows a general pattern similar to Hyd-1 (Figure 3.1), progressing sequentially from Ni_a-SI to Ni_a-C/Ni_a-L and ultimately to Ni_a-R states. However, Figure 3.31B reveals that there are significant populations of Ni_a-SI and Ni_a-C persist at low potentials, and the speciation profile stabilises below -275 mV with only minor interconversion between Ni_a-SI and Ni_a-R. These observations can be explained by Hyd-2's bidirectional catalytic activity in the H_2/H^+ couple. Under the inert atmosphere (absence of H_2) of the SEC cell, the equilibrium favours H_2 production, maintaining a dynamic steady-state where Ni_a-R acts as a fast-consumed intermediate. This explains both the persistent Ni_a-SI population and the stabilisation of speciation below -275 mV. Supporting evidence comes from PFIRE studies of electrode-immobilised Hyd-2, which reported similar speciation under argon and confirmed proton reduction activity through reductive current measurements.[31] However, the SEC experiments on Hyd-1 and Hyd-2 single crystals cannot provide useful information from chronoamperometry due to high concentration of redox mediators. The current induced from hydrogenases sample is buried under high current from the mediators. The eventual predominance of the Ni_a-R state at extreme reducing potentials (Figure 3.31B) further demonstrates the

electrochemical control over the catalytic equilibrium.

3.3.3 The Reproducibility of Redox Titration on Hyd-2 Single Crystal

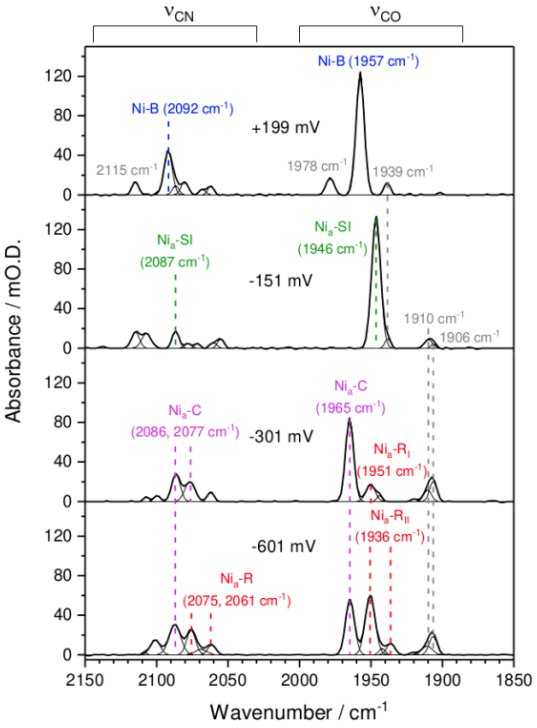

Figure 3.32: The comparison of redox titration of Hyd-2 single crystals from different batches in the experimental set-up but performed in in-house IR source. Baseline-corrected IR spectra in ν_{CO} and ν_{CN} region at selected potentials collected are shown in stacked format and both set of spectra are recorded in 4 cm^{-1} resolution, 512 scans. Data collected and analysed together with Dr. Rhiannon Evans.

Section 3.2.3 demonstrates that oxidative titrations of Hyd-1 show remarkable consistency across multiple crystals from different preparations. This reproducibility likely stems from Hyd-1's catalytic silence in proton reduction at pH 6. In contrast, reductive titrations of Hyd-2 single crystals exhibit significant variability between experiments, as clearly shown in Figure 3.32 which compares an alternative titration from different protein batches. While the Hyd-2 titration displays the same fundamental sequence of active site state conversions: progressing from the most oxidised Ni-B state

through Ni_a-SI to Ni_a-C/Ni_a-L and finally to the most reduced Ni_a-R, state they differ substantially in their detailed speciation profiles, particularly at catalytically active potentials below -150 mV. Since only selected potential steps were applied for testing the speciation of Hyd-2 crystals at specific potential of interest, the speciation curves are not shown here.

Several factors may contribute to this variability in Hyd-2 behaviour. First, Hyd-2 maintains proton reduction activity at pH 6, as discussed previously. Second, there are inherent variations in crystal size between different preparations. Third, batch-to-batch differences in protein activity may affect the results, however, the activity of Hyd-2 samples for crystalllisation were not tested. These factors collectively influence not only proton reduction at low potentials but may also impact H_2 oxidation activity in the range of -100 mV to -150 mV, since electrochemically generated H_2 could potentially serve as substrate in the sealed spectroelectrochemical cell. [50]

Despite these variations, careful analysis reveals consistent patterns in Hyd-2's redox behaviour that enable reliable isolation of specific active site states. Most notably, the Ni_a-SI state consistently dominates at mild reducing potentials between -100 and -150 mV across all titrations, while the Ni_a-C state becomes predominant around -250 mV in every case. These reproducible features, identified through comprehensive *in-situ* microspectroelectrochemical experiments, provide the critical foundation for Chapter 4. There we describe the development of an ex-situ electrochemical cell system designed to generate hydrogenase single crystals poised at specific redox levels, enabling isolation and characterisation of catalytically relevant states.

3.4 Summary

This chapter presents the application of IR microspectroelectrochemical methods to investigate Hyd-1 and Hyd-2 single crystals at pH 6. Through detailed redox titration experiments, we have systematically analysed the intrinsic CO vibrational bands associated with the common active site redox states of

both hydrogenases. The comprehensive characterisation of these spectral features has enabled precise assignment of each redox state based on their characteristic ν_{CO} absorption bands. These assignments are summarised in Table 3.3, which provides a complete reference of IR band positions for both Hyd-1 and Hyd-2 that will serve as the foundation for subsequent analyses throughout this thesis.

Table 3.3: Assigned ν_{CO} wavenumber positions of *E. coli* Hyd-1 and Hyd-2 in crystalline state. The values are obtained from pH 6.0.

Redox state	Hyd-1 / cm^{-1}	Hyd-2 / cm^{-1}
Ni-B	1943	1958
Ni_a-SI	1929	1945
Ni_a-C	1952	1965
Ni_a-L_I	n.d.	1914
Ni_a-L_{II}	1877	1909
Ni_a-L_{III}	1867	n.d.
Ni_a-R_I	n.d.	1951
Ni_a-R_{II}	1922	1936
Ni_a-R_{III}	1914	n.d.

Beyond the characteristic wavenumber positions of assigned vibrational bands, this study has systematically investigated the potential dependence of active site states in both Hyd-1 and Hyd-2. The redox behaviour of both hydrogenases follows a similar progression from the most oxidised Ni-B state through Ni_a-SI to Ni_a-C/Ni_a-L intermediates, and finally to the most reduced Ni_a-R state as the applied potential is varied. However, Hyd-2 exhibits more complex behaviour due to its proton reduction activity at pH 6, resulting in mixed populations of activated states during titration.

Through comprehensive spectroelectrochemical analysis, it elucidated the interconversion pathways between active site states and their precise redox dependence. This approach has enabled the assignment of previously uncharacterised bands, including two Ni_a-SI_r substates in Hyd-1 (observed at

1921 cm^{-1} and 1911 cm^{-1}) that appear at the Ni_a-SI redox level. The detailed structural and electronic information derived from these spectroelectrochemical experiments provides a crucial foundation for Chapter 4 and 5, where the examination of the crystal structures of redox-manipulated single crystals is described.

Table 3.4: The optimum conditions to manipulate Hyd-1 and Hyd-2 in specific active site-enriched states, pH 6. These conditions are obtained from the *in-situ* microSEC experiments. The ratio of occupancy is calculated via Gaussian fitted absorption band in ν_{CO} region.

Hyd-1			Hyd-2		
Active site state	**Potential / mV**	**occupancy**	**Active site state**	**Potential / mV**	**occupancy**
Ni-B	+200	~ 90%	**Ni-B**	+200	~ 90%
Ni_a-SI	-75	~ 75%	**Ni_a-SI**	-125	~ 95%
Ni_a-R	-600	~ 90%	**Ni_a-C**	-275	~ 50 to 80%

The most critical outcome of these comprehensive single-crystal potential titrations is the precise mapping of active site state speciation as a function of applied potential. Through detailed full-range potential titrations, we have identified specific redox potentials where relatively pure active site states can be obtained. These optimal conditions for generating specific redox-state-enriched single crystals of both Hyd-1 and Hyd-2 are systematically summarised in Table 3.4.

3.5 References

1 W. Lubitz, H. Ogata, O. Rüdiger and E. Reijerse, *Chem. Rev.*, 2014, **114**, 4081–4148.

2 R. P. Happe, W. Roseboom, A. J. Pierik, S. P. J. Albracht and K. A. Bagley, *Nature*, 1997, **385**, 126.

3 S. P. Best, *Coord. Chem. Rev.*, 2005, **249**, 1536–1554.

4 C. Fichtner, C. Laurich, E. Bothe and W. Lubitz, *Biochemistry*, 2006, **45**, 9706–9716.

5 A. L. de Lacey, E. C. Hatchikian, A. Volbeda, M. Frey, J. C. Fontecilla-Camps and V. M. Fernandez, *J. Am. Chem. Soc.*, 1997, **119**, 7181–7189.

6 P. A. Ash, S. E. T. Kendall-Price and K. A. Vincent, *Acc. Chem. Res.*, 2019, **52**, 3120–3131.

7 A. Volbeda, E. Garcin, C. Piras, A. L. de Lacey, V. M. Fernandez, E. C. Hatchikian, M. Frey and J. C. Fontecilla-Camps, *J. Am. Chem. Soc.*, 1996, **118**, 12989–12996.

8 A. L. De Lacey, C. Stadler, V. M. Fernandez, C. E. Hatchikian, H.-J. Fan, S. Li and M. B. Hall, *J. Biol. Inorg. Chem.*, 2002, **7**, 318–326.

9 B. Bleijlevens, F. A. van Broekhuizen, A. L. De Lacey, W. Roseboom, V. M. Fernandez and S. P. J. Albracht, *J. Biol. Inorg. Chem.*, 2004, **9**, 743–752.

10 M. Senger, K. Laun, B. Soboh and S. T. Stripp, *Catalysts*, 2018, **8**, 530.

11 B. L. Greene, C. A. Joseph, M. J. Maroney and R. B. Dyer, *J. Am. Chem. Soc.*, 2012, **134**, 11108–11111.

12 M. Saggu, I. Zebger, M. Ludwig, O. Lenz, B. Friedrich, P. Hildebrandt and F. Lendzian, *J. Biol. Chem.*, 2009, **284**, 16264–16276.

13 P. Ash, S. B. Carr, H. Reeve, J. S. Rowbotham, R. Shutt, M. Frogley, R. M. Evans, G. Cinque, F. A. Armstrong and K. A. Vincent, *Chem. Commun.*, 2017, **53**, 5858–5861.

14 M.-E. Pandelia, V. Fourmond, P. Tron-Infossi, E. Lojou, P. Bertrand, C. Léger, M.-T. Giudici-Orticoni and W. Lubitz, *J. Am. Chem. Soc.*, 2010, **132**, 6991–7004.

15 P. A. Ash, J. Liu, N. Coutard, N. Heidary, M. Horch, I. Gudim, T. Simler, I. Zebger, O. Lenz and K. A. Vincent, *J. Phys. Chem. B*, 2015, **119**, 13807–13815.

16 B. L. Greene, C.-H. Wu, P. M. McTernan, M. W. W. Adams and R. B. Dyer, *J. Am. Chem. Soc.*, 2015, **137**, 4558–4566.

17 M. Horch, L. Lauterbach, M. A. Mroginski, P. Hildebrandt, O. Lenz and I. Zebger, *J. Am. Chem. Soc.*, 2015, **137**, 2555–2564.

18 F. Germer, I. Zebger, M. Saggu, F. Lendzian, R. Schulz and J. Appel, *J. Biol. Chem.*, 2009, **284**, 36462–36472.

19 P. A. Ash, R. Hidalgo and K. A. Vincent, *ACS Catal.*, 2017, **7**, 2471–2485.

20 A. Volbeda, L. Martin, E. Barbier, O. Gutiérrez-Sanz, A. L. De Lacey, P.-P. Liebgott, S. Dementin, M. Rousset and J. C. Fontecilla-Camps, *J. Biol. Inorg. Chem.*, 2015, **20**, 11–22.

21 Y. Higuchi, H. Ogata, K. Miki, N. Yasuoka and T. Yagi, *Structure*, 1999, **7**, 549–556.

22 H. Ogata, W. Lubitz and Y. Higuchi, *J. Biochem.*, 2016, **160**, 251–258.

23 H. Tai, K. Nishikawa, M. Suzuki, Y. Higuchi and S. Hirota, *Angew. Chem. Int. Ed.*, 2014, **53**, 13817–13820.

24 R. Hidalgo, P. A. Ash, A. J. Healy and K. A. Vincent, *Angew. Chem. Int. Ed.*, 2015, **54**, 7110–7113.

25 P. A. Ash, R. Hidalgo and K. A. Vincent, *ACS Catal.*, 2017, **7**, 2471–2485.

26 P. A. Ash, S. E. T. Kendall-Price, R. M. Evans, S. B. Carr, A. R. Brasnett, S. Morra, J. S. Rowbotham, R. Hidalgo, A. J. Healy, G. Cinque, M. D. Frogley, F. A. Armstrong and K. A. Vincent, *Chem. Sci.*, 2021, **12**, 12959–12970.

27 T. Krämer, M. Kampa, W. Lubitz, M. van Gastel and F. Neese, *ChemBioChem*, 2013, **14**, 1898–1905.

28 M. Kampa, M.-E. Pandelia, W. Lubitz, M. van Gastel and F. Neese, *J. Am. Chem. Soc.*, 2013, **135**, 3915–3925.

29 M. Stein and W. Lubitz, *Curr. Opin. Chem. Biol.*, 2002, **6**, 243–249.

30 C. Lorent, V. Pelmenschikov, S. Frielingsdorf, J. Schoknecht, G. Caserta, Y. Yoda, H. Wang, K. Tamasaku, O. Lenz, S. P. Cramer, M. Horch, L. Lauterbach and I. Zebger, *Angew. Chem. Int. Ed.*, 2021, **60**, 15854–15862.

31 M. Chung, DPhil Thesis, University of Oxford, 2016.

32 R. M. Evans, E. J. Brooke, S. A. M. Wehlin, E. Nomerotskaia, F. Sargent, S. B. Carr, S. E. V Phillips and F. A. Armstrong, *Nat. Chem. Biol.*, 2016, **12**, 46–50.

33 S. Kendall-Price, DPhil Thesis, University of Oxford, 2022.

34 V. M. Fernandez, E. C. Hatchikian and R. Cammack, *BBA - Protein Structure and Molecular Enzymology*, 1985, **832**, 69–79.

35 S. Kurkin, S. J. George, R. N. F. Thorneley and S. P. J. Albracht, *Biochemistry*, 2004, **43**, 6820–6831.

36 R. Gonzalez, DPhil Thesis, University of Oxford, 2016.

37 B. J. Murphy, F. Sargent and F. A. Armstrong, *Energy Environ. Sci.*, 2014, **7**, 1426–1433.

38 M.-E. Pandelia, P. Infossi, M. Stein, M.-T. Giudici-Orticoni and W. Lubitz, *Chem. Commun.*, 2012, **48**, 823–825.

39 M. M. Roessler, R. M. Evans, R. A. Davies, J. Harmer and F. A. Armstrong, *J. Am. Chem. Soc.*, 2012, **134**, 15581–15594.

40 F. Oteri, M. Baaden, E. Lojou and S. Sacquin-Mora, *J. Phys. Chem. B*, 2014, **118**, 13800–13811.

41 M.-E. Pandelia, H. Ogata and W. Lubitz, *ChemPhysChem*, 2010, **11**, 1127–1140.

42 H. Ogata, S. Hirota, A. Nakahara, H. Komori, N. Shibata, T. Kato, K. Kano and Y. Higuchi, *Structure*, 2005, **13**, 1635–1642.

43 H. Tai, L. Xu, K. Nishikawa, Y. Higuchi and S. Hirota, *Chem. Commun.*, 2017, **53**, 10444–10447.

44 M.-E. Pandelia, H. Ogata, L. J. Currell, M. Flores and W. Lubitz, *BBA - Bioenergetics*, 2010, **1797**, 304–313.

45 H. Osuka, Y. Shomura, H. Komori, N. Shibata, S. Nagao, Y. Higuchi and S. Hirota, *Biochem. Biophys. Res. Commun.*, 2013, **430**, 284–288.

46 L. Forzi, P. Hellwig, R. K. Thauer and R. G. Sawers, *FEBS Lett.*, 2007, **581**, 3317–3321.

47 M. J. Lukey, M. M. Roessler, A. Parkin, R. M. Evans, R. A. Davies, O. Lenz, B. Friedrich, F. Sargent and F. A. Armstrong, *J. Am. Chem. Soc.*, 2011, **133**, 16881–16892.

48 F. A. Armstrong, R. M. Evans, S. V Hexter, B. J. Murphy, M. M. Roessler and P. Wulff, *Acc. Chem. Res.*, 2016, **49**, 884–892.

49 S. E. Beaton, R. M. Evans, A. J. Finney, C. M. Lamont, F. A. Armstrong, F. Sargent and S. B. Carr, *Biochemical Journal*, 2018, **475**, 1353–1370.

50 M. J. Lukey, A. Parkin, M. M. Roessler, B. J. Murphy, J. Harmer, T. Palmer, F. Sargent and F. A. Armstrong, *J. Biolog. Chem.*, 2010, **285**, 3928–3938.

51 A. F. T. Waffo, C. Lorent, S. Katz, J. Schoknecht, O. Lenz, I. Zebger and G. Caserta, *J. Am. Chem. Soc.*, 2023, **145**, 13674–13685.

Chapter 4: *Ex-situ* Electrochemical Cells for Precise Redox Control on Hydrogenase Crystals

This chapter presents the design and validation of specialised electrochemical cells developed to achieve fine redox control of Hyd-1 and Hyd-2 single crystals under *ex-situ* conditions. The custom systems enable both precise electrochemical controls to establish desired active site states and subsequent facile sample collection for further spectroscopic and crystallographic determination.

4.1 Introduction

While most spectroelectrochemical studies on hydrogenases have focused on solution-phase enzymes,[1–3] investigating crystallo-proteins enables direct correlation between crystallographic, infrared spectroscopic, and electrochemical data. The *in-situ* microspectroelectrochemical experiments on Hyd-1 and Hyd-2 single crystals (Chapter 3) probed the redox-dependent active-site state distribution via IR spectroscopy, identifying conditions for isolating crystals in well-defined redox states. This opens up a possibility for high-resolution structural determination of specific electrochemically controlled active site states.

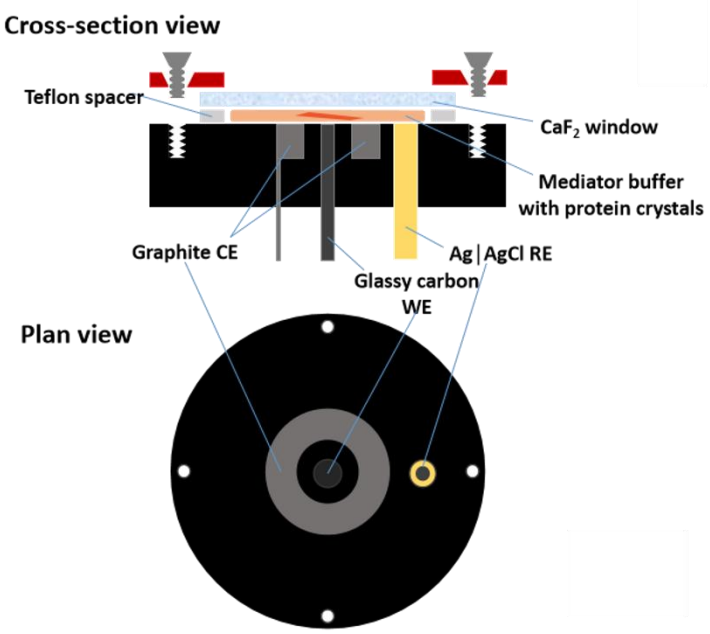

Figure 4.1: The schematic design of the IR microspectroelectrochemical cell. The cross-section view shows the protein crystals are placed in a thin layer of buffer.

The current sealed IR microspectroelectrochemical cell design (Figure 4.1) sandwiches protein crystals between an optical window and the working electrode, in a thin mediator-containing buffer layer, restricting post-experiment sample retrieval.[4] While effective for *in-situ* IR

measurements, this setup is unsuitable for subsequent crystallographic or spectroscopic analyse.

To enable comprehensive structural studies, a new electrochemical cell must fulfil three key criteria:

1. Sufficient sample accessibility: facilitate easy extraction of redox-poised crystals for crystallography, IR spectroscopy, and other techniques.
2. Precise electrochemical control: protein film electrochemistry and the *in-situ* microspectroelectrochemical experiment allow direct electron transfer between protein and electrode. The electrochemical cell should provide precise redox control on crystal sample, even they are not in direct electrode contract.
3. Rapid electrolytic equilibration: great conductivity and large surface area of the working electrode to facilitate fast redox state conversion of protein sample.

This chapter details the development of novel electrochemical cells engineered to meet these specifications. Three designs are presented including a static three-electrode cell, a convection cell and a hybrid pump-circuit cell. By integrating these systems, we establish a robust platform for generating redox-defined hydrogenase crystals.

4.2 Three-electrode Cell

The initial bulk electrochemical cell design was developed to enable *ex-situ* generation of hydrogenase single crystals in specific redox states, building upon the redox-dependent speciation profiles obtained from *in-situ* microspectroelectrochemical experiments. Unlike the microSEC cell used for redox titrations, this new system prioritises efficient bulk electrolysis while maintaining sample accessibility for post-electrochemical characterisation.

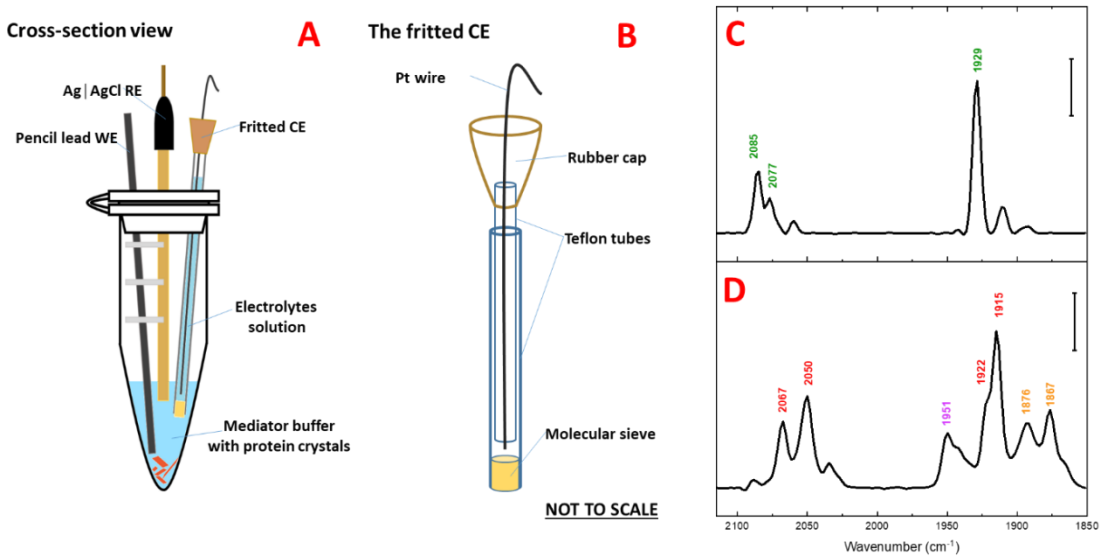

Figure 4.2: Design and application of the static three-electrode electrochemical cell for Hyd-1+cytB single crystals. (A) Cross-sectional schematic of the electrochemical cell assembly. (B) Detailed design of the fritted counter electrode compartment. (C) Infrared spectrum of a Hyd-1+cytB single crystal after electrochemical poising at -100 mV for 3 hours, pH 6. Characteristic bands correspond to ν_{CO} and ν_{CN} vibrations of the Ni_a-SI state. (D) Infrared spectrum of a Hyd-1+cytB single crystal after electrochemical poising at -600 mV for 6 hours, pH 6. Spectral features represent a mixture of Ni_a-R (red), Ni_a-C (magenta) and Ni_a-L (yellow) states. The IR spectra were recorded in 2 cm^{-1} resolution, 512 scans, baseline subtracted, and the marker indicates 20 mO.D. absorbance. Mediator cocktail contains 1 mM each of MV, BV, AQDS and IC.

The cell design, illustrated in Figure 4.2A, employed an Eppendorf tube as the cell body with

three electrodes mounted in a removable lid. A 2 mm diameter pencil lead served as the working electrode, paired with a leak-free Ag/AgCl reference electrode (eDAQ) and a custom molecular-sieve-fritted platinum counter electrode (Figure 4.2B). The fritted counter electrode compartment, filled with plain crystallisation buffer, effectively isolated the counter electrode reactions while maintaining ionic conductivity, preventing interference from oxygen evolution at the platinum surface.

Despite its simplicity, this initial design exhibited significant limitations. The system suffered from diffusion-limited electrolysis due to the absence of forced convection, compounded by the low surface area of the pencil lead working electrode. These factors resulted in extremely low working electrode currents (≤10 µA) and prolonged equilibration times (several hours, based on the colour of mediator cocktail and the current), severely restricting the system's efficiency. The chronoamperomogram of the three-electrode cell at -600 mV is shown in Figure 4.3.

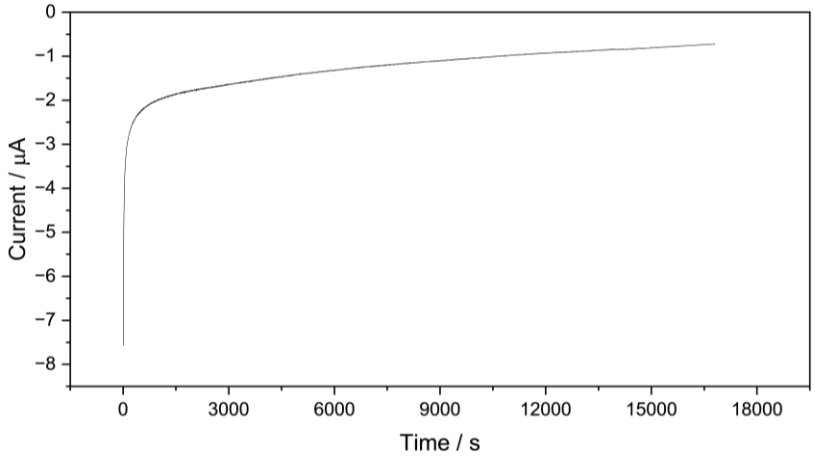

Figure 4.3: The chronoamperomogram of the simple three-electrode cell poising at -600 mV vs SHE.

Nevertheless, the cell successfully demonstrated proof-of-concept for *ex-situ* electrochemical manipulation of protein crystals. Validation experiments using Hyd-1+cytB crystals (a purification byproduct that maintains similar redox behaviour to native Hyd-1 according to SEC

studies) [5] yielded two key results shown in Figure 4.2 C-D. Crystals poised at -100 mV for 3 hours exhibited a dominant absorption band at 1929 cm^{-1}, corresponding to the Ni_a-SI state, with spectral features identical to those observed in *in-situ* SEC experiments (Figures 3.13). In contrast, crystals held at -600 mV for 6 hours showed mixed Ni_a-R, Ni_a-C, and Ni_a-L states, indicating incomplete reduction likely due to the cell's kinetic limitations.

These results confirmed the feasibility of *ex-situ* redox control while highlighting the need for improved electrolysis efficiency. The successful reproduction of the Ni_a-SI state validated the approach of translating *in-situ* SEC conditions to bulk electrochemical manipulation, while the incomplete reduction at -600 mV underscored the importance of addressing kinetic barriers in subsequent designs. This initial system established a foundation for the improved electrochemical cells described in the following sections, which incorporate enhanced geometries and electrode configurations to overcome these limitations.

4.3 Convection Cell

Building upon the limitations identified in the initial electrochemical cell, an improved design incorporated forced convection and an alternative working electrode configuration. Traditional bulk electrochemical cells such as H-cells typically employ rotating electrodes to enhance mass transport, but these prove unsuitable for protein crystal manipulation due to the fragile nature and small size of crystalline samples. The hydrodynamic forces generated by rotating electrodes risk damaging the crystals, while the rigid materials and limited surface area of laboratory rotational electrodes present additional practical constraints.

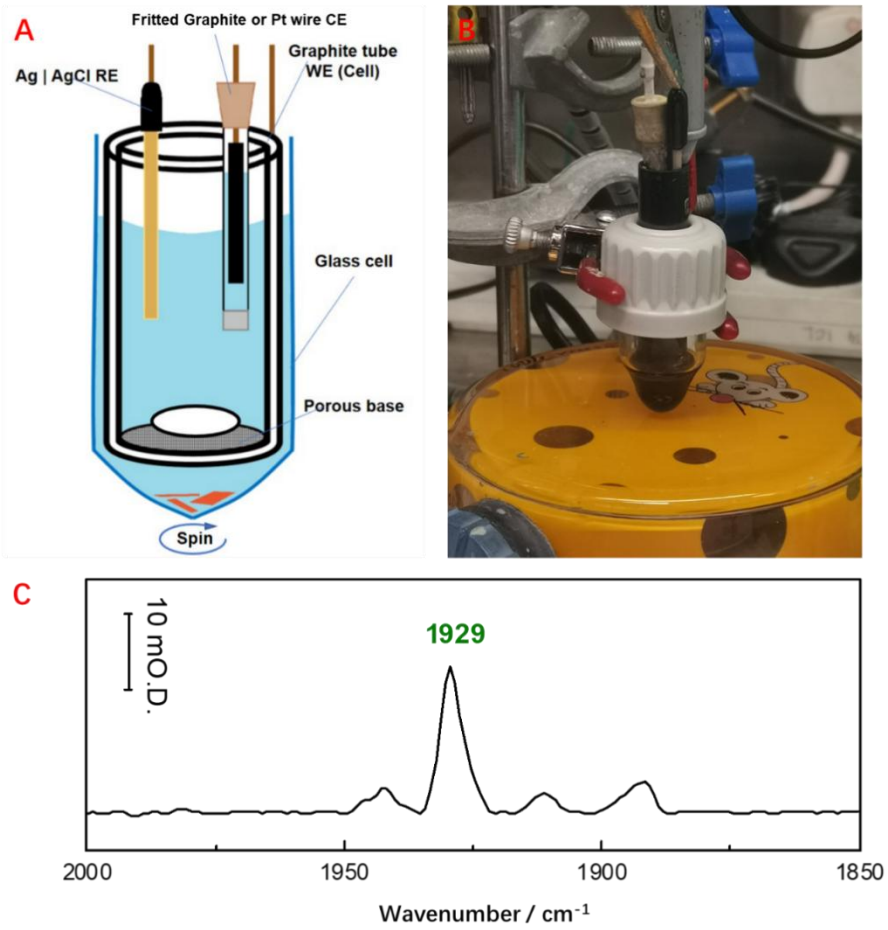

Figure 4.4: Convection electrochemical cell for deltaTM Hyd-1 single crystal manipulation. (A) Cross-sectional schematic of the cell design showing the graphite tube working electrode and crystal compartment. (B) Photograph of the experimental setup during operation. (C) Infrared spectrum in the ν_{CO} region (1900-2100 cm^{-1}) of a deltaTM Hyd-1 single crystal after electrochemical poising at -100 mV for 1.5 hours (pH 6.0, 2 cm^{-1} resolution, 512 scans, baseline-corrected). The spectrum demonstrates successful enrichment of the Ni_a-SI state, characterised by the dominant absorption band at 1929 cm^{-1}.

The enhanced electrochemical cell design, illustrated in Figure 4.4, addresses these challenges through several key innovations. Panel A shows the cross-sectional schematic while panel B displays the experimental setup. The system features a graphite tube working electrode with a porous nylon base that serves dual functions as both electrode and cell body. This assembly

is inserted into a secondary glass container featuring a conical bottom compartment specifically designed for crystal placement. During operation, mediator solution is injected to immerse both crystals and electrodes, while a magnetic stirrer positioned above the porous electrode base provides controlled convection without direct crystal disturbance. This configuration achieves current outputs up to ±1 mA during chronoamperometry experiments with 1 mM concentration of mediator cocktail while maintaining straightforward crystal accessibility through the removable graphite tube assembly. The chronoamperomogram of the convection cell poised at -600 mV and then switched to -100 mV is shown in Figure 4.5.

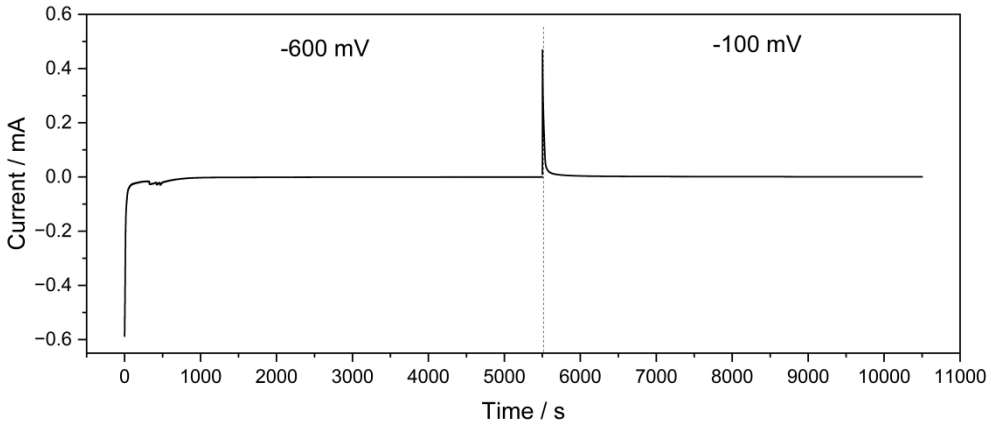

Figure 4.5: The chronoamperomogram of the convection cell poising at -600 mV and switch to -100 mV vs SHE.

The cell's performance was validated through infrared spectroscopic analysis of electrochemically manipulated the as-isolated deltaTM Hyd-1 single crystals. Figure 4.4C presents the spectrum of a crystal poised at -600 mV for 1.5 hours and then at -100 mV for 1.5 hours in pH 6, where the dominant ν_{CO} band at 1929 cm^{-1} clearly indicates successful enrichment of the Ni_a-SI state. This result demonstrates the system's effectiveness for precise redox control of protein crystals. However, the significant band at 1942 cm^{-1} suggests the proposed inactive state, Ni-A, is not fully activated due to insufficient electrochemical

activation.

While this design represents significant advancement, certain practical limitations remain for crystallographic applications requiring cryoprotection. The addition of glycerol (15% v/v) to crystallisation buffers containing 22% w/v PEG 4000 creates highly viscous solutions that substantially impede electrochemical processes. The color of the mediator cocktail responses very slowly to the set potential (ideally, the colour of indigo carmine changes from intense blue to yellow when it is reduced) and a color gradient is observed in the cell. Therefore, no further potentials were tested with this set-up. However, the cell shows particular promise for generating microcrystal slurries suitable for X-ray free-electron laser (XFEL) studies, where cryoprotection is unnecessary. Although XFEL applications fall beyond the scope of this thesis, this highlights the system's versatility for advanced structural biology techniques requiring redox-controlled protein crystals.

4.4 Pump-circuit Cell

4.4.1 Cell Design and Configuration

The circulating electrochemical cell system represents a significant advancement over previous designs through several key modifications that enhance performance. The complete setup, illustrated schematically in Figure 4.6, features two distinct compartments: a primary electrochemical cell for mediator solution conditioning and a secondary crystal-poising chamber. These components are interconnected via a peristaltic pump (Watson-Marlow 120U/D1) that continuously circulates crystallisation buffer containing selected electrochemical mediators between them.

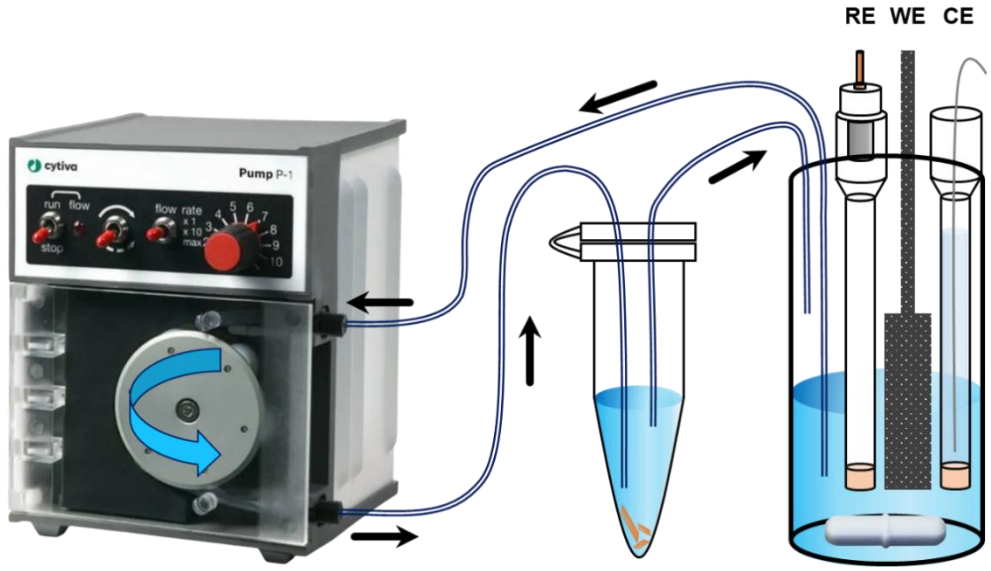

Figure 4.6: Schematic diagram of the circulating electrochemical cell system for protein crystal redox control. The complete setup consists of three main components arranged from left to right: (1) A peristaltic pump for continuous buffer circulation, (2) crystal-poising vial containing protein samples, and (3) main electrochemical cell with three-electrode configuration. The system enables separation of electrochemical conditioning (right chamber) from delicate crystal manipulation (centre vial), connected via tubing to maintain to allow redox mediator cocktail transfer between compartments.

The electrochemical cell employs a glass vial (15 ml, 22 mm diameter, Fisherbrand™) as its main body, housing three critical components. The working electrode consists of high-surface-area carbon fibre felt (35 × 15 × 3 mm, Fuel Cell Store) featuring a microporous structure that enables high current density operation. A saturated calomel reference electrode (ALS Co. Ltd, RE-2BP) provides stable potential measurement, while a custom-designed fritted platinum counter electrode completes the three-electrode system. This counter electrode configuration warrants particular attention, consisting of a reference electrode body compartment fitted with porous glass fritting, filled with 3 M KCl electrolyte, and containing a coiled platinum wire (0.016 inches diameter, Surepure Chemetals). This specialised design addresses the challenges posed by the viscous nature of the crystallisation buffer, which contains high concentrations

of PEG and glycerol. According to Walden's rule, such solutions exhibit significantly reduced equivalent conductivity, necessitating careful electrode placement to minimise cell resistance and ohmic drop effects. [6,7]

The electrochemical cell incorporates a magnetic stir bar to enhance solution convection and accelerate redox equilibrium establishment. The poised mediator solution circulates continuously through PEEK tubing (1/16 inch diameter, IDEX Health & Science) to a separate 1.5 ml Eppendorf vial containing the protein crystals. The inlet needle extends into the headspace above the protein crystals, permitting gentle delivery of fresh mediator solution via controlled flow. The outlet needle is positioned near the solution surface, establishing a consistent bottom-to-top flow pattern within the poising vial that promotes uniform mediator distribution without creating turbulent conditions. This dual-compartment design offers complete isolation of delicate protein crystals from the vigorous stirring required for efficient electrochemical conditioning while maintaining precise control over mediator redox states through the high-current-density working electrode. The system preserves crystal integrity throughout electrochemical manipulation and enables efficient mass transport despite the high viscosity of the crystallisation buffer.

4.4.2 Cell Performances

The electrochemical performance of the pump-circuit cell was systematically evaluated through controlled potential step experiments, as illustrated in Figure 4.7. Panel A displays the current-time response during potential steps from -600 mV to -100 mV versus SHE, while panel B presents open-circuit potential (OCP) monitoring after potential removal.

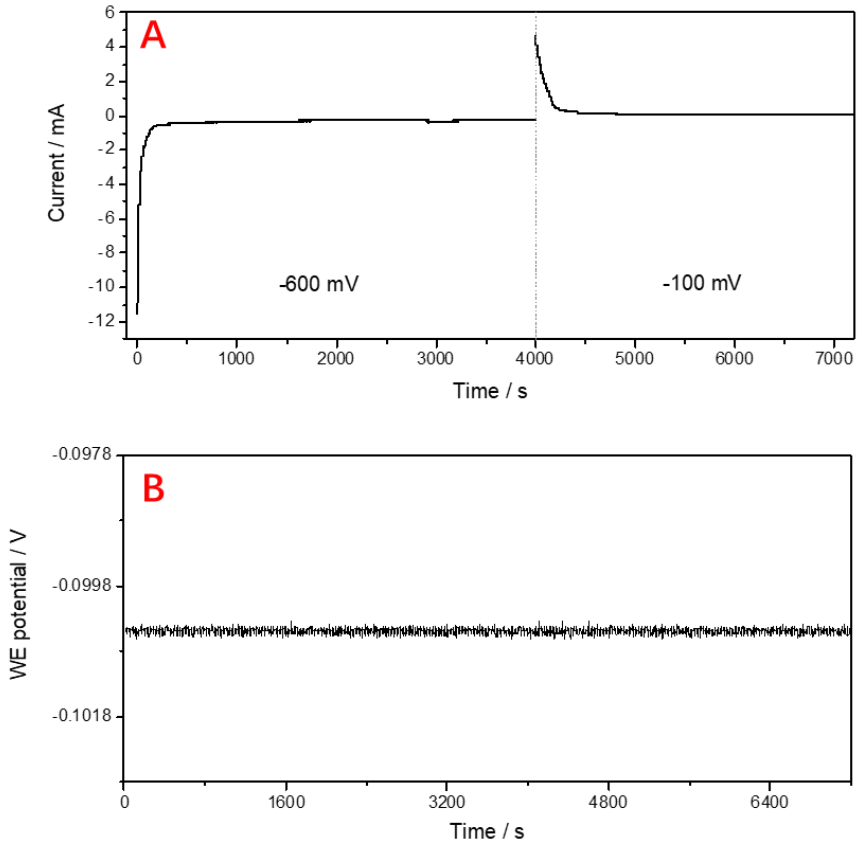

Figure 4.7: Electrochemical characterisation of the pump-circuit cell performance. (A) Chronoamperometry experiment when potential stepped from OCP to -600 mV and to -100 mV. (B) Open-circuit potential (OCP) stability measurement following one hour of electrochemical conditioning at -100 mV, showing the mediator cocktail's ability to maintain redox potential without external polarisation.

The chronoamperometric data in Figure 4.7A reveals substantial reductive current exceeding 10 mA when the cell was poised at -600 mV in the presence of fully oxidised mediator cocktail. This cocktail contained 1 mM each of IC, AQDS, MV, BV and EuBAPTA dissolved in Hyd-1 crystallisation buffer with 15% glycerol. Upon switching the potential to -100 mV, the system generated significant oxidative current and reached equilibrium within 15 minutes, demonstrating markedly faster kinetics compared to previous cell designs that required several hours for equilibration. This performance enhancement directly results from the

improved convection and electrode design in the pump-circuit configuration.

Open-circuit potential measurements following electrochemical conditioning at -100 mV for one hour under anaerobic conditions (Figure 4.7B) demonstrate the system's excellent redox memory capability. The stable OCP reading under inert atmosphere confirms the mediator cocktail's ability to maintain the poised redox level without continuous potential application. This characteristic is crucial for preserving the desired redox state during subsequent *ex-situ* characterisation of protein crystals and provides inherent protection against accidental oxygen exposure through redox buffering action. The effectiveness of mediator cocktails in maintaining target redox levels depends critically on several factors. Most importantly, the redox potential of individual mediators should be within 30 mV of the target potential, and optimal performance is achieved using blends of mediators whose potentials bracket the desired value.

This pump-circuit cell design successfully addresses the key limitations of previous systems through faster equilibration kinetics and reliable redox state maintenance. The full spectroscopic and structural characterisation of crystals produced using this system, including detailed IR spectroscopy and X-ray crystallography analysis, will be presented in Chapter 5, demonstrating its effectiveness for redox-controlled protein crystal studies.

4.4.3 Experimental

Hyd-1

The electrochemical manipulation of Hyd-1 crystals was performed using a carefully controlled protocol. A mediator cocktail solution was prepared containing selected redox mediators at 1 mM concentration each, dissolved in nitrogen-degassed crystallisation buffer (100 mM Bis-Tris,

pH 6, 200 mM Li_2SO_4, 150 mM NaCl, 22% w/v PEG 3350, 15% v/v glycerol). This solution (5 ml) was transferred into the customised electrochemical cell within a nitrogen-filled glovebox (Glove Box Technologies) to maintain anaerobic conditions throughout the experiment.

The offset value of the saturated calomel electrode reference electrode was calibrated by saturated quinhydrone solution. The mediator cocktail was initially poised at -600 mV versus SHE for a minimum of one hour to ensure complete reduction and system equilibrium. During this period, the solution was continuously circulated at 5 ml/min using a peristaltic pump between the electrochemical cell and a separate crystal vial.

For crystal treatment, the pump operation was briefly paused and 10 µL aliquots of the poised cocktail were added to each well of the crystallisation plates containing Hyd-1 crystals. The crystals were then gently transferred via pipette to the crystal vial, taking care to preserve their structural integrity. Approximately 300 µL of poised mediator solution was added to the vial, and the crystals were allowed to settle for about 5 minutes before restarting the pump circulation.

The complete electrochemical activation protocol involved continuous poising for at least 8 hours, followed by adjustment to the target potential for a minimum of one additional hour to establish equilibrium. Finally, the treated crystals were transferred with approximately 20 µL of mediator solution to an empty crystallisation plate well and immediately flash-frozen under anaerobic conditions to preserve their redox state for subsequent crystallographic analysis.

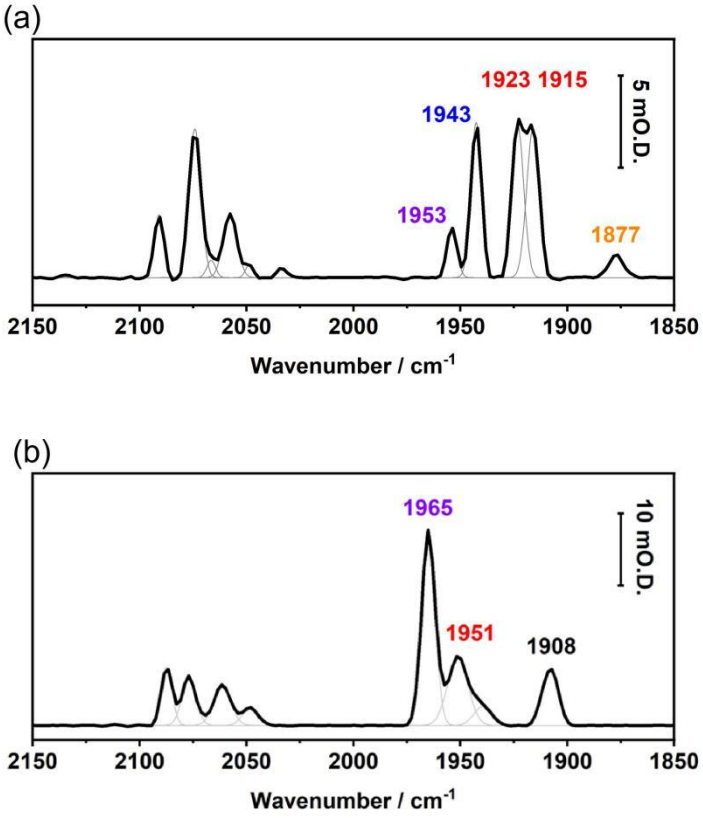

Figure 4.8: The baseline-subtracted IR spectra of Hyd-1 and Hyd-2 single crystal after 30 min H_2-activation, pH 6, 2 cm^{-1} resolution, showing the ν_{CO} and ν_{CN} regions. The catalytic intermediates are assigned in CO region. Fitted peaks are shown in grey. (a) Hyd-1 single crystals after H_2-activation. Apart from the catalytically active states, significant amount of inactive species is presented (1943 cm^{-1}), presumably Ni-A. (b) Hyd-1 single crystals after H_2-activation. No inactive state is observed.

Hyd-2

The electrochemical treatment of Hyd-2 crystals followed a modified protocol compared to Hyd-1, reflecting their distinct activation requirements. The experiments were conducted in Hyd-2 crystallisation buffer (100 mM Bis-Tris, pH 6, 200 mM $MgCl_2$, 22% w/v PEG 3350, 15% v/v glycerol) using the same experimental setup as for Hyd-1. The key difference in procedure stemmed from Hyd-2's requirement for 30-min-hydrogen-activation prior to electrochemical

manipulation instead of long electrochemical activation process. The IR spectra of Hyd-1 and Hyd-2 single crystals after 30-min-hyrdogen-activation are shown in Figure 4.8.

The activation process began with careful transfer of Hyd-2 crystals from crystallisation plates to a 500 µL Eppendorf tube containing approximately 50 µL of buffer solution. The tube, with its lid partially removed, was placed inside a sealed vial. Hydrogen gas (BOC Ltd) was purged through this assembly at a flow rate of approximately 10 ml/min for at least one hour to ensure complete activation of the hydrogenase crystals.

Following hydrogen activation, the mediator cocktail solution (5 ml) was introduced into the system and circulation was initiated. The solution was first poised at -600 mV versus SHE for one hour to establish baseline reduction conditions, followed by adjustment to the target potential for a minimum of one additional hour to achieve equilibrium. During this period, the activated Hyd-2 crystals were carefully loaded into the crystal vial and suspended in 300 µL of poised mediator solution.

The final electrochemical treatment involved maintaining the crystals at the selected potential for at least one hour before collection for subsequent X-ray diffraction (XRD) and Fourier-transform infrared (FTIR) spectroscopic analyses. This protocol ensured proper redox state establishment while preserving crystal integrity throughout the manipulation process.

Single crystal infrared spectroscopy measurements

Infrared spectroscopic analysis was performed on multiple crystals from each poising experiment to verify active site state uniformity across the sample batch. Since direct spectral measurement was not possible for crystals used in diffraction experiments, this quality control step ensured consistent response to the applied potential conditions throughout each

preparation.

The measurement protocol involved carefully transferring poised crystals anaerobically with 20 µL of mediator solution into a transmission IR cell (PIKE). Samples were prepared between two calcium fluoride (CaF_2) windows separated by a 50 µm spacer to maintain optimal sample thickness for infrared measurements. Spectroscopic data were acquired using a Bruker Vertex 70 FTIR spectrometer equipped with a Hyperion 2000 microscope and mercury cadmium telluride (MCT) detector. All spectra were collected across the 4000-600 cm^{-1} range at resolutions of either 2 or 4 cm^{-1}, with more than 254 co-added scans per spectrum acquired using OPUS 8.2.28 software.

IR spectra of poised single hydrogenase crystals via the convection cell

Figure 4.9 shows the IR spectra of single Hyd-1 and Hyd-2 crystals poised at selected redox levels using the convection cell. The spectra are collected from different crystal batches and poising attempts to show the reproducibility of the method. Each targeted active site state is assigned by the absorption band in the ν_{CO} region as shown in Figure 4.9. This demonstrates that targeted active-site-state enriched hydrogenase single crystals can be successfully generated and reproduced using the developed convection cell.

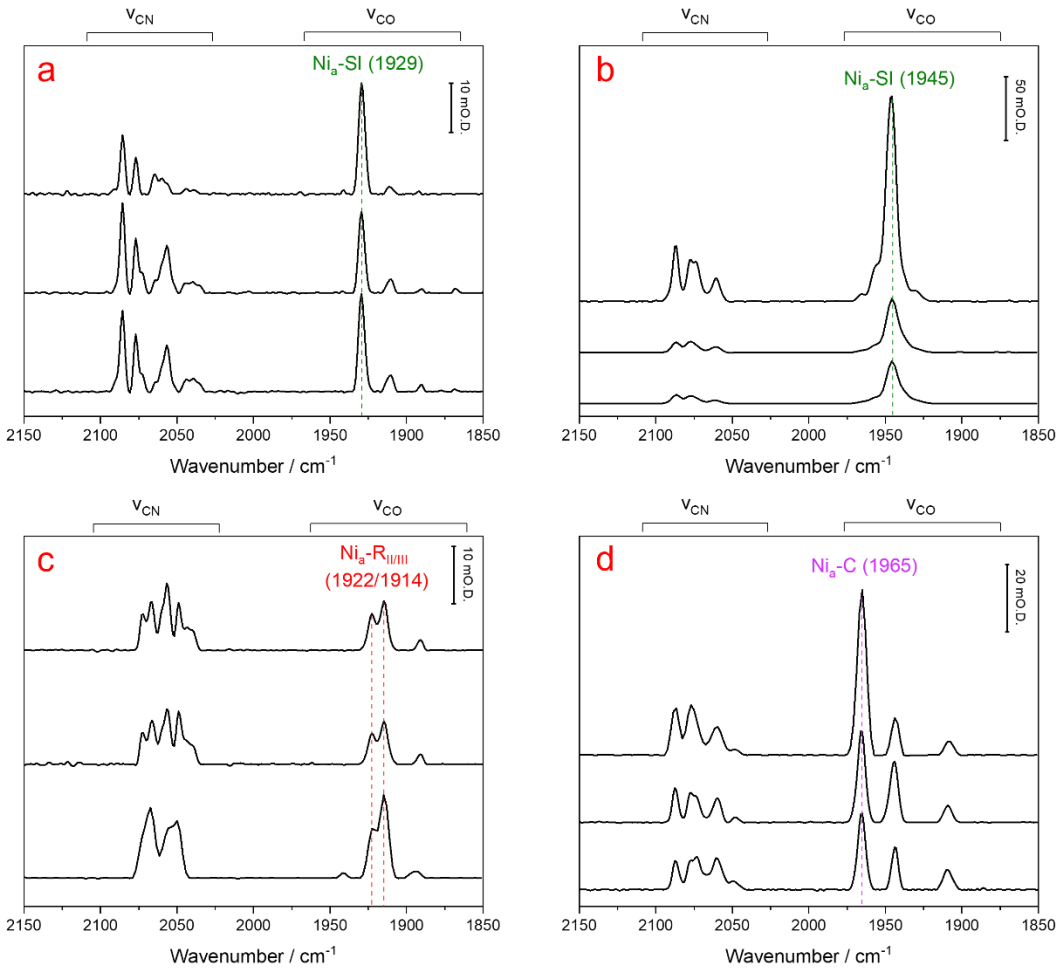

Figure 4.9: IR spectra of hydrogenase single crystals poised at different redox levels via using the convection cell from different attempts, pH 6. Either 2 or 4 cm^{-1} resolution are measured depend on attempts, 256 scans. Both ν_{CO} and ν_{CN} are shown, while the ν_{CO} band(s) of the target active site state is assigned. (a) Hyd-1 in the Ni_a-SI state (-75 mV); (b) Hyd-2 in the Ni_a-SI state (-120 mV); (c) Hyd-1 in Ni_a-R states (-600 mV); (d) Hyd-2 in the Ni_a-C state (-300 mV).

The PIKE transmission IR cell is not tightly sealed and the microscopic IR spectrometer is on the bench under air. Therefore, the stability of specific poised single crystals was not tested in the transmission cell over time. However, after removing the applied potential, a series of IR spectra of Hyd-2 crystals from one poising attempt were collected at various time points, as shown in Figure 4.10. Even though the IR spectra are not collected from a single crystal, the

spectra in Figure 4.10 demonstrate different single crystals after a single poising hold their states reliably over 2 hours.

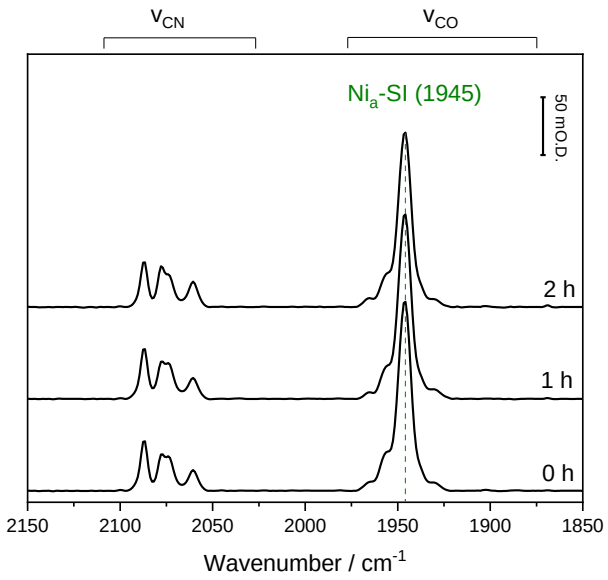

Figure 4.10: IR spectra of Hyd-2 crystals from a same poising attempt after removing the external potential at different time points. 2 cm^{-1} resolution, 256 scans. The spectra are highly identical, while the different intensities are due to crystal size variation.

4.5 References

1 M.-E. Pandelia, H. Ogata and W. Lubitz, *ChemPhysChem*, 2010, **11**, 1127–1140.

2 M.-E. Pandelia, P. Infossi, M. T. Giudici-Orticoni and W. Lubitz, *Biochemistry*, 2010, **49**, 8873–8881.

3 M. Senger, K. Laun, B. Soboh and S. T. Stripp, *Catalysts*, 2018, **8**, 530.

4 P. A. Ash, S. B. Carr, H. A. Reeve, A. Skorupskaitė, J. S. Rowbotham, R. Shutt, M. D. Frogley, R. M. Evans, G. Cinque, F. A. Armstrong and K. A. Vincent, *Chem. Commun.*, 2017, **53**, 5858–5861.

5 S. Kendall-Price, DPhil Thesis, University of Oxford, 2022.

6 Atkins Peter and Paula de Julio, *Atkins' Physical Chemistry*, Oxford University Press, Oxford, 10 th., 2014.

7 D. A. C. da Silva, M. J. Pinzón C., A. Messias, E. E. Fileti, A. Pascon, D. V Franco, L. M. Da Silva and H. G. Zanin, *Mater. Adv.*, 2022, **3**, 611–623.

Chapter 5: Crystal Structures of Hyd-1 and Hyd-2 in Well-Defined Redox States

In this chapter, the *ex-situ* electrochemical cell with circuit pump set up discussed in Chapter 4 is employed to generate Hyd-1 and Hyd-2 in a specific active-site-state-enriched condition. The crystal structures of each long-lived catalytically relevant states of [NiFe]-hydrogenases and all redox conformation of Hyd-1 proximal cluster are obtained in high resolution together with IR spectroscopic verification.

5.1 Introduction

5.1.1 Structural Study on [NiFe]-hydrogenases

Extensive X-ray crystallographic studies of [NiFe]-hydrogenases have revealed key structural features of the enzyme and, more importantly, provided mechanistic insight into its catalysis.[1–10] *E. coli* Hyd-1 and Hyd-2 exist as a heterodimer, each catalytic unit comprising one large and one small subunit (Figure 5.1).[11] The active site, buried within the large subunit, consists of a binuclear NiFe centre in which two cysteine thiolate residues bridge the metal atoms. The Fe is further coordinated by three unusual biological ligands, two cyanides and one carbon monoxide, while the Ni is bound by two terminal cysteine thiolates (Figure 5.1).[12] A third bridging ligand sits between the two metals and varies with the active site's redox state. [9]

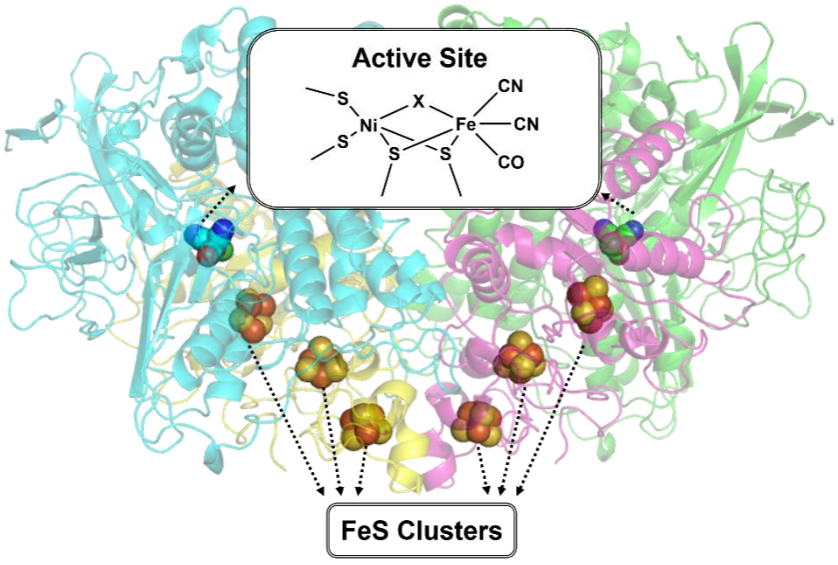

Figure 5.1: The crystal structure of *E. coli* Hyd-1, shown as a dimer of heterodimers (PDB code: 9EQI, this work). The NiFe active site and the three FeS clusters (proximal, medial and distal) are highlighted to illustrate their relative positions. The active site is also shown in skeletal structure.

The small subunit contains three FeS clusters that mediate electron transfer between the protein surface and the NiFe active site, where catalysis occurs. These clusters are designated proximal, medial

and distal according to their increasing distance from the active site.[11]

Proximal FeS Cluster

Recent studies have shown that the unique architecture of the proximal [4Fe3S] cluster in O_2-tolerant, membrane-bound [NiFe]-hydrogenases is crucial for their oxygen tolerance.[4–6,13] Unlike most O_2-sensitive [NiFe]-hydrogenases, which contain the standard [4Fe4S] cluster in the +2 and +1 oxidation states and undergo no structural changes upon dioxygen attack, the specialised [4Fe3S] cluster can adopt three oxidation states (+5, +4 and +3), including an unprecedented high-potential super-oxidised form.[6] This redox property enables the [4Fe3S] cluster to donate two electrons when the active site undergoes exogenous dioxygen attack. By sacrificing two electrons from the proximal cluster, alongside one electron from both the nickel centre and the medial/distal cluster, O_2-tolerant [NiFe]-hydrogenases achieve complete oxygen reduction to water/hydroxide.[13]

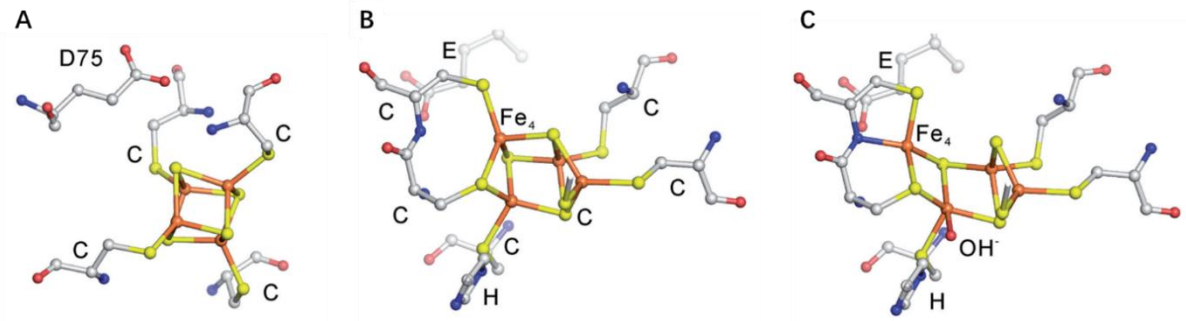

Figure 5.2 The structure of the proximal FeS cluster. (A) The standard [4Fe4S] cluster from *Desulfovibrio vulgaris* Miyazaki F (*DvM*F) [NiFe]-hydrogenase. (B) The [4Fe–3S] cluster in the reduced form of the O_2-tolerant *Ralstonia eutropha* membrane-bound hydrogenase (*Re*MBH). (C) The proximal [4Fe3S] cluster in the super-oxidised form of *Re*MBH. Adapted with permission from H. Ogata, W. Lubitz and Y. Higuchi, *The Journal of Biochemistry*, 2016, 160, 251–258. © 2016 Oxford University Press.

The proximal [4Fe4S] cluster in O_2-sensitive hydrogenases adopts the canonical cubane geometry, in which each iron centre is coordinated by a cysteine thiolate, as shown in Figure 5.2 A.[1,14–16] By contrast,

the O_2-tolerant enzymes feature a distinctive [4Fe3S] cluster that coordinates to six cysteines. In its reduced form (Figure 5.2B), four cysteines bind to the iron atoms as in a cubane, one bridging sulfide is replaced by a cysteine thiolate, and a sixth cysteine coordinates terminally at Fe_4.[4–6,17,18] In the super-oxidised state (Figure 5.2C), Fe_4 swings out of the cluster core to coordinate to the amide nitrogen of that same cysteine, creating an unusual geometry.[6,18,19] This mobility of Fe_4 appears to be the site of redox activity, allowing the cluster to access a +5 oxidation state in its super-oxidised form.[6,7,20]

The [NiFe] active site states

Extensive biophysical studies including FTIR, EPR and X-ray crystallography, have elucidated much of the catalytic mechanism of [NiFe]-hydrogenases.[20–25] In addition to the catalytically inactive Ni-A and Ni-B states, the catalytic cycle is proposed to proceed through four active intermediates: Ni_a-SI; Ni_a-R; Ni_a-C and Ni_a-L.[24] Although these states and various substates are well characterised spectroscopically, obtaining crystal structures of each individual catalytic intermediate remains challenging, and complete structural evidence for some states is still lacking.[26] The skeletal representations of the NiFe centre in its principal redox states, ordered by increasing reduction level, are shown in Figure 5.3.

The unready Ni-A inactive state exhibits a slow activation rate upon treatment with H_2 or chemical reduction.[27] X-ray crystallographic studies have shown that its bridging ligand is OH^-, the same as in the Ni-B state.[28] Recently, Volbeda and co-workers presented high-resolution (1.22–1.80 Å) structures of *Desulfovibrio fructosovorans* [NiFe]-hydrogenase and variants in the Ni-A state, confirming OH^- as the bridging ligand. They furthermore observed oxidative modification of a terminal cysteine, yielding an $S–O–Ni^{3+}–OH^-$ motif.[29] By contrast, the Ni-B inactive state has been characterised more extensively. Crystal structures of Ni-B in multiple [NiFe]-hydrogenases uniformly display an OH^- ligand at the bridging position (Figure 5.3).[1,7,14,15,18]

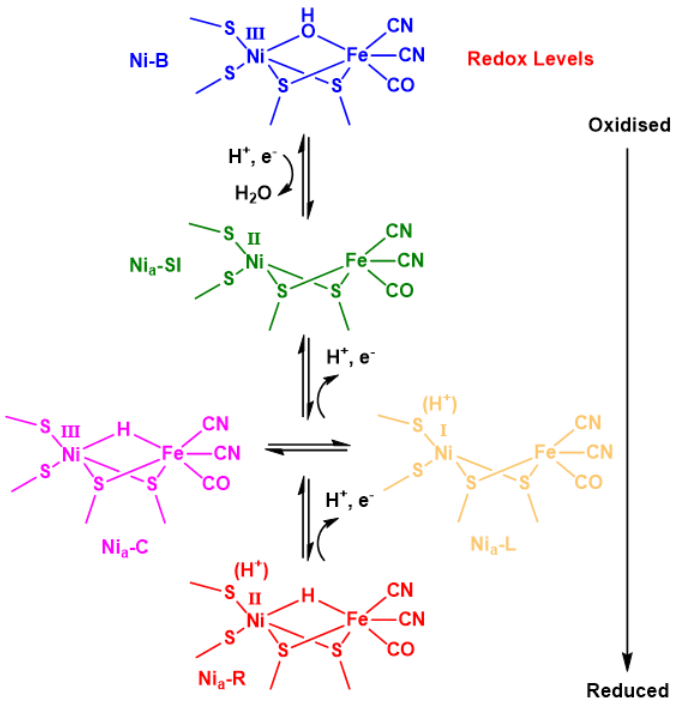

Figure 5.3: The most common redox states of the [NiFe]-hydrogenases active site and their redox transformation. All states are ordered by redox level from most oxidised to most reduced.

The crystal structures of the four catalytically active states of [NiFe]-hydrogenases are challenging to obtain because they interconvert rapidly under catalytic conditions and exist only in a narrow potential window under equilibrium condition. Very limited experimental evidence for the Ni_a-SI state has been reported.[8,10,30] The first crystallographic glimpse of Ni_a-SI came from a CO-liberated *Desulfovibrio vulgaris* Miyazaki F crystal (1.4 Å resolution), obtained by illuminating the CO-inhibited Ni-SCO form with intense white light, demonstrating a vacant bridging site between the metals, consistent with extensive theoretical studies.[10] More recently, Llinás and co-workers solved the structure of an F_{420}-reducing [NiFe]-hydrogenase from *Methanosarcina barkeri* in a Ni_a-SI-enriched state at 1.84 Å resolution, achieved by exposing the as-isolated protein to H_2 for a defined period before crystallisation.[8] However, relatively little is known about the active site states of this specific enzyme.

The Ni_a-R state is the most structurally well characterised catalytic active intermediate. Introducing H_2 as both substrate and reductant to the enzyme produces the Ni_a-R state, which often coexists with the Ni_a-C state.[18] A high resolution structure of Ni_a-R from *DvM*F revealed a hydride bridging the Ni and Fe

ions (Figure 5.3),[15] supporting a heterolytic H_2-cleavage mechanism. Similarly, electron density attributable to a bridging hydride has been observed in the O_2-tolerant membrane-bound hydrogenase (MBH) and its variants from *Escherichia coli* at 1.2–1.5 Å resolution.[18]

Crystal structures of the Ni_a-C and Ni_a-L states remain elusive. However, ENDOR, HYSCORE, EPR and DFT investigations of Ni_a-C suggest that a hydride binds to both Ni and Fe at the active site.[23,31,32]

5.1.2 Opening Questions

The complete structural characterisation of [NiFe]-hydrogenases throughout their catalytic cycle is crucial for understanding their enzymatic mechanism. To date, X-ray structures of [NiFe]-hydrogenases have been limited to chemically or air-oxidised forms, as-isolated preparations and chemically or H_2-reduced states, and consequently have failed to capture all the catalytically active intermediates.[4,11,14,18,28,29] This lack of precise redox control also hinders the investigation of the FeS clusters' redox chemistry, for example, the structure of the oxidised proximal FeS cluster in O_2-tolerant [NiFe]-hydrogenases remains elusive. Moreover, available structures come from many different hydrogenases are hard to compare and study the catalysis systemically. In this chapter, crystal structures of *E. coli* Hyd-1 and Hyd-2 [NiFe]-hydrogenase are presented in defined active-site and FeS cluster states.

5.2 Crystal Structures of [NiFe]-hydrogenase in Well-Defined Active Site State.

In this chapter, crystal structures of [NiFe]-hydrogenase Hyd-1 and Hyd-2 in the Ni_a-SI redox state were determined, together with Ni-SCO structures obtained by CO treatment of pre-poised crystals.

Structures of the more reduced intermediates (Ni_a-R from Hyd-1 and Ni_a-C from Hyd-2), and a Hyd-1 Ni_a-L_{II}-enriched form, were also solved. Finally, the oxidised and super-oxidised forms of the Hyd-1 proximal FeS cluster were rationally prepared and characterised. The data present in this chapter has been submitted on ChemRxiv.[33] All crystallographic data are collected and analysed by Dr. Stephen Carr at the Research Complex at Harwell / Diamond Light Source, and diffraction data reduction was carried out according to published methods. [33]

Table 5.1: The poising conditions of targeting a specific intermediate-enriched state.

Hydrogenases crystal	Redox state	Poised redox level / mV vs SHE	Mediator compositions and pH
Hyd-1	Ni-B	+100	1 mM PMS; 1 mM DCIP, pH6
	Ni-B superoxidised-1	+300	1 mM DCIP; 1 mM FcMeOH, pH6
	Ni-B superoxidised-2	+500	1 mM DCIP; 1 mM FCN, pH6
	Ni_a-SI	-75	1 mM BV; 1 mM AQDS, pH6
	Ni-SCO	-75	1 mM BV; 1 mM AQDS, pH6
	Ni_a-R	-600	1 mM EuEGTA; 1 mM EuBAPTA; 1 mM MV, pH6
	Ni_a-L_{II}	-275	1 mM MV; 1 mM BV; 1 mM AQDS, pH8
Hyd-2	Ni_a-SI	-120	1 mM BV; 1 mM AQDS, pH6
	Ni_a-SCO	-120	1 mM BV; 1 mM AQDS, pH6
	Ni_a-C	-300	1 mM MV; 1 mM BV; 1 mM AQDS, pH6

The crystals in defined redox potential are generated using the electrochemical methods described in Chapter 4.4.3, and the exact electrochemical poising conditions of each crystal are summarised in Table 5.1, including the redox level and mediator compositions and pH. The redox potential of each mediator and their molecular structures are summarised in Table 2.2.

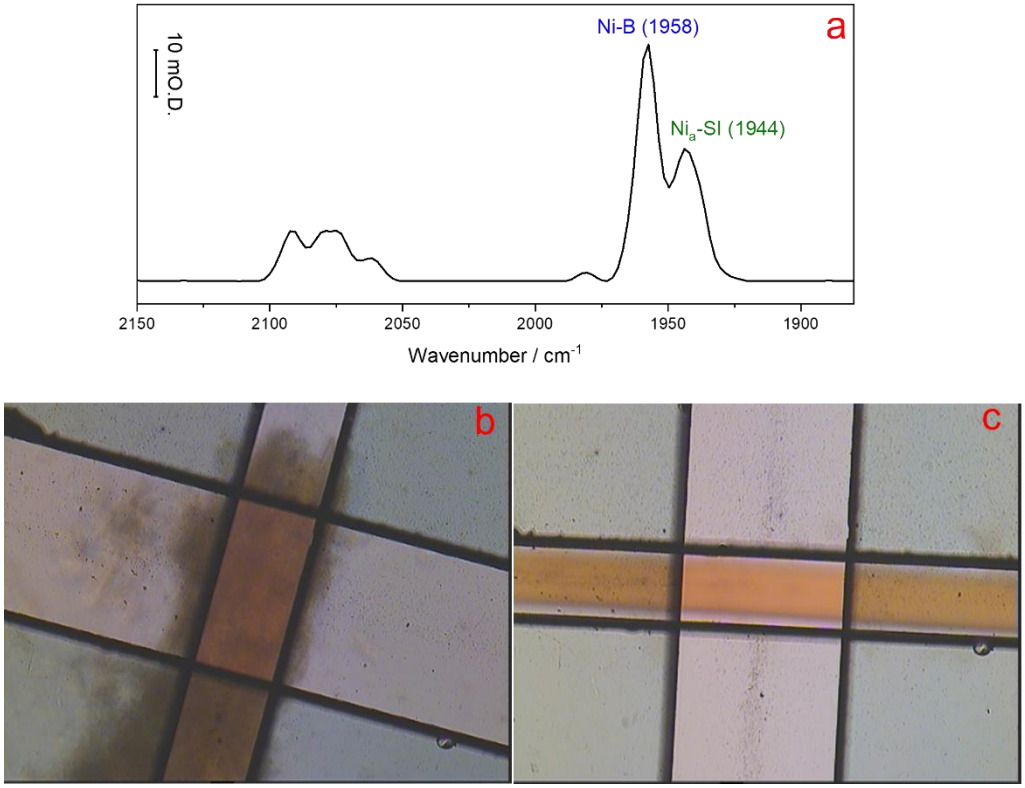

Figure 5.4: (a) The IR spectrum of a Hyd-2 crystal originally poised at the Ni$_a$-SI redox level post X-ray diffraction measurement. Baseline corrected, 256 scans, 4 cm^{-1} resolution. (b) The visible images of the Hyd-2 single crystal post the X-ray diffraction in 15 × magnification, and (c) a fresh Hyd-2 crystal for comparison.

Corresponding IR spectra were recorded on crystals from the same batch (not the exact crystals for structural determination). This is because the redox level and integrity of the crystal are disturbed after multiple freeze and thaw processes and measurements. Figure 5.4a shows the IR spectrum of a Hyd-2 single crystal (poised at Ni$_a$-SI redox level) after the X-ray diffraction experiment. The spectrum shows the majority of the active site in the crystal sample is in the inactive Ni-B state, even though it was stored in liquid nitrogen after the measurement. Figure 5.4b shows the visible image of the Hyd-2 crystal and a freshly prepared (without freezing, panel c) Hyd-2 crystal for comparison. Low-dose (< 1 mGy) helical scans at 16 keV minimised X-ray–induced photoreduction and RCP versus dose plots showed no global signs of radiation damage.[33] Consequently, crystals are assumed to remain in their poising-defined redox and active-site states throughout both crystallographic and spectroscopic measurements, allowing direct correlation of structural and IR data.

5.2.1 Crystal Structure of the Ni_a-SI state

Ni_a-SI is the most oxidised catalytically active state and is believed to be the form that initially reacts with H_2. Under physiologically relevant potentials and inert atmosphere, extensive spectroelectrochemical studies have demonstrated that Ni_a-SI exists within a relatively narrow potential window.[25,34]

The crystal structure of electrochemically poised Hyd-1 at -75 mV (pH 6), corresponding to the Ni_a-SI active site state, is shown in Figure 5.5 a, at a resolution of 1.45 Å. The 2Fo–Fc electron density map (blue mesh) is contoured at 1.5 r.m.s.d., and the Fo–Fc difference density map (green mesh) is contoured at 5 r.m.s.d. The conventional active site architecture of [NiFe]-hydrogenase is observed. Two cyanide ligands and one carbonyl ligand are clearly defined in the 2Fo–Fc electron density map, and the distance between Ni and Fe is measured as 2.70 Å, which is consistent with a reduced active site, as previously reported.[7]

No fully occupied ligand is observed at the bridging position, consistent with previous hypotheses regarding the Ni_a-SI state. However, the Fo–Fc difference map reveals an unprecedented residual electron density at the bridging position at this redox level, with the centroid located approximately 1.9 Å from the Ni atom. This observation is consistent with the presence of a Ni–O coordination bond, and the relatively low peak height compared to a well-ordered water molecule suggests that the Ni_a-SI state contains a partially ordered, or partially occupied water molecule at the bridging site. However, this electron density might also account for other additional states which contains bridging oxygen ligands (such as Ni_a-SI_{rl} at 1911 cm^{-1}).

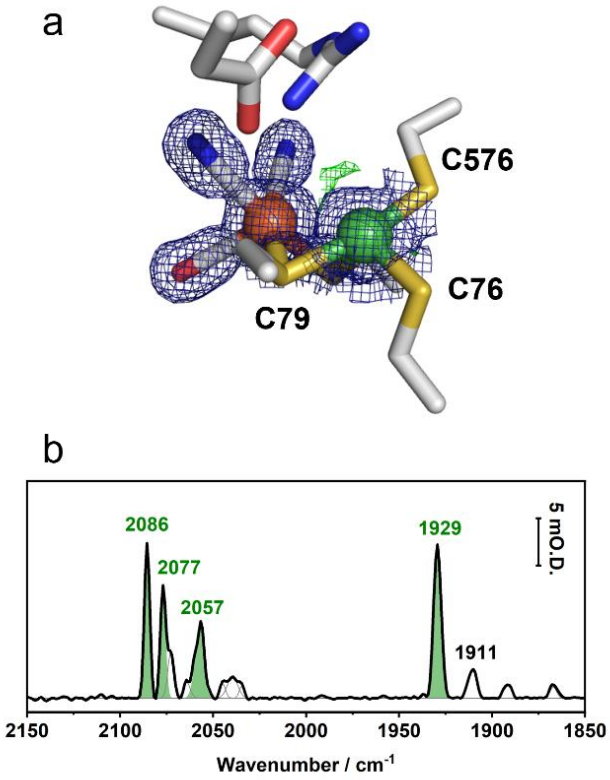

Figure 5.5: Structure and IR spectrum of the Ni_a-SI state of Hyd-1, poised at -75 mV, pH 6. (a) 2Fo-Fc maps (blue mesh) are contoured at 1.5 r.m.s.d., and Fo-Fc density (green mesh) is contoured at 5 r.m.s.d. Nickel (green) and iron (brown) ions in the active site are shown according to the default colour scheme in PyMOL. (b) IR spectrum of a Hyd-1 single crystal from the same electrochemical poising batch for structural determination. The spectrum was recorded with 2 cm^{-1} resolution and 256 scans. Bands associated with the Ni_a-SI state are shaded in olive according to SEC experiments in Chapter 3.

In general the positions of the amino acids are unchanged between poises and crystals, as judged by calculation of r.m.s.d.' s for all atoms. The backbone is pretty rigid with the exception of one or two short loops at the surface, with all other shifts being confined to side chain positions and again on the surface of the protein. Any shifts of amino acids at the active site are slight and could easily be ascribed to modelling error. This agrees with a computational study on *Cupriavidus necator* (NiFe)-hydrogenase that shows the active site of [NiFe]-hydrogenases is very rigid and agrees with Marcus Theory.[35]

Additionally, extra electron density is observed around the thiol group of Cys576, indicating that the

side chain adopts multiple conformations or displays a greater degree of flexibility than is captured in the current model. In Figure 5.6 (2Fo-Fc = 1.5 r.m.s.d., Fo-Fc = 4 r.m.s.d.), the electron density map shows that there is some additional Fo-Fc (green mesh) between C576 and E28, to the right of C576. The larger green blob of density just to the left of C576 is what has been proposed to be a partially occupied water molecule at the active site in the Ni_a-SI state.

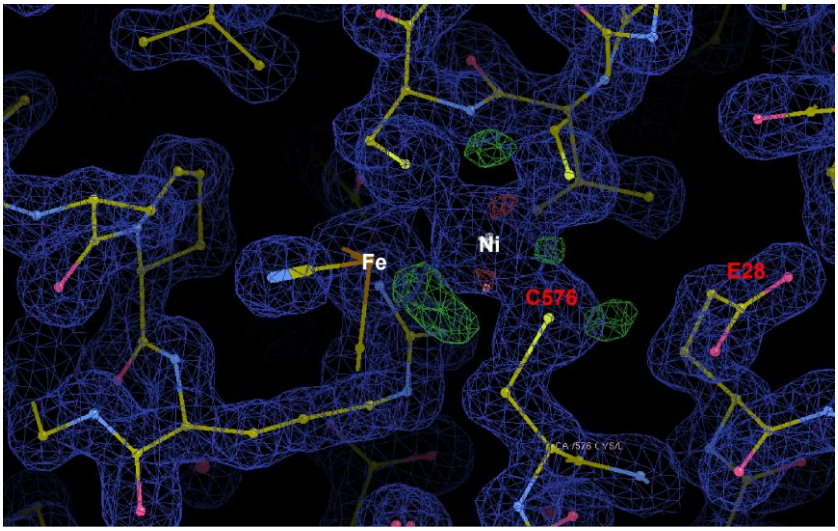

Figure 5.6: The electron density map of the Hyd-1 in the Ni_a-SI state, which demonstrates the extra disorder/motion of C576 in the direction of E28. 2Fo-Fc maps (blue mesh) are contoured at 1.5 r.m.s.d., and Fo-Fc density (green mesh) is contoured at 4 r.m.s.d.

In Figure 5.5 b, the IR spectrum of the Hyd-1 single crystal confirms that the major active site state of the measured sample corresponds to the Ni_a-SI state, based on the predominant absorption band in the ν_{CO} region at 1929 cm^{-1}.[24,25] According to Gaussian peak fitting of the ν_{CO} region, the active site speciation of the Hyd-1 single crystal at this redox level comprises Ni_a-SI (1929 cm^{-1}, 72.8%), Ni_a-SI_{rl} (1911 cm^{-1}, 15.7%), Ni_a-L_{III} (1867 cm^{-1}, 3.3%), and a species with ν_{CO} at 1892 cm^{-1} (6.9%) which does not correspond to one of the known active site states.

The IR spectrum shows three major absorption bands in the ν_{CN} region. The bands at 2086 and 2077 cm^{-1} correspond to the two CN stretching modes of the Ni_a-SI state, associated with the 1929 cm^{-1} band in the ν_{CO} region. The band at 2057 cm^{-1} has been controversially assigned to a CN stretching vibration

of the Ni_a-SI_{rl} state,[36] although its low population complicates definitive attribution. The presence of a partially occupied water molecule, suggested by crystallographic data, indicates that this band may correspond to a water-bound form of the Ni_a-SI state.

Although ca. 15% of the active sites in the Hyd-1 crystal are assigned to the Ni_a-SI_{rl} state, which is proposed to feature an OH^- ligand at the bridging position, the low population of this state likely does not contribute significantly to the observed electron density maps. Therefore, the green mesh electron density observed at the active site is most plausibly attributed to a partially occupied water molecule in the predominant Ni_a-SI state. This is further supported from the observation made for the Ni_a-SI state of Hyd-2. The refinement of Ni_a-SI crystal structure (performed by Dr. Stephen Carr) did not include a water molecule. Refinement of a water at 15% occupancy (the population of the Ni_a-SI_r suggested from the IR spectrum) equates to 1.5 electrons (10 electrons in a water molecule), but actually only the oxygen atom is modelled in these structures as hydrogens are rarely "seen by the x-rays". This means trying to model 1.2 electrons i.e. about the same scattering contribution as a hydrogen atom, which cannot be done reliably at this measured resolution. Modelling with a water at 100% occupancy, led to disappearance of the green density and the water molecule had a very high B-factor ~80 compared to ~10-15 for the rest of the active site. The decision to omit explicit modeling of this water molecule is also motivated by the risk of misinterpretation: without carefully examining the coordinate data a reader may erroneously assume the active site is fully hydrated.

Therefore, the proposal that the observed residual density is a water is based on three main reasons. First, the active site is highly hydrated as evidenced by good electron density for several waters in the active site cavity. Second, the separation between the centre of the peak and the Ni is ~1.9 Å, which matches Ni-O coordination distances well. Third, reductive activation of Ni-B proceeds via formation of a water molecule.

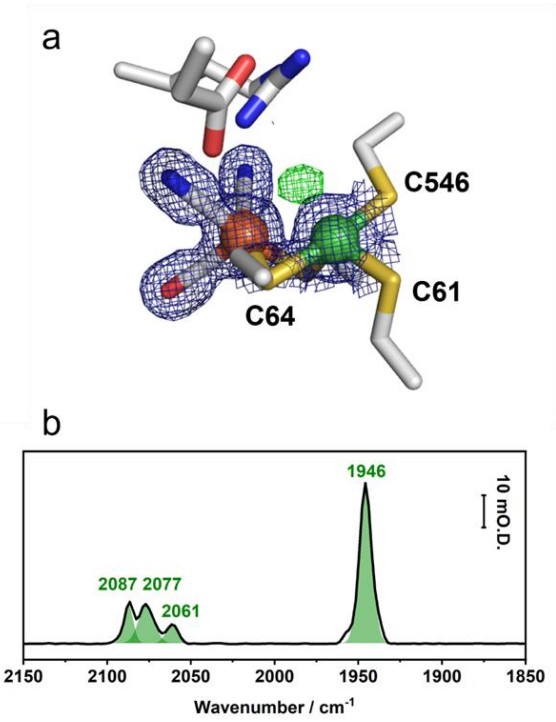

Figure 5.7: Structure and IR spectrum of the Ni_a-SI state of Hyd-2, poised at -120 mV, pH 6. (a) 2Fo-Fc maps (blue mesh) contoured at 1.5 r.m.s.d., and Fo-Fc density (green mesh) contoured at 5 r.m.s.d. (b) IR spectrum of a Hyd-2 single crystal, recorded with 4 cm^{-1} resolution and 256 scans, from the same electrochemical poising batch for structural determination. Bands associated with the Ni_a-SI state are shaded in olive according to SEC experiments in Chapter 3.

The crystal structure of Hyd-2 in the Ni_a-SI state is highly similar to that of Hyd-1. The structure of electrochemically poised Hyd-2 at the Ni_a-SI redox level (-120 mV, pH 6) was solved at 1.37 Å resolution, and the corresponding electron density maps are shown in Figure 5.7 a. The Fo–Fc map (green mesh) contoured at 5.0 r.m.s.d. reveals residual electron density at the bridging position, indicating a partially ordered water molecule located 1.85 Å from the Ni atom and 2.54 Å from the Fe atom. Additionally, residual density is observed near the Ni atom and Cys546 (equivalent to Cys579 in Hyd-1), suggesting similar flexibility of the thiolate group.

The IR spectrum (Figure 5.7 b) of the crystal sample, collected from the same poising batch, exhibits strong absorption bands at 1946, 2077, and 2087 cm^{-1}, confirming that the protein crystal predominantly occupies the Ni_a-SI state (96.8%).[33,37] An additional absorption band at 2061 cm^{-1} is

observed, which is likely associated with a state with a mobile water molecule at the active site in the Ni_a-SI state. This feature is comparable to the 2057 cm^{-1} band previously found in Hyd-1 at the same redox level. Together, the crystallographic and spectroscopic data from Hyd-1 and Hyd-2 provide the first direct structural evidence that the Ni_a-SI state, rather than being completely vacant at the bridging position, is hydrated.

This observation contrasts with another Ni_a-SI structure (1.84 Å resolution) reported for a bidirectional F_{420}-reducing [NiFe]-hydrogenase from the archaeon *Methanosarcina barkeri* MS (*Mb*FRH), which shows no evidence of a bridging ligand.[8] Unlike the precise electrochemical redox control methods employed in this study, the Ni_a-SI state of *Mb*FRH was generated by crystallisation under anoxic conditions (5 % H_2 and 95 % N_2).[8] Despite differences in bridging site coordination, the active sites of *E. coli* Hyd-1/Hyd-2 and *Mb*FRH share common structural features in the Ni_a-SI state. For example, all exhibit a "seesaw" geometry at the Ni centre (exclude the bridging coordination site), with ∠S-Cys(bridging)–Ni–S-Cys(terminal) bond angle of approximately 170°.

5.2.2 The Ni-SCO Crystal Structures

Carbon monoxide (CO) is considered a reversible inhibitor of [NiFe]-hydrogenases although O_2-tolerant [NiFe]-hydrogenases have been shown to be very weakly inhibited during H_2 oxidation.[37,38] The identity of the Ni_a-SI state in both Hyd-1 and Hyd-2 crystals was further confirmed by reaction with CO to generate the CO-bound Ni-SCO state.

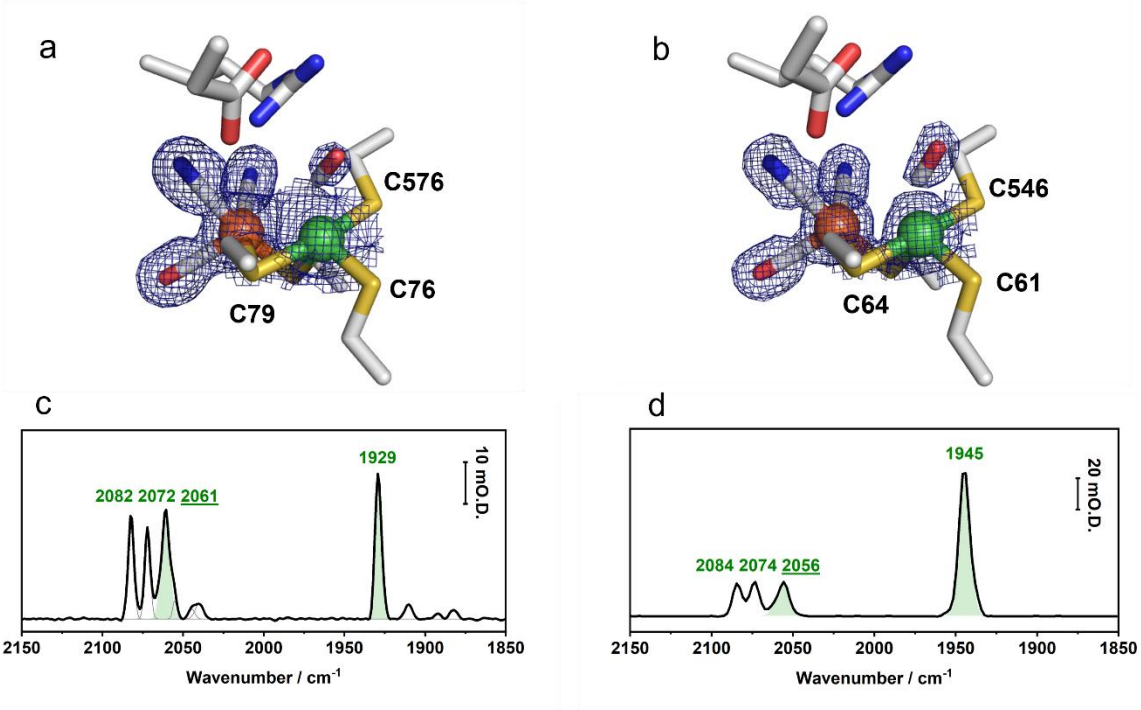

Figure 5.8: Structures and IR spectra of the Ni-SCO state of Hyd-1 and Hyd-2. The crystals in Ni-SCO state are generated from electrochemically poised crystal in Ni_a-SI state with additional CO gas treatment, 2Fo-Fc maps (blue mesh) contoured at 1.2 r.m.s.d.. IR absorption bands associated with the Ni-SCO state are shaded in light olive. (a) Crystal structure of Hyd-1 Ni-SCO state with exogenous CO is modelled at headspace of Ni near the terminal of gas channel, crystal poised at -75 mV. (b) Crystal structure of Hyd-2 Ni-SCO state with bounded exogenous CO has higher peaks compared with that in Hyd-1 and is modelled at similar position compared with that of Hyd-1 Ni-SCO state, crystal poised at -120 mV. (c) IR spectrum of a Hyd-1 single crystal in Ni-SCO state, poised at -75 mV, recorded with 2 cm^{-1} resolution and 256 scans. (d) IR spectrum of a Hyd-2 single crystal in Ni-SCO state, poised at -120 mV, recorded with 4 cm^{-1} resolution and 256 scans.

The electrochemically poised protein crystals at the Ni_a-SI state were collected using 50 µL of a mediator cocktail containing 1 mM of each collected redox mediator (Table 5.1). Ni-SCO crystals were generated by flowing CO gas over the headspace of the container at a rate of 10 mL/min for 30 min. The crystal structures of Hyd-1 and Hyd-2 in the Ni-SCO state were resolved both at a resolution of 1.40 Å and are shown in Figure 5.8, alongside their corresponding IR spectra.

Both structures show clear 2Fo-Fc electron density (blue mesh) for a diatomic ligand bound to Ni,

contoured at 1.2 r.m.s.d. (Figure 5.8 a and b). This is modelled as a CO ligand, coordinated with a distance of 2.0 Å and a Ni–CO bond angle of 134° for Hyd-1 Ni-SCO, and a distance of 1.8 Å and a bond angle of 154° for Hyd-2 Ni-SCO, respectively. In Figures 5.8a and 5.8b, the exogenous CO is observed to coordinate terminally to Ni, pointing directly towards the end of the hydrophobic gas channel above the Ni site, suggesting that exogenous CO is transferred from the protein surface to the active site via the same hydrophobic gas tunnel used for hydrogen transport.[39]

Notably, at the same contour level, the electron density peak for the exogenous CO in Hyd-1 Ni-SCO is weaker compared to that in Hyd-2, suggesting either weaker binding or greater mobility of the bound CO in Hyd-1. This observation is consistent with the longer Ni–CO bond distance observed in Hyd-1 and the electrochemical data reported earlier.[37,40] The CO inhibitor was refined with 100% occupancy (as suggested from IR spectrum (ignoring any difficulties of accurately quantifying 100 % CO vs 90 % CO when the intrinsic CO shift is ~ 1 wavenumber) and allowing the B-factors to adjust to give the best fit between model and electron density. In structural modeling, the conventional approach is to assign full occupancy to well-defined sites unless experimental data, such as difference density or refinement statistics, supports a lower fractional occupancy. In crystallographic refinement, the B-factor and occupancy are highly correlated parameters. To refine one, the other must typically be constrained. Both parameters can be adjusted to improve agreement with the electron density, with occupancy scaling the peak height and the B-factor modulating its width. In practice, their effects on the calculated density post-refinement are often comparable; thus, neither parameter is intrinsically superior for optimising model fit.

The IR spectra of the Ni-SCO states of Hyd-1 and Hyd-2, shown in Figures 5.8c and 5.8d, demonstrate spectroscopic features consistent with exogenous CO binding. Compared to the IR spectra of Hyd-1 at the Ni_a-SI state, an additional band appears in the ν_{CN} region at 2061 cm^{-1}. Similarly, Hyd-2 Ni-SCO shows a new absorption band at 2056 cm^{-1}. These bands are assigned to the exogenous CO ligand from earlier PFIRE assays[37,41] and have similar wavenumbers to those reported for other CO-bound [NiFe]-

hydrogenases in solution, as summarised in Table 5.2.

It is not surprising that the absorption band of the exogenous CO differs from that of the intrinsic CO ligand on Fe. Although the Ni(II) centre is more electron-rich than Fe(II), the relatively long Ni–CO coordination distances (2.0 and 1.8 Å) suggest a weak interaction between the exogenous CO and active site Ni. Additionally, the distorted trigonal bipyramidal coordination geometry and the non-linear Ni–CO bonding fashion indicate poor orbital overlap between CO and Ni. Consequently, the weak pπ–dπ back-donation leads to a higher absorption frequency for the exogenous CO compared to the intrinsic Fe–CO bond.

Table 5.2: Infrared peak positions of the exogenous CO for range of [NiFe]-hydrogenases in Ni-SCO states.

Hydrogenase	Exogenous CO peak position / cm^{-1}	Measured temperature / K	Change of intrinsic CO peak position compared to Ni_a-SI / cm^{-1}
*DvM*F[42]	2056	298	−2
	2061	40	−5
Citrobacter S77-HyB[43]	2059	123	−2
A. aeolicus[44]	2066	298	−2
	2072	40	−4
D. f.[38]	2056	298	−2
MbFRH[8]	2048	80	−9
E. coli Hyd-1	2061	RT	0
E. coli Hyd-2	2056	RT	−1

Although the water-bound Ni_a-SI state appears to have the same absorption in the ν_{CO} region compared with the Ni_a-SI state with a vacant bridging position, it may have different bands in the ν_{CN} region. The additional absorption bands at 2057 and 2061 cm^{-1} observed in the ν_{CN} region in the Ni_a-SI state of Hyd-1 and Hyd-2 are plausibly attributed to the state which contains the partially ordered water molecule bound at the active site. As an additional molecule bound to the active site at the bridging

position, it may alter the electron density at the active site, hence showing an additional band in the ν_{CN} region. These bands disappear upon CO treatment, as the mobile water ligand is displaced by the exogenous CO, consistent with the loss of electron density at the bridging position in the active site.

On the other hand, the position of the endogenous CO absorption band shows minimal change following CO inhibition of the Ni_a-SI state. In Hyd-1 Ni-SCO, the intrinsic CO band remains unchanged compared to that of Ni_a-SI, whereas in Hyd-2 Ni-SCO, the intrinsic CO band shifts by only 1 cm^{-1} to lower wavenumbers. This is comparable to that observed in other [NiFe]-hydrogenases, as summarised in Table 5.2. The stability of the intrinsic CO band position suggests that the overall electron density at the active site remains similar before and after the coordination of an additional CO ligand at the Ni ion. This observation may indicate that the σ-donating effect of the exogenous CO ligand compensates for its π-accepting interaction, thereby maintaining the electronic structure of the [NiFe]-hydrogenase active site during CO inhibition.

5.2.3 Crystal Structure of the Ni_a-R and Ni_a-C States

Electrochemical poising of Hyd-1 and Hyd-2 single crystals at potentials lower than that stabilising Ni_a-SI results in the active sites equilibrating to a mixture of Ni_a-C, Ni_a-L, and Ni_a-R states. Based on information from the microspectroelectrochemical assays (Chapters 3), Hyd-1 and Hyd-2 exhibit potential windows with high populations of Ni_a-R and Ni_a-C, respectively (Table 3.4).

The crystal structures of Ni_a-R (Hyd-1) and Ni_a-C (Hyd-2) were resolved at 1.40 Å and 1.59 Å resolution, respectively, and show a high degree of similarity between them (Figure 5.9 a and 9). Both structures contain 2Fo-Fc maps (blue mesh) displaying the core active site architecture and omit Fo-Fc maps (green mesh) revealing residual electron density at the bridging position. Figures 5.9 c and d show the corresponding IR spectra of single protein crystals poised at the Ni_a-R and Ni_a-C levels, respectively, confirming a high population of the targeted active site species based on the dominant absorption

bands, according to the previous SEC experiment.

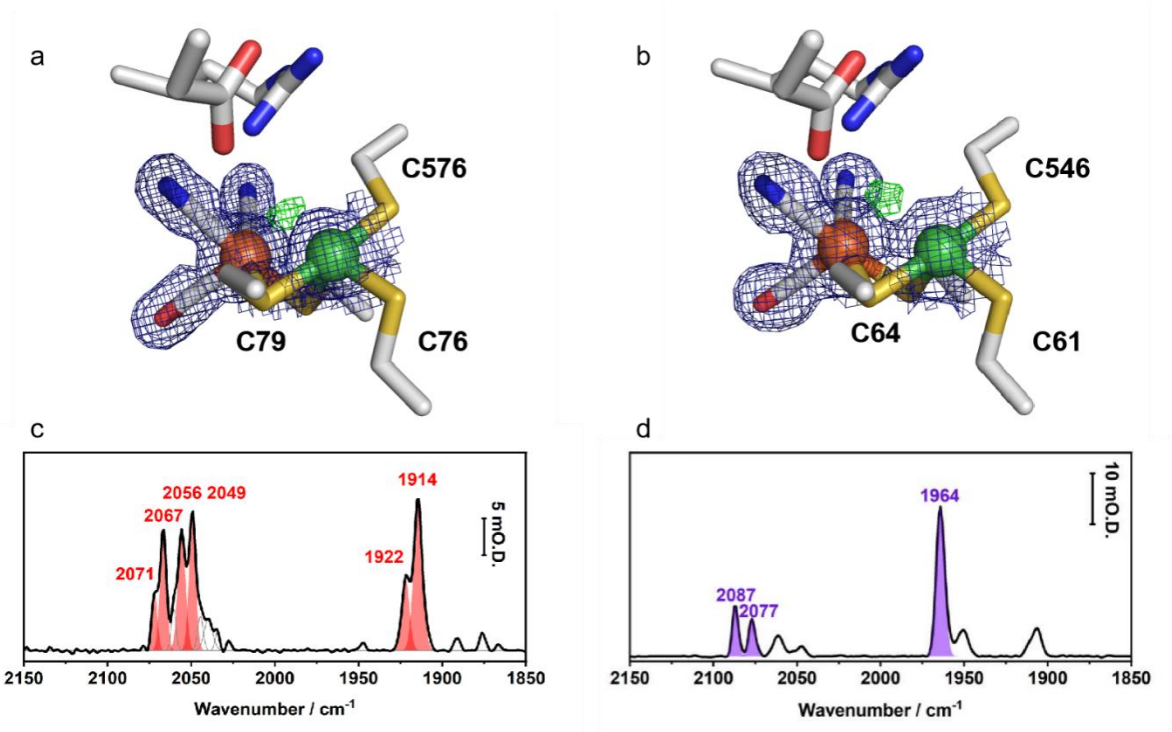

Figure 5.9: Structures and IR spectra of the Ni_a-R state of Hyd-1 and Ni_a-C state Hyd-2. The crystals in Ni_a-R are generated from an electrochemical poise at -600 mV, pH 6 and Ni_a-C state crystals are poised at -300 mV, pH 6. 2Fo-Fc maps (blue mesh) contoured at 1.5 r.m.s.d., Fo-Fc map (green mesh) contoured at 5.0 r.m.s.d.. (a) Crystal structure of Hyd-1 Ni_a-R state. Fo-Fc map (green mesh) showing the electron density at the bridging position. (b) Crystal structure of Hyd-2 Ni_a-C state and the green mesh shows the residual electron density at the bridging position as well. (c) IR spectrum of a Hyd-1 single crystal in Ni_a-R state, recorded with 2 cm^{-1} resolution and 256 scans. Bands associated with the Ni_a-R states are shaded in red. (d) IR spectrum of a Hyd-2 single crystal in Ni_a-C state, recorded with 4 cm^{-1} resolution and 256 scans. Bands associated with the Ni_a-C state are shaded in purple.

When poised at -600 mV (pH 6), the Hyd-1 single crystal contained a mixture of two Ni_a-R substates, Ni_a-R_{II} and Ni_a-R_{III}, with their absorption bands appearing at 1922 and 1914 cm^{-1} in the ν_{CO} region, as shown in Figure 5.9c. These assignments are based on previous crystallo and solution SEC experiments.[34] Ni_a-R states comprise approximately 94% of the enzyme active site population (28.2% assigned to Ni_a-R_{II} and 65.8% to Ni_a-R_{III}). These two substates share the same active site structure,

differing only in the position of the proton on adjacent proton-acceptor amino acid side chains. The positions of the amino acids are unchanged between them, as judged by calculation of r.m.s.d.'s for all atoms. Therefore, the resolution of the electron density maps (approximately 1.4 Å) is insufficient to resolve differences in hydrogen positioning between these substates, and the interpretation of the electron density at the catalytic site remains unaffected. In Figure 5.9a, the electron density around the NiFe cofactor of the electrochemically poised Ni_a-R crystal is shown. A significant peak in the Fo–Fc map (green mesh) is observed between the active site metals. The geometry of this residual electron density is consistent with both Ni_a-R substates containing a bridging hydride.

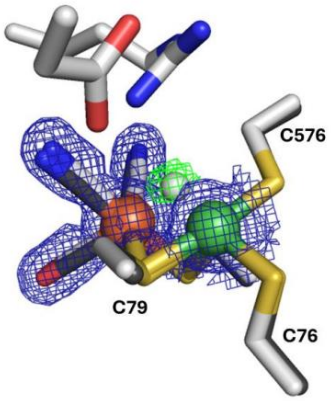

Figure 5.10: Comparison of the Ni_a-R state of Hyd-1 (PDB code 9ER9) with *DvM*F (PDB code 4U9H). Fo–Fc density (green mesh) is contoured at 5 r.m.s.d., and 2Fo–Fc density (blue mesh) is contoured at 1.5 r.m.s.d. The modelled bridging hydride in 4U9H structure superimposes the residual electron density of Ni_a-R structure obtained in this work.

The first crystallographic evidence for a bridging hydride at the active site in Ni_a-R states was obtained from the ultra-high-resolution (0.89 Å) structure of *DvM*F hydrogenase (PDB ID: 4U9H).[15] Figure 5.10 shows the superposition of the Hyd-1 Ni_a-R structure (white bonds) and the *DvM*F Ni_a-R structure (black bonds). Comparison of the electron densities at the active sites demonstrates that the bridging hydride (white sphere), modelled for the *DvM*F enzyme, coincides well with the centre of the residual

Fo-Fc density (green mesh) observed in Hyd-1, further supporting the assignment of the bridging hydride in the electrochemically poised Hyd-1 crystal.

Poising at -300 mV (pH 6) resulted in approximately 90 % of the active sites in the Hyd-2 single crystal equilibrating to the Ni_a-C state (Figure 5.9d). The corresponding Ni_a-C crystal structure (Figure 5.7b) shows no significant deviations from that of the Ni_a-R state. The Fo-Fc omit map reveals residual density at the bridging position, with geometry closely matching that of the hydride observed in the Ni_a-R structure. Such crystallographic similarity between Ni_a-C and Ni_a-R is expected, since conversion of Ni_a-R to Ni_a-C involves proton-coupled oxidation of Ni^{2+} to Ni^{3+} without major rearrangement of the metal-ligand framework, and the change in formal oxidation state has minimal impact on the overall electron density detected by X-ray crystallography.

Table 5.3: Metal-hydride geometry in Hyd-1 Ni_a-R and Hyd-2 Ni_a-C states.

Active site state (map resolution)	Ni_a-R (1.4 Å)	Ni_a-C (1.59 Å)
Fe-Ni separation	2.56 Å	2.61 Å
Ni-H bond length	1.69 Å	1.66 Å
Fe-H bond length	1.64 Å	1.68 Å
Fe-H-Ni angle	89.9°	102.3°

Table 5.3 summarises the active site geometry of Hyd-1 in its Ni_a-R state and of Hyd-2 in its Ni_a-C state. The overall arrangements at the NiFe cofactor are very similar in both states. Although Ni_a-R represents a more reduced state than Ni_a-C, the Ni–H and Fe–H bond lengths are comparable, whereas the Fe–H–Ni bond angle differs by approximately 12°.

The metal–hydride bond would theoretically be expected to shorten in Ni_a-C, owing to a more electron-deficient bimetallic centre. However, these unexpected results may arise from:

1. Electron buffering by π-accepting ligands (CO and CN^-) at the Fe site, which can delocalise charge and minimise bond-length changes; and/or

2. Limitations of the crystallographic resolution (~1.4 Å), which restricts precise determination of subtle bond-length differences.

5.2.4 Crystal Structure of the Ni_a-L state

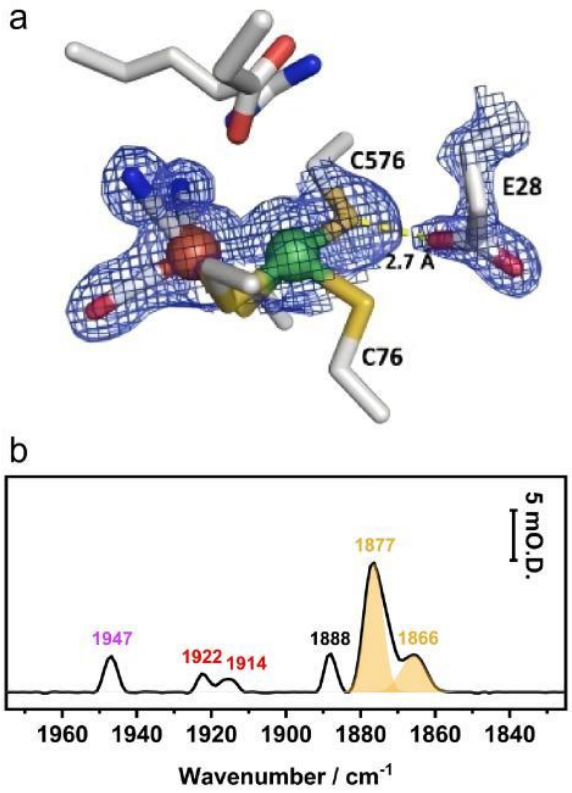

Figure 5.11: Structure and IR spectrum of the Ni_a-L state of Hyd-1 both poised at -275 mV, pH 8. (a) 2Fo-Fc maps (blue mesh) contoured at 1.5 r.m.s.d., the hydrogen bond between C576 and E28 is shown in yellow dash line. (b) IR spectrum (ν_{CO} region) of a Hyd-1 single crystal recorded with 2 cm^{-1} resolution and 256 scans. Bands associated with the Ni_a-L state are shaded in light yellow according to previous assignment.

Ni_a-L state has been shown as a long-lived intermediate during turnover conditions.[24] Electrochemical poising of a single Hyd-1 crystal at a mild reducing potential (-275 mV, pH 8) enriches the active site into a mixture of Ni_a-L substates, based on earlier SEC studies.[36,45] Figure 5.11 b shows the IR spectrum of the poised crystal (same batch) in the ν_{CO} region. The spectrum is dominated by bands at 1877 cm^{-}

[1] and 1866 cm^{-1}, corresponding to Ni_a-L_{II} (65 %) and Ni_a-L_{III}, respectively, as established in previous spectroelectrochemical studies.[24,25] These Ni_a-L substates resemble those of Ni_a-R and are thought to arise from sequential proton transfers away from and into the active site. Additional residual peaks at 1947, 1922 and 1914 cm^{-1} indicate that the crystal sample also contains reduced active-site species (Ni_a-C and Ni_a-R substates), which remain in equilibrium with Ni_a-L at the retained redox level.

Figure 5.11a shows the crystal structure of the Hyd-1 single crystal poised at the Ni_a-L redox level, with the 2Fo-Fc map (blue mesh) contoured at 1.5 r.m.s.d. The primary coordination sphere of the active site closely resembles those of the reduced Ni_a-C and Ni_a-R states. The Ni-Fe separation remains at ca. 2.6 Å, consistent with an active conformation rather than the 2.95 Å separation observed for the Ni-B state.

Elongated electron density is visible for the Ni atom in the NiFe plane, and anomalous difference density extends along the same axis. Overlapping peaks for Ni and Fe, together with residual Fo-Fc density between the two metals, are consistent with the presence of a direct metal–metal bond in the Ni_a–L state in agreement with previous computational predictions.[46]

In contrast to these similarities, no electron density is observed at the bridging position in either the 2Fo-Fc or Fo-Fc maps, indicating that the bridging site is vacant and the hydride bridging ligand has been lost. This is consistent with the proposed catalytic cycle, in which Ni_a-L undergoes one-electron oxidation coupled with proton removal to regenerate Ni_a-SI which also carries a vacant coordination site.

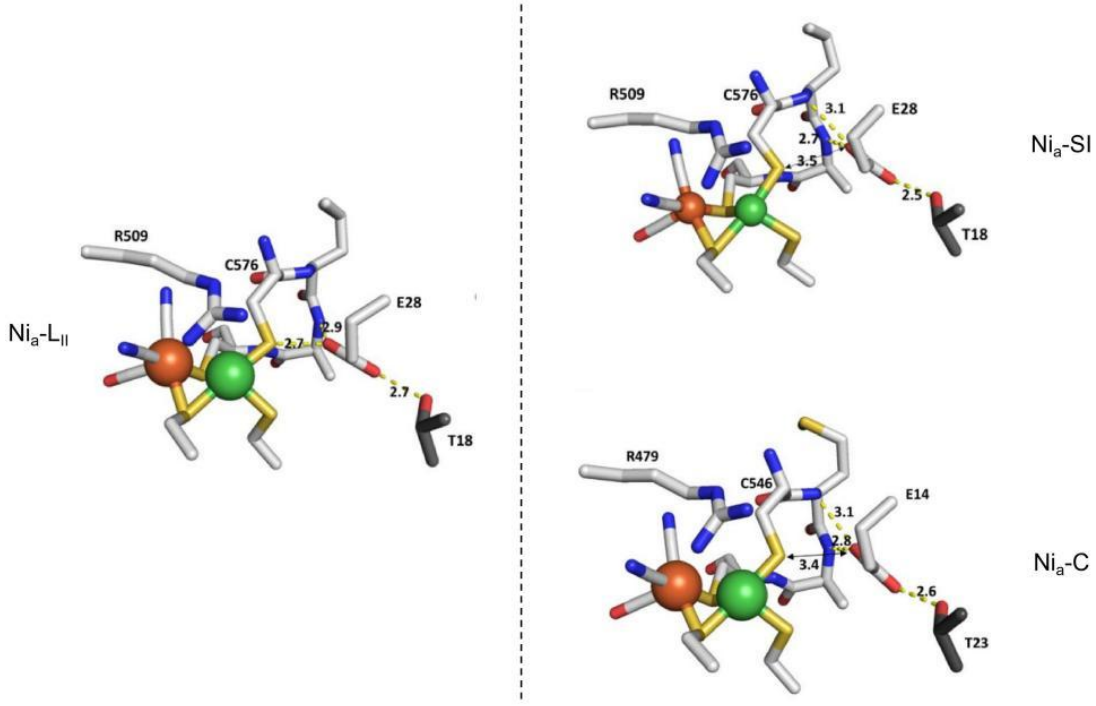

Figure 5.12: The comparison of the amino acid conformation between the Ni_a-L_{II} and Ni_a-SI and Ni_a-C states. The Glu28 (E28) in the Ni_a-L_{II} shows the "swung-in" conformation with respect to the active site and its carboxylate group is 2.7 Å away from the thiol group on Cys576 (C576). In contrast, the E28 in the Ni_a-SI state and E14 (Hyd-2 equivalent) in the NI_a-C state show the "swung-out" conformation with distance 3.5 Å and 3.4 Å to the terminal cysteine, respectively.

In the outer coordination sphere, reduced 2Fo-Fc density for the Glu28 side chain is evident, accompanied by an increased B-factor for its side chain relative to the main chain (~1.5 versus ~1.2). Unmodelled Fo–Fc density between Glu28 and Cys576 can be accounted for by rotation about the C_{beta}/C_{gamma} bond, bringing the Glu28 carboxylate closer to Cys576 to accept a proton. This conformational change requires breaking the hydrogen bond to the backbone amide of Ala578, that the geometry consistent with proton transfer. As shown in Figure 5.11 and 5.12, the "swung-in" conformation of Glu28 in the Ni_a-L_{II} substate shortens the oxygen-sulphur distance to 2.7 Å. In contract, the E28 in the Ni_a-SI state and E14 (Hyd-2 equivalent) in the NI_a-C state show the "swung-out" conformation with distance 3.5 Å and 3.4 Å to the terminal cysteine, repectively. This provides the first direct structural evidence for Glu28's role in proton delivery to or transfer away from the active site.

5.3 Structural Changes of Proximal FeS Cluster in Different Redox States

The unusual structural and redox properties of the proximal FeS cluster in oxygen-tolerant [NiFe]-hydrogenases (including Hyd-1) are believed to underlie their remarkable O_2-tolerance. The [4Fe3S] cluster adopts three distinct redox states and is capable of undergoing two consecutive one-electron oxidations to protect the active site from oxygen attack.[13] Precise redox control of electrochemically poised Hyd-1 crystals at increasingly oxidising potentials permits the decoupling of structural changes occurring at the NiFe centre from those in the proximal cluster.

In Figure 5.13, IR spectra measured from Hyd-1 crystals poised at +100 mV, +300 mV and +550 mV versus SHE (pH 6) confirms that the predominant active site species is Ni–B (ν_{CO} 1943 cm^{-1}). As expected, clear 2Fo–Fc density for a bridging hydroxide is visible between the catalytic Ni and Fe atoms. No evidence of cysteine oxygenation is observed, in contrast to the air-oxidised Hyd-1 structure.[7]

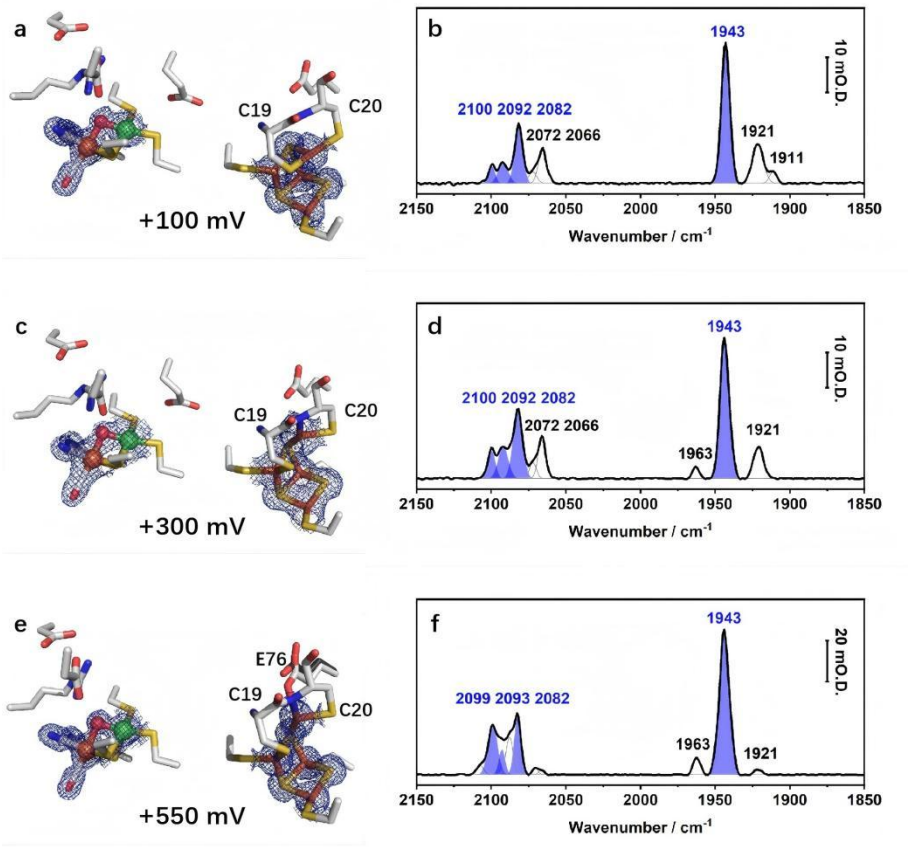

Figure 5.13: Potential-dependent crystal structures and IR spectra collected during oxidative inactivation of Hyd-1. 2Fo-Fc electron density electron density (blue mesh) is contoured at 1.5 r.m.s.d. for both the Ni–Fe active site and the proximal FeS cluster. (a, b) Poising at +100 mV (vs SHE) reveals a bound hydroxide at the active site; the proximal cluster remains in its closed (reduced) conformation (1.40 Å resolution). The IR spectrum confirms predominant Ni-B formation. (c, d) Increasing the potential to +300 mV causes no change at the active site but triggers the proximal cluster to adopt the open, super-oxidised conformation (1.51 Å resolution). (e, f) Further raising the potential to +550 mV induces rotation of Glu76 toward the mobile iron of the proximal cluster, stabilising the super-oxidised form and enabling electron transfer back to the active site, reducing inhibitory hydroxide to water (1.40 Å resolution). All IR spectra were recorded at 2 cm^{-1} resolution with 256 scans.

At +100 mV, the proximal [4Fe3S] cluster remains in the closed conformation, with the mobile Fe atom coordinated by the side-chains of Cys19 and Cys20. Analysis of Fo-Fc maps suggests that the closed form is present in ~90 % of molecules, with the remainder adopting the open, super-oxidised state.

Raising the potential to +300 mV versus SHE causes over 90 % of the proximal clusters to switch to the open conformation, now featuring additional coordination of the mobile Fe by the main-chain amide of Cys20. Further increasing the potential to +550 mV does not alter the metal cluster itself, but induces Glu76 to swing toward the mobile Fe, thereby stabilising the open, super-oxidised form. This is illustrated in Figure 5.14 that contains superposed structures of oxidised active site and proximal FeS cluster of Hyd-1, showing conformational changes under increasing applied potentials. While the active site barely changes its conformation or composition, the proximal cluster undergoes two-step conformational change.

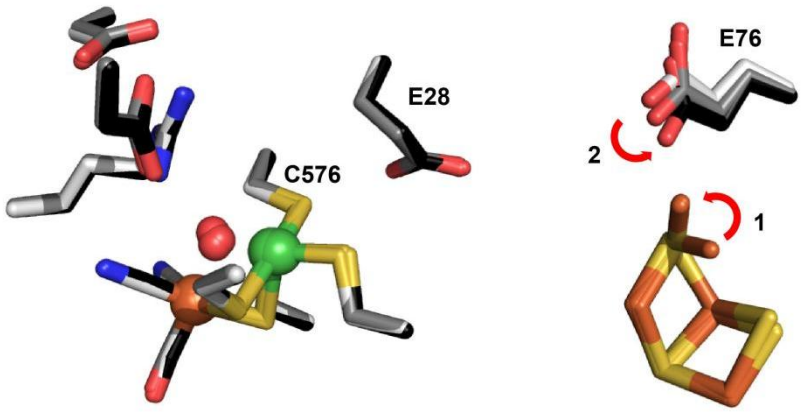

Figure 5.14: Superposed structures of oxidised active site and proximal FeS cluster of Hyd-1 show conformational changes that occur as the enzyme responds to oxidative inactivation, +100 mV state shown in white, +300 mV state shown in grey and +550 mV state shown in black. The red arrows show the order of conformation change in order to the increasing redox levels.

5.4 Discussion

By combining data from microspectroelectrochemical assays and the flow electrochemical cell, crystals in each long-lived redox intermediate state of [NiFe]-hydrogenase have been isolated, verified and

structurally characterised. Overall, the [NiFe]-hydrogenase active site exhibits only minor structural alterations in its primary coordination sphere across all catalytically relevant redox states.

The root-mean-square deviations (r.m.s.d.) of all atoms in the NiFe cofactor and its coordinating residues (Cys76, Cys79, Cys576, Cys579 for Hyd-1 and Cys61, Cys64, Cys546, Cys549 for Hyd-2), relative to the Ni_a-SI state of Hyd-1, are summarised in Table 5.4. [NiFe]-hydrogenases catalyse the H_2/H^+ interconversion with very high turnover frequencies. These observations are consistent with the Marcus theory, which predicts that minimising reorganisation energy, achieved here by the structural rigidity of the conserved residues surrounding the NiFe active site, facilitates efficient electron tunnelling.[33]

Table 5.4: R.M.S.D values in the positions of all atoms in the NiFe active site and metal coordinating residues for each redox state relative to the Hyd-1 Ni_a-SI state.

Hydrogenase	Redox state	R.M.S.D. (Å)
Hyd-1	Ni-B (+100mV)	0.082
	Ni-B (+300mV)	0.107
	Ni-B (+550mV)	0.098
	Ni-SCO	0.046
	Ni_a -R	0.059
	Ni_a -L_{II}	0.084
Hyd-2	Ni_a -C	0.128
	Ni_a -SI	0.129
	Ni-SCO	0.143

The first high-resolution structures of the Ni_a-SI state of [NiFe]-hydrogenase generated under controlled conditions have now been determined for Hyd-1 and Hyd-2. These structures confirm earlier, limited reports of a vacant bridging site at Ni_a-SI but also reveal residual density near the Ni centre in

each enzyme. The geometry of this density is consistent with Ni–O coordination and likely suggests a sub-population (~30 %) of enzyme molecules in the crystal lattice that retain a water ligand. The refinement of the structure did not include any molecule in the bridging position, and the water-occupancy ratio is estimated from the comparison of the observed peak height and a 100 % occupied water. Overall, this provides the first direct structural evidence that the Ni_a-SI state can be hydrated and suggests that a functionally relevant water molecule may occupy the active-site cavity.

Structures of *Mb*FRH [NiFe]-hydrogenases in the Ni_a-SI state do not show density at this position, but those were solved at lower resolution (~1.84 Å) and may not resolve minor features.[8] Likewise, the *DvM*F Ni_a-SI structure obtained by photolysis of Ni-SCO (1.40 Å resolution) lacks residual density at the bridge.[10] This is because photodissociation in frozen crystals likely prevents water from relaxing into the cavity once CO is liberated.[43] By contrast, IR spectroscopy and DFT studies of the regulatory hydrogenase from *C. necator* previously postulated a water-bound intermediate, termed Ni_r-S_{II}.[32]

Nevertheless, the crystallographic data presented here are not sufficient to prove that the water ligand participates directly in catalysis. Electrochemical poising equilibrates the enzyme to various redox states, but under inert atmosphere and mild potentials, extended equilibration may favour the thermodynamically most stable species. [NiFe]-hydrogenases catalyse H_2/H^+ turnover at rates exceeding 10^3 s^{-1};[16] the truly catalytically relevant form of Ni_a-SI may be the vacant bridge species, acting as a kinetic intermediate to enable rapid substrate binding and product release.

The exogenous CO coordination geometries in Hyd-1 and Hyd-2 Ni-SCO states agree with those of other CO-bound [NiFe]-hydrogenases (Table 5.5) yet display higher ligand occupancies than O_2-sensitive enzymes. This likely reflects the ease of CO binding to Ni_a-SI state in absence of H_2, owing to the vacant bridging site. Although CO has not traditionally been viewed as an inhibitor of O_2-tolerant hydrogenases,[44] IR spectroscopy clearly demonstrates its reversible binding in absence of H_2.[37] The Ni-SCO structure of Hyd-1 thus provides the first visualisation of CO bound to an O_2-tolerant enzyme at high occupancy.

Attenuated electron density and relatively long Ni–C distances (2.0 and 1.8 Å) indicate weaker CO affinity in Hyd-1. Weaker binding may also result from the narrower gas-tunnel terminus in Hyd-1 (~0.3–0.5 Å smaller than in Hyd-2), which sterically restricts CO access to the Ni centre. In general, A more restricted environment at the active site will also induce a greater steric restraint on the ligand binding geometry. Such confinement forces CO into a bent conformation (Ni–C≡O < 180°), despite its sp hybridisation, to avoid clashes with conserved cysteine and headspace amino residues. A comparable bent geometry is seen in haemoproteins (e.g. Fe–C≡O ~ 140° in myoglobin–CO),[47] where the distal histidine hinders linear binding. This bent binding mode may additionally prevent irreversible CO poisoning, in agreement with protein-film electrochemistry demonstrations of reversible CO inhibition of [NiFe]-hydrogenases.[37]

Table 5.5: Geometry of exogenous CO ligands bound to the active site of different [NiFe]-hydrogenases.

Hydrogenase	Resolution / Å	CO occupancy	Ni–C distance / Å	Ni–C≡O angle / °
MbFRH[8]	1.99	50 %	1.74	162
DvMF[10]	1.2 – 1.4	80 – 96 %	1.77	160
Citrobacter S77-HyB[43]	1.77	26 %	1.84	158
***E. coli* Hyd-1**	1.4	100%	2.0	134
***E. coli* Hyd-2**	1.4	100%	1.8	154

Previously, crystal structures of the Ni_a-R state, or mixtures of Ni_a-R and Ni_a-C, have been obtained by H_2 incubation or sodium dithionite reduction,[3,8,11,14,18] but the Ni_a-C state alone has not been structurally characterised. In this chapter, an electrochemically isolated Ni_a-C crystal structure has been verified and analysed. The Ni_a-R and Ni_a-C structures display highly similar first coordination spheres at the NiFe active site, and both exhibit residual electron density at the bridging position consistent

with a hydride ligand. Although the Ni_a-C cofactor is formally more oxidised, and thus more electron-deficient than Ni_a-R, the Ni–H and Fe–H bond lengths and Fe–H–Ni angles are almost identical (Table 5.3). This similarity may arise from (1) intrinsic electronic differences between Hyd-1 and Hyd-2, (2) π-accepting CO and CN^- ligands at Fe acting as electronic buffers to equalise metal electron density between redox states, and (3) the moderate resolution of the Ni_a-C structure (1.59 Å), which limits the detection of subtle sub-atomic variations.

The crystal structure of the Ni_a-L_{II} state has been characterised for the first time. The Ni_a-L substates are believed to correspond to sequential protonation events on active-site amino acid side chains. In the Ni_a-L_{II} structure, Glu28 adopts a "swung-in" conformation relative to its positions in Ni_a-SI and Ni_a-C (Figure 5.12). The hydrogen-bonding networks in Ni_a-SI and Ni_a-C (right side of Figure 5.12) are highly similar, with only slight differences in bond lengths arising from minor alterations in the active-site geometry. In Ni_a-L_{II}, the Glu28 carboxylate moves from approximately 3.5 Å to 2.7 Å from the Cys576 thiolate sulphur (Figure 5.12), placing it within hydrogen-bonding distance.

Previously, ultra-high-resolution (0.89 Å) crystallography of the Ni_a-R state (*DvM*F, PDB 4U9H) identified the terminal cysteine (Cys576) as the first proton acceptor in the proton-transfer pathway.[15] The "swung-in" Glu28 in Ni_a-L_{II} provides direct structural evidence that protonation of an active site atom is a prerequisite for catalysis, with Glu28 acting as a critical facilitator of proton transfer. This observation is consistent with steady-state kinetic analyses that implicated Glu28 in initiating multiple proton egress routes via a Grotthuss-type hopping mechanism.[18] Interestingly, however, the crystal structure of Ni_a-R_{II} and Ni_a-R_{III} mixture does not show the same "swung-in" conformation of Glu28 residual, plausibly implying the Ni_a-R to Ni_a-C and Ni_a-L to Ni_a-SI might have different proton transfer pathway. These data, however, do not conclusively establish Glu28 as the second proton acceptor. Crystallographic characterisation of the Ni_a-L_I and Ni_a-L_{III} substates, under optimised redox and pH conditions, or other methods, will be required to capture further conformational changes and complete the structural sequence of the proton-transfer pathway.

Electrochemical poising of Hyd-1 crystals at progressively more oxidising potentials isolates the Ni-B active site state in each case, while triggering distinct conformational changes in the proximal FeS cluster. As the potential is raised from +100 mV to +550 mV versus SHE (pH 6), the primary coordination sphere of the NiFe cofactor remains essentially unchanged, whereas the mobile Fe_4 ion is progressively stabilised closer to Glu 76 (Figure 5.12). At poising potential of +100 mV, the proximal cluster retains the closed conformation.[17] The closed conformation of the proximal cluster is typically associated with the reduced (+3) state.[20] However, the applied poising potential (+100 mV) lies between the midpoint potentials of the oxidised (+30 mV) and superoxidised (+230 mV) states, indicating predominant occupancy of the oxidised (+4) state.[17] This represents the first isolation of an oxidised proximal cluster conformation in an oxygen-tolerant hydrogenase, which has previously been observed as an approximately equal mixture of oxidised and superoxidised forms[5,20] or entirely in the superoxidised (+5) state.[20,48] The subtle conformational changes of proximal cluster at +3 and +4 state is very subtle due to the oxidation typically results in only a slight contraction of Fe-S bond length.

Upon increasing the potential above the midpoint of the oxidised/superoxidised couple, the cluster switches almost entirely to the open, superoxidised conformation, and further potential increments reveal how the protein scaffold, notably Glu 76, adjusts to stabilise this highly oxidised state, presumably due to strong electrostatic attraction. Previous analysis of oxidised Hyd-1 structures suggested that mobility of Glu76 enabled its carboxylate side chain to accept a proton from the backbone amide of Cys20, thereby facilitating coordination to Fe_4.[20] However, our +300 mV structure shows that Fe_4 is already coordinated by the Cys20 main-chain amide, implying that deprotonation has occurred prior to any observable movement of Glu76. This finding suggests that Glu76 instead serves to electrostatically stabilise the cluster in its most oxidised state. The ability to isolate each active-site and proximal-cluster state independently demonstrates the precision of the electrochemical method and provides unique insight into the redox mechanism of [NiFe]-hydrogenases.

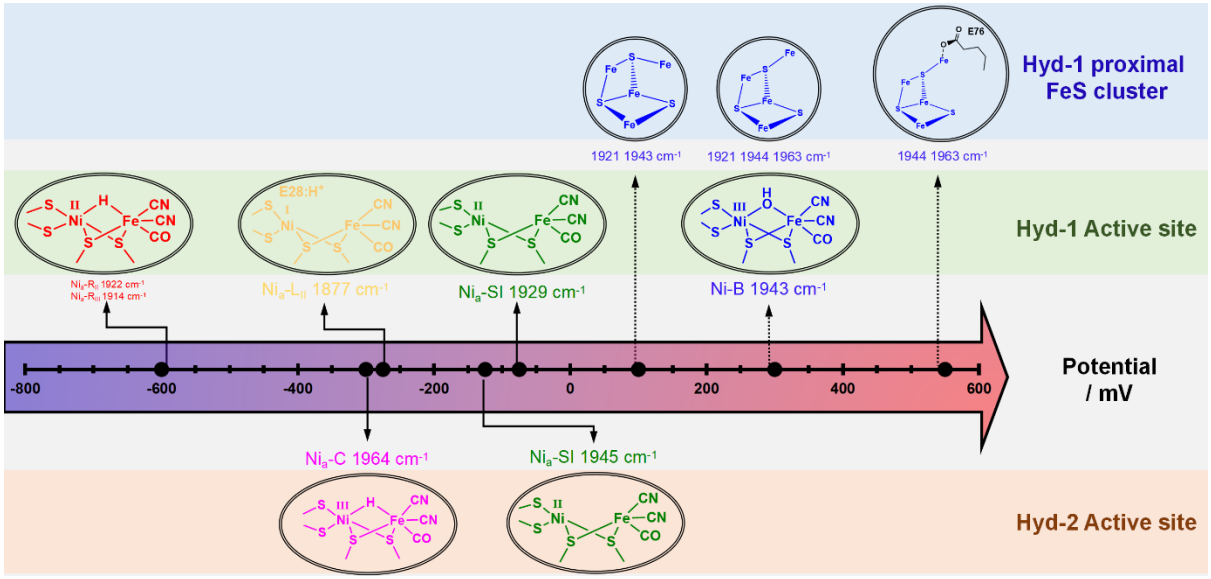

Figure 5.15: The redox level ladder diagram shows the skeleton representation of active site and proximal cluster states of [NiFe]-hydrogenase discussed in this chapter. The characteristic IR absorption band position in ν_{CO} region of each state is also shown.

Conclusion

In conclusion, each long-lived redox intermediate of the [NiFe]-hydrogenase catalytic cycle has been isolated, verified and structurally characterised (Figure 5.15). Only minimal changes are observed in the primary coordination sphere of the NiFe centre across all catalytically relevant states, in line with the low reorganisation energy required for efficient electron tunnelling as described by the Marcus theory. This structural rigidity is also evident among the highly conserved amino-acid residues that surround the active site.

The precision afforded by in crystallo electrochemical poising will be particularly valuable for the study of complex, multi-centre redox proteins, for example, multi-haem enzymes in lithotrophic bacteria, by enabling the isolation of individual intermediate states prior to detailed structural and spectroscopic analysis. Although emerging computational and machine-learning approaches are beginning to offer alternative routes to protein structure prediction,[49] the methodology and results presented in this

thesis demonstrate that only direct, experimentally determined three-dimensional geometries can reveal the subtle coordination changes that underpin enzymatic redox chemistry.

By combining crystal structures with complementary spectroscopic data, the exact geometry of both the active-site and its surrounding coordination spheres can be defined for each catalytic intermediate, thereby providing an unprecedented window into the mechanisms of redox enzymes.

5.5 References

1 Y. Higuchi, H. Ogata, K. Miki, N. Yasuoka and T. Yagi, *Structure*, 1999, **7**, 549–556.

2 A. Volbeda, E. Garcin, C. Piras, A. L. de Lacey, V. M. Fernandez, E. C. Hatchikian, M. Frey and J. C. Fontecilla-Camps, *J. Am. Chem. Soc.*, 1996, **118**, 12989–12996.

3 C. Schäfer, M. Bommer, S. E. Hennig, J.-H. Jeoung, H. Dobbek and O. Lenz, *Structure*, 2016, **24**, 285–292.

4 J. Fritsch, P. Scheerer, S. Frielingsdorf, S. Kroschinsky, B. Friedrich, O. Lenz and C. M. T. Spahn, *Nature*, 2011, **479**, 249–252.

5 Y. Shomura, K.-S. Yoon, H. Nishihara and Y. Higuchi, *Nature*, 2011, **479**, 253–256.

6 T. Goris, A. F. Wait, M. Saggu, J. Fritsch, N. Heidary, M. Stein, I. Zebger, F. Lendzian, F. A. Armstrong, B. Friedrich and O. Lenz, *Nat. Chem. Biol.*, 2011, **7**, 310–318.

7 R. M. Evans, E. J. Brooke, S. A. M. Wehlin, E. Nomerotskaia, F. Sargent, S. B. Carr, S. E. V Phillips and F. A. Armstrong, *Nat. Chem. Biol.*, 2016, **12**, 46–50.

8 Y. Ilina, C. Lorent, S. Katz, J.-H. Jeoung, S. Shima, M. Horch, I. Zebger and H. Dobbek, *Angew. Chem. Int. Ed.*, 2019, **58**, 18710–18714.

9 H. Ogata, S. Hirota, A. Nakahara, H. Komori, N. Shibata, T. Kato, K. Kano and Y. Higuchi, *Structure*, 2005, **13**, 1635–1642.

10 H. Ogata, Y. Mizoguchi, N. Mizuno, K. Miki, S. Adachi, N. Yasuoka, T. Yagi, O. Yamauchi, S. Hirota and Y. Higuchi, *J. Am. Chem. Soc.*, 2002, **124**, 11628–11635.

11 A. Volbeda, M.-H. Charon, C. Piras, E. C. Hatchikian, M. Frey and J. C. Fontecilla-Camps, *Nature*, 1995, **373**, 580–587.

12 H. Ogata, W. Lubitz and Y. Higuchi, *Dalton Trans.*, 2009, 7577–7587.

13 M.-E. Pandelia, W. Nitschke, P. Infossi, M.-T. Giudici-Orticoni, E. Bill and W. Lubitz, *Proc. Natl. Acad. Sci.*, 2011, **108**, 6097–6102.

14 S. E. Beaton, R. M. Evans, A. J. Finney, C. M. Lamont, F. A. Armstrong, F. Sargent and S. B. Carr, *Biochemical Journal*, 2018, **475**, 1353–1370.

15 H. Ogata, K. Nishikawa and W. Lubitz, *Nature*, 2015, **520**, 571–574.

16 W. Lubitz, H. Ogata, O. Rüdiger and E. Reijerse, *Chem. Rev.*, 2014, **114**, 4081–4148.

17 M. M. Roessler, R. M. Evans, R. A. Davies, J. Harmer and F. A. Armstrong, *J. Am. Chem. Soc.*, 2012, **134**, 15581–15594.

18 R. M. Evans, P. A. Ash, S. E. Beaton, E. J. Brooke, K. A. Vincent, S. B. Carr and F. A. Armstrong, *J. Am. Chem. Soc.*, 2018, **140**, 10208–10220.

19 I. Dance, *Chem. Sci.*, 2015, **6**, 1433–1443.

20 A. Volbeda, P. Amara, C. Darnault, J.-M. Mouesca, A. Parkin, M. M. Roessler, F. A. Armstrong and J. C. Fontecilla-Camps, *Proc. Natl. Acad. Sci.*, 2012, **109**, 5305–5310.

21 M.-E. Pandelia, D. Bykov, R. Izsak, P. Infossi, M.-T. Giudici-Orticoni, E. Bill, F. Neese and W.

Lubitz, *Proc. Natl. Acad. Sci.*, 2013, **110**, 483–488.

22 Ch. Geßner, O. Trofanchuk, K. Kawagoe, Y. Higuchi, N. Yasuoka and W. Lubitz, *Chem. Phys. Lett.*, 1996, **256**, 518–524.

23 S. Foerster, M. van Gastel, M. Brecht and W. Lubitz, *J. Biol. Inorg. Chem.*, 2005, **10**, 51–62.

24 R. Hidalgo, P. A. Ash, A. J. Healy and K. A. Vincent, *Angew. Chem. Int. Ed.*, 2015, **54**, 7110–7113.

25 P. A. Ash, S. E. T. Kendall-Price and K. A. Vincent, *Acc. Chem. Res.*, 2019, **52**, 3120–3131.

26 H. Ogata, W. Lubitz and Y. Higuchi, *J. Biochem.*, 2016, **160**, 251–258.

27 A. Abou Hamdan, B. Burlat, O. Gutiérrez-Sanz, P.-P. Liebgott, C. Baffert, A. L. De Lacey, M. Rousset, B. Guigliarelli, C. Léger and S. Dementin, *Nat. Chem. Biol.*, 2013, **9**, 15–17.

28 H. Ogata, P. Kellers and W. Lubitz, *J. Mol. Biol.*, 2010, **402**, 428–444.

29 A. Volbeda, L. Martin, E. Barbier, O. Gutiérrez-Sanz, A. L. De Lacey, P.-P. Liebgott, S. Dementin, M. Rousset and J. C. Fontecilla-Camps, *J. Biol. Inorg. Chem.*, 2015, **20**, 11–22.

30 T. Krämer, M. Kampa, W. Lubitz, M. van Gastel and F. Neese, *ChemBioChem*, 2013, **14**, 1898–1905.

31 S. Foerster, M. Stein, M. Brecht, H. Ogata, Y. Higuchi and W. Lubitz, *J. Am. Chem. Soc.*, 2003, **125**, 83–93.

32 G. Caserta, V. Pelmenschikov, C. Lorent, A. F. Tadjoung Waffo, S. Katz, L. Lauterbach, J. Schoknecht, H. Wang, Y. Yoda, K. Tamasaku, M. Kaupp, P. Hildebrandt, O. Lenz, S. P. Cramer and I. Zebger, *Chem. Sci.*, 2021, **12**, 2189–2197.

33 S. B. Carr, W. Li, K. L. Wong, R. M. Evans, S. E. T. Kendall-Price, K. A. Vincent and P. A. Ash, 2024, preprint, DOI: 10.26434/chemrxiv-2024-mn36l.

34 P. A. Ash, R. Hidalgo and K. A. Vincent, *ACS Catal.*, 2017, **7**, 2471–2485.

35 J. Dragelj, C. Karafoulidi-Retsou, S. Katz, O. Lenz, I. Zebger, G. Caserta, S. Sacquin-Mora and M. A. Mroginski, *Front. Microbiol.*, 2023, **13**, 1073315.

36 S. Kendall-Price, DPhil Thesis, University of Oxford, 2022.

37 M. Chung, DPhil Thesis, University of Oxford, 2016.

38 A. L. De Lacey, C. Stadler, V. M. Fernandez, C. E. Hatchikian, H.-J. Fan, S. Li and M. B. Hall, *JBIC Journal of Biological Inorganic Chemistry*, 2002, **7**, 318–326.

39 J. Kalms, A. Schmidt, S. Frielingsdorf, T. Utesch, G. Gotthard, D. von Stetten, P. van der Linden, A. Royant, M. A. Mroginski, P. Carpentier, O. Lenz and P. Scheerer, *Proc. Natl. Acad. Sci.*, 2018, **115**, 2229–2237.

40 M. J. Lukey, A. Parkin, M. M. Roessler, B. J. Murphy, J. Harmer, T. Palmer, F. Sargent and F. A. Armstrong, *Journal of Biological Chemistry*, 2010, **285**, 3928–3938.

41 R. González, DPhil Thesis, University of Oxford, 2016.

42 M.-E. Pandelia, H. Ogata, L. J. Currell, M. Flores and W. Lubitz, *BBA - Bioenergetics*, 2010, **1797**, 304–313.

43 T. Imanishi, K. Nishikawa, M. Taketa, K. Higuchi, H. Tai, S. Hirota, H. Hojo, T. Kawakami, K.

Hataguchi, K. Matsumoto, H. Ogata and Y. Higuchi, *Acta Crystallog. Section F*, 2022, **78**, 66–74.

44 M.-E. Pandelia, P. Infossi, M. T. Giudici-Orticoni and W. Lubitz, *Biochemistry*, 2010, **49**, 8873–8881.

45 K. L. Wong, DPhil Thesis, University of Oxford, 2024.

46 M. Kampa, M.-E. Pandelia, W. Lubitz, M. van Gastel and F. Neese, *J. Am. Chem. Soc.*, 2013, **135**, 3915–3925.

47 J. T. Sage, *J. Biol.l Inorg. Chem.*, 1997, **2**, 537–543.

48 S. Frielingsdorf, J. Fritsch, A. Schmidt, M. Hammer, J. Löwenstein, E. Siebert, V. Pelmenschikov, T. Jaenicke, J. Kalms, Y. Rippers, F. Lendzian, I. Zebger, C. Teutloff, M. Kaupp, R. Bittl, P. Hildebrandt, B. Friedrich, O. Lenz and P. Scheerer, *Nat. Chem. Biol.*, 2014, **10**, 378–385.

49 P. Cramer, *Nat. Struct. Mol. Biol.*, 2021, **28**, 704–705.

Chapter 6: Inhibitory Effects of Cyanide and Isocyanides on Hyd-1 and Hyd-2

This chapter demonstrates that exogenous inhibitors cyanide (examined in Hyd-1) and isocyanides (RNC, R = methyl, ethyl) coordinate terminally to the Ni atom in the active site of both Hyd-1 and Hyd-2. This coordination is supported by infrared spectroscopic evidence and, for the first time, direct crystallographic verification. For bulkier isocyanides (R = isopropyl and n-butyl), while no significant electron density is observed in diffraction maps, infrared spectroscopic data confirm their interaction with the bimetallic active site. The tuneable R-group of isocyanides serves as an effective molecular probe to map steric constraints within the enzyme's catalytic pocket. These findings establish that the maximum dynamic aperture of the substrate access tunnel lies between the dimensions of isopropyl isocyanide and tert-butyl isocyanide, revealing a surprisingly substantial volume within the active site cavity.

6.1 Introduction

In Chapter 5, the crystal structures of Hyd-1 and Hyd-2 in the Ni_a-SI state show that the bridging position in the active site is predominantly vacant. This active site state has been proposed to react with substrate hydrogen molecules to start catalysis and also to interact with other inhibitors. Based on that, single crystals in the Ni-SCO state were obtained from electrochemically generated Ni_a-SI by treating with a CO atmosphere, and the crystal structures of the Ni-SCO state of both Hyd-1 and Hyd-2 were obtained. The crystallographic data provides understanding of the coordination chemistry of the active site and insight into the substrate binding site of this fast-turnover catalyst. In this chapter, the rational and reproducible electrochemical generation of hydrogenase crystals in the Ni_a-SI state is exploited to facilitate systematic characterisation of Hyd-1 and Hyd-2 with other inhibitors. Infrared spectra and crystal structures were analysed for both enzymes complexed with a series of π-acceptor inhibitors exhibiting incrementally varied molecular dimensions. This approach provided direct spectroscopic and crystallographic evidence for probing active site coordination chemistry and structural flexibility within the catalytic pocket.

Cyanide (CN^-) is a strong σ-donor ligand that coordinates with many transition metals and inhibits several metalloproteins.[1–3] The inhibitory effects of cyanide on Hyd-1 and Hyd-2 (electrode-immobilised) have been studied via a solution IR spectroelectrochemical method and protein film electrochemistry.[4,5] At low concentration, cyanide promotes the formation inactive state Ni-B and the effect is much more pronounced in Hyd-2 under N_2. A high concentration of cyanide solution leads to a permanent coordination of cyanide to the active site of Hyd-1. The difference IR spectra shown in Figure 6.1 a,b and c reveal a new band for a species named “Ni-X” at 1899 cm^{-1} in ν_{CO} region.[4] This state is formed at Ni_a-SI redox level with gradient KCN concentration. The difference spectrum in Figure 6.1 d shows that Ni-X is directly

formed from Ni_a-SI, implying that the exogenous cyanide interacts with Ni_a-SI to have this irreversible coordination to the active site. Furthermore, ATR-IR spectroscopy of ^{13}C-labled Hyd-1 sample which contains endogenous ^{13}CO ligand confirms that the band at 1899 cm^{-1} is attributed to the endogenous CO ligand.[4] However, the IR band of exogenous cyanide was not identified due to low signal-to-noise ratio of ATR-IR in the ν_{CN} region and crystallographic characterisation is necessary to fulfil the conclusion.

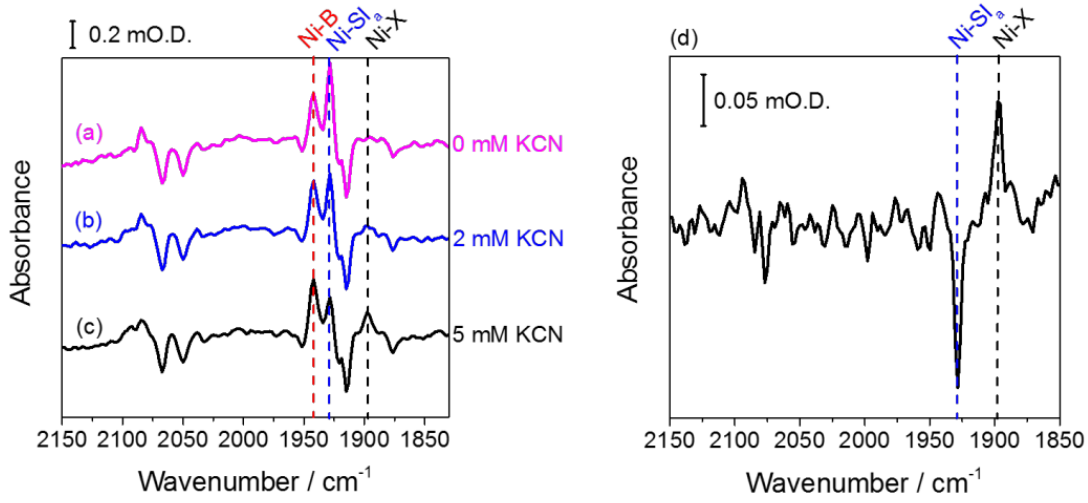

Figure 6.1: ATR-IR difference spectra of Hyd-1 immobilised on BP2000 at -0.09 V and -0.6 V with different concentrations of cyanide: (a) 0 mM; (b) 2 mM; and (c) 5 mM KCN. The background spectrum was collected at -0.6 V without cyanide present. Panel (d): A difference spectrum of Hyd-1 triggered by the change of cyanide concentration from 2 mM to 5 mM; the potential was poised at -0.09 V. All spectra were recorded in N_2-saturated buffer (pH 7). Figure adapted from the DPhil thesis of Min-Wen Chung, University of Oxford.

Isocyanide (RNC) has an isoelectronic functional group to π-acid ligands CO and CN^-. The general molecular structure of RNC is shown in Figure 6.2. Due to the reactive lone pair on carbon and the positive charge on nitrogen, RNCs are better σ-donors but weaker π-acceptors than CO. The σ-donating effect increases with the inductive effect of the alkyl group (R)

attached to the nitrogen. RNCs serve as strong field ligands with high reactivity towards low valence transition metals.[6,7]

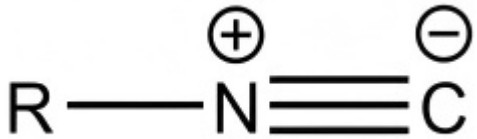

Figure 6.2: The general molecular structure of isocyanide (RNC). R represents the alkyl group.

RNCs have been studied in *E. coli* hydrogenases as reversible inhibitors using PFE and IR spectroelectrochemistry.[4] The inhibition constant (K_I) of methyl isocyanide (MeNC) for Hyd-2 was established to be in the range of 5–20 µM, approximately two orders of magnitude smaller than that for Hyd-1 (0.8–1.8 mM). Treating electrode-immobilised Hyd-1 and Hyd-2 with MeNC at Ni_a-SI redox level, the exogenous MeNC inhibits the active site and corresponding new absorption bands appear along with lowering of the of Ni_a-SI bands (1929 cm^{-1} in Hyd-1 and 1946 cm^{-1} in Hyd-2). Figure 6.3 a and b show the IR difference spectrum for Hyd-1 and Hyd-2, MeNC-added minus no MeNC, respectively. The new band in the ν_{CO} region, 1917 cm^{-1} (Hyd-1) and 1935^{-1} (Hyd-2) is assigned as the endogenous CO absorption from the enzyme with MeNC coordinated to the active site. In addition, new absorption bands at 2157 and 2161 cm^{-1} are assigned to the N≡C stretching from the exogenous inhibitory MeNC. Moreover, PFE studies showed that ethyl- and *n*-butyl isocyanide with longer alkyl chains also inhibit Hyd-1 reversibly. [4]

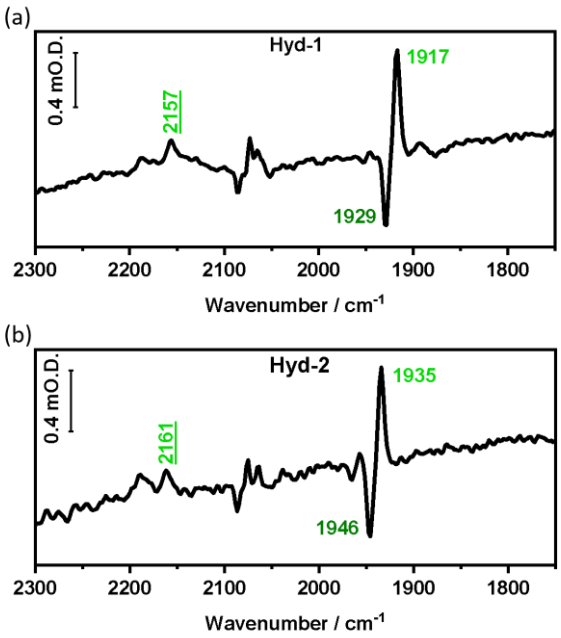

Figure 6.3: ATR-IR difference spectra of Hyd-1 and Hyd-2 obtained by using spectra after introducing MeNC into the cell minus before injection. Panel (a): Hyd-1, 9 mM MeNC minus no MeNC; -100 mV vs SHE; 100% N_2; 4 cm^{-1} resolution; 1000 scans. Panel (b): Hyd-2, 8 mM MeNC minus no MeNC; -100 mV vs SHE; 100% N_2; 4 cm^{-1} resolution; 1000 scans. Data provided by Min-Wen Chung.

The PFE and spectroscopic characterisation confirmed the strong interactions between cyanide and isocyanides. However, there are no crystal structures of those inhibitor-bound forms resolved yet, likely because they interact solely with the Ni_a-SI active site state that exists in a small redox window. This chapter describes how the cyanide- and isocyanide- bound Hyd-1 and Hyd-2 crystals are strategically generated by soaking electrochemically generated Ni_a-SI single crystals with target inhibitors according to the procedure described in Chapter 4. The crystals were then transferred with poised mediator buffer to mix with inhibitors under anaerobic conditions. The inhibitor-treated crystals are studied and verified by IR spectroscopy, and their crystal structures are resolved in high-resolution. All crystallographic data are collected and analysed by Dr Stephen Carr at the Harwell Research Complex using the same method described in Chapter 5.1.

6.2 IR Spectroscopy and Crystal Structures of Cyanide-bound Hyd-1

The direct interaction between exogenous cyanide and Hyd-1 active site is revealed by the combination of IR spectroscopy and X-ray crystallography as shown in Figure 6.4. The Hyd-1 crystals in Ni_a-SI state were soaked in mediator cocktail containing 20 mM potassium cyanide (also poised at Ni_a-SI redox potential) for 30 min for further characterisation. The cyanide-bound Hyd-1 active site state is herein labelled Ni-SCN state.

Figure 6.4 A shows the IR spectrum of a Hyd-1 single crystal in Ni-SCN state. In the ν_{CO} region, a dominant band appears at 1898 cm^{-1}, together with two minor features at 1892 cm^{-1} and 1883 cm^{-1}. The 1898 cm^{-1} absorption reproduces the Ni-X signal which was previously observed at 1899 cm^{-1} in spectroelectrochemical studies of cyanide inhibition.[4] This band was assigned to the intrinsic CO stretch in the cyanide-inhibited state. The complete disappearance of the 1929 cm^{-1} band (Ni_a-SI CO stretch) demonstrates that a high proportion of active sites have converted from Ni_a-SI state to the cyanide-bound state (Ni-SCN).

The 31 cm^{-1} downward shifts of the major band in ν_{CO} (from 1929 cm^{-1} in Ni_a-SI to 1898 cm^{-1} in Ni-SCN) arises from cyanide's exceptionally strong σ-donor character. When CN^- binds at the terminal Ni site, it donates electron density into the NiFe bimetallic active site. This increased electron density enhances π-backbonding from iron into the CO ligand, weakening the CO triple bond (reducing its force constant k) and thereby shifting its ν_{CO} to lower frequency. By contrast, exogenous CO in the Ni-SCO state is a weaker σ-donor and simultaneously a π-acceptor; its two opposing electronic effects partially cancel, so the intrinsic CO absorption band position in Ni-SCO remains close to 1929 cm^{-1}, like that of Ni_a-SI.

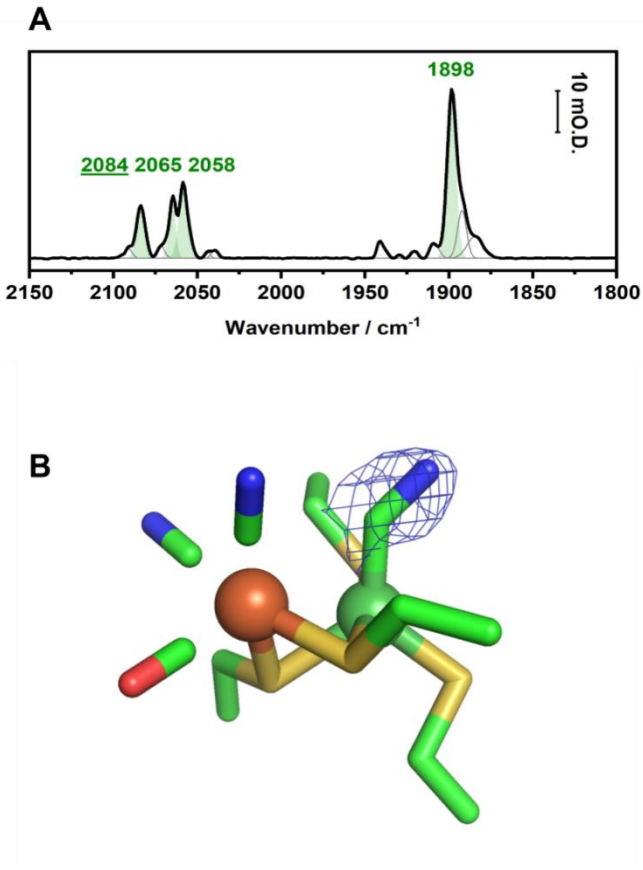

Figure 6.4: IR spectra and crystal structures of the Ni-SCN state of Hyd-1. (A) Baseline subtracted IR spectrum of Hyd-1 in the Ni-SCN state, measured at 2 cm^{-1} resolution, 256 scans. Light olive shaded absorption band at ν_{CO} (1898 cm^{-1}) and at ν_{CN} (2058 and 2065 cm^{-1}) are assigned to intrinsic ligand stretches of Ni-SCN with additional band at 2084 cm^{-1} attributed to exogenous CN stretching. Unassigned minor species and fitted Gaussian peaks and are shown as thin grey lines. (B) Active site structure of Hyd-1 Ni-SCN state shows classic NiFe bimetallic active site with exogenous cyanide ligand 2 Å away from Ni, pointing to the end of the gas channel. The blue mesh represents the Fo-Fc difference map subtracted from the Hyd-1 Ni_a-SI structure (2.5 r.m.s.d) and it is modelled as a diatomic cyanide ligand.

In the ν_{CN} region, three distinct bands are present. Two bands at 2065 cm^{-1} and 2058 cm^{-1} lie about 20 cm^{-1} below Ni_a-SI's intrinsic CN stretches (2085 cm^{-1} and 2077 cm^{-1}) and are therefore assigned to the two native cyanide ligands on iron in the Ni_a-SCN state. The intrinsic CN

stretches are less sensitive to changes in electron density at the active site compared with that of CO. A third band at 2084 cm^{-1}. It likely corresponds to the ν_{CN} stretch of the exogenous CN^- inhibitor itself due to its high vibrational frequency. This band in the ν_{CN} region observed in Hyd-1 crystals is consistent with the previous spectroelectrochemical study on electrode-immobilised Hyd-1 and cyanide (Figure 6.1 d).[4] The difference spectrum of Ni_a-SI and Ni-SCN suggested the band at 2084 cm^{-1} is not from residual Ni_a-SI, but as an induced band due to cyanide inhibition. However, further isotope-label experiments should be conducted in future to verify the identity of the absorption band caused by exogenous CN^-. Methods include treating the ^{13}C-labled Hyd-1 active site with cyanide, treating the Hyd-1 with $KC^{15}N$ or $K^{13}CN$ would resolve the puzzle.

Notably, in the ν_{CO} region, a minor absorption band at 1941 cm^{-1} might account for the inactive state, Ni-B, which is associated with the band at 2095 cm^{-1} in the ν_{CN} region. The formation of the Ni-B state in Hyd-1 upon CN^- inhibition have been reported in protein film infrared electrochemistry studies.[4]

The crystal structure of Hyd-1 Ni-SCN is resolved at 1.30 Å resolution and atomic structure of the active site is presented in Figure 6.4B. The blue mesh represents the Fo-Fc difference map (subtracted density of Ni_a-SI from the Ni-SCN) contoured at 2.5 r.m.s.d and modelled with a diatomic CN^- ligand. The bimetallic NiFe active site remains intact and the exogenous CN^- ligand coordinates to Ni at the terminal position in a bent conformation with the Ni–C distance of 2.0 Å and the Ni–C≡N bond angle of 135 °. The coordination geometry of cyanide in the Hyd-1 active site here in Figure 6.4B highly mirrors that of the Ni-SCO structure (coordination distance of 2.0 Å and the Ni–C≡O bond angle of 134 °). This shows the active site of Hyd-1 accommodate these two isoelectric diatomic ligands in nearly identical conformation and the steric effects on the exogenous ligands in the active site are also comparable. Identical ligand-

active site binding conformation for CO/CN^- is also found in other metalloproteins.[8] Furthermore, the clear electron density in the difference map confirms the cyanide-nickel coordination in the active site and explains the intrinsic CO absorption band shift and the additional induced band (2084 cm^{-1}) observed in IR spectrum. No residual electron density is observed at the bridging position in the Fo-Fc map which suggests the partially occupied water molecule observed in the Ni_a-SI state crystal structure is absent after inhibitor interaction. There were no appreciable differences observed between structures of the active site or anywhere else between enzymes in the asymmetric unit.

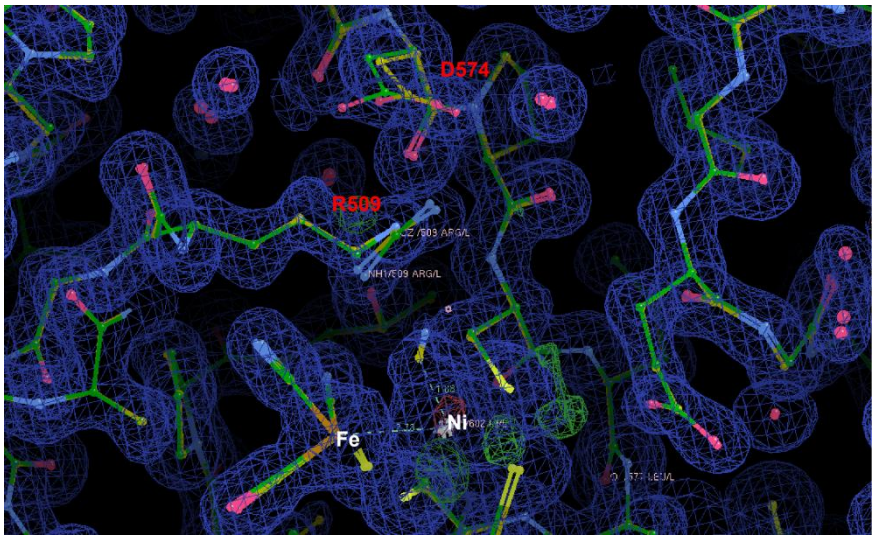

Figure 6.5: The comparison of the electron density map between Ni-SCN (yellow) and Ni_a-SI (green). The shifts in sidechain are observed on R509 and D574.

Cyanide is a more hydrophilic molecule compared with CO. The hydrophilic water channel in the protein has been proposed to lead towards the headspace of the active site above the pendent arginine, and the crystallographic result shows a small shift in position of R509 (the pendent arginine on the Hyd-1 active site) and a significant shift in postion of D574 (Figure 6.5). However, based on the active site structure, the coordinated exogenous cyanide on Ni points towards the end of the hydrophobic gas channel, suggesting that exogenous cyanide is

transferred from the protein surface to the active site via the same hydrophobic gas tunnel for CO and H_2, possibly in protonated form as HCN. Nevertheless, this does not preclude the hydrophilic water channel in the protein as the cyanide transport pathway to the active site.

Protein film infrared electrochemistry on Hyd-2 demonstrated cyanide serves as a reversible inhibitor, promoting the formation of the Ni-B state and no inhibitor-bound active site state was observed. Therefore, Hyd-2 protein crystal is not investigated for cyanide inhibition.[4]

6.3 Methyl- and Ethyl- Isocyanide Bound to Hyd-1 and Hyd-2 Active Site

6.3.1 Methyl Isocyanide Inhibition

Soaking hydrogenase crystals in Ni_a-SI state with 20 mM methyl isocyanide (MeNC) for 30 min, the coordination of exogenous MeNC in the active site of both Hyd-1 and Hyd-2 are confirmed by IR spectroscopic and crystallographic methods. The inhibitor-bound active state is named as Ni-SMeNC, indicating the presence of MeNC at the active site.

Infrared spectra presented in Figure 6.6 panels A and B demonstrate that MeNC-soaked Hyd-1 and Hyd-2 crystals predominantly adopt the Ni-SMeNC state. Spectra for both enzymes exhibit three characteristic absorption regions: ν_{CO}, ν_{CN}, and ν_{NC}, corresponding to specific molecular vibrations.

In the ν_{CO} region, Hyd-1 and Hyd-2 Ni-SMeNC exhibit dominant absorptions at 1917 and 1935 cm^{-1} respectively, consistent with prior spectroelectrochemical data (Figure 6.3). The redshifts of 12 cm^{-1} (Hyd-1) and 11 cm^{-1} (Hyd-2) relative to each Ni_a-SI state indicate electron density

enrichment at the active site upon MeNC coordination. The σ-donor capacity of MeNC exceeds that of CO due to its alkyl substituent and reduced heteroatom electronegativity, but remains weaker than formally anionic cyanide. Consequently, the intrinsic ν_{CO} position of Ni-SMeNC occur at higher wavenumbers than that of Ni-SCN but lower than Ni-SCO state. Notably, a minor peak at 1946 cm^{-1} in the Hyd-2 Ni-SMeNC spectrum (Figure 6.6B, grey peak) suggests incomplete conversion from the Ni_a-SI state.

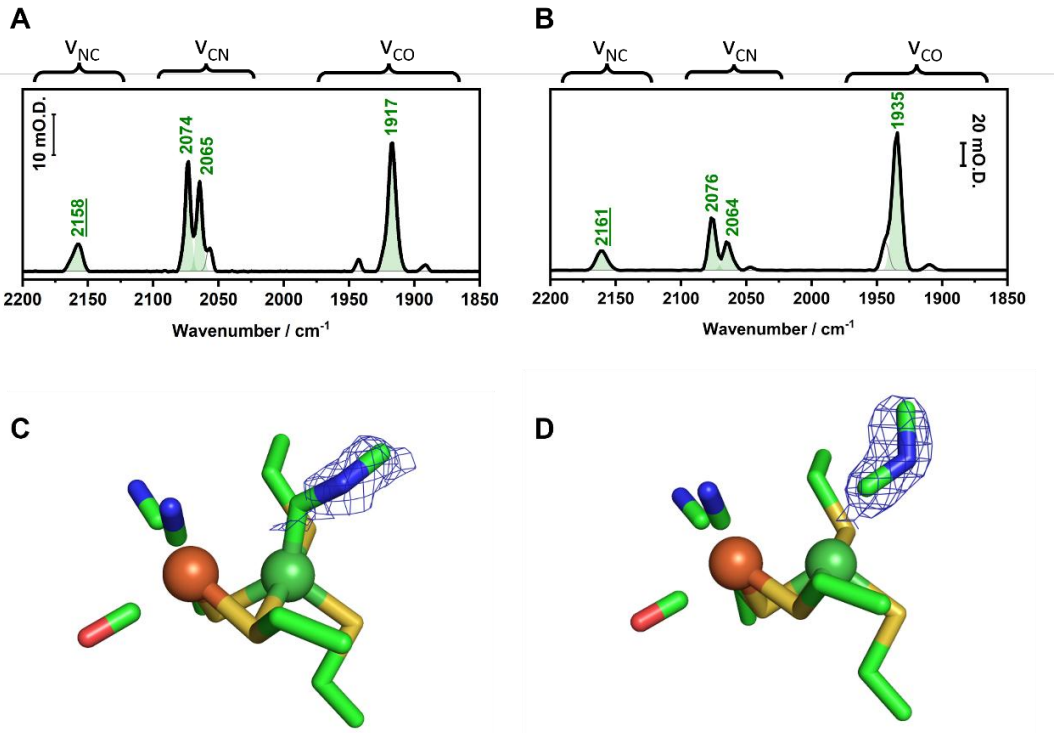

Figure 6.6: IR spectra and crystal structures of the Ni-SMeNC state of Hyd-1 and Hyd-2. Baseline subtracted IR spectra of Hyd-1 (A) and Hyd-2 (B) Ni-SMeNC state contain absorption bands of active site ligands in three frequency ranges (ν_{CO}, ν_{CN} and ν_{NC}). The active site structures of Hyd-1 (C) and Hyd-2 (D) Ni-SMeNC state show the exogenous cyanide ligand bound 1.9 Å (C) and 2.3 Å (D) to Ni. IR spectra were recorded with 2 cm^{-1} resolution and 256 scans. IR absorption bands associated with the Ni-SCO state are shaded in light olive. The blue mesh in the electron density map represents the Fo-Fc difference electron density (Ni-SMeNC minus lNi$_a$-SI), contoured at 2.5 r.m.s.d..

Both inhibited enzymes display two prominent ν_{CN} bands corresponding to endogenous

cyanide ligands, coupled with the singular ν_{CO} signal. These exhibit consistent redshifts of approximately 11 cm^{-1}, confirming high Ni-SMeNC population.

Exogenous MeNC coordination generates additional peaks at 2158 cm^{-1} (Hyd-1) and 2161 cm^{-1} (Hyd-2), assigned to bound isocyanide ν_{NC} stretches. Comparing with neat MeNC (2166 cm^{-1}) in hydrophobic conditions,[9] the coordinated MeNC exhibits slightly lower absorption frequency, likely due to the π-backbond donating effect from ligated Ni(II). The peak broadening of the exogenous MeNC might suggests conformational flexibility at the terminal coordination site.

X-ray crystallography unambiguously confirmed MeNC binding at the nickel centre. Structures refined to 1.36 Å (Hyd-1) and 1.60 Å (Hyd-2) resolution reveal distinct coordination geometries, and their active site structures are shown in Figure 6.6 C and D. The blue meshes are the Fo-Fc difference density subtracted from of each Ni_a-SI structure, contoured at 2.5 r.m.s.d. and they are modelled as the 3 larger atoms of exogenous MeNC, while no residual density at the bridging position was observed in either enzyme. In Hyd-1 (Figure 6.6 C), MeNC adopts a highly distorted conformation with Ni-C distance of 1.9 Å. Bond angles of Ni–C≡N and C≡N–C are 125 and 117 °, respectively. This indicates significant steric constraint at the binding site of the active site. Conversely, Hyd-2 (Figure 6.6 D) exhibits longer Ni-C separation (2.3 Å) and wider angles (∠Ni–C≡N = 132 ° and ∠C≡N–C = 128 °), suggesting greater spatial accommodation. With the exception of local structural changes at the active site, no significant global differences are observed between the Ni-SMeNC and Ni_a-SI states in either Hyd-1 or Hyd-2. The large differences in the Ni-SMeNC crystal structures at the active site between Hyd-1 and Hyd-2 are not explicitly reflected by the IR spectra. This might account for the more conformational flexibility of MeNC in the active site cavity at ambient temperature (condition for IR spectroscopy) compare with that in for the frozen state. There were no appreciable

differences observed between structures of the active site or anywhere else between enzymes in the asymmetric unit. The global structures are basically identical in the presence and absence of the RCN ligands, with any differences at the surface of the protein. Since these are also seen with different poises, and to an extent between different crystals at the same poise, there is no sufficient reason to ascribe this to the presence of the isocyanide. Amino acids in the substrate channel are invariant in their position and this may be in part why we fail to see any clear density for anything larger than ethylisocyanide (see later structures).

Comparative analysis reveals fundamental conformational differences: MeNC in Hyd-1 bound to the Ni(II) more closely but suffers from substantial steric strain, while Hyd-2 permits greater ligand freedom. The distinct alignment of methyl groups relative to nitrogen atoms and divergent tail orientations further highlight the spatial variations in the active site between these isoenzymes.

6.3.2 Ethyl Isocyanide Inhibition

Introduction of ethyl isocyanide (EtNC) to a final concentration of 60 mM in contact with Hyd-1 and Hyd-2 single crystals in the Ni_a-SI state for 30 minutes resulted in conversion to the EtNC-bound state (Ni-SEtNC), confirmed by FTIR and X-ray crystallographic characterisation.

In Figure 6.7A, characteristic peaks at 1916 cm^{-1} (ν_{CO}) and 2067/2073 cm^{-1} (ν_{CN}) confirm transition from Hyd-1 Ni_a-SI (1929, 2077, 2086 cm^{-1}) to Ni-SEtNC. The 13 cm^{-1} redshift in ν_{CO} and dual ν_{CN} bands indicates enhanced electron density at the active site following coordination of the σ-donating EtNC ligand. The additional 1 cm^{-1} shift relative to Ni-SMeNC (1917 cm^{-1}) reflects the ethyl group's stronger inductive effect. Two new ν_{NC} peaks (2149 and 2177 cm^{-1}) are assigned to the exogenous isocyanide group and they suggest either multiple

EtNC binding conformations or Fermi resonance between C≡N stretching and ethyl group vibrations (e.g., $\delta(CH_3)$ + ν(C-C)). Even though the Fermi resonance is observed in free aqueous EtNC, but it was not observed in aqueous MeNC. [4] Furthermore, the large difference in band splitting between Hyd-1 and Hyd-2 makes this explanation less likely.

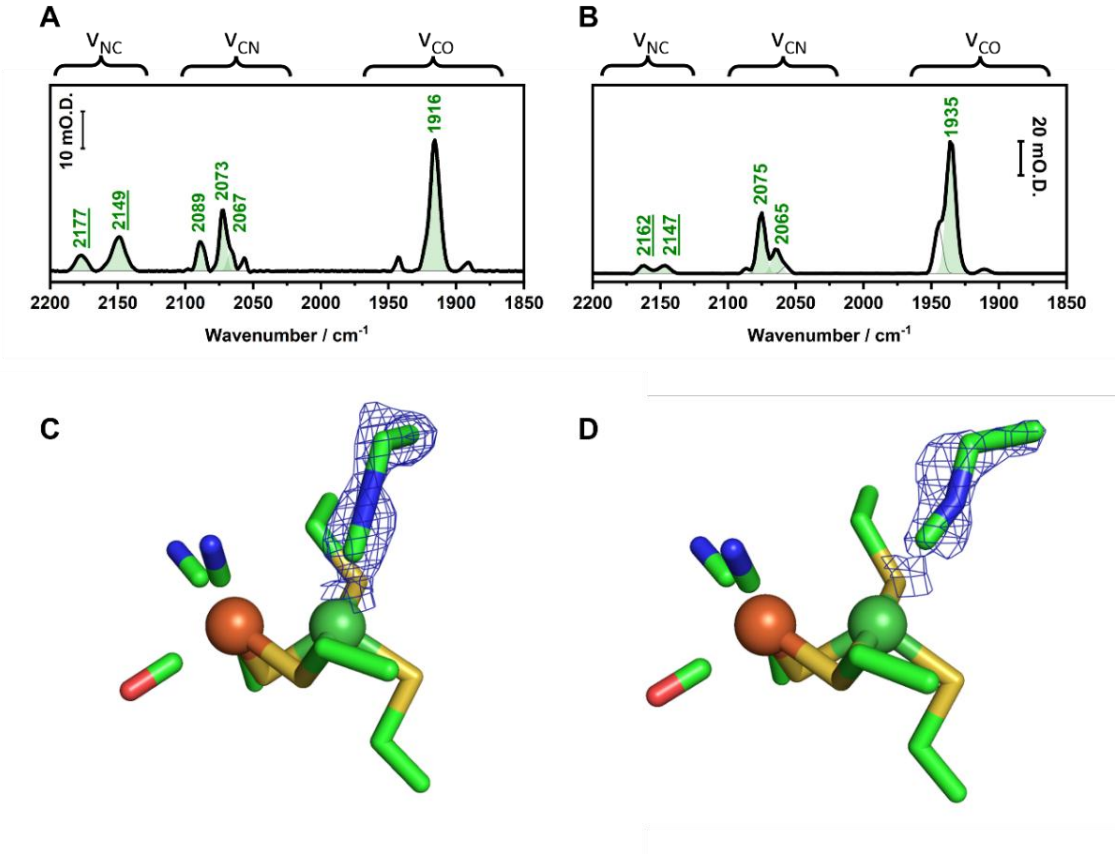

Figure 6.7: IR spectra and crystal structures of the Ni-SEtNC state of Hyd-1 and Hyd-2. Baseline subtracted IR spectra of Hyd-1 (A) and Hyd-2 (B) Ni-SEtNC state contain absorption bands of active site ligands in three frequency ranges (ν_{CO}, ν_{CN} and ν_{NC}). The active site structures of Hyd-1 (C) and Hyd-2 (D) Ni-SEtNC state show the exogenous cyanide ligand bound 2.2 Å (C) and 2.4 Å (D) to Ni. IR spectra were recorded with 2 cm^{-1} resolution and 256 scans. IR absorption bands associated with the Ni-SEtNC state are shaded in light olive. The blue mesh in the electron density map represents the Fo-Fc difference electron density (Ni-SEtNC subtract Ni_a-SI), contoured at 2.5 r.m.s.d..

Figure 6.7 B demonstrates analogous spectral changes in Hyd-2 Ni-SEtNC, with dominant ν_{CO}

(1935 cm^{-1}) and ν_{CN} (2065/2075 cm^{-1}) absorptions. The two additional bands in the ν_{NC} region at 2147 and 2162 cm^{-1} are attributed to the C≡N stretch from exogenous EtNC. Notably, a substantial residual peak at 1946 cm^{-1} (ν_{CO}, gray line fitted with Gaussian peak) indicates incomplete inhibition, with ∼20% of Hyd-2 active sites remaining in the Ni_a-SI state.

High-resolution crystal structures of Hyd-1 (1.30 Å) and Hyd-2 (1.59 Å) in the Ni-SEtNC state confirm ethyl isocyanide coordination within their active sites (Figure 6.7 C-D). The Fo-Fc difference density (blue mesh, contoured at 2.5 r.m.s.d.) unambiguously verifies the presence of the EtNC ligand, revealing binding to the nickel centre. Modelled EtNC adopts a bent conformation at the terminal position through negatively charged carbon, analogous to other π-acceptor ligands, with the ethyl group oriented toward the gas channel terminus. No residual electron density is observed at the bridging position in either active site. Besides the active site structure, no appreciable differences between the Hyd-1 and Hyd-2 enzymes in their Ni_a-SI, Ni-SMeNC and Ni-SEtNC state.

Despite IR spectra indicating full inhibition in Hyd-1 Ni-SEtNC (single ν_{CO} band at 1916 cm^{-1}), the best-modelled inhibitor in chain L (one of the large subunits) exhibits weak electron density for the ethyl group. Coordination metrics show Ni-C distance of 2.2 Å with ∠Ni-C≡N = 148.1°. Similarly, in Hyd-2, EtNC in chain L displays clear density only for the isocyanide moiety (C≡N), bound at 2.4 Å with ∠Ni-C≡N = 141.2°. The poorly defined electron density suggests the ethyl tail is highly likely to occupy multiple conformations.

Notably, well-defined EtNC density appears exclusively in one heterodimer unit of Hyd-2. This observation is consistent with the persist Ni_a-SI population after EtNC inhibition in the IR spectrum (Figure 6.7 B). Occupancy differences likely originate from crystalline packing constraints, where closely stacked enzymes generate steric hindrance limiting dimer accessibility. Alternatively active sites lacking modelled EtNC exhibit higher temperature

factors indicating greater mobility. The reduced chain order and a weakly bound/mobile inhibitor could be enough to blur out the density for the R group. Relatively defined density for the isocyanide functional group of EtNC is observed in this more mobile chain, but not enough of the rest to model it. The differences in two chains also applies for Hyd-1: clearer Fo-Fc density for the whole ligand in the lower mobility active site (chains L and S), the more mobile active site (chains M and T) only show clear density for the isocyanide functional group (CN).

6.4 Inhibition by Bulkier Isocyanides

The inhibition of [NiFe]-hydrogenase by bulkier isocyanides was investigated using Hyd-1 single crystals. Although Hyd-2 shows greater sensitivity to RNC inhibition compared with Hyd-1 as shown by activity assays, bulky inhibitors have trouble accessing the Hyd-2 active site in the crystalline state, results in substantial fraction of the Ni_a-SI state left after crystal-inhibitor incorporation (eg. Figure 6.7B). Consequently, all further experiments employing bulkier RNCs were performed on Hyd-1 crystals to ensure greater chance of structural determination of the inhibitor response.

Crystal Soaking and Incubation Protocol

Hyd-1 single crystals were first poised electrochemically in the Ni_a-SI state using an appropriate mediator cocktail but with additional 20 % v/v DMSO present. The experimental procedure is described in Chapter 4. A 1 M stock solution of each RNC in neat DMSO solution was then added to the equilibrated Ni_a-SI crystals to achieve a final RNC concentration of 100 mM in poised crystallisation mediator buffer. All manipulations were conducted under strictly

anaerobic conditions to prevent oxidative artefacts. Each crystal was incubated for 30 minutes to allow sufficient time for RNC binding.

6.4.1 Isopropyl Isocyanide Inhibition

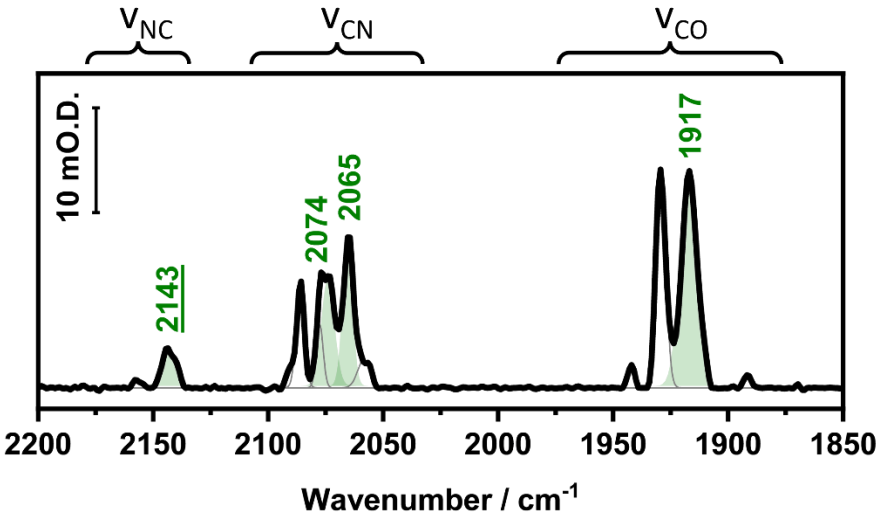

Figure 6.8: Baseline subtracted IR spectrum of iPrNC soaked Hyd-1 single crystal (100 mM, 30min). IR spectra were recorded with 2 cm^{-1} resolution and 256 scans. IR absorption bands associated with the Ni-SiPrNC state are shaded in light olive.

Figure 6.8 presents the FTIR spectrum of a Ni_a-SI Hyd-1 single crystal following 30 minutes' incubation with 100 mM isopropyl Isocyanide (iPrNC). Two prominent bands appear in the ν_{CO} region at 1929 and 1917 cm^{-1}. The 1929 cm^{-1} band corresponds to the characteristic intrinsic CO stretch of the Ni_a-SI state of Hyd-1, whereas the 1917 cm^{-1} feature aligns with the intrinsic CO stretch following by iPrNC inhibition. A Gaussian-type deconvolution of these two peaks indicates an approximate 40:60 ratio in population, signifying that roughly 40 % of active sites

remain uninhibited and remain in the Ni_a-SI state, while 60 % have been converted to an iPrNC-inhibited state (Ni-SiPrNC).

The 1917 cm^{-1} band is broader than the Ni_a-SI signal (1929 cm^{-1}), suggesting that multiple iPrNC conformations are present within the active-site pocket. Compared with the ν_{CO} of Ni-SMeNC and Ni-SEtNC, the 1917 cm^{-1} frequency lies close to that of MeNC inhibition but is approximately 1 cm^{-1} higher than in the EtNC-inhibited state. If the alkyl tail were exerting a purely inductive effect, a larger substituent would be expected to shift the ν_{CO} band to lower frequency; the observed slight upward shift therefore suggests that steric crowding attenuates the σ-donor ability of iPrNC and reduces π-backbonding from Fe to the intrinsic CO ligand.

In the ν_{CN} region of the same IR spectrum, the residual Ni_a-SI CN stretching bands at 2086 and 2077 cm^{-1} are still visible. In addition, a pair of broader bands at 2074 and 2065 cm^{-1} appear and are attributed to the CN stretches of the Ni-SiPrNC active sites, coupling to the 1917 cm^{-1} ν_{CO} feature. Finally, a distinct band arises at 2143 cm^{-1}, which corresponds to the ligand CN stretch of coordinated iPrNC.

6.4.2 n-Butyl Isocyanide Inhibition

Figure 6.9 shows the IR spectrum of a Ni_a-SI Hyd-1 crystal after 30 minutes' incubation with 100 mM n-butyl Isocyanide (^{n}BuNC). In the ν_{CO} region, a single, exceptionally broad band centred at 1915 cm^{-1} is observed, representing a 14 cm^{-1} downward shift relative to the Ni_a-SI signal at 1929 cm^{-1}. This pronounced red shift is consistent with the stronger inductive effect and extended alkyl chain of ^{n}BuNC compared with MeNC and EtNC. The breadth of the 1915 cm^{-1} band indicates significant conformational heterogeneity: the straight chain ^{n}BuNC tail can

adopt multiple orientations within the active site pocket and maybe extend to the hydrophobic gas channel.

In the ν_{CN} region, the Ni_a-SI peaks at 2086 and 2077 cm^{-1} persist, but two dominant bands at 2072 and 2065 cm^{-1} emerge, corresponding to the CN stretches of inhibited active sites. At higher wavenumbers, a strong band appears at 2147 cm^{-1} with a smaller shoulder at 2141 cm^{-1}. The 2147 cm^{-1} feature matches the CN stretch of ^{n}BuNC in a hydrophobic environment,[4] indicating that bulk ^{n}BuNC partitions into the packed protein crystal and presumably in the protein hydrophobic gas channel. The shoulder at 2141 cm^{-1} is assigned to the CN stretch of Ni-bound ^{n}BuNC, with the slight red shift arising from weak π-backbond donation from Ni to the coordinated isocyanide. Collectively, these spectral features confirm that the Hyd-1 active site is essentially inhibited by ^{n}BuNC under these conditions, consistent with reported activity assay.

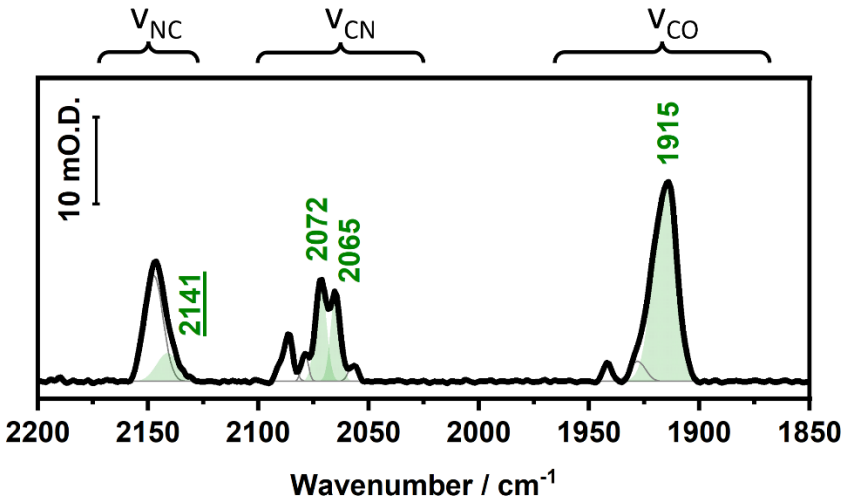

Figure 6.9: Baseline subtracted IR spectrum of ^{n}BuNC soaked Hyd-1 single crystal (100 mM, 30min). IR spectra were recorded with 2 cm^{-1} resolution and 256 scans. IR absorption bands associated with the Ni-S^{n}BuNC state are shaded in light olive.

6.4.3 X-ray Diffraction of ^{i}PrNC-Inhibited Crystals

Figures 6.10 shows the electron-density map (2Fo-Fc, blue mesh, contoured at 1.5 r.m.s.d.) for Hyd-1 single crystals treated with ^{i}PrNC, resolved to 1.30 Å. The first and second coordination spheres of the NiFe active site remain virtually identical to the Ni_a-SI structure; no high-occupancy extra density is visible at the terminal Ni site. Omit maps reveal no residual density at the Ni terminus position that could correspond to a bound isocyanide. In contrast, no residual density at bridging position was found, indicating the active site structure does not look exactly identical to the electrochemically poised Ni_a-SI (Figure 5.4) where it contains a partially occupied water molecule.

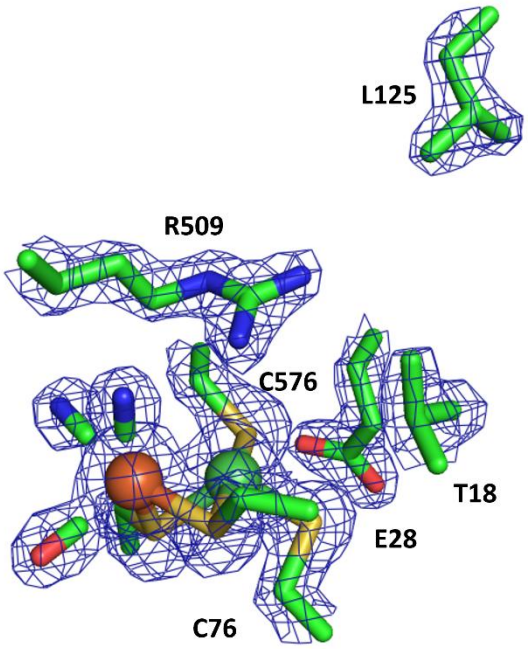

Figure 6.10: The crystal structure of the ^{i}PrNC soaked Hyd-1 shows identical active site and adjacent residual geometry to Ni_a-SI. They blue mesh electron density is 2Fo-Fc map contoured at 1.5 r.m.s.d.. The L125 lies at the end of the hydrophobic gas channel and shows the same conformation to that of Ni_a-SI, indicating no distortion of gas channel due to ^{i}PrNC inhibition.

This observation is consistent with all inhibitor-bounded active site structure (eg. Ni-SCO and Ni-SMeNC): when the active site interacts with an exogenous inhibitor, there is no detectable density at the bridging position. The absence of terminal ligand density at Ni demonstrates that, although IR shows partial ^{i}PrNC inhibition, the isocyanide ligands do not adopt a single, well-defined orientation in the crystal. This observation was also found in case of nBuNC, while IR shows nearly full inhibition at the active site, the X-ray diffraction shows classic Ni_a-SI features with vacant active site highly identical to what is shown in Figure 6.10.

The lack of observable electron density at Ni for iPrNC and nBuNC likely results from several factors:

1. Conformational Heterogeneity: Each RNC can bind in multiple orientations, smearing out electron density.
2. High Mobility: Although the C≡N moiety is rigid, the alkyl tail is fully rotatable, causing partial or complete disorder even near the proximal carbon and nitrogen atoms.
3. Partial Occupancy: Even if IR indicates strong inhibition, sub-stoichiometric or fractional occupancy in each lattice site may prevent a coherent, crystallographically detectable density.

These effects also account for the unusually broad ν_{CO} bands in the IR spectra, where the distribution of binding geometries broadens the vibrational transitions.[10,11] Nevertheless, there are many studies that report biophysical evidence for detect ligand binding to a protein while x-ray crystallography fails to reveal electron density for the ligand.[12,13] For example, studies on CYP2D6 cytochrome P450 shows ligands like thioridazine bind in multiple conformations. While NMR and other techniques confirm binding, X-ray crystallography

sometimes only captures one conformation or fails to detect the ligand altogether due to its dynamic nature within the active site.[14]

6.4.4 Tert-Butyl Isocyanide Does Not Inhibit Hyd-1

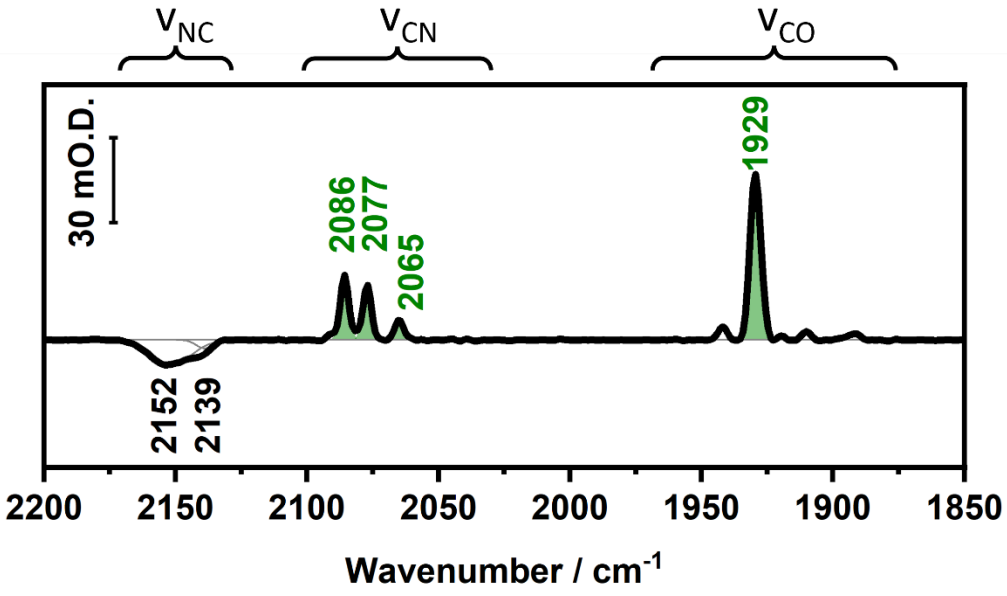

Figure 6.11: Baseline subtracted IR spectrum of ^{t}BuNC soaked Hyd-1 single crystal (100 mM, 30min). IR spectra were recorded with 2 cm^{-1} resolution and 256 scans. IR absorption bands associated with the Ni$_a$-SI state are shaded in olive. The negative peaks represent lower ^{t}BuNC in the crystalline sample compared with the surrounding aqueous background (100 mM tBuNC).

Figure 6.11 displays the IR spectrum of a Ni$_a$-SI Hyd-1 crystal after 30 minutes' incubation with 100 mM tert-butyl isocyanide (^{t}BuNC). The ν_{CO} and ν_{CN} regions match those of unmodified Ni$_a$-SI, indicating no detectable inhibition. Negative features at 2152 cm^{-1} and 2139 cm^{-1} arise from depletion of ^{t}BuNC in the crystal relative to the background, rather than active site binding. Despite the high solvent content (approximately 50 % by volume) and large solvent channels (>2 nm) common to membrane-associated proteins,[15,16] ^{t}BuNC does not appear to penetrate

the closely packed Hyd-1 crystal or the active site, likely due to its excessive steric bulkiness. This means the nBuNC exhibits the upper limit of our inhibitor size titration to the Hyd-1 active site.

6.5 Discussion and Outlook

The IR spectra of Hyd-1 and Hyd-2 single crystals bound by cyanide, methyl isocyanide and ethyl isocyanide demonstrate a successful inhibition by exogenous ligands. In the crystal structures of them, the π-acceptor ligands occupy the terminal position on nickel in a highly similar manner. This observation parallels the binding geometry seen in Ni-SCO reported in Chapter 5. In each case, the ligand's carbon atom directly coordinates to Ni with distance from 2.0 to 2.4 Å, and the Ni–C≡N angle is observed to be significantly less than 180°, indicating a bent coordination geometry. Similarly, the C≡N–C angle within the isocyanide moiety is also found to be below 180°, confirming that the active-site scaffold imposes a non-linear conformation on these sp-hybridised ligands.

The requirement for a bent geometry suggests that the amino acid framework surrounding the NiFe centre is relatively rigid at the terminus of the gas channel. Although the Ni–C bond is formed via an sp-hybrid orbital on carbon, the rigid protein environment forces the ligand into a higher-strain conformation. The N≡C bond aligns with the guanidinium of R509 (in Hyd-1) and R479 (Hyd-2) may suggest a pi-interaction between them, which contribute to the bent conformation. In the case of EtNC, electron density corresponding to the β-carbon is notably weak or nearly absent in the crystallographic maps. This lack of density implies that the terminal alkyl group of EtNC does not adopt a single, well-ordered position but instead remains dynamically disordered. Infrared spectra of EtNC-inhibited crystals further support this

interpretation by displaying two distinct ν_{CN} bands, which are consistent with multiple inhibited conformations of the ligand within the active site. The alkyl tail of the isocyanide projects toward the gas channel, where it is afforded considerable conformational freedom, allowing several energetically similar orientations.

A bent coordination of pi-acceptor ligands is not unique to [NiFe]-hydrogenases. For example, n-butyl isocyanide bound to cytochrome P450cam adopts a similarly distorted geometry,[17] and so does ethyl isocyanide bound to myoglobin.[18] In [Fe]-hydrogenase/isocyanide complexes, the iron–carbon bond also exhibits a pronounced bend due to steric interactions with the protein scaffold.[19] In Ni-SCO structures of [NiFe]-hydrogenase, an analogous geometric distortion is observed when carbon monoxide binds to nickel. In all these systems, the bent bond angle arises from a combination of backbonding optimisation and steric constraints imposed by the surrounding protein matrix. These examples collectively illustrate that, although the first coordination sphere of the metal centre is chemically robust, the protein environment can dictate significant deviations from linear ligand geometry in order to accommodate both small and moderately bulky inhibitors.

Hydrogenation reactions catalysed by [NiFe]-hydrogenases have been hypothesised to involve a frustrated Lewis pair (FLP) mechanism at the active site.[20] In this model, heterolytic cleavage of dihydrogen yields a hydride and a proton, which could, in principle, participate in subsequent hydrogenation of substrates. Synthetic NiFe complexes have demonstrated FLP-like behaviours in activating H_2, where H_2 binds to the Fe site acting as a Lewis acid, while a base abstracts a proton to form a 'proton+hydride' complex.[21]

However, structural evidence presented in this chapter suggests that such hydrogenation reactions on exogenous inhibitors like ketones, aldehydes, and imines are unlikely to be catalysed at the active site of [NiFe]-hydrogenase. In Chapter 5, crystallographic studies of the

Ni_a-R and Ni_a-C states reveal that the hydride is bound at a bridging position between Ni and Fe during catalysis. The terminal cysteine ligand of Ni has been proposed as the initial proton acceptor following dihydrogen splitting, a hypothesis supported by the Ni_a-L_{II} crystal structure. In the current chapter, the results demonstrate that exogenous inhibitors can access the active site and bind to Ni at the terminal position, with their alkyl tails extending into the gas channel. This binding conformation may also apply to potential new substrates. However, if such substrates interact with the active site in the Ni_a-R state, they may lack the appropriate orbital alignment to engage effectively with the hydride and proton. Although the Ni_a-R state provides a relatively reducing environment, the local structural features are unlikely to stabilise the transition state necessary for a hydrogenation reaction. These findings suggest that, despite the theoretical potential for the Frustrated Lewis pair (FLP)-type hydrogenation at the [NiFe]-hydrogenase active site, the structural constraints and binding orientations of exogenous ligands render such reactions improbable under physiological conditions.

Titration of the alkyl substituent on RNCs reveals a clear size cutoff beyond which no inhibition occurs. Methyl isocyanide binds in a single, ordered conformation that can be resolved crystallographically, whereas ethyl isocyanide shows higher degree of freedom on R group. Isopropyl isocyanide achieves partial inhibition but remains disordered, and n-butyl isocyanide fully inhibits but exhibits extensive conformational freedom. tert-Butyl isocyanide, by contrast, is too large to access the active site and shows no inhibitory effect. These findings define the effective tunnel aperture in Hyd-1 crystals: it must accommodate linear alkyl chains of up to four carbon atoms but not sterically branched groups larger than that. Longer linear RNCs (e.g. n-pentyl isocyanide) were not tested due to rare sample availability, but they also represent a possibility to bind the NiFe active site. Molecular-dynamics simulations have identified a principal gas channel in Hyd-1 whose time-averaged minimum diameter is approximately 2 Å.[22] Such a constriction would appear to preclude passage of any ligand significantly larger

than dihydrogen. However, our crystallographic and infrared data demonstrate that bulkier isocyanides, for example isopropyl isocyanide and n-butyl isocyanide, can nonetheless access and inhibit the active site of Hyd-1 in the crystalline state. This finding implies that the nominal 2 Å bottleneck observed by simulation represents a time-averaged, static snapshot rather than an absolute steric barrier.

In these experiments, isocyanide ligands served as molecular rulers by exploiting their strong affinity for the NiFe centre to probe active-site plasticity. For isopropyl isocyanide (^{i}PrNC), infrared spectroscopy indicates only partial inhibition, with roughly 40 percent of active sites remaining unoccupied. In contrast, n-butyl isocyanide (^{n}BuNC) produces an infrared signature consistent with full inhibition, albeit featuring a very broad ν_{CO} band that suggests multiple binding modes or conformations. X-ray diffraction for both ^{i}PrNC and ^{n}BuNC shows no well-defined electron density at the Ni site, implying disorder, partial occupancy or multi-state binding under crystallographic conditions. Taken together, these data imply that the alkyl substituent's bulk and width determine whether the ligand can adopt a single, ordered orientation; ^{i}PrNC is too large to occupy every site consistently, whereas ^{n}BuNC barely fits and binds in multiple conformations. By contrast, tert-butyl isocyanide does not produce any IR signature of inhibition nor any discernible electron density at the active site, indicating that its steric bulk exceeds the tunnel's tolerance. These observations delineate a practical size limit for ligand passage under crystallographic conditions and furnish a direct experimental measure of gas-channel flexibility. Consequently, the maximum dynamic aperture of the tunnel lies between the dimensions of isopropyl isocyanide and tert-butyl isocyanide.

Furthermore, the unmatched IR spectra and X-ray crystallographic data underscore the importance of using complementary techniques alongside X-ray crystallography to fully understand protein-ligand interactions. Relying solely on crystallographic data may lead to

incomplete or misleading conclusions, especially when dealing with flexible or weakly binding ligands.

This size-titration approach may be extended to other metalloenzymes with buried active sites, such as carbon monoxide dehydrogenase, which also features a Ni centre. By employing a series of isoelectronic ligands of increasing steric demand, one can experimentally determine tunnel dimensions and hence validate or refine computational models. The resulting structural and spectroscopic data sets can provide benchmarks for more accurate atomistic simulations, thereby improving our understanding of substrate gating, turnover rates and inhibitor design.

6.6 References

1 J. Duan, A. Hemschemeier, D. J. Burr, S. T. Stripp, E. Hofmann and T. Happe, *Angew. Chem. Int. Ed.*, 2023, **62**, e202216903.

2 J.-H. Jeoung and H. Dobbek, *J. Am. Chem. Soc.*, 2009, **131**, 9922–9923.

3 W. P. Griffith, *Q. Rev. Chem. Soc.*, 1962, **16**, 188–207.

4 M. Chung, DPhil Thesis, University of Oxford, 2016.

5 S. V Hexter, M.-W. Chung, K. A. Vincent and F. A. Armstrong, *J Am Chem Soc*, 2014, **136**, 10470–10477.

6 J. F. Rubinson, J. L. Corbin and B. K. Burgess, *Biochem.*, 1983, **22**, 6260–6268.

7 F. P. Pruchnik and S. A. Duraj, in *Organometallic Chemistry of the Transition Elements*, eds. F. P. Pruchnik and S. A. Duraj, Springer US, Boston, MA, 1990, pp. 617–645.

8 Y. Kung, T. I. Doukov, J. Seravalli, S. W. Ragsdale and C. L. Drennan, *Biochem.*, 2009, **48**, 7432–7440.

9 H. W. Thompson and R. L. Williams, *Trans. Faraday Soc.*, 1952, **48**, 502–513.

10 P. Ormos, A. Ansari, D. Braunstein, B. R. Cowen, H. Frauenfelder, M. K. Hong, I. E. Iben, T. B. Sauke, P. J. Steinbach and R. D. Young, *Biophys. J.*, 1990, **57**, 191–199.

11 K. Nienhaus, D. C. Lamb, P. Deng and G. Ulrich Nienhaus, *Biophys. J.*, 2002, **82**, 1059–1067.

12 Z. Chilingaryan, Z. Yin and A. J. Oakley, *Int. J. Mol. Sci.*, 2012, **13**, 12857–12879.

13 T. C. Pochapsky and S. S. Pochapsky, *Acc. Chem. Res.*, 2019, **52**, 1409–1418.

14 A. Wang, C. D. Stout, Q. Zhang and E. F. Johnson, *J. Biol. Chem.*, 2015, **290**, 5092–5104.

15 R. M. Evans, P. A. Ash, S. E. Beaton, E. J. Brooke, K. A. Vincent, S. B. Carr and F. A. Armstrong, *J. Am. Chem. Soc.*, 2018, **140**, 10208–10220.

16 S. E. Beaton, R. M. Evans, A. J. Finney, C. M. Lamont, F. A. Armstrong, F. Sargent and S. B. Carr, *Biochem. J.*, 2018, **475**, 1353–1370.

17 D.-S. Lee, S.-Y. Park, K. Yamane, E. Obayashi, H. Hori and Y. Shiro, *Biochem.*, 2001, **40**, 2669–2677.

18 K. A. Johnson, J. S. Olson and G. N. Phillips, *J. Mol. Biol.*, 1989, **207**, 459–463.

19 H. Tamura, M. Salomone-Stagni, T. Fujishiro, E. Warkentin, W. Meyer-Klaucke, U. Ermler and S. Shima, *Angew. Chem. Int. Ed.*, 2013, **52**, 9656–9659.

20 H. Ogata, K. Nishikawa and W. Lubitz, *Nature*, 2015, **520**, 571–574.

21 M. Isegawa, T. Matsumoto and S. Ogo, *RSC Adv.*, 2021, **11**, 28420–28432.

22 J. Kalms, A. Schmidt, S. Frielingsdorf, P. van der Linden, D. von Stetten, O. Lenz, P. Carpentier and P. Scheerer, *Angew. Chem. Int. Ed.*, 2016, **55**, 5586–5590.

Chapter 7: *In-situ* X-ray Absorption Spectroscopy Study on Azurin at Room Temperature

This chapter details a novel *in-situ* spectroelectrochemical X-ray absorption spectroscopy (SEC-XAS) method for blue-copper proteins, developed at Diamond Light Source (DLS)'s I20 beamline. X-ray absorption spectra were measured using the I20-Scanning wiggler beamline of DLS. The four-bounce monochromator equipped with Si (111) crystals gives an energy resolution, $\Delta E/E$, better than 1.4×10^{-4} with a flux $>10^{12}$ photons s^{-1} and a focal spot size at the sample position of 0.4 mm (H) × 0.3 mm (V) FWHM. A Canberra 64-pixel Monolithic Segmented Hyper Pure Germanium Detector (HPGe) partnered with the Xspress4 digital pulse processor was used to measure the fluorescence signal emitted from the sample. Initial cryogenic studies established reference spectra for Cu-azurin, followed by room-temperature measurements using a custom flow-cell under electrochemical control to acquire XANES and EXAFS data. By optimizing pulse stroke, net flow rate, redox mediator selection, and X-ray beam intensity, high-quality XAS spectra with minimal photodamage can be acquired *in-situ* from relatively small sample volumes. This optimized approach establishes a promising methodological platform applicable not only to the I20 beamline but also transferable to other XAS studies

These experiments were performed in collaboration with Dr. Stephen Best (University of Melbourne), Dr. Philip Ash (University of Leicester) and Prof. Sofia Diaz-Moreno (DLS). I20-

Beamline was applied for its 64-pixel Monolithic Segmented HPGe detector, aiming for higher data quality.

7.1 Introduction

X-ray absorption spectroscopy (XAS) is a powerful biophysical technique for the study of metalloproteins. By tuning the energy of incident X-ray around a selected metal's absorption edge, two complementary regions of the spectrum can be examined: X-ray absorption near-edge structure (XANES), which reports on oxidation state and coordination geometry, and extended X-ray absorption fine structure (EXAFS), which yields quantitative interatomic distances and local structural information.[1] The core-level excitation underlying XAS renders it one of the few methods capable of probing d^{10} "spectroscopically silent" ions such as Zn(II) and Cu (I), whose filled valence shells preclude conventional optical or magnetic spectroscopies. However, because XAS is element-specific rather than site-selective, it can be challenging to deconvolute signals in metalloproteins containing multiple equivalent metal centres, since the measured spectrum represents an ensemble average of all such sites.[2]

XAS has previously been employed to elucidate the active-site structure of [NiFe]-hydrogenases.[3,4] Although high-resolution crystallography has revealed many details of the protein scaffold over the past two decades, XAS offers unique access to the electronic and coordination environment of the nickel centre. Infrared spectroscopy remains the only common spectroscopic technique for studying [NiFe]-hydrogenases under *in-situ* turnover conditions at ambient temperature, but it reports only on the IR-active CO and CN ligands bound to iron since it is difficult to assign the many overlapping vibrational bands from the protein.[5] Consequently, information concerning the nickel ion is inferred indirectly. Electron paramagnetic resonance (EPR) can probe Ni (III) and Ni (I) states but is silent for diamagnetic intermediates such as Ni_a-SI and Ni_a-R.[6] As a result, a complete characterisation of all catalytic redox states has not been achieved owing to the difficulty of isolating specific redox levels for XAS measurement.

Conventionally, redox control for XAS has been achieved *ex-situ* by electrochemical generation of the desired state followed by cryogenic trapping; coupling electrosynthesis with rapid freeze-quenching has been shown to yield high-quality XAS data from reactive intermediates.[7,8] Nevertheless, this approach does not allow real-time monitoring of dynamic redox processes in solution. Spectroelectrochemical (SEC) methods overcome this limitation by combining electrochemical control with *in-situ* spectroscopic measurement. SEC has proven invaluable in *operando* studies of electrocatalysts[9] and battery[10] materials and is increasingly applied to redox proteins such as hydrogenases,[11] where it enables precise manipulation and simultaneous characterisation of individual redox states.

Multiple methodologies enable *in-situ* XAS measurements under controlled redox conditions, ranging from bulk electrochemical cells[12–14] with large surface area electrodes to disc-shape thin layer cell configurations[15] and sample-electrode immobilisation set-up.[16] While bulk electrochemical cells have been used to obtain XAS spectra (1-10 mL), the long equilibration period (typically >10 min) makes them impractical for the study of short-lived reactive species,[12] or for samples, such as metalloproteins, that are only available in small quantities. The thin layer cells are not volume-demanding (≤100 µL), but the static sample solution is at risk of photodamage. *In-situ* XAS measurements on *DvM*F [NiFe]-hydrogenase was achieved via direct immobilisation protein sample on redox-active polymers at a glassy carbon working electrode.[16] However, it is challenging to control the homogeneity of sample as the electrochemical process is highly diffusion-controlled, and no *in-situ* EXAFS of [NiFe]-hydrogenase has been reported.

Metalloprotein samples are usually ≤ 1 mM, thus requiring a high flux density of the X-ray beams or long data collection times. This introduces a key challenge of photoreduction (photon damage) to the sample. Enzymes such as [NiFe]-hydrogenases are particularly

vulnerable, as photoelectrons or reactive oxygen species generated during irradiation can destabilise both the metal centre and protein structure.[11,17] This risk extends beyond unintended electron reductions at the catalytic metal site to broader structural degradation of the enzyme.[18] High X-ray flux on sample over long exposure duration induce significant sample heating which leads to protein structural damage and accelerated radiation damage. By cooling samples to liquid nitrogen or helium temperatures, the diffusion of radicals and the rate of secondary chemical reaction are severely hindered, dramatically increasing the dose tolerance of the sample and allowing for longer data collection times. Other methods including soft-beam irradiation (L-edge)[3] to flash-freezing[19] and flow cells[20] have also been reported to address photodamage.

Developing a photodamage-free, *in-situ* XAS method for biological samples would enable determination of the precise electronic structure of metal centres during catalysis and deepen our understanding of complex metalloproteins such as hydrogenases and nitrogenases. Such a methodology must be validated on a well characterised, but X-ray-sensitive, model system. Copper centres are especially prone to X-ray-induced photoreduction during XAS measurements, even at cryogenic temperatures.[21] Soft-XANES studies have demonstrated that Cu (II) can be rapidly reduced to Cu (I) under intense X-ray irradiation via low-energy electrons generated in the sample, often accompanied by ligand dissociation or rearrangement. [22]

Azurin, a small (~14 kDa), monomeric cupredoxin from bacteria, was therefore selected to evaluate photodamage in the XAS-SEC setup. Its type 1 ("blue") copper site features a distorted trigonal-planar Cu coordination by two histidine sidechains and one cysteine sulfur, together with weaker axial contacts to a methionine sulfur and a backbone glycine oxygen (Figure 7.1).[23] The highly covalent Cu–S bond confers the protein's characteristic blue colour and supports rapid, reversible one-electron transfer. The Cu^{+}/Cu^{2+} redox couple of azurin lies

at +310 mV versus the standard hydrogen electrode at pH 7.[8]

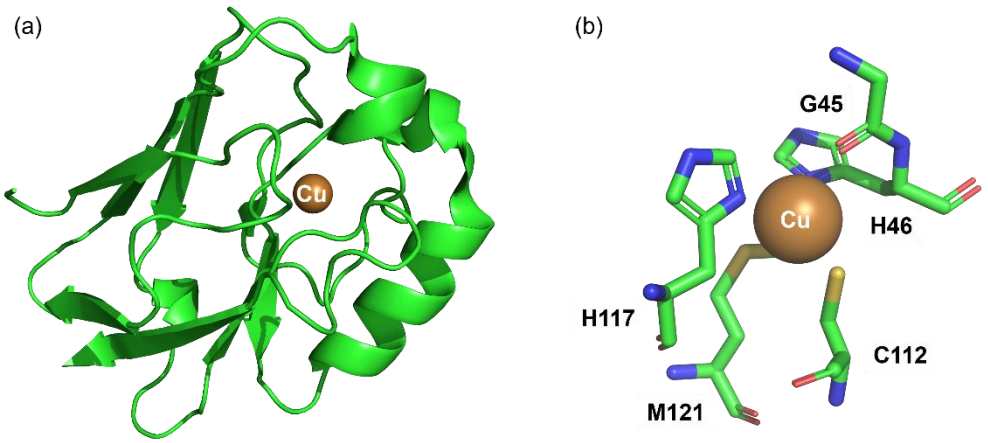

Figure 7.1: (a) X-ray diffraction crystal structure of Pseudomonas aeruginosa azurin (PDB code 4AZU). (b) The local structure of copper site in azurin, and the copper adopts a distorted trigonal bipyramidal structure, coordinating with 5 amino acid residues. Figure prepared in Pymol.

This chapter describes the development of *in-situ* spectroelectrochemical XAS method, testing with a blue-copper protein using the I20 beamline at Diamond Light Source. Initial studies were conducted under cryogenic conditions to establish reference spectra of Cu-azurin. Finally, a customised XAS-SEC cell, featuring a syringe-based flow system designed by Dr. Stephen Best, was employed to acquire *in-situ* XANES and EXAFS data on Cu-azurin under electrochemical control at room temperature. These experiments were performed in collaboration with Dr. Stephen Best (University of Melbourne), Dr. Philip Ash (University of Leicester) and Prof. Sofia Diaz-Moreno (DLS).

7.2 Cell Design and Experimental Procedures

7.2.1 Cryogenic Sample Stick and Holder

A cryogenic sample stick and holder were employed to acquire reference XAS spectra of Cu-azurin *ex-situ* at cryogenic temperature. Both components were designed by Dr Stephen Best in OpenSCAD and fabricated on a Connex3 Objet350 printer using a UV-curable ink (Vero™ resin comprising exo-1,7,7-trimethylbicyclo[2.2.1]hept-2-yl acrylate and camphene) with a water-soluble support material (acrylic acid 2-hydroxyethyl ester).

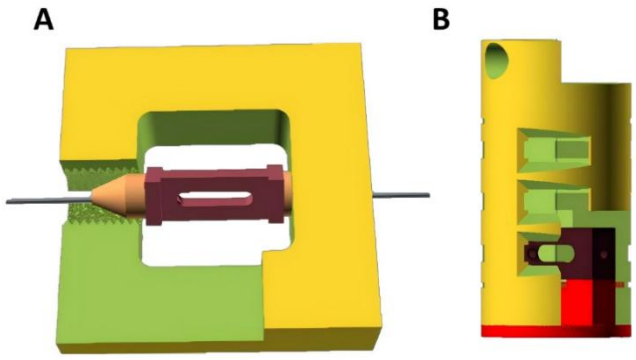

Figure 7.2: The tools for cryo-fluorescence XAS experiment. (A) The schematic representation of injection cage and the sample holder (dark red). (B) The schematic representation of the sample stick with the sample holders fit inside. The sample stick is assembled onto the end of cryo-stick in the cryostat.

The sample holder is a rectangular container (20 mm × 8 mm × 3 mm) with an internal volume of approximately 12 µL (dark-red component in Figures 8.1A and B). A 10 mm × 2.5 mm aperture on one side permits X-ray irradiation and fluorescence detection. After sealing the two hollow faces with PTFE tape, the protein solution was injected through a tin mesh injection cage connected to two PEEK capillaries fitted with ferrules (Figure 7.2A). Each capillary was attached to a gas-tight syringe, and approximately 15 µL of sample was introduced to eliminate

air bubbles. The assembly was then plunged into liquid nitrogen to freeze the sample rapidly, thereby trapping the desired redox state of the copper centre. Finally, the frozen holder, containing the immobilised protein solution, was removed and stored under cryogenic conditions.

XAS measurements were performed in a cryogenic sample chamber to enhance data quality. The sample holders were mounted on a detachable sample stick, as shown in Figure 7.2B. Each holder was inserted into the stick via its open end and secured with a matching lid. The assembled sample stick was then affixed to the cryo-stick before measurement. Side windows in the stick permitted the incident X-ray beam to impinge upon the sample and allowed the resulting fluorescence to reach the detectors.

7.2.2 XAS-SEC Cell Set-up

The XAS-SEC cell

The XAS-SEC cell set-up is primarily designed by Dr. Stephen Best and the design principles were described previously.[11] Two key challenges of XAS-SEC are addressed in the design: minimisation of sample volume and prevention of radiation-induced photodamage. The total cell volume was lowered to under 300 µL, with approximately 50 µL residing in the working-electrode chamber (sample measuring site). Photodamage was mitigated by integrating a syringe-pump flow system.

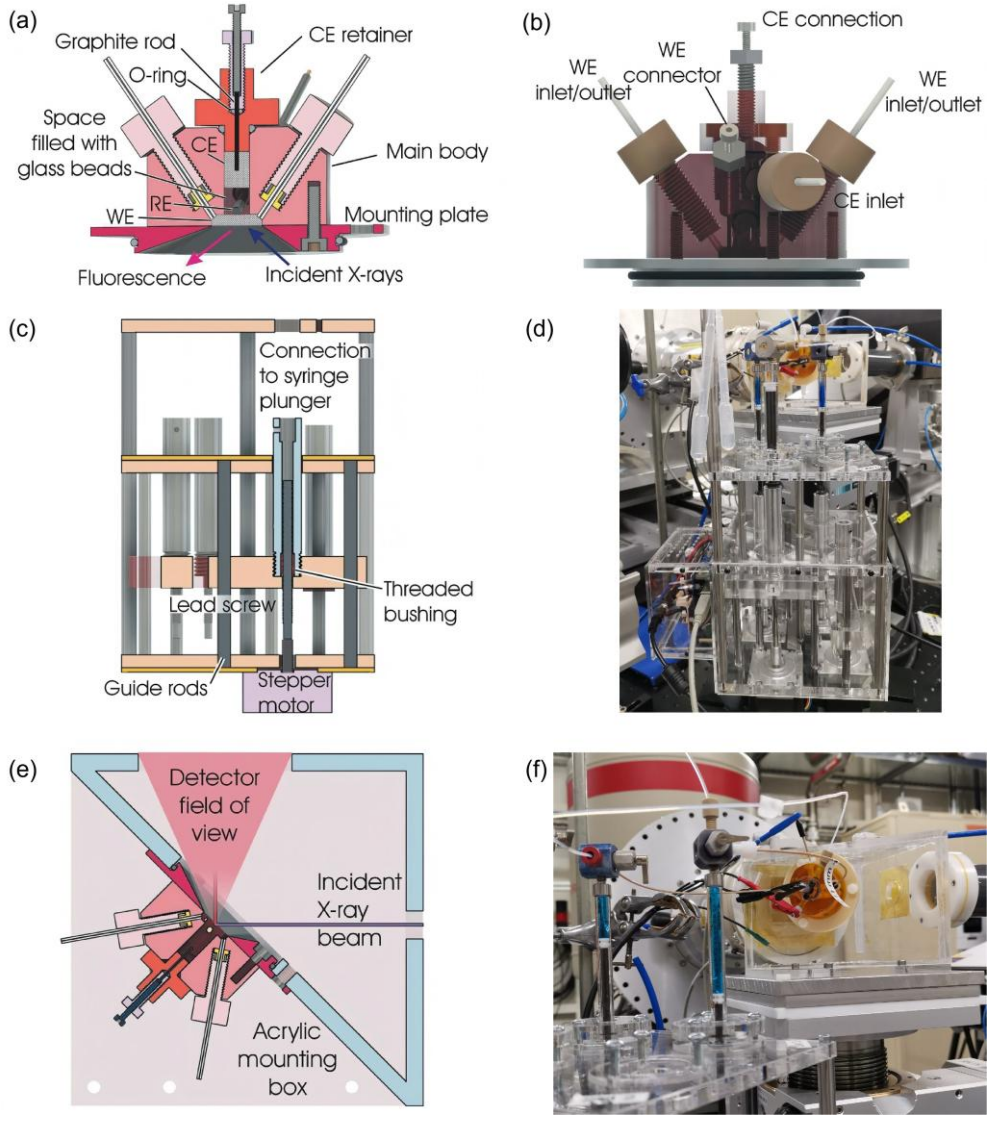

Figure 7.3: The schematic representations of the XAS-SEC cell and the picture of the cell assembled on Diamond I20 beamline.[11] (a): Cross-sectional view of the assembled XAS-SEC cell body showing the sample inlet/outlet, the positioning of the working, counter and reference electrodes and the electrical connection to the CE. (b) 3D-CAD view of the assembled cell. (c) Cross-sectional schematic of a stepper motor syringe driver assembly. (d) Syringe pump assembly mounted on the beamline sample. (e) Cross-sectional view of the XAS-SEC cell mounted onto an acrylic box. (f) The whole XAS-SEC cell with syringe pump assembly while working on beamline. The sample inlet/outlet are connected to sample syringes, and the blue sample solution is as-isolated Cu-azurin with oxidised DCIP. Adapted with permission from S. P. Best *et a*l, *J. Synchrotron Radiat.*, 2021, 28, 472-479.

The cell body (Figures 7.3 a and b) was printed in the same UV-curable resin as the cryogenic holder; the mounting plate was machined from ULTEM™, a thermoset polymer devoid of detectable copper, thus eliminating spectral contamination. Porous reticulated vitreous carbon (RVC) served as both working and counter electrodes, and a 2 mm Ag/AgCl reference electrode was positioned immediately adjacent to the working electrode. To prevent solution mixing between chambers, the inter-electrode gap was packed with glass beads (>100 µm), chosen over ion-exchange membranes to facilitate rapid filling and flushing.

The working electrode was sealed behind a Teflon-coated Kapton film, clamped between body and plate. A custom-cut PTFE gasket ensured a leak-proof interface. Electrical contact was made via a graphite rod (0.9 mm HB pencil lead) O-ring-sealed into the main body (WE) or counter-electrode retainer. An M4 nylon screw (with internal M2 thread) compressed the O-ring, and an M2 screw advanced the rod into the RVC (grey screws in Figures 7.3 a–b). Solution flow was delivered through 1/16-inch tubing and sealed with flangeless LC fittings. Prior to XAS, deoxygenated electrolyte was circulated, and the cell's electrochemical response was verified.

The flow system

Precise volume and rate control of the electrolyte flow was achieved with a stepper-motor assembly (Figure 8.2 c) managed by a commercial four-axis controller with USB interface (KTA-290). Gas-tight syringes were mounted on the motorised drive; the complete beamline pump setup is shown in Figure 7.3 d. A pulsed-flow operation of a matched pair of syringes was adopted to minimise sample exposure: after ca. 0.6 µL (3 pulses) had flowed, 0.4 µL (2 pulses) of sample was flowed backward. When the sample from the inlet syringe is running down, the net flow direction was reversed. This approach reduced mean dwell time under the beam and

flushed photoproducts from the measurement zone, while permitting systematic optimisation of pulse volume, residence time and beam intensity.

Mounting configuration

The XAS-SEC cell was located inside a helium-flushed acrylic enclosure to minimise air scatter and to fix the incident beam at 45° to the working-electrode surface (Figure 7.3 e). A translation stage allowed the electrode to be moved over a 5 mm × 1.2 mm area while maintaining an unobstructed fluorescence path. This clearance accommodated a 4 × 2 grid of non-overlapping 0.4 mm × 0.3 mm beam spots (I20-Scanning), facilitating routine assessment of beam-induced damage. The complete setup, with blue-coloured Cu-azurin in the gas-tight syringes ready for measurement, is shown in Figure 7.3 f.

7.2.3 Experimental

All cell components were cleaned by sonication in deionised water for three minutes. The tubing threads were gently drilled (1.6 mm for the WE inlet/outlet and CE inlet; 1.0 mm for the WE connection) to clear blocks and strips. PEEK tubing (1/16 inch) was then inserted into the CE inlet, WE inlet and WE outlet, with O-rings in place.

Porous reticulated vitreous carbon (RVC) electrodes were fabricated using pre-designed metal cutters. A cylindrical counter-electrode (4 mm diameter, 10 mm length) and a cuboid working electrode (12 × 12 × 2 mm) were freshly cut, then immersed in concentrated sulfuric acid for at least five minutes to sulfonate and render the carbon surface hydrophilicity. Both electrodes were rinsed thoroughly with deionised water and buffer thereafter. Electrical contact to the RVC electrodes was made via 0.9 mm graphite rods (HB pencil leads). Each 20 mm lead was

placed into a nylon M4 screw (with M2 internal thread) fitted with an O-ring. After screwing the assembly into the cell body, an M2 metal screw was used to advance the lead into the RVC, establishing contact. The counter-electrode connection was prepared identically. A 2 mm-diameter Ag/AgCl reference electrode was mounted in an M6 screw with O-ring seal and inserted until its tip lay immediately above the WE headspace, minimising uncompensated resistance.

Dry glass beads (0.22 g) were introduced into the cell via the CE port using a funnel. The sulfonated RVC CE was then seated on top the beads, and its connection holder was fastened to the cell body with three M3 screws. The assembly was inverted, the silica tube fraction used as a temporary plug was removed from the WE chamber, and the prepared WE was installed. The electrode surface was trimmed flush with the cell face to minimise defects. A PTFE gasket, cut to match the WE aperture, was applied over the window, followed by a Teflon-coated Kapton film. The cell was closed with its mounting plate and secured by five M3 screws. Finally, the M2 screws were tightened to ensure graphite-to-RVC electrical contact. Sample and electrolyte solutions (2 mM azurin, 2.5 mM dichloroindophenol (DCIP), 2.5 mM ferricyanide (FCN), 2.5 mM methyl viologen (MV), 150 mM NaCl in 50 mM PBS) were degassed under nitrogen in a glovebox and loaded into gas-tight syringes fitted with multi-port valves. A syringe containing PBS was dedicated to the CE; two syringes served the WE inlet and outlet, only one of which was filled with sample. The syringes were connected to the cell via 1/16-inch tubing and flangeless LC fittings. Prior to sample introduction, the cell and tubing were filled with at least 5 mL deoxygenated PBS via the CE port, and cyclic voltammetry was performed to verify the electrochemical response. The electrolyte in the WE circuit was then replaced by flowing approximately 60 µL of sample to waste, thereby establishing an enclosed WE volume free of significant concentration gradients. The desired net flowing rate in measurement at WE chamber was optimised and set at 100 µL/h.

7.3 Optimising Operational Conditions of the XAS-SEC Cell

All data in this section are processed by *Athena v0.9.26* software.

The syringe-pump flow system and the electrode geometry proved essential for mitigating photodamage during prolonged measurements. Nevertheless, experimental parameters must be carefully refined to achieve optimal performance. In particular, the choice and concentration of redox mediators and the incident X-ray flux should be adjusted to balance redox control with minimal radiation dose.

Mediators

Figure 7.4 illustrates the importance of redox mediators in SEC-XAS experiments. Azurin samples were electrochemically poised at -300 and +300 mV vs Ag/AgCl since the reduction potential of azurin is around +110 mV vs Ag/AgCl. Ideally, azurin will be electrochemically reduced and oxidised under these applied potentials and show distinct XANES spectra. However, in the absence of mediators, the near-edge features of the XANES spectra for azurin are identical under both oxidizing and reducing conditions (red and blue spectra, respectively). This indicates an absence of expected changes, such as edge shifts or variations in pre-edge peak signatures. The overlaid spectra recorded without mediators display no discernible structure at or beyond the edge, suggesting severe photodamage and potential distortion of the copper coordination environment. Notably, the spectrum recorded at +300 mV vs Ag/AgCl, a potential well above the redox couple of azurin, exhibits an edge at 8980.5 eV which is characteristic of reduced Cu (I). This implies that oxidation at the working electrode was

incomplete and that X-ray-induced photoreduction dominated the sample's state.

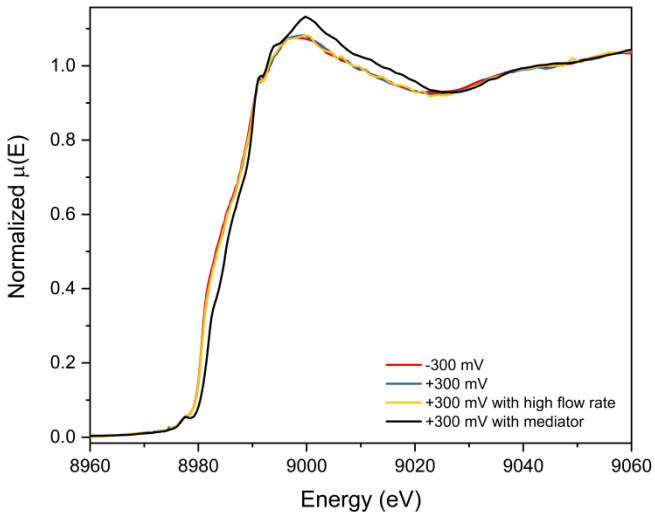

Figure 7.4: The comparison of near edge features of XANES spectra recorded in the XAS-SEC cell when mediators are absent/present with azurin sample. Applied potential is compared against Ag/AgCl reference electrode. The three spectra are collected at a same position under different conditions and each of them are merged from at least 3 raw spectra. Red: electrochemically poised at -300 mV. Blue: electrochemically poised at +300 mV. Yellow: at +300 mV but with much higher sample flow rate from 100 to 300 µL/h. Black: electrochemically poised at +300 mV with mediators (2.5 mM DCIP, FCN and MV).

Redox mediators are small, reversible electron carriers that efficiently shuttle electrons between the electrode and the redox-active species in solution. They significantly enhance the rate of electron transfer, overcoming the limitations of sluggish direct heterogeneous electron transfer and raising the effective current density.[24] Although the syringe-pump system in the XAS-SEC setup enables laminar-like flow over the working electrode, this alone is insufficient to drive the redox conversion of azurin, especially under intense X-ray irradiation. Doubling the sample flow rate did not prevent photodamage, as shown by the yellow spectrum. The black spectrum in Figure 7.4 shows the edge features of azurin at +300 mV vs Ag/AgCl with

presence of mediators, including 2.5 mM of DCIP, FCN and MV. In addition to the pre-edge peak at 8978 eV, the spectrum shows an edge position at 8982 eV, approximately 1.5 eV higher than the overlaid spectra. A significantly more intense absorption is also observed on the white line at 9000 eV. These distinctive features suggest that the azurin sample measured with mediators is likely one electron more oxidised than the sample measured without mediators. The presence of mediators enables better electrochemical control of the SEC-XAS cell and may also contribute to mitigating photodamage.

In addition to facilitating electron transfer, mediators may act as sacrificial species, intercepting photogenerated electrons and mitigating the impact of X-ray–induced reduction. By continuously reoxidising or re-reducing the sample, the mediators help maintain the intended redox state and prevent the accumulation of artefacts.[11] Therefore, they preserve spectral fidelity across multiple scans. This observation suggests that the presence of mediators is as effective as cryogenic cooling in suppressing photoreduction.

Filters

The intensity of the incident X-ray beam must be carefully adjusted to minimise photodamage. A 0.2 mm aluminium filter was selected based on prior testing. This filter reduced the photon flux from 2×10^{12} photons per second to approximately 3×10^{11} photons per second at 9 eV. However, under these conditions, the azurin sample still suffered significant photodamage, even with mediators present and a flow rate of 100 µL/h, as illustrated in Figure 7.5a.

The initial potential was set at -300 mV vs Ag/AgCl (compare with reduction potential +110 mV) and each spectrum takes approximately 14 min to measure. The red spectrum in Figure 7.5a shows the near-edge features of XANES at this potential. It shows a reasonable Cu (I) profile with the edge position at 8980.5 eV, although the characteristic shoulder features on

the absorption edge were already diminished. After two consecutive scans over a period of approximately 28 minutes, the sample was fully photodamaged. The second and third scan (blue and yellow spectrum in Figure 7.5 a) exhibited a nearly featureless edge and loss of the distinct white line peak at 9000 eV, indicating disruption of the Cu coordination environment and suggesting that the Cu (I) centres were no longer chemically intact.

Increasing the aluminium filter thickness to 0.5 mm significantly reduced the beam intensity. This configuration transmitted only 0.8% of the original photon per second, resulting in a photon flux of approximately 1.7×10^{10} photons per second at 9 eV, as measured by the ion chamber. Under these optimised conditions, the XAS-SEC cell enabled reliable, room-temperature XAS measurements of azurin without apparent photodamage.

Figure 7.5b shows a series of seven consecutive XANES scans recorded at +500 mV vs Ag/AgCl. At this potential the azurin should be electrochemically oxidised with the copper have the formal oxidation state of +2. The spectra are nearly identical, showing consistent edge and post-edge features, including a pre-edge peak at 8978 eV and an elevated edge position typical of Cu (II) at 8982 eV. This demonstrates that the oxidised azurin sample preserved its electronic and geometric structure throughout the 98-minute acquisition period.

By combining careful control of beam intensity with a syringe-pump system, redox mediators, and the XAS-SEC cell design, this setup effectively mitigates photodamage during in-situ XAS measurements of Cu-azurin at room temperature under a photon flux of approximately 1.7×10^{10} photons per second.

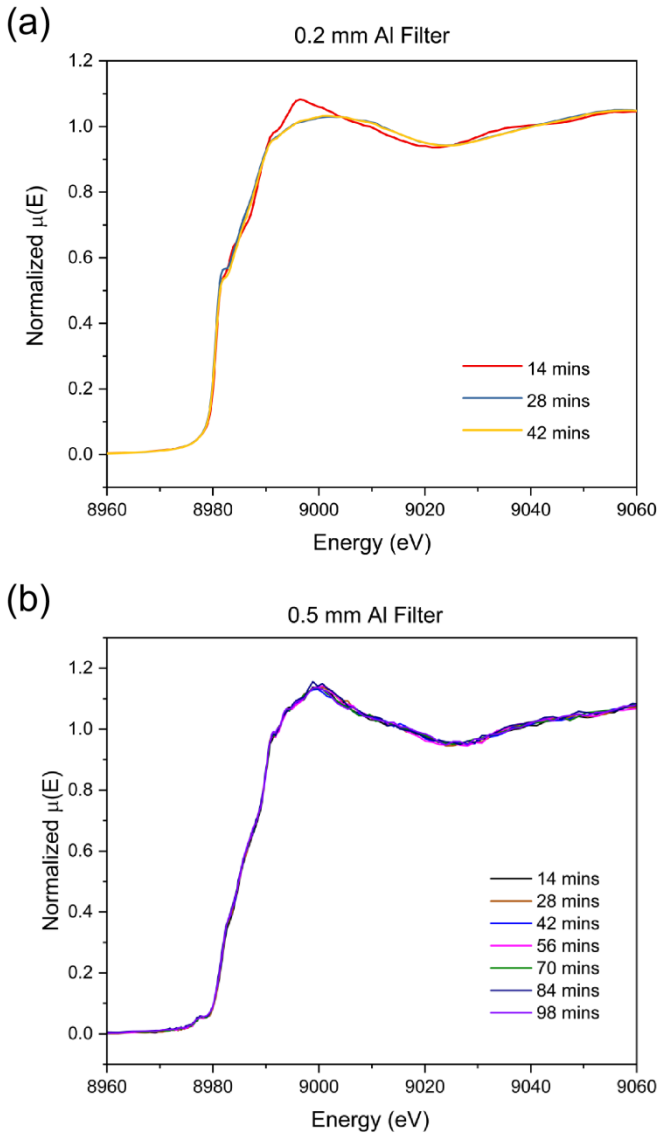

Figure 7.5: The effect on the spectra from filter thickness and measurement duration. (a): 0.2 mm Al filter is applied, photon flux is 3×10^{11} ph/s at 9 eV compared to full beam 2×10^{12} ph/s, potential poised at -300 mV vs Ag/AgCl. The red spectrum is recorded at a fresh WE spot, and the blue and yellow spectra is the second and third scan on the same spot, respectively. (b) 0.5 mm Al filter is applied, photon flux is 1.7×10^{10} ph/s at 9 eV, potential poised +500 mV vs Ag/AgCl. Consecutive XANES spectra measured at same spot in the XAS-SEC cell, each spectrum takes approximately 14 min.

7.4 *In-situ* XANES Potential Titration on Cu-azurin at Room Temperature

All data in this section are processed by *Athena v0.9.26* software.

7.4.1 Comparison to Spectrum Collected at Cryogenic Conditions

The azurin samples, including as-isolated (asiso), chemically reduced (26 mM sodium dithionite) and electrochemically reduced were first tested at 4 K under static conditions in prior to collect their XAS spectra at room temperature.

The azurin samples, including as-isolated (asiso), chemically reduced (26 mM sodium dithionite) and electrochemically reduced were first tested at 4 K under static conditions prior to collecting their XAS spectra at room temperature. In Figure 7.6a, the XANES of asiso (black spectrum), chemically reduced (blue) and electrochemically reduced (violet) azurin collected at cryogenic temperature and static conditions are compared. The asiso and two reduced spectra show similar edge features to oxidised and reduced azurin reported previously in literature by DeBeer *et al*.[8] The asiso azurin (oxidised) spectrum displays all the hallmarks of Cu (II): no pronounced feature appears below 8985 eV apart from a weak, Laporte-forbidden 1s→3d transition at approximately 8978 eV, and edge position at 8982 eV.[25] In contrast, the reduced azurin spectrum is characteristic of Cu (I), with no pre-edge peak observed due to full $3d^{10}$ electronic configuration. Measurement of the first-derivative peak positions reveals a ~1.5 eV shift of the edge position (1s→4p, Laporte-allowed) between the oxidised and reduced forms, in excellent agreement with a one-electron redox change.[26] However, the desired spectrum of asiso azurin (black spectrum, Figure 7.6a) was collected with much lower X-ray

flux compared to the spectra of the intentionally reduced sample. The red spectrum in Figure 7.6a shows the XANES of asiso azurin measured with same irradiation conditions as the reduced samples. The spectrum is comparable to those of reduced samples and shows typical Cu (I) features near the edge, notably the absence of a pre-edge peak at 8978 eV and an edge position at 8980.5 eV. This similarity demonstrates that unintended photoreduction occurred during the measurement of the as-isolated sample.

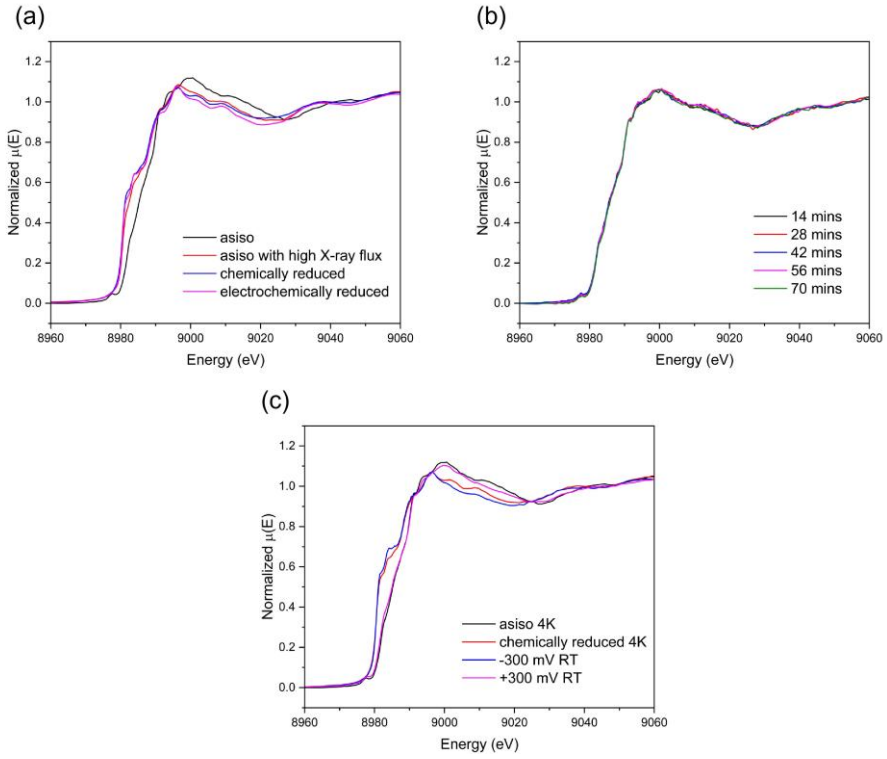

Figure 7.6: (a) The XANES of azurin samples in different redox states measured under cryogenic temperature and static condition. The black spectrum is measured with less photon irradiation (photon flux is 9.3×10^{9} ph/s at 9 eV, 0.5 mm Al, 1 mm C, ca. 14 min exposure) and the other spectra is measured with (photon flux is 3×10^{11} ph/s at 9 eV, filter 0.2 mm Al, ca. 14 min exposure). (b) XANES spectra of asiso azurin at a single sample area with function of time under cryogenic temperature and low X-ray flux. (c) The comparison of XANES spectra of azurin samples collected from the cryogenic holder and the XAS-SEC cell under different conditions, redox potential is shown against Ag/AgCl electrode. At least five raw spectra are merged to obtain each final spectrum except panel (b).

Figure 7.6b presents a series of XANES spectra for asiso azurin, collected under cryogenic conditions with a low incident X-ray flux on a single sample area. The overlaid spectra are highly reproducible with characteristics of Cu (II), exhibiting a consistent pre-edge peak at approximately 8978 eV and an edge position at 8982 eV. Throughout the 70-minute X-ray exposure, no significant edge shift or diminishment of the pre-edge peak is observed. This spectral stability indicates that the chemical environment of the copper center is retained, providing clear evidence that no photoreduction occurred during the measurement.

A direct comparison of the X-ray absorption near-edge structure (XANES) spectra for azurin was conducted between measurements taken under cryogenic conditions and those acquired using the *in-situ* XAS-SEC cell at room temperature under electrochemical control (Figure 7.6c). The XANES spectrum measured at +300 mV (vs. Ag/AgCl) and room temperature (violet spectrum) successfully reproduces the spectrum of the asiso sample collected at 4 K (black spectrum). Both exhibit identical edge features, specifically a pre-edge peak at 8978 eV and an edge position at 8982 eV, confirming that the oxidised Cu (II) state is maintained in the electrochemical cell. Similarly, the spectrum of the reduced sample measured at -300 mV (vs. Ag/AgCl) (blue spectrum) matches the corresponding spectrum obtained at cryogenic temperature (red spectrum), demonstrating a full one-electron reduction to the Cu (I) state. A minor discrepancy between the reduced spectra is noted in the absorption profile around 8982-8984 eV; the origin of this subtle difference will be discussed in a subsequent section. Overall, the close agreement of the near-edge energies and spectral features with those established in prior XAS studies of azurin and spectra collected at cryogenic condition confirms that the customised XAS-SEC cell reliably reproduces the characteristic spectral signatures of the Cu (I) and Cu (II) states under *in-situ* electrochemical control.[8,27]

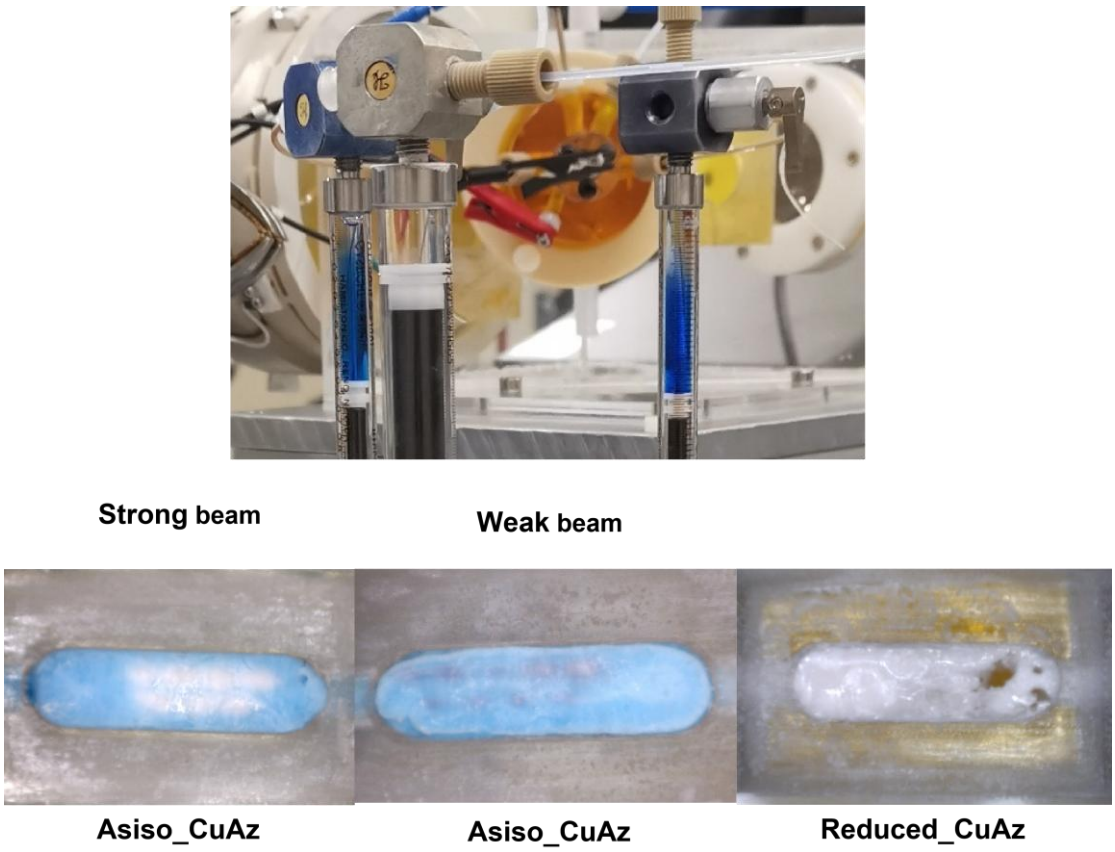

Figure 7.7: (Top) The syringes with azurin sample while the XAS-SEC is applying negative potential. The head space is colourless and bottom sample remains oxidised. (Bottom) Frozen sample holders post measurements. The left sample is as-isolated oxidised azurin with high X-ray flux (red spectrum, Figure 7.6a), middle sample is as-isolated oxidised azurin with much lower X-ray flux (black spectrum, Figure 7.6a) and the right sample is sodium dithionite chemically reduced azurin (blue spectrum, Figure 7.6a).

In the top panel of Figure 7.7, the syringes used during spectral acquisition in the flow XAS-SEC cell are shown. The headspace fluid appears colourless, demonstrating that both DCIP (colourless when reduced) and azurin (colourless in its reduced form) were reduced electrochemically. By contrast, the solution in the lower syringe remains oxidised and appears blue. The bottom panel of Figure7.7 shows the frozen sample holder post-exposure. White patches on the left correspond to regions subjected to high-intensity illumination; the middle holder, which received filtered photons during XAS collection, serves as a contrast, illustrating

the effect of dose on sample integrity.

7.4.2 *In-situ* XANES on Azurin under Electrochemical Control

Serial, rapid-scan XANES spectra of azurin were recorded in the XAS-SEC cell while the applied potential was stepped from -300 mV to +300 mV (vs Ag/AgCl). Figure 7.8 presents the near-edge features observed during this *in-situ* potential titration. As the potential was made more positive, three spectral features evolved, indicating that the copper centre was oxidised from Cu (I) to Cu (II).

The first and last spectra of the potential titration exhibit distinct features characteristic of reduced and oxidised azurin, respectively, and these spectral features align with those established in prior XAS studies of azurin by DeBeer *et al*.[8,27]Firstly, the Cu K-edge edge-position shifted to higher energy by approximately 1.5 eV between the most reduced and most oxidised spectra (from 8980.5 to 8982 eV), consistent with the increased energy required for the 1s → 4p excitation upon oxidation.[26] Secondly, two shoulder peaks at 8982 eV and 8984 eV in the white-line region diminished progressively, which suggests there are features from Cu (I). Such multiple shoulders are generally attributed to ligand-field splitting of the degenerate 4p orbitals, a phenomenon most pronounced in low-coordinate, low-symmetry sites.[14] In the reduced form, the two axial ligands of azurin are thought to interact only weakly with Cu (I) owing to its higher electron density, and the site are more likely to adopt a distorted trigonal-bipyramidal geometry (three equatorial ligands defining a trigonal plane with two more distant, weakly bound axial ligands, Figure 7.1).

Finally, a weak pre-edge feature at 8978 eV appeared in the composite of the final five spectra recorded at +100 mV and became more distinct at +300 mV. This pre-edge is ascribed to the

Laporte-forbidden 1s → 3d transition of Cu (II), confirming the progressive oxidation from d^{10} (Cu (I), which lacks any pre-edge) to d^9 (Cu (II), in which 3d/4p orbital mixing in a non-centrosymmetric, five-coordinate site renders the transition partially allowed).

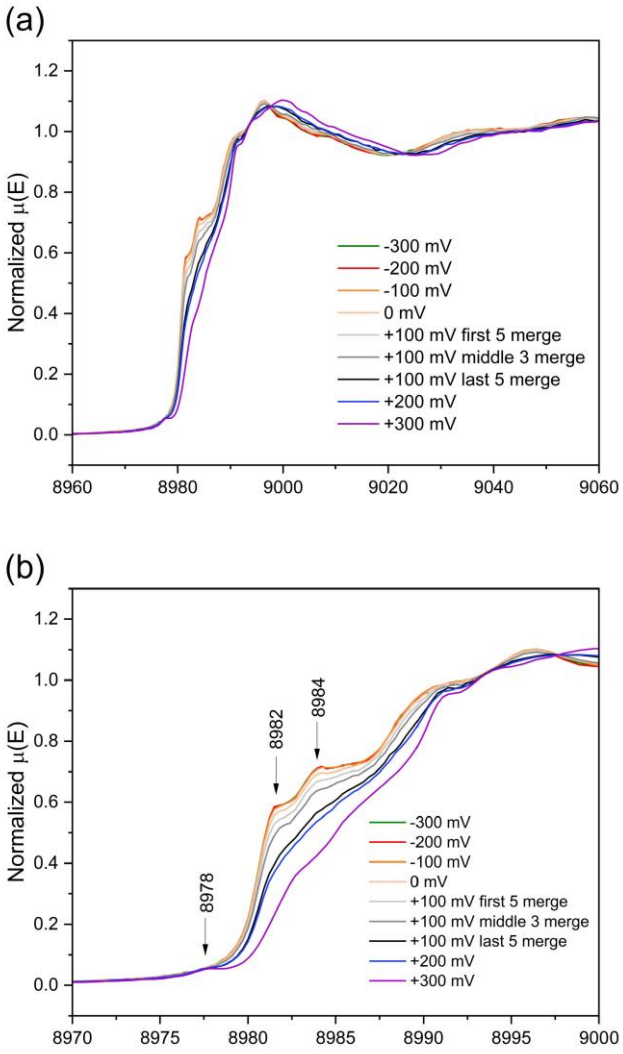

Figure 7.8: The oxidative potential titration of azurin measured in XAS-SEC cell step-up. Applied potential is compared against Ag/AgCl reference electrode, and each spectra takes ca. 14 min to collect. (a) XANES spectra. (b) Near edge features of azurin at room temperature. A gradual shift in edge position is observed through the oxidative potential steps. The spectra collected at +100 mV are separately merged respect to the order of collection.

Figure 7.8 b presents an enlarged view of the XANES spectra between 8970 and 9000 eV, revealing subtle changes at each potential step. At applied potentials well below the reduction potential of azurin (–300, –200, –100 and 0 mV versus Ag/AgCl), the edge features remain essentially unchanged, aside from a slight diminished of the shoulders at 8982 and 8984 eV.

When the potential was stepped to +100 mV, thirteen spectra were collected and subsequently grouped into three sequential sets according to the order of data collection, as shown in Figure 7.8 b. The final five spectra (pink trace) exhibit marked differences at the edge compared with the first five and the middle three: the shoulders at 8982 and 8984 eV become broader, the main edge shifts to higher energy, and the pre-edge feature at 8978 eV increases slightly in intensity.

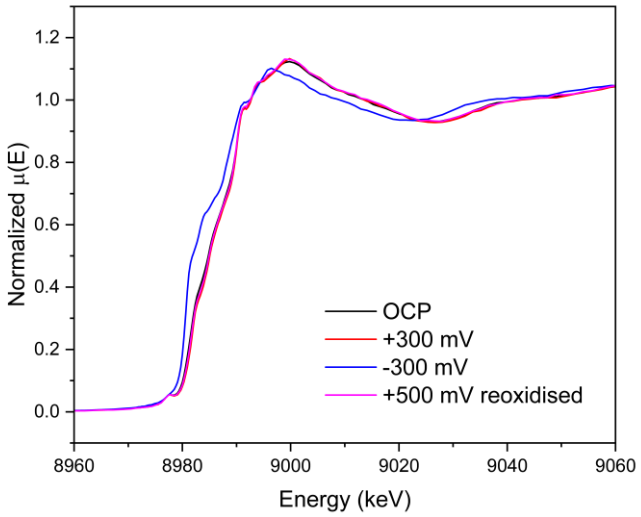

Figure 7.9: The electrochemical reversibility of azurin in the XAS-SEC cell as demonstrated by near edge features of XANES measured at different redox levels. The applied potential is compared against Ag/AgCl reference electrode. Each result spectrum is merged from at least nine raw spectra. The spectra are measured at the same WE spot, starting with OCP (+150 mV), then step to +300 mV, -300 mV and reoxidised to +500 mV.

At +300 mV, a potential well above the midpoint potential, the sample is expected to be fully oxidised at equilibrium. This is confirmed by the XANES spectrum at +300 mV, which displays the greatest edge energy and the most pronounced pre-edge peak, in accordance with Cu (II) features.

The reversibility of the XAS–SEC cell was also evaluated. XANES spectra were recorded at the same working-electrode spot under successive redox conditions: initial open-circuit potential (OCP, +150 mV), oxidative potential (+300 mV), reductive potential (–300 mV) and finally a second oxidative step (+500 mV). A higher re-oxidation potential was chosen to compensate for potential reference-electrode drift, as the mass-exchange may happen over long measurement time between working electrode and counter electrode via the sand beads. Figure 7.9 compares the edge regions of the XANES spectra obtained at each redox level. Except for the spectrum recorded at –300 mV, all spectra acquired under oxidising conditions are essentially superimposable in terms of pre-edge intensity, edge energy, white-line shape and post-edge features. These observations confirm that (i) no significant beam-induced alterations occur during the XAS–SEC experiment and (ii) The one electron redox reaction one azurin can be fully reversible in the cell via potential control. Cyclic voltammetry cannot directly measure the redox potential of azurin as the presence of high mediator concentration in the cell (2.5 mM) . However, in the oxidative potential titration, the XANES of azurin has the edge shift started at +100 mV vs Ag/AgCl (redox potential at +110 mV vs Ag/AgCl as reported in literature[8]).

7.5 *In-situ* EXAFS of Cu-Azurin at Room Temperature

All EXAFS data were processed and normalised using *Athena v0.9.26*, and fits were performed in *Artemis v0.9.26*.

Scattering paths for photoelectrons emitted by the absorbing copper atom were calculated with the FEFF code, and these theoretical paths were fitted to the experimental χ(k) data to extract interatomic distances and coordination numbers.

The FEFF input for Cu-azurin was prepared as follows:

1. Structural Model: The oxidised *Pseudomonas aeruginosa* azurin crystal structure (PDB 4AZU, pH 9, 1.90 Å resolution) was downloaded.
2. Selection of Local Environment: In *PyMOL*, all atoms within 6 Å of the copper centre were selected and exported as a CIF file. Figure 7.10 illustrates the selected atoms and their spatial arrangement.
3. Preparation of Coordinates: Cartesian coordinates of each atom were converted to fractional coordinates by dividing by the unit-cell dimensions along the x, y and z axes. These fractional coordinates were imported into *Artemis* and used to generate a FEFF "ATOM" card.
4. FEFF Input Generation: The FEFF input file was created with a real-space cluster margin of 0.03 Å to ensure inclusion of all relevant scatterers.

This procedure yielded a FEFF model accurately representing the immediate coordination sphere of Cu-azurin, enabling robust fitting of the first and second coordination shells in

the EXAFS analysis.

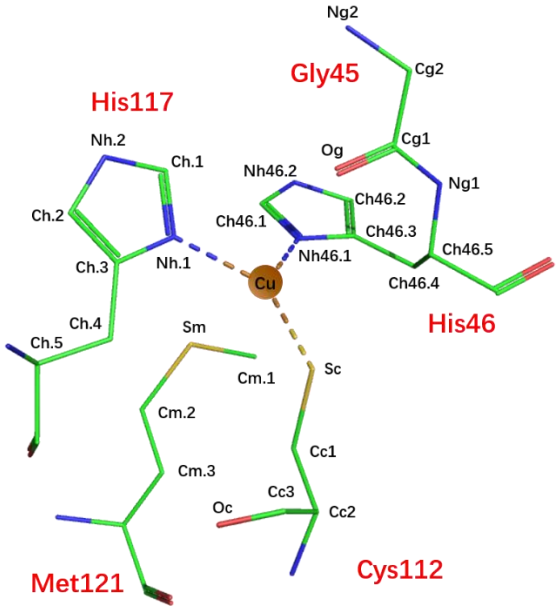

Figure 7.10: Structural illustration of FEFF generation for EXAFS analysis. Crystal structure (PDB code: 4AZU) and each atom of five ligated amino acids with distance to Cu centre small than 5 Å is noted accordingly.

Upon loading the 'asiso' Cu-azurin into the XAS-SEC cell, the sample was first poised at -300 mV (versus Ag/AgCl) for collection of the reduced form, and then at +500 mV for the oxidised form. For each redox state, at least three identical raw EXAFS scans were acquired (≈45 min per measurement) and merged together to improve the signal-to-noise ratio. Figure 7.11 shows a serial EXAFS spectrum collected in the cell which they are overlaid on each other, suggesting no photodamage during the measurement.

The k-weighted χ(k) spectra (k^3 weighting) were Fourier-transformed using a Hanning window over k = 3.66–11.2 $Å^{-1}$ (reduced form) or k = 4.0–10.6 $Å^{-1}$ (oxidised form) (Figures 7.11 a and 7.12 a). The resulting R-space data (Figures 7.11 b and 7.12 b) exhibit a distinctive "triplet" arising from the first and second coordination shells. Back-transforms were performed over R

= 1.0–3.2 Å to isolate these shells for fitting.

Each fit incorporated single-scattering paths to all directly bound ligands (two histidine nitrogen, one cysteine sulfur, one methionine sulfur and one backbone oxygen) as well as four carbon atoms (Ch.1, Ch.2, Ch46.1 and Ch46.2) of the imidazole rings (Figure 7.10). In R-space, the dominant feature at ≈1.8 Å corresponds to the first shell of the two His N and one Cys S scatterers, while the second peak of the "triplet" features are contributed from single scatterings of further atoms such as histidine carbons and two axial ligands. There are few multiple scattering paths show contribute between 2.0 to 3.0 Å in R-space according to FEFF calculation, but there are omitted due to non-linear geometry and associated parameter uncertainty. From the feff calculations, the third peak at 3.6 Å in the R-space is associated further carbon atoms from ligands (e.g. Cg1 and Cg2) and complicated multiple scattering paths. However, the EXAFS analysis in this thesis focuses on the first coordination sphere of Cu, therefore, the R range is set as R = 1.0–3.2 Å for the fitting.

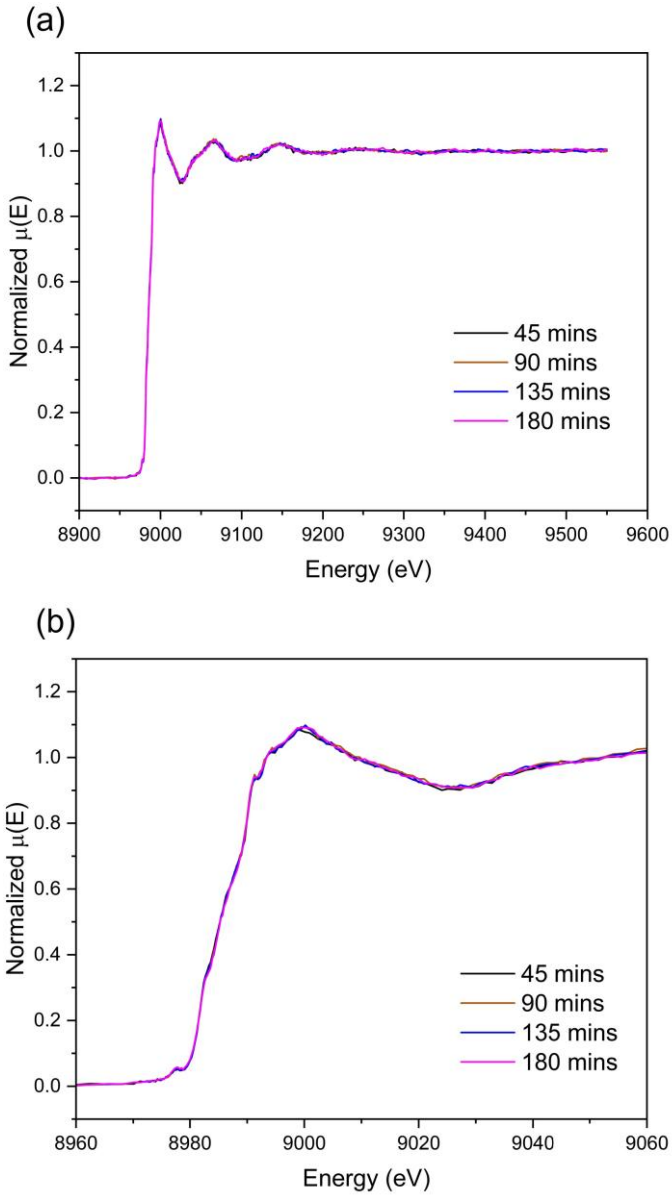

Figure 7.11 (a) The EXAFS spectra of azurin at a single sample area with function of time in the XAS-SEC cell, potential poised at +500 mV vs Ag/AgCl. (b) The enlarged near edge features of the spectra. The overlaid spectra suggest the no edge shifts and pre-edge peak diminished during the EXAFS data collection.

The final fit for the oxidised form yielded an R-factor of 0.0087 and reduced χ^2 of 70.1, whereas the reduced form gave an R-factor of 0.0158 and reduced χ^2 of 22.8. These statistics attest to the excellent agreement between the FEFF-derived model and the experimental EXAFS data.

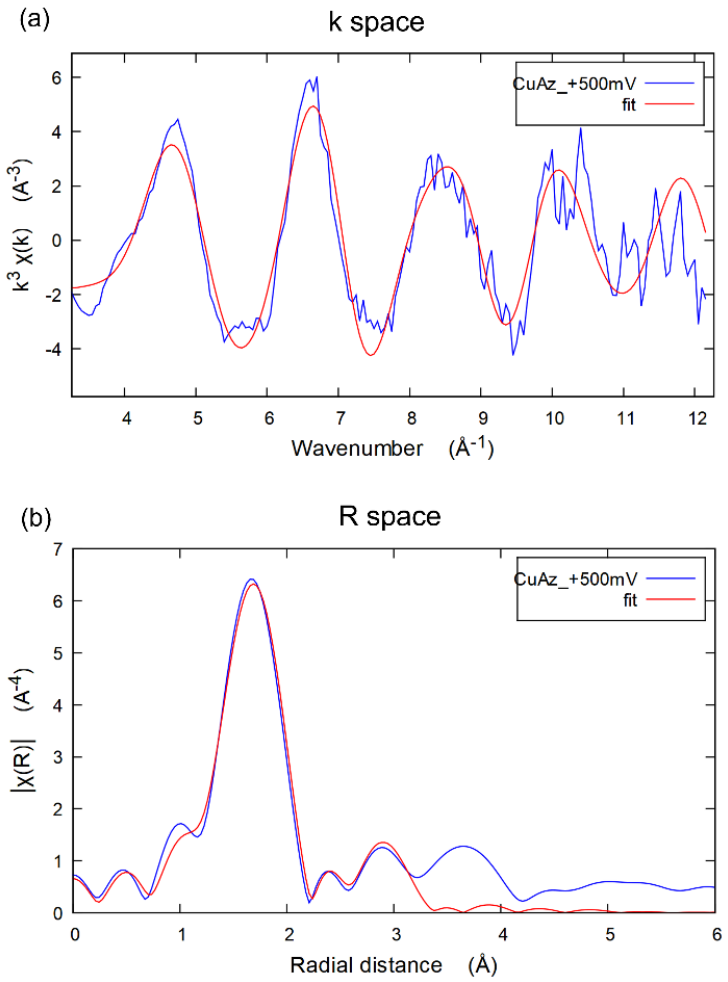

Figure 7.12: Experimental EXAFS data (blue) and fitted data(red) of electrochemically oxidised azurin measured in XAS-SEC cell at +500 mV. (a) EXAFS spectrum of electrochemically oxidised azurin in k-space. (b) The phase shift-corrected Fourier transform of the EXAFS in R-space.

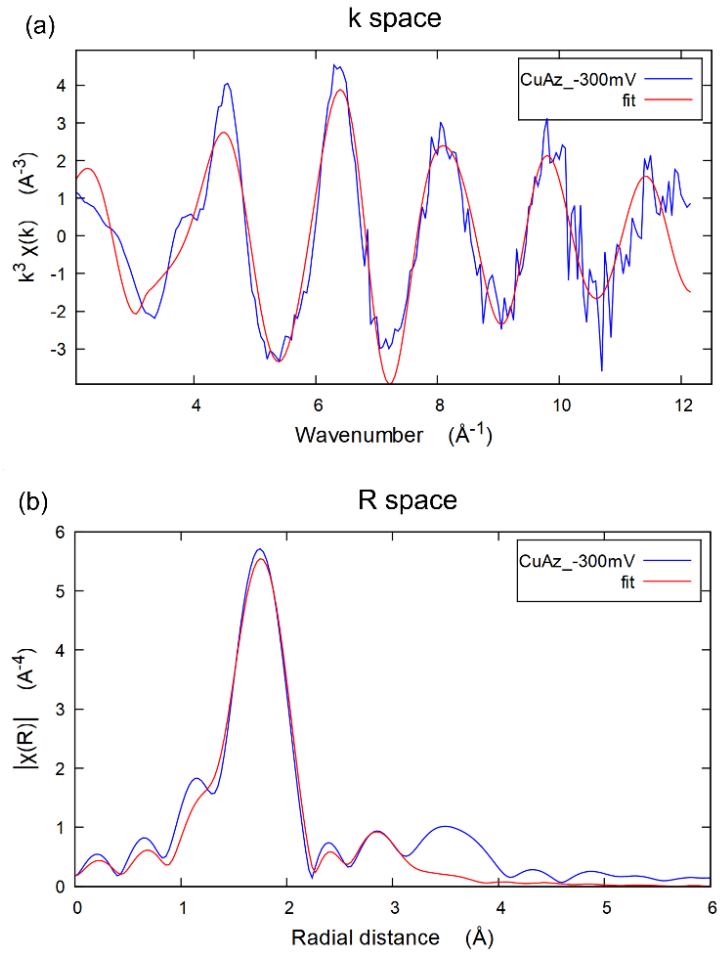

Figure 7.13: Experimental EXAFS data (blue) and fitted data(red) of electrochemically reduced azurin measured in XAS-SEC cell at -300 mV. (a) EXAFS spectrum of electrochemically reduced azurin in k-space. (b) The phase shift-corrected Fourier transform of the EXAFS in R-space.

The EXAFS fits were based on seven independent data points, with the amplitude reduction factor (S_0^2) fixed at 0.90 to yield the most reliable results. Apart from the energy-shift parameter (ΔE_0), each ligand atom was assigned its own bond-length adjustment (Δr), except that the two histidine nitrogen shared a single Δr value to reflect their nearly identical coordination environment. The Debye–Waller factor (σ^2) for the first-shell scatterers was constrained to be uniform, since these donors are tightly bound to the Cu centre and exhibit minimal thermal disorder. The glycine-carbonyl oxygen was also given the same σ^2, whereas the methionine sulphur required a separate σ^2 owing to its longer Cu–S distance. All four

imidazole-ring carbons were assigned Δr and σ^2 values matching those of the histidine nitrogens, on the basis that the ring is a rigid moiety and its atoms should undergo similar dynamic and static disorder.

Table 7.1 summarises the refined bond lengths and Debye–Waller factors for oxidised and reduced azurin measured in the XAS–SEC cell. Across the board, the Cu–ligand distances in the Cu (II) form are shorter by 0.06–0.09 Å than those in Cu (I), consistent with stronger electrostatic attraction to the more electron-deficient metal ion. The room-temperature EXAFS-derived distances agree closely with values obtained from EXAFS at cryogenic temperature[8,28] and computational predication from QM/MM models,[29] confirming the validity of the *in-situ* measurement approach and provide a good comparison between structural information obtained from crystallography and solution sample (Table 7.2).[23]

Table 7.1: The EXAFS fit parameters of electrochemically oxidised and reduced azurin measured in the XAS-SEC cell.

Atom	Oxidised Azurin / Å (Debye-Waller factor σ^2 / Å^2)	Reduced Azurin / Å (Debye-Waller factor σ^2 / Å^2)
N (his46）	1.85 ± 0.03 (0.001)	1.93 ± 0.02 (0.002)
N (his117)	1.97 ± 0.03 (0.001)	2.04 ± 0.02 (0.002)
S (cys112)	2.15 ± 0.01 (0.001)	2.21 ± 0.01 (0.002)
O (gly45)	3.03 ± 0.07 (0.001)	3.12 ± 0.05 (0.002)
S (met121)	3.42 ± 0.06 (0.005)	3.49 ± 0.05 (0.008)

Several alternative scattering-path combinations were evaluated as the roadmap of EXAFS fitting and fitting parameters are summarised below in Table 7.3. The set of single scattering

paths used to analyse the coordination bond distances discussed above is noted as "add C_{his}", meaning the carbon atoms on histidine are included. Apart from this set, the first shell fit was achieved by only considering the three strongest back scatters on the equatorial plane with R range 1-2.3 Å, with the Debye-Waller factors constrained to share the same value.

Table 7.2: The ligand-copper distances of azurin measured or calculated from different approaches.

Atom	Reduced Azurin / Å [28]		QM/MM [29]	Crystallography [23]	
	Oxidised / Å	Reduced / Å	Oxidised / Å	Oxidised / Å	Reduced / Å
N (his46)	1.86 ± 0.02	1.91 ± 0.02	1.90	2.04	1.91
N (his117)	1.94 ± 0.02	2.01 ± 0.02	1.89	1.99	2.01
S (cys112)	2.12 ± 0.01	2.19 ± 0.02	2.14	2.14	2.19
O (gly45)	2.82 ± 0.05	2.98 ± 0.05	2.95	2.72	2.98
S (met121)	3.39	3.35	3.07	3.26	3.35

The R range was then expanded to 3.2 Å to study the axial scatterers. This fit considers the single scattering path of all ligated atoms, while yield a slightly worse fit compared with the "add C_{his}" fit. Comparing the three fits, the distance of scatterers related to the first shell are highly consistent and the deviation is 0.1 Å within the error. The close agreement of first-shell distances across all three approaches confirms the reliability and robustness of the refined coordination parameters.

Table 7.3: EXAFS fit parameters using different sets of single scattering. The unit of distances between ligand atom to Cu is in Å. The "first shell" fitting means only single scatterings of two histidine nitrogen atoms, and a cysteine sulfur is considered. "All ligands" fitting means two axial ligand atoms are considered, including an oxygen atom from glycine and a sulphur from methionine. "Add C_{his}" fitting is the reported fitting methods in this chapter, representing singe scatterings of two carbon atoms on two histidine are included.

Data	Fitting	N_{his41}	N_{his117}	S_{cyc112}	O_{gly45}	S_{met121}
Reduced	First shell	1.94	2.05	2.21		
	All ligands	1.94	2.05	2.22	2.95	3.50
	Add C_{his}	1.93	2.04	2.21	3.12	3.49
Oxidised	First shell	1.87	1.98	2.16		
	All ligands	1.86	1.98	2.16	2.86	2.82
	Add C_{his}	1.85	1.97	2.15	3.03	3.42

The *in-situ* EXAFS measurements provide the first structural characterisation of azurin in solution at ambient temperature. The refined Cu–ligand distances closely match those obtained from frozen or crystalline samples, demonstrating that the XAS–SEC configuration can perform reliable and accurate in situ Cu K-edge EXAFS experiments on a sensitive biological sample.

7.5 Conclusion and Discussion

In summary, this chapter shows the novel XAS–SEC cell set-up originally designed by Dr. Stephen Best for small molecules enables reliable *in-situ* characterisation of sensitive blue-copper proteins at ambient temperature. It has remarkably enhanced electrochemical performance, photodamage prevention, and spectral quality, while significantly lowering the

required sample volume compared to the earlier version of XAS-SEC cell and conventional cytostatic methods. The key to this success lies in the precise control of solution flow through the working electrode chamber. By optimising the pulse stroke, net flow rate, redox mediator selection, and X-ray beam intensity, high-quality, photodamage-free XAS spectra can be acquired *in-situ* from relatively small sample volumes.

The spectra of Cu-azurin recorded *in-situ* at room temperature within the flow XAS-SEC cell exhibit markedly diminished photoreduction compared with those obtained under static cryogenic conditions. *In-situ* XANES extracts subtle changes on edge during the redox reaction under refined redox levels. *In-situ* EXAFS analysis of both electrochemically oxidised and reduced azurin yields Cu–ligand distances for the five coordinating residues that are in excellent agreement with crystallographic data and previously reported XAS results.

The flow cell enables desired electrochemical control over the distribution of redox species. It also may acts as a sink for photogenerated reactive species, as the OCP of the cell appears to be highly sensitive to exposure of the sample to the beam which is reported previously.[11] Once flow parameters are established, as little as 100 µL of sample can be cycled more than ten times over several hours without any detectable spectral degradation, allowing for complete data collection from total volumes as low as 300 µL.

The successful XANES titration of azurin illustrates that the XAS–SEC cell enables *in-situ* XAS studies of redox enzymes under ambient conditions. The Cu K-edge XANES spectra showed a progressive shift in edge position upon oxidative stepping, especially near the redox potential of azurin. This confirms that the electrochemical cell precisely controls the sample's redox state while coupled XAS detects corresponding changes in local geometry and electronic structure. Furthermore, this set-up facilitated the first room-temperature *in-situ* EXAFS analysis of a redox enzyme, enabling real-time structural interrogation of biological systems

under catalytically relevant conditions.

While only a limited number of XAS–SEC studies on molecular and enzymatic catalysts have been published, the approach holds great promise. For instance, Crespilho and co-workers demonstrated operando Cu K-edge XAS of bilirubin oxidase from *Myrothecium verrucaria* under turnover conditions.[14] The enzyme was immobilised on carbon nanoparticle-modified electrodes to enhance loading. Their study revealed redox-state changes among the four copper sites during oxygen reduction catalysis. However, this approach suffered from limited electrochemical control due to high enzyme loading. The immobilised nature of the enzyme raised concerns about signal contributions from photodamaged or electrochemically unresponsive populations, given that XAS provides a cumulative signal from all metal atoms present.

Similarly, DeBeer and colleagues conducted in-situ XAS studies of *D. vulgaris MF* [NiFe]-hydrogenase using redox polymers to immobilise the enzyme on electrodes. While this approach demonstrated feasibility, it also highlighted unresolved challenges with electrode coverage, stability, photodamage, and redox control.[16]

The success of the *in-situ* XAS–SEC cell experiments with azurin underscores the capability of this system to reliably and reproducibly characterise metalloenzymes and catalytic systems in solution at room temperature. Key advantages include minimised sample volume (below 300 µL), reproducible electrochemical control, and robust photodamage suppression. These features establish the cell as a versatile and valuable tool for future XAS investigations. Given the longstanding importance of XAS in elucidating metalloenzyme structure and function, the present methodology provides a powerful platform for probing redox-active systems such as the FeMo-cofactor of nitrogenase, the oxygen-evolving complex of photosystem II, and particularly [NiFe]-hydrogenases, with precise electrochemical control.

7.6 References

1 F. de Groot, *Chem, Rev*, 2001, **101**, 1779–1808.

2 S. Stripp, O. Sanganas, T. Happe and M. Haumann, *Biochem,*, 2009, **48**, 5042–5049.

3 H. Wang, C. Y. Ralston, D. S. Patil, R. M. Jones, W. Gu, M. Verhagen, M. Adams, P. Ge, C. Riordan, C. A. Marganian, P. Mascharak, J. Kovacs, C. G. Miller, T. J. Collins, S. Brooker, P. D. Croucher, K. Wang, E. I. Stiefel and S. P. Cramer, *J. Am. Chem. Soc.*, 2000, **122**, 10544–10552.

4 Z. Gu, J. Dong, C. B. Allan, S. B. Choudhury, R. Franco, J. J. G. Moura, I. Moura, J. LeGall, A. E. Przybyla, W. Roseboom, S. P. J. Albracht, M. J. Axley, R. A. Scott and M. J. Maroney, *J. Am. Chem. Soc.*, 1996, **118**, 11155–11165.

5 P. A. Ash, S. E. T. Kendall-Price and K. A. Vincent, *Acc. Chem. Res.*, 2019, **52**, 3120–3131.

6 S. Foerster, M. Stein, M. Brecht, H. Ogata, Y. Higuchi and W. Lubitz, *J. Am. Chem. Soc.*, 2003, **125**, 83–93.

7 C. M. Groeneveld, M. C. Feiter, S. S. Hasnain, J. van Rijn, J. Reedijk and G. W. Canters, *BBA*, 1986, **873**, 214–227.

8 S. DeBeer, C. N. Kiser, G. A. Mines, J. H. Richards, H. B. Gray, E. I. Solomon, B. Hedman and K. O. Hodgson, *Inorg, Chem.*, 1999, **38**, 433–438.

9 M. Hävecker, A. Knop-Gericke, H. Bluhm, E. Kleimenov, R. W. Mayer, M. Fait and R. Schlögl, *App. Surf. Sci.*, 2004, **230**, 272–282.

10 S. Permien, T. Neumann, S. Indris, G. Neubüser, L. Kienle, A. Fiedler, A.-L. Hansen, D. Gianolio, T. Bredow and W. Bensch, *Phys. Chem. Chem. Phys.*, 2018, **20**, 19129–19141.

11 S. P. Best, V. A. Streltsov, C. T. Chantler, W. Li, P. A. Ash, S. Hayama and S. Diaz-Moreno, *J. Synchrotron Radiat.*, 2021, **28**, 472–479.

12 R. N. Samajdar and A. J. Bhattacharyya, *J. Phys. Chem. B*, 2021, **125**, 5258–5264.

13 J. Timoshenko and B. Roldan Cuenya, *Chem. Rev.*, 2021, **121**, 882–961.

14 L. J. A. Macedo, A. Hassan, G. C. Sedenho and F. N. Crespilho, *Nat. Commun.*, 2020, **11**, 316.

15 R. J. K. Wiltshire, C. R. King, A. Rose, P. P. Wells, M. P. Hogarth, D. Thompsett and A. E. Russell, *Electrochim. Acta.*, 2005, **50**, 5208–5217.

16 K. Cząstka, A. A. Oughli, O. Rüdiger and S. DeBeer, *Faraday Discuss.*, 2022, **234**, 214–231.

17 R. Chatterjee, C. Weninger, A. Loukianov, S. Gul, F. D. Fuller, M. H. Cheah, T. Fransson, C. C. Pham, S. Nelson, S. Song, A. Britz, J. Messinger, U. Bergmann, R. Alonso-Mori, V. K. Yachandra, J. Kern and J. Yano, *J. Synchrotron. Radiat.*, 2019, **26**, 1716–1724.

18 S. P. Best and M. H. Cheah, *Radiation Phy. and Chemi.*, 2010, **79**, 185–194.

19 M. I. Bondin, G. Foran and S. P. Best, *Aust. J. Chem.*, 2002, **54**, 705–709.

20 S. P. Best, A. Levina, C. Glover, B. Johannessen, P. Kappen and P. A. Lay, *J. Synchrotron Radiat.*, 2016, **23**, 743–750.

21 G. N. George, I. J. Pickering, M. J. Pushie, K. Nienaber, M. J. Hackett, I. Ascone, B. Hedman, K. O. Hodgson, J. B. Aitken, A. Levina, C. Glover and P. A. Lay, *J. Synchrotron Radiat.*, 2012, **19**, 875–886.

22 R. S. K. Ekanayake, V. A. Streltsov, S. P. Best and C. T. Chantler, *J. Appl. Crystallogr.*, 2024, **57**, 125–139.

23 H. Nar, A. Messerschmidt, R. Huber, M. van de Kamp and G. W. Canters, *J. Mol. Biol.*, 1991, **221**, 765–772.

24 A. G. Tamirat, X. Guan, J. Liu, J. Luo and Y. Xia, *Chem. Soc. Rev.*, 2020, **49**, 7454–7478.

25 L. S. Kau, D. J. Spira-Solomon, J. E. Penner-Hahn, K. O. Hodgson and E. I. Solomon, *J. Am. Chem. Soc.*, 1987, **109**, 6433–6442.

26 J. L. DuBois, P. Mukherjee, T. D. P. Stack, B. Hedman, E. I. Solomon and K. O. Hodgson, *J. Am. Chem. Soc.*, 2000, **122**, 5775–5787.

27 S. DeBeer, P. Wittung-Stafshede, J. Leckner, G. Karlsson, J. R. Winkler, H. B. Gray, B. G. Malmström, E. I. Solomon, B. Hedman and K. O. Hodgson, *Inorganica. Chim. Acta.*, 2000, **297**, 278–282.

28 K.-C. Cheung, R. W. Strange and S. S. Hasnain, *Acta. Crystal. Section D*, 2000, **56**, 697–704.

29 C. E. Schulz, M. van Gastel, D. A. Pantazis and F. Neese, *Inorg. Chem.*, 2021, **60**, 7399–7412.

Chapter 8: Conclusions and Outlook

The work presented in this thesis demonstrates new methodologies that integrate information on [NiFe]-hydrogenases from various sample-handling approaches and spectroelectrochemical techniques. Single [NiFe]-hydrogenase crystals at well-defined redox levels and active site states were systematically generated by electrochemical poising, guided by infrared spectroelectrochemical characterisation. In parallel, an *in-situ* X-ray absorption spectroelectrochemical technique was developed to allow real-time characterisation of biological samples under electrochemical control. By combining the strengths of multiple biophysical techniques, a comprehensive understanding of these complex metalloenzymes has been achieved, encompassing catalytic mechanisms, structural determination, and reactivity towards a range of π-acid ligands.

IR microspectroelectrochemical characterisation on Hyd-1 and Hyd-2 single crystals

In Chapters 3, microscopic IR spectroelectrochemical titrations defined the potential windows for catalytically relevant states, Ni-B, Ni_a-SI, Ni_a-R, Ni_a-C and Ni_a-L, in both Hyd-1 and Hyd-2 crystals. Dynamic equilibria between these states were mapped, providing the foundation to identify specific poising conditions that enrich a targeted redox state. These results established a reference speciation map for all subsequent structural studies.

Development of circulating electrochemical cell for single hydrogenase crystals

Chapter 4 describes the development of a circulating electrochemical cell capable of precise redox control over single crystals of Hyd-1 and Hyd-2. This was achieved by circulating a redox mediator buffer between a sample chamber and a three-electrode electrochemical cell. Redox states identified from *in-situ* IR spectroelectrochemistry were reproducibly generated in crystals. The cell successfully mimics redox control achieved via previous microscopic techniques and enables access to single crystals in well-defined active site states.

Atomic-resolution structures of each catalytically-relevant active site state

Using the electrochemical approach developed in Chapter 4, Chapter 5 reports atomic-resolution structures of Hyd-1 and Hyd-2 in spectroscopically verified redox states. The crystal structures of the Ni_a-SI state for both enzymes reveal a vacant bridging coordination site, with residual electron density consistent with a partially ordered water molecule located 1.9 Å from the Ni atom. This is the first direct evidence for hydration of the Ni_a-SI state and suggests a potentially functional water molecule at the active site. The identity of Ni_a-SI in both Hyd-1 Hyd-2 crystals was further confirmed by reaction with CO to generate the inhibited, Ni-SCO state. The structure shows clear electron density for a diatomic ligand bound to Ni in a bent conformation.

The structures of Ni_a-R in Hyd-1 and Ni_a-C in Hyd-2 are nearly identical and exhibit residual electron density at the bridging position, consistent with a bridging hydride. In the Ni_a-L_{II} structure, Glu28 adopts a unique 'swung-in' conformation, forming a hydrogen bond with

Cys576 at 2.7 Å. This provides the first direct structural evidence of Glu28's involvement in proton transfer during catalysis.

Studies of reactions of Hyd-1 and Hyd-2 single crystals with a series of π-acid ligands

In Chapter 6, a series of isoelectronic π-acid ligands, including cyanide, and various isocyanides, were used to investigate inhibition of Hyd-1 and Hyd-2 single crystals at the Ni_a-SI state. IR spectroscopy and crystallography confirm that cyanide binds at the Ni position like CO and forms a stable inhibited state, counter to previous claims that it induces Ni-B formation.

Isocyanides were found to inhibit Hyd-1 and Hyd-2 Nia-SI in crystalline state and they bound to the active site at Ni in terminal position. The clear electron density in the methyl- and ethyl-isocyanide bounded crystal structures show they adopt a distorted conformation at the active site, consisting of a bent coordination bond and nitrogen-alkyl bond. Electron density maps reveal low occupancy for the ethyl tail, indicating a high degree of freedom within the gas channel. IR spectra confirm that isopropyl and n-butyl isocyanides also inhibit the active site, despite the absence of ordered electron density in X-ray structures. This likely reflects multiple conformations or partial occupancy near the active site.

Overall, titrating the alkyl substituent size establishes a practical size threshold for inhibitor access under crystallographic conditions. This offers a direct experimental measure of gas channel flexibility, with the maximum dynamic aperture falling between the dimensions of isopropyl and tert-butyl isocyanide.

Development of an X-ray absorption spectroscopy spectroelectrochemical cell

In Chapter 7, a novel XAS–SEC cell with a flow system was tested using azurin, a photo-sensitive metalloprotein. The success of *in-situ* XAS–SEC experiments at room temperature underscores the capability of this setup to study metalloenzymes under physiologically relevant conditions. Key advantages include reduced sample volume, precise electrochemical control, and suppression of photodamage.

Fine potential titrations captured subtle shifts in XANES features and, for the first time, enabled room-temperature *in-situ* EXAFS analysis on a redox enzyme. This allows real-time structural interrogation of biological systems under catalytically relevant redox conditions.

Outlook and future work

The microscopic IR spectroelectrochemical technique has been demonstrated as powerful tool for hydrogenase study in this Thesis. The structural determination of all long-lived catalytic relevant states of [NiFe]-hydrogenases are completed through this systemic and rational roadmap methodology by combing sample handing and spectroelectrochemical techniques. This encourages to extend this methodology to explore other redox proteins. In particular, [FeFe]-hydrogenases could benefit from this approach, as existing structural data are limited to the H_{ox} and H_{inact} states. Precise electrochemical control could allow trapping of more elusive intermediates, such as H_{red}, particularly if supported by tailored ligand modifications at the active site. Moreover, the structural determination of catalytic intermediate in other redox

protein such as nitrogenases and carbon monoxide dehydrogenase is also possible based on the methodology developed in this Thesis.

Trapping the state of enzyme which binds to natural substrate not only provide opportunities for studying its inhibitory behaviour to other molecules, but also feasible to trap the Michaelis-complex, insights into catalytic mechanism.

The XAS–SEC cell opens further opportunities for *in-situ* and *operando* XAS studies of complex metalloenzymes. Extending this application to [NiFe]-hydrogenases via Ni K-edge measurements could yield valuable insights into the redox behaviour of the Ni centre. A key challenge, however, would be obtaining informative and distinctive XANES spectra at the Ni K-edge under *in-situ* redox conditions. Although the formal oxidation state of the Ni ion changes between different active-site states, the total electron density of the entire [NiFe] cluster is likely buffered and remains relatively stable, largely due to the three π-accepting ligands on the Fe. Consequently, the Ni K-edge position may shift less dramatically across redox conditions than one might initially expect. Nevertheless, the XAS-SEC technique presents a significant opportunity for conducting *in-situ* EXAFS measurements on [NiFe]-hydrogenases, which would allow direct investigation of the number and identity of atoms ligated to the Ni ion. Moreover, probing other biological systems like the FeMo cofactor of nitrogenase could help bridge gaps between crystallographic and spectroscopic data, contributing to a more complete understanding of catalytic mechanisms in metalloenzyme.